**SLAC-R-571**
August 2001

# The Next Linear Collider Design: NLC 2001

*Stanford Linear Accelerator Center, Stanford University, Stanford, CA 94309*

Work supported by Department of Energy contract DE–AC03–76SF00515.

# 2001 Report on the
# NEXT LINEAR COLLIDER

A Report Submitted to Snowmass 2001

FERMILAB-Conf-01/075-E
LBNL-PUB-47935
SLAC-R-571
UCRL-ID-144077

# 2001 Report
*on the*
# NEXT LINEAR COLLIDER

## A Report Submitted to Snowmass '01

**June 2001**

**The NLC Collaboration**
**Nan Phinney, General Editor**

Prepared for the Department of Energy under contract number DE-AC03-76SF00515 by Stanford Linear Accelerator Center, Stanford University, Stanford, California. Printed in the Untied States of America. Available from National Technical Information Service, U.S. Department of Commerce, 5285 Port Royal Road, Springfield, Virginia 22161.

# Preface

There have been many advances in elementary particle physics since the U.S. High Energy Physics (HEP) community last met at Snowmass, CO in 1996. New results have made the need for a linear collider able to reach TeV energies with high luminosity more compelling than ever. International research and development for such a linear collider has kept pace, and the technology for such a collider now exists.

Work in the United States on the Next Linear Collider (NLC), and the writing of this Report, is led by the Stanford Linear Accelerator Center (SLAC), Fermi National Accelerator Laboratory (FNAL), Lawrence Berkeley National Laboratory (LBNL), and Lawrence Livermore National Laboratory (LLNL). Teams from Bechtel Nevada, the University of California at Davis, Los Alamos National Laboratory, the University of Massachusetts, and Stanford University have also made major contributions to the results in this Report.

There is broad international collaboration on R&D needed for the NLC. Scientists and engineers from the University of British Columbia, the Budker Institute of Nuclear Physics, Oxford University, Brunel University, and Royal Holloway University of London have contributed to the work reported here. The CLIC Study group at CERN has also collaborated on numerous topics. A long history of collaboration on X-Band technologies exists between the NLC development team and the Japanese Linear Collider (JLC) group. The content of this Report overlaps extensively with that of the SLAC-KEK ISG Report, *International Study Group Progress Report on Linear Collider Development,* N. Toge, ed., KEK Report 2000-7, SLAC-R-559, April 2000, and much of this work can also be found in the 1997 report of the JLC study group, *JLC Design Study,* JLC Design Study Group, N. Toge, ed., KEK Report 97-1, 1997.

This *2001 Report on the Next Linear Collider* has been prepared as a contribution to the 2001 DPF/DPB Snowmass Summer Study. It is an update of the *Zeroth-Order Design Report* that was prepared for Snowmass in 1996. This document provides a broad description of the NLC that touches on major issues and results in the development of the collider, but is not intended as a complete design document and much detail and discussion is left for presentatiton anad discussion at Snowmass. Chapters 1, 2 and 3 provide an introductionto the NLC for the general Snowmass audience. Chapters 4, 5, 6 and 7 provide a basis for discussions that will be held in the Snowmass machine working groups. Chapter 8 outlines work in progress on the possible use of the NLC beams to produce high-energy photon-photon collisions.

The world is entering a time of increasingly global planning for exploration of the HEP frontier. The U.S. physics community will meet at Snowmass with the DOE/NSF High Energy Physics Advisory Panel to recommend a long-range plan for HEP in the United States. These recommendations will be an important part of a global strategy for HEP for decades to come.

# Contents

## Chapter 1

## Chapter 2

## Chapter 3

# Chapter 5

# Chapter 6

# Chapter 7

# Chapter 1

## Overview

### 1.1 The Next Linear Collider

Recent studies in elementary particle physics have made the need for an $e^+e^-$ linear collider able to reach energies of 500 GeV and above with high luminosity more compelling than ever [1]. Observations and measurements completed in the last five years at the SLC (SLAC), LEP (CERN), and the Tevatron (FNAL) can be explained only by the existence of at least one particle or interaction that has not yet been directly observed in experiment. The Higgs boson of the Standard Model could be that particle. The data point strongly to a mass for the Higgs boson that is just beyond the reach of existing colliders. This brings great urgency and excitement to the potential for discovery at the upgraded Tevatron early in this decade, and almost assures that later experiments at the LHC will find new physics. But the next generation of experiments to be mounted by the world-wide particle physics community must not only find this new physics, they must find out what it is. These experiments must also define the next important threshold in energy. The need is to understand physics at the TeV energy scale as well as the physics at the 100-GeV energy scale is now understood. This will require both the LHC and a companion linear electron-positron collider.

A first *Zeroth-Order Design Report* (ZDR) [2] for a second-generation electron-positron linear collider, the Next Linear Collider (NLC), was published five years ago. The NLC design is based on a high-frequency room-temperature rf accelerator. Its goal is exploration of elementary particle physics at the TeV center-of-mass energy, while learning how to design and build colliders at still higher energies. Many advances in accelerator technologies and improvements in the design of the NLC have been made since 1996. This Report is a brief update of the ZDR.

There are other technologies that could be used as the basis for the next generation of linear collider. The DESY laboratory has submitted a design report [3] for a collider with a low-frequency superconducting rf accelerator. Both the NLC and the TESLA designs are extremely mature and have behind them a strong experience base of operating accelerators and specialized test facilities. Both designs and technologies can be expected to reach center-of-mass (cms) energies of 500 GeV with high luminosity, but each comes with its own risks, and each has its own connection to future colliders. Research and development is underway on two-beam acceleration that could lead to a multi-TeV linear collider in the future [4]. This is a high-frequency, room-temperature accelerator, which in many ways naturally extends the NLC technology.

The NLC is designed for optimal performance at 1-TeV cms energy, but with flexibility to begin operation at 500 GeV and be upgraded to match the needs of physics as they evolve. Key areas and systems are designed for energies above 1 TeV. The collider configuration is shown schematically in Fig.1.1. It has been developed jointly with the groups of physicists studying the physics goals for the collider [5]. The beam sources and damping rings that make up the injector for the main linacs are designed to meet specifications for 1.5-TeV collisions. Bypass lines along the main linac allow beams of various energies to be transported to the experiments. The main-linac rf systems are capable of generating 250-GeV beams (500-GeV cms collisions) in one half of the tunnel length that is included in the initial configuration. Upgrade to 1-TeV cms energy can be achieved by completion of the main linacs with replicas of the rf components used in the initial construction, or perhaps improved versions of those components. A main feature of the layout is a slight tilt (20 mrad) between the electron and positron main linacs that minimizes the bend angle needed to transport high-energy beams to one of the interaction regions, the high energy IR. The beam delivery system is sufficiently long to allow the high energy IR to be ultimately upgraded to energies in excess of 3 TeV. A synopsis of staging scenarios for the NLC is given in Table 1.1.

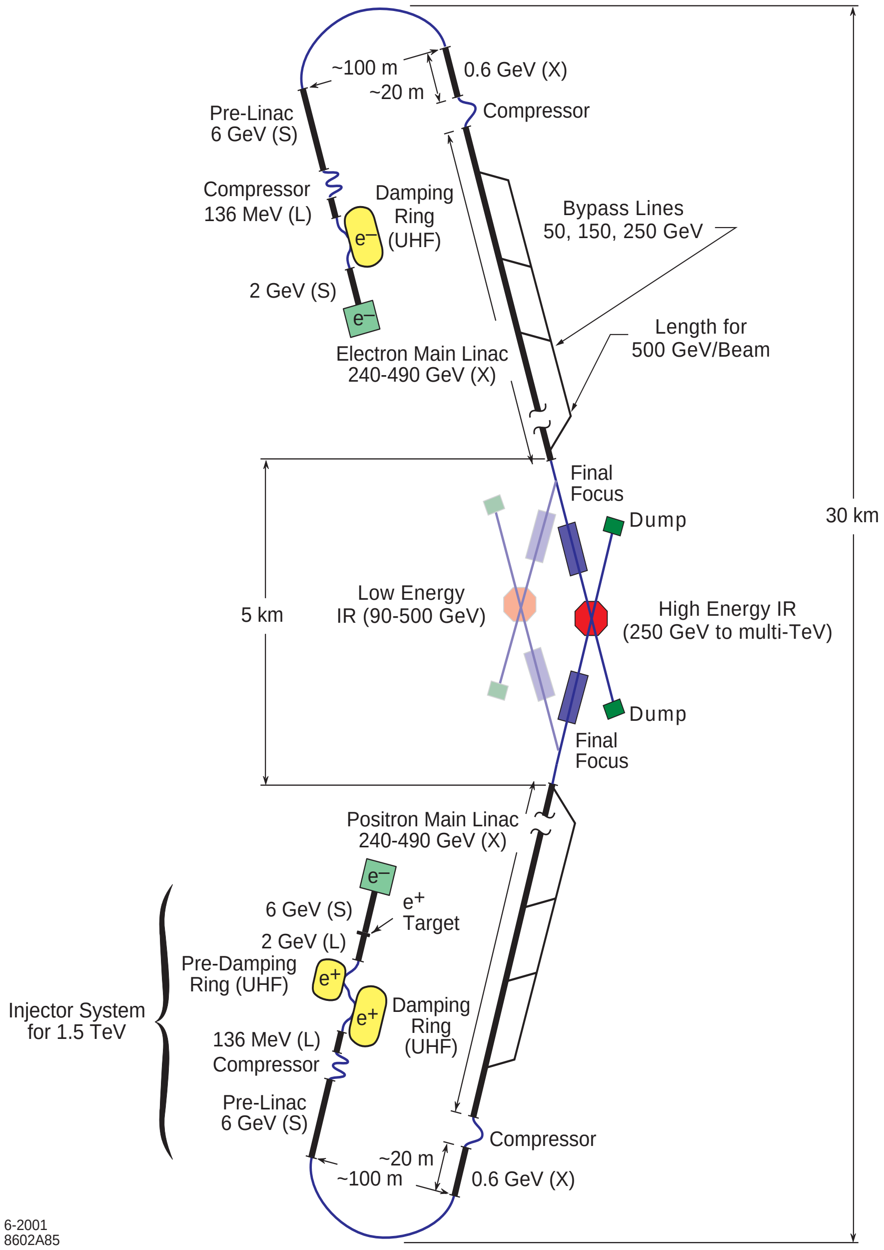

**Figure 1.1:** NLC Configuration.

**Table 1.1:** Staging of the NLC Center-of-Mass Energy

| STAGE | ENERGY (TEV) | INJECTOR | MAIN LINAC | BEAM DELIVERY |
|---|---|---|---|---|
| I | 0.5 | Initial Config | Initial Config | Initial Config |
| II | 1.0 | Initial Config | Install components in second half of the tunnel. | Initial Config |
| III | 1.5 | Initial Config | Extend linac 50%<br>Or<br>Double rf power | Reconfigure and strengthen final focus magnets. |

The remainder of this Report discusses the NLC project in more detail. Chapter 2 describes the layout of the accelerator, the parameters and luminosity, options for extending the physics capabilities, and multi-TeV considerations. Chapter 3 presents the possible sites under study for the NLC and the conventional facilities infrastructure. This is followed by chapters on the main-linac X-band rf system, the electron and positron injector complexes, and the beam delivery system. Beam dynamics and tolerance issues are discussed in Chapter 7. The $\gamma\gamma$ collider option is described briefly in Chapter 8 and in more detail in reference [1].

## 1.2 Experience Base and Performance Goals

The design of the NLC, and the technologies that have been chosen for it, are based on experience gained at the SLC, and at test facilities that are prototypes for the subsystems of the collider. The most important of these test facilities and their primary goals are listed later in Table 1.3. Together these provide demonstrations of each of the functions critical to producing, accelerating, transporting, focusing, colliding, and using beams with the qualities needed for the NLC. Each is a major facility, and combined (but not including the SLC) they represent an investment of several hundred million dollars. Their operation has become routine and, in fact, several of them are presently used in part for R&D not related to the NLC. Combined with the successful use of the SLC to study the physics of the $Z^0$ boson, these facilities represent more than a decade of experience and learning with the accelerator physics, operational techniques, and underlying technologies required for the next-generation linear collider.

A summary of the high-level design parameters of the NLC is given in Table 1.2. More detailed discussion of the design and other important parameters are given in later chapters of this Report, but this set illustrates the physics potential of the collider, and serves to guide this introductory discussion.

The energy goal for the NLC is ten times the mass (91 GeV) of the $Z^0$ studied at the SLC, and the luminosity goal is $10^4$ times that reached at the SLC. This clearly makes it important to understand the factors that determine the luminosity, and to demonstrate that they can be achieved. The luminosity of a linear collider is given by,

$$L = \frac{2H_D}{4\pi E_{cms}} \frac{N}{\sigma_x} \frac{P_b}{\sigma_y}$$

where N is the number of particles in each colliding bunch, $P_b$ is the power in each beam, and $\sigma_x$ and $\sigma_y$ are the horizontal and vertical dimensions of the beams at the collision point. The parameter $H_D$ is the enhancement of the luminosity due to the pinch that each beam experiences as it passes through the opposing beam. The ratio $N/\sigma_x$ determines $\Upsilon_{ave}$, the ratio of the peak fields in the beam-beam interaction to the critical field for spontaneous production of electron-positron pairs. This parameter is restricted by the fact that the $e^+e^-$ pairs can cause excessive backgrounds in the experimental detector. To achieve high luminosity requires beams with high power $P_b$, or high beam current, and small transverse phase space (emittance) that can be focused to a small vertical height $\sigma_y$ at the collision point.

**Table 1.2**: Summary of Design Parameters for the High Energy Interaction Region

| **PARAMETER** | **STAGE I** | **STAGE II** |
|---|---|---|
| Energy (GeV in CMS) | 500 | 1000 |
| Luminosity ($10^{34}$ $cm^{-2}$ $s^{-1}$) | 2.0 | 3.4 |
| Pulse Format | $0.75 \times 10^{10}$ particles in each of 190 bunches spaced 1.4ns apart (120 pulses per second) | $0.75 \times 10^{10}$ particles in each of 190 bunches spaced 1.4 ns apart (120 pulses per second) |
| $\sigma_x/\sigma_y$ at the Collision Point (nm) | 245 / 2.7 | 190 / 2.1 |
| Pinch Enhancement ($H_D$) | 1.4 | 1.5 |
| $\Upsilon_{ave}$ (fraction of critical field) | 0.11 | 0.29 |
| Effective Gradient (MV/m) | 48 | 48 |
| Linac Length (km per linac) | 6.3 | 12.8 |

Except for the NLCTA, the facilities listed in Table 1.3 have all been constructed to learn how to create high luminosity at a linear collider. The SLC was the first linear collider. Its goal was simultaneously to deliver timely and important results from experiments in particle physics while developing the accelerator physics and techniques needed to make a linear collider work. This required an intense effort that constantly pushed the boundaries of accelerator technology. The most important of these developments was the engineering of the SLC as a 'smart' machine with sophisticated diagnostics and a flexible control system. The FFTB addressed the problem of nanometer-scale mechanical stability, beam instrumentation and control. The ATF addressed the problem of creating a very-low-emittance beam. The X-Band linear collider requires manufacture, alignment, and stabilization of machine components to high precision. Microns and nanometers are small. But modern techniques in manufacture can comfortably achieve these accuracies, and instrumentation exists that can measure the beam properties to the required precision. The ASSET facility in the SLAC linac is a place where these capabilities can be verified. The remainder of this section will discuss some of the highlights from these experiments, and discuss some of the work at the NLCTA. The remainder of this Report will provide more in-depth coverage.

**Table 1.3:** Prototype Test Facilities

| **TEST FACILITY** | **PURPOSE** | **DATES** |
|---|---|---|
| ATF | Learn to create a small beam phase space. | 1995 - present |
| ASSET | Learn to maintain beam phase space. | 1996 - present |
| FFTB | Learn to measure and manipulate phase space to focus the beam. | 1994 - 1998 |
| NLCTA | Learn to accelerate beams and control energy. | 1995 - present |
| SLC | Learn to put it all together and do physics. | 1989 - 1998 |

### 1.2.1 The Stanford Linear Collider (SLC)

The development of the SLC opened new territory in accelerator design and operation. Sophisticated on-line modeling of nonlinear physics was developed to provide rapid diagnosis and tuning of the machine. Correction techniques were extended from first-order trajectory steering to include second-order tuning of the emittance of the beam, and from hands-on tuning by operators to fully automated control. Beam steering, beam collision, and spot-size optimization (luminosity) were ultimately done entirely by automated computer feedback systems. The fundamental lessons learned were that rapid and precise diagnostic instrumentation, on-line and automated analysis of data, and computer control of the machine are the keys to achieving high luminosity in a linear collider. Submicron colliding beams ($\sigma_y \approx 700$ nm) became the norm in the SLC. Significant pinch enhancement ($H_D \cong 2.0$) was achieved. The experimental detector routinely acquired luminosities of 2-3x$10^{30}$ cm$^{-2}$s$^{-1}$ with > 80% uptime (approaching the peak luminosity in the original conceptual design, however with very different beam parameters).

### 1.2.2 The Final Focus Test Beam

The Final Focus Test Beam (FFTB) significantly extended the lessons learned at the SLC. The FFTB was built by an international collaboration [6] to learn how to control and focus beams to produce high luminosity at linear colliders. The FFTB is a 200-meter-long, final-focus prototype built at the end of the SLAC linac to use the 46-GeV SLC damped electron beam. Instrumentation able to measure beam positions with a precision of 25 nanometers, and remotely controlled supports able to reproducibly move quarter-ton magnets in 300-nanometer steps were developed. Beam-based algorithms were used to align the FFTB with micron accuracy. Special care was taken to passively stabilize the temperature of the tunnel to 0.1 degree centigrade for extended periods of time. Component support foundations stabilized the transverse positions of FFTB components to within nanometers of each other. The FFTB demonstrated the optical principles and techniques needed for a linear collider final focus. It achieved a larger demagnification factor than the NLC will require, and demonstrated control of second-order chromatic dilutions. Spot sizes of 60-70 nanometers were measured, in good agreement with theory [7].

Experiments at the FFTB also studied the nonlinear quantum electrodynamics that will occur in the beam-beam interaction of the NLC. A laser pulse of high peak power (0.5 J in 2 ps) was focused to small dimensions and collided with the FFTB electron beam. The electromagnetic fields of the laser focus as seen by the electron beam were those that will occur in the NLC with $\Upsilon = 0.15\text{-}0.20$. The measured yields of electrons, positrons, and high-energy photons from these collisions were found to be in excellent agreement with theory [8]. The results and experience from the FFTB lend confidence in the design of the NLC final focus and the understanding of the beam-beam interaction.

### 1.2.3 The Damping Ring at the Accelerator Test Facility (ATF)

The beam can be focused to a small spot only if the phase space occupied by the beam particles is sufficiently condensed. The emittance goals for the NLC are two orders of magnitude smaller than achieved at the SLC. Like the SLC, the NLC is designed to use synchrotron-radiation damping in a storage ring to produce the required emittance. Unlike the SLC, the NLC ring includes a length of wiggler magnets to enhance damping. A full-scale wiggler-enhanced prototype ring has been built as part of the Accelerator Test Facility (ATF) at KEK [9]. When fully damped, the beam size in the ATF ring is typically a few microns in dimension. It has been necessary to develop noninvasive instrumentation to measure this size. A 'laser wire' created by focusing a laser beam through a waist perpendicular to the ring orbit has been successfully commissioned for this purpose. Emittances within a factor 2 of the desired values have been measured with this device. Beam studies show strong signals of the intrabeam scattering of particles expected to occur in such dense beams. Intrabeam scattering is a common phenomenon in proton storage rings, but rarely seen in electron rings. The observed strength of the intrabeam scattering indicates that it may be possible to achieve emittances below the initial ATF specifications. Improvements in the beam-position-monitor electronics are being sought that will allow beam-based alignment procedures to reduce residual dispersion and coupling to the levels needed to reach this goal.

### 1.2.4 Accelerator Structure Design and ASSET

Each particle in the beam leaves electromagnetic wakefields as it passes through the physical apertures of the machine. These wakefields exert forces on other particles in the beam, and so there is a correlation between the charge and phase space of the beam as it reaches the interaction region. Control of transverse (dipole) wakefields, which dilute the beam emittance, is one of the most critical issues posed by the NLC performance goals. Many years of work have been devoted to solving this problem, and today there is confidence that the NLC design contains sufficient margin to assure that the machine will perform as planned. Reduction of the effects of wakefields is done in part by reducing the charge in each NLC bunch by a factor of five below that in the SLC. Nonetheless it remains essential that the machine apertures are nearly azimuthally symmetric, and that the beam passes close to their centers. Of greatest concern are the accelerating structures of the linacs. The wavelength of the rf in the X-band NLC accelerator (2.6 cm) is four times smaller than the wavelength of the rf in the SLAC S-band accelerator (10.4 cm), so the dimensions of the NLC structures are four times smaller than the SLC structures. Tolerances on the manufacture and alignment of the structures, and the steering of the beam, are one to two orders of magnitude tighter in the NLC than in the SLC. It is necessary not only to use state-of-the-art techniques to manufacture the NLC structures, but also to have a proven strategy to align the structures with respect to each other and with respect to the magnetic lattice of the linac that defines the beam trajectory.

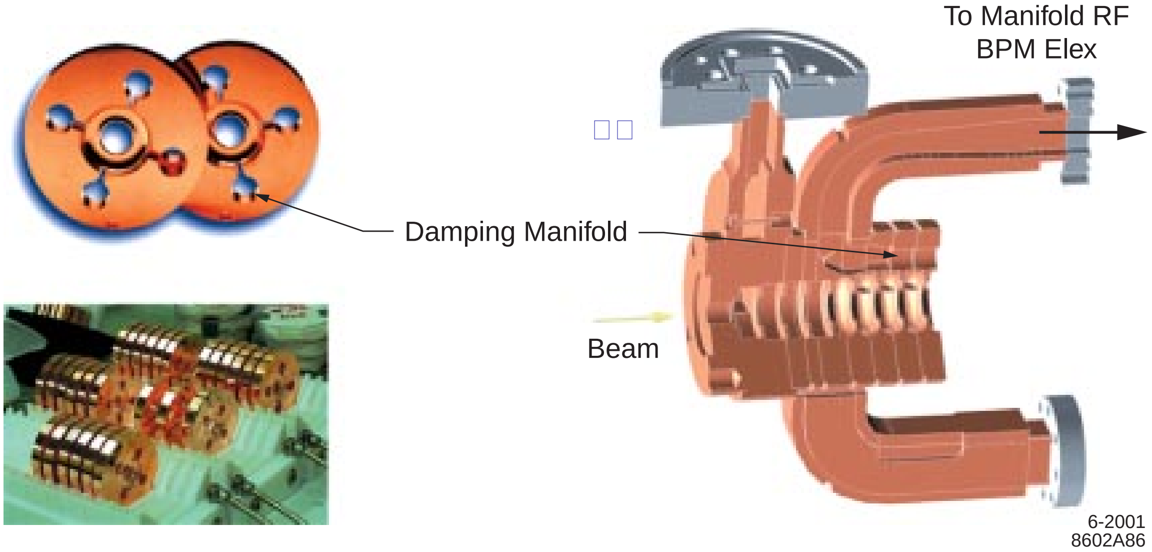

**Figure 1.2:** An X-Band Accelerator Structure. Individual cells are manufactured on precision high-speed lathes and bonded into meter-long structures. Highlighted in the figure are the manifolds that are used to decouple and damp dipole wakefields left by beam particles as they pass through the structure. The power in these manifolds is extracted and used to measure the position of the beam with respect to the center of the azimuthally symmetric structure.

Since it is not possible to completely eliminate manufacturing errors, the structures of the NLC accelerator are designed to inherently minimize wakefields. The design also provides a direct readout of the position of the beam in the structure, so that it is possible to align the linac with micron accuracy. First, the dipole wakefields are (detuned) by varying the transverse dimensions of the structure slightly from cell-to-cell. This avoids a coherent buildup of contributions from the many cells (approximately 100) in a meter-long structure. Further reduction of the wakefields is accomplished by coupling each cell to an rf manifold designed to extract power above the fundamental accelerating frequency of 11.424 GHz. As shown in Fig. 1.2, these damping manifolds can also be used as rf beam-position monitors by recording the power left in each of the channels. By mounting the structures on movable supports similar to those used in the FFTB, beam-based measurements can be used to dynamically align the accelerator.

Modern manufacturing tools are capable of accuracies considerably better than required for the NLC structures. Individual cells can be turned on high-speed lathes to achieve frequency errors below 1 MHz to be compared to a tolerance of 3 MHz. Techniques to bond cells into meter-long structures have been developed that maintain their straightness within NLC requirements. Figure 1.3 shows the cell-to-cell alignment in a 1.8-meter structure measured mechanically in the laboratory (with a Coordinate Measurement Machine). Also shown in the figure is the straightness of the same structure measured with the readout of signals induced in the rf damping manifold by an electron beam pulse. The detailed agreement is spectacular. This prototype easily satisfies the rms tolerance of 10 μm on the combination of the structure straightness and the alignment of its centroid to the beam.

Final verification of the microwave properties of detuned and damped structures is done at the ASSET facility in the SLAC linac. Bunches of positrons from the SLC damping rings are used to excite wakefields and then directly measure their affect on the trajectory of a trailing electron bunch. The data shown in Fig. 1.4 are in excellent agreement with theoretical calculations over the full length of the NLC bunch train, and over three orders of magnitude in wake amplitude [10]. These studies demonstrate that the design, manufacture, and operational strategy for the X-band structures will allow the beam emittance to be preserved during acceleration to high energies.

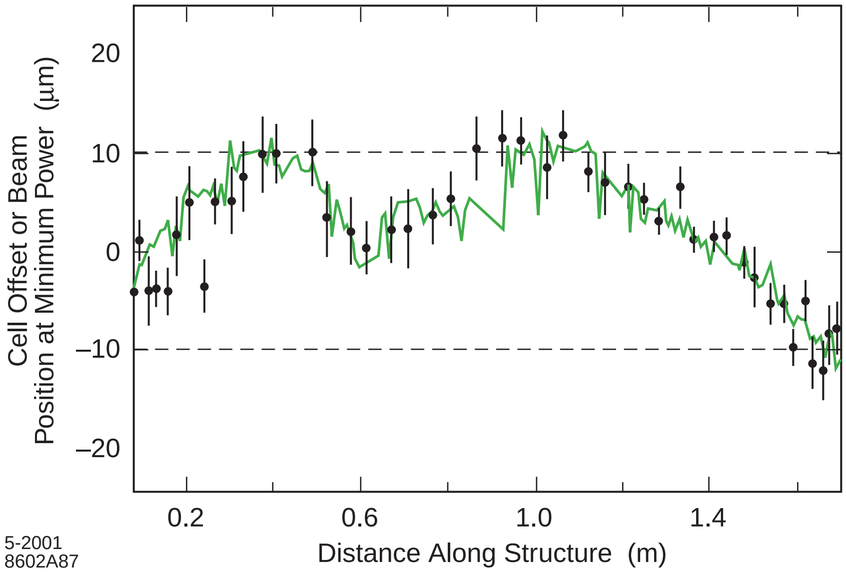

**Figure 1.3:** The Cell-to-Cell Alignment of a 1.8-meter Accelerator Structure. Measurements made on a coordinate measuring machine (CMM) are given by the solid curve, and the data points are the result of measurements made by passing a beam of electrons through the structure and determining the position of each cell from the power induced in the wakefield damping manifolds. The position of the beam in each cell can be determined because the frequency of the manifold signal from each cell is unique - the structure is also detuned. The rms tolerance on the combined manufacture and readout accuracy is shown.

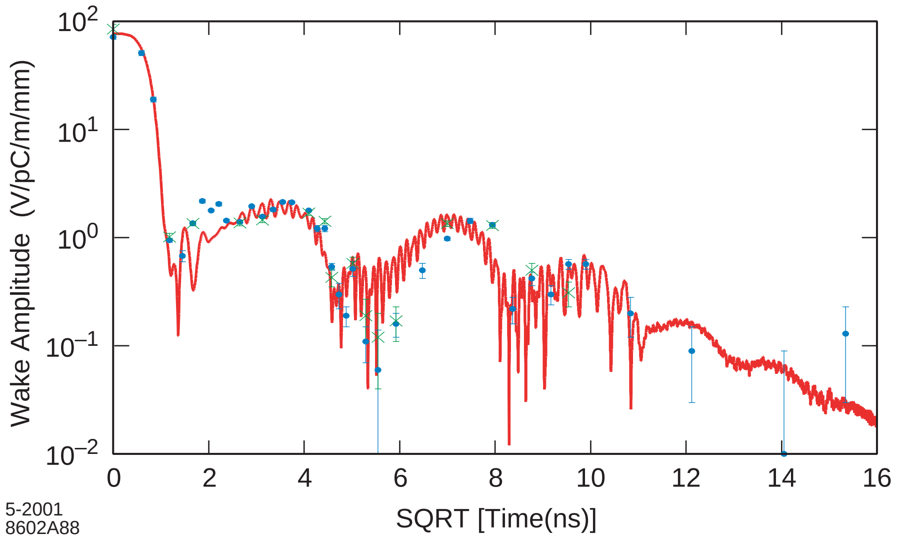

**Figure 1.4:** Measurement of Wakefields at the ASSET Facility. Wakefields left by bunches of positrons as they pass through a 1.8-meter damped and detuned X-Band accelerator structure are sampled by a trailing electron bunch. The positions, relative times, and total charge of each bunch can be varied individually to map out the dipole wakefields. The data points in the figure are measured wakefield strengths, and the curve is the prediction from theory.

### 1.2.5 The NLCTA, X-band Rf Components, and Accelerator Gradients

The goal of the NLC is to reach center-of-mass energies an order of magnitude beyond that achieved at the SLC. The choice of a room-temperature X-band (11.424 GHz) accelerator has been made to reach this goal, and to provide a path to still higher energies. There are four major components that make up the rf system - modulators, klystrons, pulse compression systems, and accelerator structures. The NLC Test Accelerator (NLCTA) [11] was commissioned in 1996 to provide experience with integrated X-band rf systems. This facility continues today to be the ultimate test bed for NLC rf power sources and beam acceleration. The power sources (modulators, klystrons, and SLED-II systems) have operated reliably for thousands of hours. The NLCTA has been able to generate high-quality beams with energy spread well within the NLC specification of 0.3%. These proven NLCTA power sources could be used as the basis for a 500-GeV cms energy collider.

The goal of the NLC R&D program is an rf system able to operate with maximum efficiency at 1-TeV cms, and to be built at minimum cost. The components of the NLC TeV rf system are designed to improve significantly (by 60%) the overall ‘wall-plug-to-beam’ power efficiency, and to provide more energy per rf pulse than available from the NLCTA system. Table 1.4 lists the rf components installed in the NLCTA and the corresponding components for the 1-TeV NLC design.

**Table 1.4:** X-Band Rf Components

| COMPONENT | NLCTA RF SYSTEM | NLC "TEV" RF SYSTEM |
|---|---|---|
| DC Pulse Modulator | Thyratron-Switched PFN | IGBT-Switched Induction |
| Klystron Tube | 50 MW/1.2 μs Solenoid Focus | 75 MW/3 μs PPM Focus |
| Rf Pulse Compression | SLED-II | 2-Mode DLDS |
| Accelerator Structure | Damped/Detuned at 50 MV/m | Damped/Detuned at 70 MV/m |

The concepts, designs, and states of development of these components are described fully in Chapter 4 of this Report, but a brief scorecard is given here. (1) A prototype IGBT-switched induction modulator has been successfully used to power one of the S-band klystrons on the SLAC linac. A full-scale 500-kV modulator has been fabricated and is undergoing initial tests. It will be used to power four S-band klystrons, and later will form the basis for the '8-Pack' test described below. (2) A prototype periodic permanent magnet (PPM) klystron with 75-MW pulses of 3-µs duration has been tested successfully at 10 pulses per second. This tube did not include cooling circuits on the permanent magnet column, and its pulse rate was limited by average heating of the magnets. A tube with an improved design is being fabricated, and tests on a 'diode stick' have verified excellent (99.9%) beam transmission through the cooled magnetic circuit. A high-power full-repetition-rate test of the klystron tube will take place later this year. (3) The intrinsic technologies of the SLED-II system and Delay Line Distribution System (DLDS) are very similar, and experience gained with the NLCTA rf system is applicable to the TeV goals. The transport of multiple rf modes through a single waveguide is unique to the DLDS, and has been demonstrated at low power at the ATF in Japan. High-power tests of critical DLDS components have been successful, and the 8-Pack test will verify the ability of the DLDS system to fully handle the stored energy required for the 'TeV' configuration.

An important parameter of the rf system is the unloaded field gradient produced in the accelerating structures. This parameter, combined with the beam loading fraction (the effective gradient in the presence of beam) and the physical packing fraction of accelerator along the tunnel, determine the length of the linac. In the NLC TeV design, the unloaded gradient ($G_U$) is 70 MV/m, the effective loaded gradient ($G_L$) is 50 MV/m, and the packing fraction is 80%. The gradient per running length of tunnel is 40 MV/m, and the length of filled tunnel required to reach 250 GeV beam energy (500 GeV cms) is 6.3 km (Table 1.2). The cost of the linac is the sum of two contributions: those proportional to length (i.e., $\sim 1/G_L$), such as tunnels, magnets, and vacuum; and those proportional to the rf power that must be generated to accelerate the beams (i.e., $\sim G_U^2/G_L$), such as klystrons, modulators, and DLDS components. The total cost of the facility also includes many items whose cost is independent of the acceleration gradient, such as the Injector and Beam Delivery Systems. The minimum in the total cost is a surprisingly shallow function of gradient. For the NLC design (Table 1.5), the minimum occurs at $G_U$ of 70 MV/m and the cost to build a 500-GeV cms collider with a $G_U$ of 50 MV/m is about 10% above the minimum.

To test accelerator structures at gradients beyond 50 MV/m, the number of klystrons per rf station in the NLCTA was doubled, and the control system improved to allow continuous unattended operation. Damage began to be observed in the NLCTA 1.8-meter-long accelerator structures as the gradient was increased. An aggressive R&D program to determine the source of this damage is proceeding on all fronts: theory and modeling, accelerator design, manufacture, and operations. International collaboration on this R&D is intense as KEK and CERN have joined in the effort. The status and results of this work are described in more detail in Chapter 4, but there has been good progress in understanding the source of the damage and ways to design structures to avoid it. A key parameter is the velocity with which energy flows through the structure, the group velocity $v_g$ of the rf field. This determines the power that can be deposited at a breakdown site, and hence the ability of breakdowns to damage the structure. Shown in Fig. 1.5 are operational histories of structures with differing $v_g$ patterns. It is clear that lower group velocity structures operate well at 50 MV/m, and come close to the NLC TeV design goal. But there is not yet sufficient operational overhead to meet the criterion for large-scale use at the higher gradient. Tests are continuing on structures with still lower $v_g$, and also on standing-wave structures. This problem is not yet solved, but we have confidence that structures capable of operation at the design values will be demonstrated soon.

## 1.3 Construction of the NLC

The physics goals and the status of the technical development of the NLC were reviewed in 1998 by the Department of Energy's (DOE) High Energy Physics Advisory Panel, and by the National Research

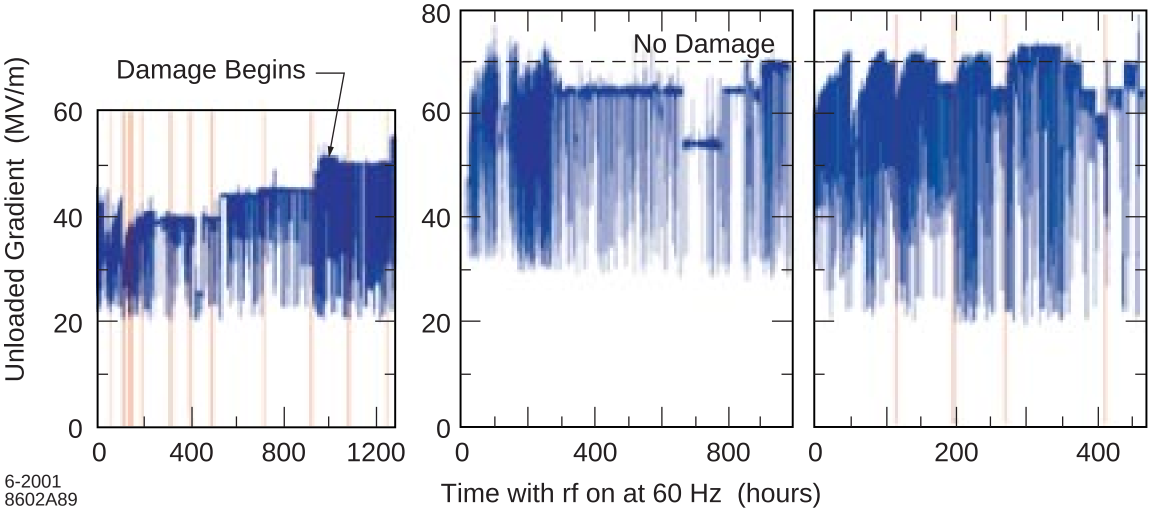

**Figure 1.5:** Operational Histories of Three Accelerator Structures as they are processed to high gradients. (a) A 1.8-meter-long NLCTA structure with group velocity 12% the speed of light at the input end. (b) A 0.5-meter-long test structure with group velocity 5% the speed of light at the input end. (c) A 1.0-meter-long test structure with group velocity 5% the speed of light at the input end. The data are unselected and correspond to a range of operational conditions.

Council Committee on Elementary Particle Physics. Both supported the completion of a Conceptual Design (CD) of the collider with initial capability to reach 1-TeV cms energy. The NLC R&D was subsequently focused more tightly on rf technologies aimed at the TeV energy goal put forward by these recommendations. In May of 1999, the Division of Construction Management of the DOE reviewed the NLC project (a 'Lehman Review') and concluded, "the NLC is ready and should be authorized to proceed with a CD." Subsequent budget and priority considerations by the DOE prevented formal approval of the start of a CD for the NLC, but strong support of the R&D program has continued. Approval and completion of the CD, with the necessary supporting R&D, is the next important step in the construction of the facility. In addition to producing the Conceptual Design Report (CDR), work on the CD would include detailed studies of potential sites for the collider, and estimation of the cost of the facility to a degree that careful review of its accuracy can be done. The CDR, and results from the continued R&D, would be the basis for authorization of the project, selection of a site, and establishment of a baseline cost and schedule for the project.

A model for construction of the NLC was created for the May 1999 DOE review. The purpose of this exercise was to identify all items needed to complete the construction of the facility, and to provide a 'ballpark' estimate of the cost and schedule on which it could be ready to carry out physics experiments. At that time the estimated total project cost of the initial 500-GeV cms stage was ~ 7.5B$. This included a correction for inflation over the eight years estimated to complete the project following acceptance of the CDR, and a contingency factor, but not the cost of the detectors for the experimental program. The DOE committee was not asked to verify the accuracy of this cost estimate, but they did examine carefully the completeness of the project model. They found that, "the technical, cost, and schedule information appear to be a good starting point, with all major systems and subsystems covered," and that, "estimates for other project costs, R&D, commissioning, preoperations, and special capital equipment appear to be conservative." The committee concluded that the, "CD study and supporting R&D must give absolute first priority to reducing cost and to achieving higher machine performance."

Completion of the 1999 model for construction of the NLC gave a clear picture of the cost and schedule drivers. With this information, the NLC project group has aggressively pursued design changes and R&D to reduce costs and extend the performance of the collider. All areas of the machine and its technical systems have been examined, and many design changes and technology substitutions have been made in the project model presented in this Report. Some of the major changes include a new design for the beam delivery system that has reduced its length by a factor two, new designs for the Injector complex that substantially reduce the required number of components and length of tunnel, and inclusion of TeV main linac rf technology (Table 1.4) into the baseline model. There have also been increases in the scope of the project. In particular, the number of beam bunches to be accelerated on each rf pulse has been doubled to provide higher luminosity than in the 1999 design, and full implementation of the low energy IR has been included in the present model. The changes have substantially increased the expected performance of the collider, and have reduced the estimated total project cost of the initial 500-GeV cms stage to ~ 6B$ (with escalation and contingency, but without detectors). A breakout of the relative parts of this total is given in Table 1.5. The cost to increase the cms energy to 1 TeV would be an increment of about 25%.

## 1.4 Work in Progress and Milestones on the Road to the NLC

The NLC is ready to begin work on the Conceptual Design that will form the basis for authorization of the project. In parallel, construction and testing of a TeV rf ‘8-Pack’ will be completed to support the CD. The 8-Pack consists of eight PPM klystrons pulsed by one IGBT induction modulator, a 2-Mode DLDS arm, and a set of high-gradient accelerator structures. (See Chapter 4.) This system will be installed at the NLCTA for testing with beam. Preparation of this 8-Pack is already underway and it is the pacing R&D item. The needed solid-state modulator is being fabricated and final engineering designs of needed klystrons and DLDS components are in progress. With appropriate support, the Conceptual Design Report and the accompanying 8-Pack demonstration can both be completed in U.S. FY03-04. This will be an important milestone in the overall schedule for construction of the NLC facility. It is estimated that construction would take about eight years following acceptance of the CDR.

A broad spectrum of work is also going forward, and will continue throughout the preparation of the CDR. More detailed accounts of this design effort and technology R&D are given in the remainder of this Report. None of this work, however, is pacing the readiness of the technology nor is it driving the cost or schedule of the project.

**Table 1.5:** NLC 2001 Cost Model

| COST COMPONENT | FRACTION OF TOTAL COST (%) |
|---|---|
| Injectors | 17 |
| Main Linacs | 46 |
| ML Power Systems | 13 |
| ML Beamline Systems | 16 |
| ML Conventional Facilities | 17 |
| Beam Delivery | 9 |
| Central Facilities and Systems | 13 |
| Other Project Costs | 15 |
| Total | 100 |

On a longer time scale, continued R&D will be needed to support the construction of the NLC following completion of the CDR and project authorization. At that time, R&D would focus on industrialization of machine components and optimization of systems engineering and design. Potential industrial partners have already begun to produce X-band rf power sources, but overall this effort is still much below what will be needed to support the final engineering design of the collider. The Engineering Test Facility (ETF) at Fermilab is conceived to be a centerpiece and test bed for industrial R&D. This is a 400-meter-long beamline planned to be a prototype for a complete sector of the main linac of the NLC. The ETF will be a place to study the integration of main linac systems, and serve as a location to test industrially produced components of all kinds. It will also allow hands-on studies of installation and maintenance procedures that must be understood as part of the final engineering design of the collider. Acceleration of beam in the ETF will provide operational experience and optimization of overall systems design and engineering. Properly funded, this facility could be completed in U.S. FY06/07, and would be another milestone on the road to completion of construction of the NLC in approximately 2012.

## 1.5 Outlook

The design, construction, and operation of the accelerators that will be needed to explore elementary particle physics in the coming decades will necessarily be shared among many institutions from many nations. The scope, cost, and universal purpose of these instruments dictate that their ownership be held by the international community. It is necessary to reach a global strategy and long-range view of how to share the tasks and opportunities presented by the frontier of high-energy physics. The model for construction of a U.S. facility outlined in the previous section will necessarily be reshaped by these international discussions.

There has long been strong international collaboration and cooperation on the R&D for future linear colliders. Good communications among groups working in the field have been established through international workshops that began in 1988 as commissioning of the SLC got underway [12]. These workshops have continued at approximately two-year intervals, with host institutions rotating through the American, Asian, and European regions. In 1994, an International Linear Collider Technical Review Committee (ILC-TRC) was established and tasked to bring together working groups with representatives from all of the major design teams. The ILC-TRC did an excellent job of establishing a common set of definitions and conventions that have become the common language of the field. It also created an important set of tables of the parameters for all linear collider designs. The ILC-TRC published, in 1995, a report on its work [13] and has continued to keep the major informational tables up to date on its web site [14]. The International Committee on Future Accelerators (ICFA) recently commissioned and charged the ILC-TRC to reconvene as a working group to release a new report. Completion of this report is expected in the year 2002. This is a step in a process intended to lead to a choice of design and technology for the next-generation linear collider, and to a strategy by the international community to build and operate such a facility.

The technology to build the next-generation linear collider is here. The TESLA Collaboration has completed technical documentation of a superconducting accelerator, and has made a proposal to construct it as an international project. The NLC Collaboration, with its Japanese partners, has developed the design and technology for a warm accelerator. The particle physics communities in Europe and Asia have endorsed a linear collider to complement the LHC, and have stated their willingness to make the commitments needed to host such a facility. The U.S. physics community will meet at Snowmass with the 2001 DOE/NSF HEPAP subpanel to recommend a long-range plan for high energy physics in the United States. This plan must reach a conclusion on the role to be played by the U.S. in building and using the next-generation linear collider. These recommendations will be important in setting the global strategy for high energy physics for decades to come.

## References

[1] American Linear Collider Working Group, *"Linear Collider Physics Resource Book for Snowmass 2001,"* BNL-52627, CLNS 01/1729, FERMILAB-Pub-01/058-E, LBNL-47813, SLAC-R-570, UCRL-ID-143810-DR, LC-REV-2001-074-US.

[2] The NLC Design Group, T. Raubenheimer, ed., *"Zeroth-Order Design Report for the Next Linear Collider",* LBNL-PUB-5424, SLAC Report 474, UCRL-ID-124161, 1996.

[3] *TESLA Technical Design Report,* DESY 2001-011, March 2001.

[4] *A 3 TeV* $e^+e^-$ *Linear Collider Based on CLIC Technology,* CERN 2000-008, July, 2000.

[5] http://lcwws.physics.yale.edu/lc/

[6] *The FFTB Collaboration:* BINP (Novosibirsk/Protvino*),* DESY, Fermilab, KEK, LAL(Orsay), MPI(Munich), Rochester, and SLAC.

[7] Balakin, V., et al., *Phys. Rev. Lett.,* **74***:*2479, 1995.

[8] Bamber, C., et al., *Phys. Rev.* **D60**, 1999.

[9] J.Urakawa and Yoshioka, M., eds. *Proceedings of the SLAC/KEK Linear Collider Workshop on Damping Ring,* KEK 92-6, 1992.

[10] Adolphsen, C., et al., *Phys. Rev. Lett.,* **74:**2475, 1995.

[11] Ruth, R.D., et al., "A Test Accelerator for the Next Linear Collider", *Proceedings of the ECFA Workshop on Linear Colliders (LC92),* Garmisch Partenkirchen, 1992.

[12] *Proceedings of the VIII International Workshop on Linear Colliders,* Frascati, Italy, October 1999, http://wwwsis.lnf.infn.it/lc99/, and references therein.

[13] Loew, G., ed., *"International Linear Collider Technical Review Committee Report,"* SLAC-R-95-471.

[14] *http://www.slac.stanford.edu/xorg/ilc-trc/ilc-trchome.html*

# Chapter 2

## NLC Parameters and Layout

### 2.1 Introduction

Over the last five years, the physics program for a linear collider has evolved significantly [1], and as a consequence, the layout of the NLC has been modified to provide greater energy flexibility. Recent precision measurements of electroweak parameters provide a convincing case that some new physics to explain the mechanism of electroweak symmetry breaking will be seen at energies of 0.5 to 1.0 TeV. A linear collider in this energy range will be able to make precision measurements to complement the results from the Tevatron and LHC. In addition, there is considerable interest in precision measurements at lower energies, such as the $Z^0$, W-pair, or Top thresholds. The physics scenarios considered also indicate that the collider should eventually be able to support an upgrade to multi-TeV energies, once a suitable rf technology can be developed. This is discussed further in section 2.4.

The NLC was presented in detail in the 1996 *Zeroth-Order Design Report for the NLC* (ZDR) [2]. During the last five years, the linear collider R&D program has led to substantial improvements in that design. As described in the previous chapter, the NLC design is based on extensive experience from the first linear collider, the SLC, as well as other modern accelerators, and from numerous test facilities including ASSET, FFTB and NLCTA at SLAC and the ATF at KEK. These are described briefly in Chapter 1 and in more detail in later chapters. The polarized electron source and the positron production system are modest extensions of the SLC sources. The damping rings are similar to third-generation synchrotron light sources and are required to produce an equilibrium emittance that is only a factor of two below what has been achieved at the ALS in Berkeley or the ATF. A prototype X-band rf system has been operated successfully at the NLCTA since 1996. In principal, this system could be used today to build a 500-GeV cms collider, but there is active R&D on a next generation of components that are more efficient and less expensive to build and operate.

To preserve the small beam emittance during acceleration, the X-band structures must be designed to minimize wakefields, and both the structures and the focusing quadrupoles must be aligned to very tight tolerances. The wakefield properties of prototype structures have been measured precisely in the ASSET test facility and agree well with the calculations [3]. Structures have been fabricated which meet tolerances far tighter than those required for NLC. The required alignment accuracy has also been demonstrated in ASSET. Beam-based alignment techniques developed for the SLC and FFTB have achieved close to the necessary accuracy, and extensive simulations indicate that these techniques are capable of preserving the emittance through a 10- km linac with diagnostics and correction hardware which need to be only a factor of 3 to 5 better than those used at the FFTB. The FFTB also demonstrated the validity of the final-focus optics and achieved a demagnification of the beam size greater than required for NLC. All of these results have led to improvements in the design and increased confidence in its capabilities.

Together with the accelerator hardware and optics, the beam parameters and the NLC collider layout have evolved since the 1996 design. These changes have been motivated by a desire to provide additional physics functionality and to reduce the capital costs of the facility. A schematic of the NLC is shown in the previous chapter in Fig. 1.1. The collider is roughly 30 km in length. It consists of two 13-km-long X-band linacs that will accelerate the beams to 500 GeV for collisions at 1 TeV in the center-of -mass. In addition to the linacs, there are electron and positron injector complexes and a beam-delivery system that supports two interaction regions. The collider is intended to begin operation at a center-of-mass energy of 500 GeV, in which case the linac tunnels would only be half filled with accelerator structures and rf power sources. In addition, there are bypass lines to deliver low-energy beam to either IR as desired.

In the following sections, the collider layout is discussed in more detail. The beam and IP parameters are described in section 2.2. The last sections cover further options for additional functionality and possible routes to a multi-TeV facility.

## 2.2 Layout

The layout of the linear collider is described starting first with the final focus and interaction regions, and following with the main linacs and injector systems.

### 2.2.1 Final Focus and Interaction Regions

Given sufficient acceleration to produce a beam of the desired energy, a major limitation on the energy range of a linear collider is the final-focus system. In order to cancel the chromaticity of the final quadrupoles that focus the beams to the necessary small size at the interaction point (IP), the final-focus optics include pairs of sextupoles separated by bending magnets. The bends must be weak to avoid emittance dilution from synchrotron radiation. Because of this, the magnets must be long, and their length determines the overall length of the final focus. For a given optics design, the strength of the bends also limits the maximum energy beam that can be delivered without excessive emittance growth. A linear-collider final focus can typically span a factor of 4 in energy. Over this range, the luminosity increases linearly with energy as the beam emittance shrinks through adiabatic damping. Above the maximum design energy, the luminosity falls due to emittance dilution from synchrotron radiation in the bends. Below the minimum design energy, the luminosity is usually proportional to the square of the beam energy because apertures and aberrations in the collimation or final-focus regions limit the achievable demagnification at the IP.

To accommodate the physics demand for energy flexibility, the NLC design now includes two interaction regions. One is optimized for high energy, 250 GeV to 1 TeV, and is configured so that it is ultimately upgradeable to multi-TeV. The other is designed for precision measurements at lower energy, 90 to 500 GeV. The luminosity for each IR increases linearly with energy over the design energy range as shown in Fig. 2.1. This configuration was inspired by a breakthrough in the final-focus optics design that made the system much more compact [4]. By interleaving the chromatic correction sextupoles with the final quadrupoles, fewer long bending magnets are required. The new optics are described in more detail in Chapter 6. With this design, the final focus can accommodate beams of up to 2.5 TeV in a length of about 800 meters. By comparison, a conventional design for the CLIC final focus is 3-km long for 1.5-TeV beams.

To capitalize on the multi-TeV potential of the new design, it was also necessary to eliminate other bending between the linac and the high energy IP. In the NLC design, a 20-mrad crossing angle at the IP is needed to avoid parasitic interactions of one bunch with the later bunches in the opposing train. The earlier NLC design had two symmetrically placed interaction regions (IR) with a 'Big Bend' to separate the beams and generate this crossing angle. To reduce synchrotron-radiation emittance growth, the Big Bend was long (and expensive) and ultimately limited the maximum beam energy. In the new asymmetric layout, the linacs are no longer collinear but are oriented with a shallow 20-mrad angle between them to produce the desired crossing angle at the high-energy IR without additional bending. The beams to the second IR are bent by about 25 mrad, which is acceptable because they are at lower energy. This allows reasonable luminosity up to 1 TeV. The low-energy IR has a larger 30-mrad crossing angle for compatibility with a possible $\gamma\gamma$ option which is described in Chapter 8.

The beam line for the high energy IR is 2.5 km from the end of the linac. This distance includes a long 1.4-km collimation region, the 800-m final focus and an additional 300 m 'stretch' to accommodate the beamlines for the low-energy IR. The low-energy IR beam line splits off at the end of the collimation region and includes the 25-mrad bend and a shorter 500-m final focus. Both beam lines share the same collimation system but, as a future upgrade, parallel collimator beam lines could be installed in the same tunnel. An alternate configuration with separate beam lines from the end of the linac to the two IRs is possible, but the extra tunnel length makes it more costly. In the present layout, the two IRs are separated by about 20 m transversely and 440 m longitudinally to provide vibration isolation and shielding so either IR hall may be accessed while the other is in operation.

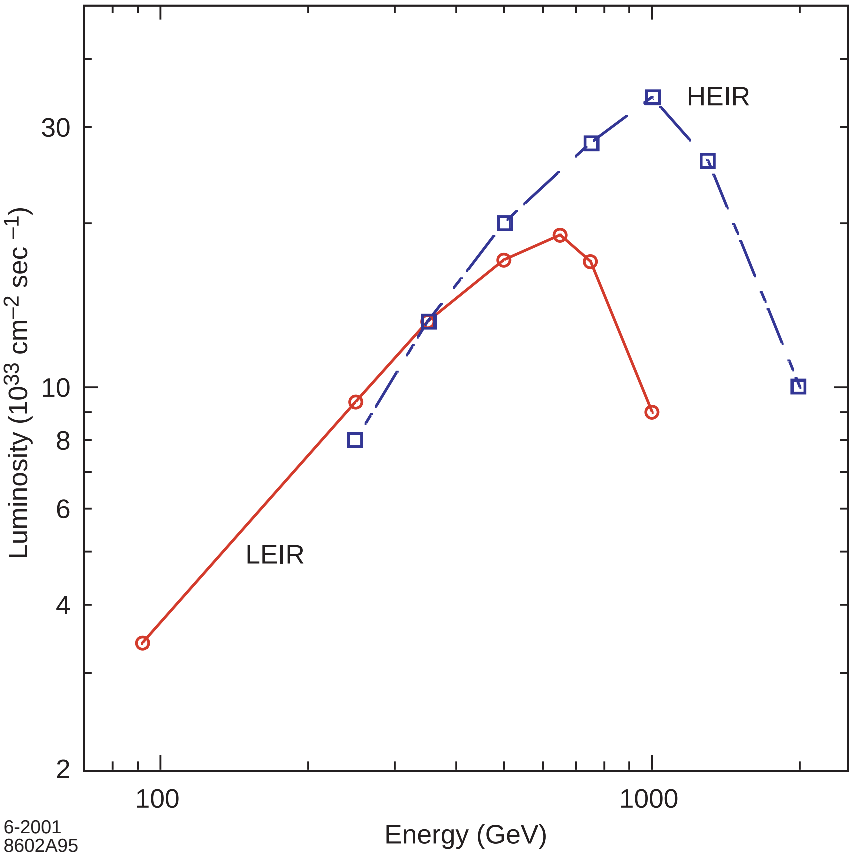

**Figure 2.1:** Luminosity as a function of energy for the high and low energy IRs.

### 2.2.2 Main Linacs

The main-linac rf system has been outlined in Chapter 1 and will be described in detail in Chapter 4. Each linac consists of 26 rf sectors which are 468-meters long. The rf power is generated in modulator/klystron ‘8-packs’ where one solid-state modulator drives 8 attached klystrons. Each sector is powered by nine of these 8-packs that feed the rf distribution waveguide. The 8-packs would not be installed in the main linac tunnel but in a separate enclosure. This simplifies access and maintenance, and it is essential to ensure the desired reliability and collider availability.

The main-linac tunnels are designed to be long enough to hold the full complement of accelerating structures in the 26 sectors required to reach 500 GeV per beam. The tunnels are roughly 12.8 km in length. In the first stage of the project, only the first 13 sectors - half the tunnel length - would be filled with structures. The installation would start from the low-energy end of the tunnel to allow maximum flexibility in choosing the appropriate energy upgrade steps to match physics interest and funding profiles.

Because of the transverse wakefields of the accelerator structures, it is undesirable to transport the beam through a large number of unpowered structures. In order to maximize luminosity at lower energy, a nonaccelerating 'bypass' line is provided to bring the low-energy beams to the end of the linac. This system is similar to that used for PEP-II injection at SLAC. The bypass line will share the main-linac tunnel, and will be installed at the same elevation as the main beam line. The design includes three transfer points where the beam can be diverted into the bypass line at 50, 150 and 250 GeV, and a return at the end of the linac to bring the beam back into the collimation section. These are sufficient to support a continuous variation of beam energy over the whole range. The bypass line will also be used to transport the beam from the end of the installed rf to the end of the linac, eliminating the need to provide a drift tube and focusing magnets in the unfilled part of the main-linac beam line.

In addition, there will be four diagnostic regions along the length of the linac where the beam emittance and the beam energy and energy spread can be monitored parasitically. Continuous, noninvasive monitoring was found to be essential during the SLC operation because it facilitates rapid diagnosis of faults and makes it possible to correlate disparate effects. The bypass line injection and extraction regions and special nonaccelerating diagnostic regions increase the linac tunnel length by roughly 500 m.

### 2.2.3 Injector Systems

There are two separate injector complexes to produce the low-emittance trains of electron and positron bunches for injection into the main linac. Each train consists of 190 bunches of $0.75 \times 10^{10}$ particles per bunch, separated by 1.4 ns. The electrons have 80% polarization and the positrons are unpolarized. The electron injector includes a polarized photocathode gun, a bunching system and an S-band booster linac to deliver 1.98-GeV beam to the damping ring. For the positron injector, an unpolarized electron gun and bunching system followed by a 6-GeV drive linac provides the electron beam needed to produce positrons. Multiple positron targets are required to keep the energy deposited in each target below the threshold for material damage. The electrons are split by an rf separator and directed onto 3 of 4 multiplexed targets and positron capture sections. The bunches are then recombined into the desired 190-bunch train format and accelerated in a 1.98-GeV L-band linac to the positron predamping ring. Because of the large emittance of the captured positrons, large-aperture L-band rf is used for acceleration and a predamping ring is required to reduce the emittance of the positrons before injection into the main damping ring. Two identical rings are used to damp the positron and electron bunch trains from the injectors to a normalized emittance of $3 \times 10^{-6}$ m-rad in the horizontal and $2 \times 10^{-8}$ m-rad in the vertical.

After extraction from the damping rings, the beam passes through a spin rotator system that can be used to orient the electron spin in an arbitrary direction to ensure longitudinal polarization of the beams at the IP. In the baseline design, the spin rotating solenoids are only installed in the electron beam line. However, the positron beam line is identical so that additional solenoids can easily be installed later. This would allow operation either with polarized positrons or with polarized electrons for $\gamma\gamma$ or $e^-e^-$ collisions.

After the spin rotators, the bunch length must be compressed from 4 mm to 110 $\mu$m before injection into the main X-band linacs. This is accomplished in a 2-stage bunch compressor that is identical for the two beams. The first stage uses an L-band rf section followed by a wiggler to compress the bunch to a length of about 0.5 mm. This is followed by a 6-GeV S-band prelinac and the second-stage bunch compressor with a 180° arc, an X-band rf section and a chicane. The second stage can produce a bunch length between 90 and 150 $\mu$m. The NLC injector complexes are described in detail in Chapter 5. In the present layout, the electron booster and prelinac are housed in the same tunnel to minimize infrastructure costs. The positron drive linac, booster and prelinacs also share a common tunnel and support buildings.

The concept of a central injector complex was investigated for possible cost savings, and many configurations with and without shared components were considered. Any centralized injector requires long, low-emittance transport lines to bring the beams to the end of the main linacs and extra tunnels to connect into the linac housing and into the second bunch-compressor 180° turnaround. These additions more than offset any potential savings. The most cost-effective location for the injectors is near the low-energy ends of the linacs as in the original ZDR design. A central injector design is being developed for the Fermilab deep-tunnel site because it has the advantage of being located entirely on land already owned by the laboratory.

## 2.3 Parameters and Luminosity Evolution

The primary parameters for the NLC are listed in Table 2.1. The beams consist of bunch trains with 190 bunches separated by 1.4 ns at a repetition rate of 120 Hz. During the initial stage the center-of-mass energy is assumed to be 500 GeV with a luminosity of $2.0 \times 10^{34}$ $\mathrm{cm}^{-2}\mathrm{s}^{-1}$, although the collider might be started with a lower initial energy depending on the physics interest. The second stage assumes the installation of the full rf system to reach a center-of-mass energy of 1 TeV with a luminosity of $3.4 \times 10^{34}$ $\mathrm{cm}^{-2}\mathrm{s}^{-1}$. Using the bypass lines and the two interaction regions, the collider is designed to cover fully the energy range between 90 GeV and 1 TeV cms. Sets of nominal parameters for operation of the low-energy IR are listed in Table 2.2. The operating energy ranges of the two interaction regions were discussed in the previous section.

The beam parameters listed in Tables 2.1 and 2.2 have been chosen to optimize the fraction of luminosity close to the center-of-mass energy and minimize the beamstrahlung-related backgrounds. The beamstrahlung can be described by two parameters, the number of beamstrahlung photons radiated per incident electron $n_\gamma$ and the average energy lost to the beamstrahlung $\delta_B$. In general, the luminosity close to the center-of-mass energy depends most sensitively on the total number of photons radiated while the tails of the luminosity distribution are described by the average energy lost. The number of hadronic background events is proportional to the square of the total number of photons and is a function of the photon energy spectrum. The number of photons depends on the ratio of the number of particles per bunch and the horizontal beam size while the beamstrahlung energy loss has a similar dependence but is also a function of the bunch length. These parameters can be traded against each other to optimize the total luminosity and the luminosity spectrum for any given experiment. The parameters presented in Tables 2.1 and 2.2 are only an illustrative set.

Since the NLC 1-TeV parameters have evolved significantly since the 1996 ZDR [2], it is worth describing those changes in detail. First, the unloaded acceleration gradient has been decreased from 85 MV/m to 70 MV/m. This reduced the rf power required in the accelerator structures, and is close to the cost optimum for the linac. Second, there have been two major changes to the bunch-train format: the single bunch charge and bunch length have decreased by 30%, reducing the average beam current and the beam loading; and the bunch train length and the number of bunches in the train have doubled, increasing the rf-to-beam efficiency and recovering the luminosity lost due to the decrease in the single bunch charge.

The decrease in the bunch charge and the average current then has three effects: (1) it reduces the capital costs because the beam loading is lower and thus, for the same unloaded gradient, the length of the linac is shorter to produce the same final energy; (2) it allows for shorter bunch lengths because the effects of the longitudinal wakefields are smaller; and (3) it reduces the emittance dilution from the transverse wakefields. In the NLC, the alignment tolerances are dominated by single bunch effects. By reducing the product of the charge and the bunch length from $1.1 \times 10^{10} \times 150$ μm to $0.75 \times 10^{10} \times 110$ μm, the expected emittance dilution due to transverse wakefields is reduced by a factor of four. The emittance dilution due to quadrupole misalignments will also be reduced by a comparable factor because the dominant dilution arises from the energy spread needed for ‘BNS damping’ (see section 7.4.1), which is proportional to the transverse wakefield.

These changes, along with expected performance improvements from the hardware, have led to a decrease in the emittance dilution budgets. This allows operating parameters with smaller beam sizes at

**Table 2.1:** Parameters for Stage 1 and Stage 2 of the NLC

| **PARAMETER NAME** | **STAGE 1** | **STAGE 2** |
|---|---|---|
| CMS Energy (GeV) | 500 | 1000 |
| Luminosity ($10^{33}$) inc. dilutions | 20 | 34 |
| Luminosity within 1% of $E_{cms}$ (%) | 55 | 44 |
| Repetition Rate (Hz) | 120 | 120 |
| Bunch Charge ($10^{10}$) | 0.75 | 0.75 |
| Bunches/Rf Pulse | 190 | 190 |
| Bunch Separation (ns) | 1.4 | 1.4 |
| Eff. Gradient (MV/m) | 48 | 48 |
| Lum. Dilution for tuning and jitter (%) | 10 | 10 |
| Injected $\gamma\varepsilon_x$ / $\gamma\varepsilon_y$ ($10^{-8}$ m-rad) | 300 / 2 | 300 / 2 |
| $\gamma\varepsilon_x$ / $\gamma\varepsilon_y$ at IP ($10^{-8}$ m-rad) | 360 / 3.5 | 360 / 3.5 |
| $\beta_x$ / $\beta_y$ at IP (mm) | 8 / 0.10 | 10 / 0.12 |
| $\sigma_x$ / $\sigma_y$ at IP (nm) | 245 / 2.7 | 190 / 2.1 |
| $\sigma_z$ at IP ($\mu$m) | 110 | 110 |
| $\Upsilon_{ave}$ | 0.11 | 0.29 |
| Pinch Enhancement | 1.43 | 1.49 |
| Beamstrahlung $\delta_B$ (%) | 4.7 | 10.2 |
| Photons per $e^+/e^-$: $n_\gamma$ | 1.2 | 1.3 |
| Linac Length (km) | 6.3 | 12.8 |

**Table 2.2:** Low energy operation parameters for the NLC

| Energy (GeV cms) | **92** | **250** | **350** |
|---|---|---|---|
| Luminosity ($10^{33}$) | 3.5 | 9.4 | 13.2 |
| Luminosity within 1% of $E_{cms}$ (%) | 92 | 75 | 65 |
| Repetition Rate (Hz) | 120 | 120 | 120 |
| Bunch Charge ($10^{10}$) | 0.75 | 0.75 | 0.75 |
| $\sigma_x$ / $\sigma_y$ at IP (nm) | 630 / 6.2 | 380 / 3.8 | 320 / 3.2 |
| Beamstrahlung $\delta_B$ (%) | 0.18 | 1.1 | 2 |
| Photons per $e^+/e^-$: $n_\gamma$ | 0.49 | 0.79 | 0.92 |
| Polarization loss (%) | 0.08 | 0.21 | 0.34 |

the IP and improved luminosity performance. The changes are summarized in Table 2.3, which compares parameters for the NLC ZDR and the present design at 1 TeV in the center-of-mass. In particular, the luminosity at 1 TeV has more than tripled but, because of the changes in the bunch-train format, the tolerances on the beam line components have only decreased by 30%. To attain these tolerances, beam-based alignment techniques are necessary. The performance of these beam-based algorithms depends primarily upon the precision of the beam diagnostics and corrections. As will be discussed in Chapter 7, the R&D program has demonstrated that the diagnostics will have much better performance than was expected at the time the ZDR was written.

**Table 2.3:** Parameters for 1996 and 2001 NLC designs at 1 TeV

| PARAMETER NAME | NLC ZDR (1996) | NLC 2001 |
|---|---|---|
| Bunch charge | $1.1\times10^{10}$ | $0.75\times10^{10}$ |
| Bunch length | 150 μm | 110 μm |
| Bunch train format | 75 bunches separated by 1.4 ns | 190 bunches separated by 1.4 ns |
| Unloaded acc. gradient | 85 MV/m | 70 MV/m |
| Active linac length | 8.8 km | 10.1 km |
| Luminosity | $1.1\times10^{34}\,\mathrm{cm}^{-2}\mathrm{sec}^{-1}$ | $3.4\times10^{34}\,\mathrm{cm}^{-2}\mathrm{sec}^{-1}$ |
| Dilution for jitter and tuning | 16 % | 10 % |
| $\sigma_x$ and $\sigma_y$ at IP | 250×4.1 nm | 190×2.1 nm |
| Alignment tolerance | 12 μm rms | 9 μm rms |

Detailed budgets for emittance dilution and beam jitter have been developed for the NLC. These are given in Chapter 7 along with a discussion of the beam-based alignment and jitter-stabilization techniques. The design luminosities, listed in Table 2.1, include an estimated 10% luminosity degradation beyond the explicit emittance dilutions to account for beam jitter and beam tuning. This tuning estimate is based on the results of the SLC 'dither-tuning feedback' [5] which very effectively optimized the linear optics automatically by using heavily averaged signals proportional to the luminosity. This technique was developed in the last year of SLC operation, and proved much more effective than the methods assumed in 1996.

**Table 2.4:** Intrinsic versus design emittances and luminosity for NLC at 1 TeV

|  | INTRINSIC x/y | DESIGN x/y |
|---|---|---|
| Damping Ring Emittance ($10^{-8}$ m-rad) | 300 / 1 | 300 / 2 |
| Main Linac Emittance ($10^{-8}$ m-rad) | 315 / 1 | 330 / 3 |
| Beam Delivery Emittance ($10^{-8}$ m-rad) | 330 / 1 | 360 / 3.5 |
| Luminosity ($\mathrm{cm}^{-2}\mathrm{sec}^{-1}$) | $6.6\times10^{34}$ | $3.4\times10^{34}$ |

Finally, it should be noted that the ultimate luminosity of the collider is roughly a factor of two higher than the design. This might be attained if the beam-based alignment techniques can be pushed to even higher precision. The ultimate luminosity, referred to as 'intrinsic luminosity,' is determined by physical limitations such as the finite damping time of the damping rings and synchrotron-radiation emission in the bunch compressors and final focus. These intrinsic beam emittances and luminosity are listed in Table 2.4 for comparison with the design values.

## 2.4 Options Beyond the Baseline Design

There are a number of options that have been considered to extend the physics reach of the NLC beyond what has been described as the baseline design. These include:

- Simultaneous delivery of luminosity to the two interaction regions
- Higher repetition rate for the low-energy portion of the linac to increase the total luminosity delivered.
- Operation in $e^-e^-$, $e^-\gamma$, and $\gamma\gamma$ modes
- Operation with polarized positrons.

Finally, while the primary purpose of the NLC linear collider lies in studies of high-energy physics in the sub-TeV to TeV energy range, the availability of ultra-low emittance, high-energy electron and positron beams could provide opportunities for research in other branches of science:

- Low-emittance, high-energy electron and positron beams extracted at various points in the linear-collider facility could be used for fixed-target experiments for either high-energy or nuclear physics. Either the incident particle beam or a high-energy photon beam could be available.
- High-energy particle beams can be used to generate low-current test beams to verify detector components or for other special experiments
- Low-emittance, short bunches of electrons at high energies, with suitably low energy spread, could be used to drive a Free Electron Laser.

In this section, we summarize briefly some considerations and issues concerning these options for the NLC.

### 2.4.1 Simultaneous Operation and 180 Hz

With an interaction region dedicated for precision low-energy measurements and bypass lines for the low-energy beams in the linac, two additional options have been considered to broaden the NLC physics program for a modest increase in cost. These are the possibility of simultaneous operation of both IRs with interleaved pulses, and the possibility of higher repetition rate for the low-energy beams. The basic operating model for all of the linear-collider designs has been to deliver beam to only one IR before switching to the other IR. With simultaneous operation, the entire bunch train would be sent to one detector or the other on a pulse-by-pulse basis and both detectors could record data at once. The bypass lines, if pulsed, would make it possible for the two detectors to operate with beams of different energy. The only significant addition required for operation with two energies would be a separate collimation system for the second energy beam. In the present layout, the two collimator lines would share the same tunnel. For simultaneous operation, one also needs to orient the electron polarization appropriately so that it is longitudinal at each IP. This is believed to be a solvable problem although it has not yet been studied in detail.

At a fixed repetition rate, the simultaneous operation described above does not increase the total luminosity but simply splits it between the experiments. The concept becomes much more attractive if the low-energy part of the collider could be run at 180 Hz with the rate shared between IRs at either 120/60 or 90/90 Hz. Most of the injector components could easily be designed to support the additional load of 180-Hz operation. The key technical challenges are the damping rings and the cooling for the X-band klystrons. In the present ring design, the damping time is insufficient at 180 Hz. An alternative possibility with two 90-Hz damping rings in a common vault has been studied and appears feasible. These rings could be 200 m in circumference instead of 300 m for the present ring, but would still require a large number of additional components at increased cost. Adequate cooling is already an issue for the periodic permanent magnet (PPM) focused X-band klystrons because of the small dimensions of the magnet assembly. More R&D would be required to demonstrate sufficient cooling for 180-Hz operation. Finally, it should be noted that the fractional increase in total ac power to the collider site is small for the higher repetition rate. For some choices of rates and beam energies, no additional site power would be required.

For the present, neither option is mature enough to be included in the NLC design, but both are attractive enough to warrant further study. As far as possible the configuration of the machine has been chosen to maintain compatibility with both options as future upgrades.

### 2.4.2 Alternate Collision Options: $\gamma\gamma$, $e^-e^-$, $e^-\gamma$

Several alternate types of collisions have been proposed for the collider because they access new physics channels or offer additional types of measurements. These include collisions of polarized photons ($\gamma\gamma$), polarized electrons ($e^-e^-$), electrons on photons ($e^-\gamma$) and polarized positrons on electrons. A number of workshops have been dedicated to these issues and discussions can be found in references [5] and [6].

Of the first three, the $\gamma\gamma$ option has elicited the strongest interest. Recent progress on a high-powered laser system to produce the photons has greatly enhanced the viability of this option and it is discussed further in Chapter 8. The NLC design includes a larger crossing angle for the low-energy IR to accommodate the larger size of the disrupted beam from $\gamma\gamma$ collisions.

To transport polarized beams through the damping-ring complex, a system of spin rotators is required before and after the rings. These are included in the design for the electron injector, and space has been reserved in the positron complex to allow them to be installed later, if required for either polarized positrons or a second polarized electron beam. The positron injector also provides a beam line to transport the drive electrons directly to the damping ring, bypassing the positron production system, as needed for any of the $\gamma$ or $e^-$ options.

### 2.4.3 Positron polarization

Polarized positrons can be important for certain precision measurements and would be crucial to reduce systematics for a ‘Giga-Z’ run. A polarized positron beam for a linear collider can be created by pair conversion of polarized photons produced either from an undulator or by Compton scattering off a high-power laser. The R&D on both of these options is discussed in Chapter 5.

### 2.4.4 Use of Extracted Beams

The high-energy beams generated by the main accelerators would likely have a number of uses other than the primary physics experiments. For example, it is almost certain that a facility would be needed for generating very-low-current test beams with close to the full beam energy. These could be produced by capturing some of the particles in the beam halo and then redirecting them to an alternate beam line. The best location for these test beams will depend on the proposed utilization.

In addition, the high-energy beams from the NLC can be used to generate a very-high-intensity photon beam for nuclear physics and other applications. For example, photons of energies from 2 to 50 MeV can be produced with electron beams of energies from 50 to 250 GeV. A 100-m-long undulator would produce roughly $1\text{x}10^{11}$ photons per bunch, or $2\text{x}10^{13}$ per train. For the 250-GeV case, this corresponds to an average power of ~75 kW in the photon beam. The output of the undulator can be collimated to produce a narrow spectrum (limited by the 0.3% energy spread of the electron beam). There will be $\sim 10^{10}$ photons per pulse ($\sim 10^{14}$ per second) in this energy width in a ~500-micron beam with a sub-microradian divergence angle. The photon beam could be produced either by a dedicated beam or parasitically by the primary beam headed towards the interaction regions. In the latter case, the undulator would have to be installed in the linac tunnel.

Finally, the primary beams could also be used for dedicated fixed-target experiments. They would have five times more energy and two times higher average current than the highest-current SLAC end-station experiments. This would allow, for example, a Möller scattering measurement of the weak mixing angle at higher $Q^2$ than the E-158 experiment at SLAC. There are a number of possible locations where the end station of NLC might be located downstream of the interaction point. When the beams are not in collision, a high-brightness beam could be transmitted through the NLC IR to the end station. If fixed-target positron experiments are desired, a second end station could be constructed on the positron dump line.

### 2.4.5 Possible Implementations of the FEL Subsystems at the NLC

A coherent pulse of X-rays can be generated by a Free Electron Laser (FEL). Because highly reflective mirrors are difficult at short wavelengths, most X-ray FELs are based on the Stimulated Amplification of Spontaneous Emission (SASE) concept. With SASE, a high-current, low-emittance electron beam is passed through a long undulator and the spontaneous radiation at the resonant wavelength is amplified. The concept of a SASE-based X-ray Free Electron Laser (FEL) has been studied at SLAC using the SLAC linac [8]. This is now the basis of a formal proposal, the Linac Coherent Light Source (LCLS) [9], which is expected to begin construction in 2004.

The idea of introducing an X-ray FEL into the linear collider facility is discussed extensively in the TESLA TDR. For the NLC, this option has not been strongly pursued because the advantages of integrating this facility into the collider are not yet clear. The FEL requires electron beams of between 15 and 50 GeV. Unfortunately, the desired beam emittance and longitudinal phase space are different from those needed for the linear collider. Thus, the FEL beam must be generated in a different electron source and compressed with additional bunch compressors. The only component of the linear collider that is reused is roughly 5% of the linac which is at most a small fraction of the facility costs for either the linear collider or the X-ray FEL. This is true for all of the linear-collider designs being considered.

If an FEL capability becomes desirable, it can easily be integrated into the NLC complex. The S-band and X-band linacs in the NLC can be used to manipulate the longitudinal phase space so that the beams can be compressed to the very small bunch lengths that are required. Furthermore, the transverse dynamics in the linacs are not an issue because the bunch length is shorter and the vertical emittance for the FEL is much larger than for collider operation.

Possible operational scenarios:

- Introduce an additional S-band linac at the end of the prelinac and add a new bunch compressor. This becomes very similar to the LCLS design. It shares much of the NLC infrastructure.
- Add a parallel X-band linac adjacent to the main linac and run the injector linacs at a higher repetition rate.
- Use the main X-band linac in dedicated FEL operational mode. This reduces the luminosity delivered for high-energy physics or requires operating the low-energy portion of the collider at a higher rate.

Each of these schemes would be very similar through the beginning of the second bunch compressor. The first scenario could be designed as nearly a straightforward copy of the LCLS. Since the S-band injector linacs have relatively long filling times, the FEL beam could be accelerated on the trailing edge of the rf pulses. At the end of the prelinacs, it would then be injected into a dedicated linac for the FEL. The second and third scenarios are similar in that the injector linacs would accelerate the FEL beam through the second bunch compressor. At this point, the FEL beam would be injected into a dedicated FEL X-band linac, which is only a few-hundred meters in length. The last scenario is distinct in that it would use the main X-band linac operating either at a higher repetition rate or with reduced rate to the high-energy IP. These three options are illustrated schematically in Fig. 2.2.

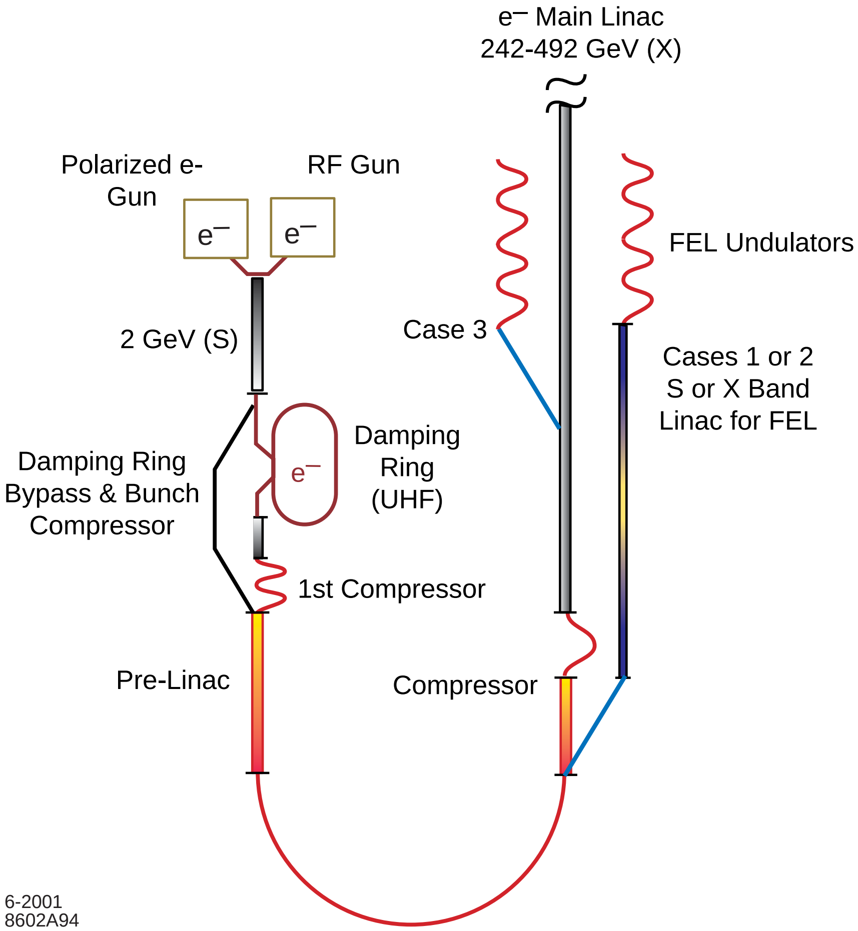

**Figure 2.2:** Schematic showing the layout of the FEL accelerator sections for three different scenarios.

## 2.5 Route to a Multi-TeV Linear Collider

The collider described in this report is designed to operate with center-of-mass energies up to 1 TeV or possibly 1.5 TeV. The next logical step for electron-positron facilities would then be a linear collider that operates in the 3- to 5-TeV center-of-mass range with a luminosity of $10^{35}\,\mathrm{cm}^{-2}\mathrm{s}^{-1}$ or more. Some of the technological issues of such a facility, and the parameters which would be required to achieve its goals, have been considered [10,11]. The principal issues that must be addressed are achieving the desired energy and the desired luminosity.

### 2.5.1 Energy and Accelerating Gradient

Attaining the desired collision energy at a reasonable cost is probably the most difficult issue. The most straightforward route to higher energy – expanding the length of the linacs while using the baseline NLC technology – would require 60 km per linac for 5-TeV cms. Under almost any assumptions, a linear collider with 120 km of total linac length does not seem to be feasible. While the length of the linacs can be reduced by increasing the accelerating gradient, the achievable gradient is not the sole parameter which determines the system cost. For example, doubling the gradient in the NLC structures would require a four-fold increase in rf power. This in turn would require a four-fold increase in rf power components, site-power usage, etc. Although the linac length would be reduced by the increased gradient, the total costs would still be prohibitive. Thus, a multi-TeV linear collider requires both a higher gradient, to limit the linac length and costs associated with length, and a more cost-effective rf power system, to limit the costs that are nominally proportional to the accelerating gradient.

The present limit on achievable accelerating gradient is set by structure damage that is caused by rf breakdowns at high power. The fundamental limits on gradient are known to be higher than the gradients at which damage is observed in prototype multicell structures. For example, the present gradient limit on NLC-type structures is at approximately 70 MV/m, but single cells at the same frequency have operated reliably at gradients of 150-200 MV/m. In Chapter 4 the extensive R&D program on this issue now being carried out by the NLC, KEK and CLIC groups is discussed. The high gradients tolerated by single-cell cavities suggest that a solution to this problem will be found, although the resulting accelerator structures will likely be significantly different from those designed for use in the NLC.

A number of approaches have been suggested that would reduce the cost of the rf system for a future linear collider. These include multibeam klystrons and active pulse compression, both of which are areas of vigorous research. A very promising approach is the two-beam accelerator (TBA) concept used in the CLIC design, in which a low-energy, high-charge drive beam is decelerated in a beamline full of low-impedance rf structures, and the power extracted is used to accelerate a high-energy, low-charge main beam in a series of high-impedance structures. This approach has been studied for some time, and at present appears to be the most likely route to an improved rf power system. A major test facility for both TBA and high-gradient studies at frequencies above X-band will be the CLIC Test Facility 3 (CTF3), which should be operational by 2004 [12].

### 2.5.2 Luminosity

Table 2.5 lists luminosity-related parameters for TESLA at 0.5-TeV cms, NLC at 1.0-TeV cms, and CLIC at 3.0-TeV cms. The CLIC design's most challenging parameters – beam power, vertical emittance, and vertical rms beam size at the IP – are all reasonable extrapolations from the NLC parameters. The vertical beam size and emittance are reduced by a factor of a few times. This implies that the alignment and jitter tolerances will be somewhat tighter, diagnostic equipment such as BPMs and laser-based profile monitors will require modest improvements, and a small number of additional magnets will require active stabilization. The horizontal beam size and emittance have been reduced by similar factors, implying that an improved damping ring, redesigned bunch compressors, and reduced bending in the beam delivery system will be required to achieve and preserve the small horizontal emittance.

The most significant differences between the NLC and CLIC parameters are related to the beam-beam interaction. The very-high beam energy causes the beamstrahlung energy spread to increase to over 30% and the number of coherent pairs produced is comparable to the number of beam particles. In order to accommodate these larger background sources, the 3-TeV cms linear collider requires a crossing angle of at least 20 mrad [13]. Such a crossing angle appears to be acceptable at higher energies as well. It should be noted that the beamstrahlung is a measure of the fraction of the luminosity far from the nominal center-of-mass energy. The fraction of luminosity close to the nominal energy does not change nearly as much although it does tend to decrease with increasing energy.

### 2.5.3 The NLC Configuration and Multi-TeV Options

While it is too early to determine the technologies that will be used at a multi-TeV linear collider, a general review of the issues discussed above reveals many of the requirements of such a facility. The NLC configuration has been developed with these requirements in mind. For example, the multi-TeV linear collider will require a site with low levels of ground motion, a crossing angle of at least 20 mrad, beam delivery systems with weak bend magnets, and in all probability a main-linac tunnel that can accommodate a second beamline for the ‘drive beam.’ All of these features are included in the NLC design. In many cases, the NLC requirements are identical to those of a future facility. In other cases, configuring the NLC design to accommodate a future linear collider incurred no financial or technical penalties. This permits the NLC injectors, beam delivery systems, and main-linac housings to be used in a multi-TeV collider, although the main-linac accelerator structures and rf power sources would need to be replaced. Some upgrades of the damping rings, bunch compressors, and final-focus beamlines would also be required.

**Table 2.5:** Key parameters for the TESLA, NLC, and CLIC designs

| **PARAMETER NAME** | **TESLA** | **NLC** | **CLIC** |
|---|---|---|---|
| Energy | 500 GeV | 1 TeV | 3 TeV |
| Luminosity | $3.4\times10^{34}\ \mathrm{cm^{-2}s^{-1}}$ | $3.4\times10^{34}\ \mathrm{cm^{-2}s^{-1}}$ | $10\times10^{34}\ \mathrm{cm^{-2}s^{-1}}$ |
| Lum. within 1% of $E_{cms}$ | $1.7\times10^{34}\ \mathrm{cm^{-2}s^{-1}}$ | $1.5\times10^{34}\ \mathrm{cm^{-2}s^{-1}}$ | $3.0\times10^{34}\ \mathrm{cm^{-2}s^{-1}}$ |
| Beamstrahlung | 3.2% | 10.2% | 31% |
| Bunch Length | 300 µm | 100 µm | 30 µm |
| Beam Emittance | 10 × 0.02 mm-mrad | 3×0.02 mm-mrad | 0.7×0.02 mm-mrad |
| IP Spot Size | 553×5 nm | 190×2.1 nm | 43×1 nm |
| Beam Power | 11.3 MW | 13.7 MW | 14.8 MW |
| Rf systems | Super Conducting | Normal Conducting | Normal Conducting |
| Peak Rf Power | 0.2 MW / structure | 170 MW / structure | 230 MW / structure |
| Repetition Rate | 5 Hz | 120 Hz | 100 Hz |
| Bunch train length | 950 µs | 265 ns | 100 ns |
| Linac tunnel length | 30 km | 26 km | 27 km |

The history of accelerator laboratories makes one point clear: the investment in the infrastructure of the accelerators, including the beamline housings, is significant and therefore the infrastructure should be used and reused for as long as possible. This has led to the use of existing synchrotrons as injectors for new synchrotrons, and in some cases to the decommissioning of existing accelerators so that the tunnels or components can be recycled for use in new accelerators. It is this history that has shaped the decision to make the NLC design as compatible as possible with future energy upgrades.

# References

[1] American Collider Working Group, *Linear Collider Physics Resource Book for Snowmass 2001*, BNL-52627, CLNS 01/1729, Fermilab-Pub-01/058-E, LBNL-47813, SLAC-R-570, UCRL-ID-143810-DR, LC-REV-2001-074-US.

[2] NLC Design Group, *A Zeroth-Order Design for the Next Linear Collider*, SLAC–474, LBL–PUB–5424, LBNL–PUB–5424, UCRL–ID–124161 (1996).

[3] Adolphsen, C., et al., *Phys. Res. Lett.*, **74**, 2475 (1995).

[4] Raimondi, P. and Seryi, A., “A novel final focus design for future linear colliders,” *Phys. Rev. Lett*., **86**, 3779 (2001).

[5] Hendrickson, L., et al., “Luminosity optimization feedback in the SLC,” *Proc. Int. Conf. on Acc. and Large Experimental Physics Control Systems* (ICALEPCS 97), Beijing, China (1997).

[6] *2nd International Workshop On High Energy Photon Colliders,* Batavia, Illinois, March 2001, URL: http://diablo.phys.nwu.edu/ggws/.

[7] “3rd International Workshop On Electron-Electron Interactions At TeV Energies”, Santa Cruz, California, December 1999, *Int. J. Mod. Phys*. **A15** 2000.

[8] *Workshop on 4th Generation Light Sources*, Stanford, California, February 1992.

[9] Cornacchia, M., “SASE based 4th generation light sources and the LCLS project,” *Proc. of the 1999 IEEE Part. Acc. Conf.,* New York 1999.

[10] Assmann R. W., et al., “A 3-TeV e+ e linear collider based on CLIC technology,” CERN-2000-008, 2000.

[11] Chen, P., et al., “A 5 TeV Linear Collider on the NLC Site,” *Proc. of the 1996 DPF/DPB Snowmass Meeting*, Snowmass, Colorado 1996.

[12] Braun, H. H., “Achievements and future plans of CLIC test facilities,” *Proc. 18th Int. Conf. on High Energy Acc.,* Tsukuba, Japan, 2001.

[13] Schulte, D., “Machine-Detector Interface for CLIC,” *Proc. of the 2000 Int. Linear Collider Workshop*, Batavia, Illinois 2000.

# Chapter 3

# Conventional Facilities

## 3.1 Introduction

The Next Linear Collider (NLC) will be a twenty-mile-long (32 kilometer) linear electron accelerator very much like the two-mile (3.2 kilometer) accelerator at SLAC. The accelerator will be located underground in a tunnel that would be suitable for housing a single-track subway. At most, the surface presence will consist of periodic access points to equipment buildings spaced several football fields apart. In one alternative these would be covered with earth and grass. In another alternative they would be replaced by additional underground housings aligned with the accelerator much like a two-track subway. In this approach there would be very little surface presence except at the central campus.

The NLC design includes potential sites in both California and Illinois, where the solutions chosen have been based on local geology and locally appropriate construction techniques. The California 135 site on the eastern slope of the California coastal mountain range is a rural, near-surface cut-and-cover solution with remote injectors, a distributed three-laboratory campus, adjacent power and water, and uniform geology . The Illinois North-South site is a suburban deep-tunnel solution with a central injector complex that takes maximum advantage of the uniform rock strata and the existing Fermilab site infrastructure. Additional sites being considered are an East-West cut-and-cover site in Illinois as well as bored tunnel sites in California which take advantage of the hilly terrain to provide horizontal access to a tunnel in competent rock.

The basic requirements of the configuration will be to include accelerator housings long enough to provide adequately for 1-TeV center-of-mass beams in the future even though the main linac housings would initially contain components to reach just 500 GeV. The total of enclosed beam line will be 36.5 km. By comparison, the existing LEP tunnel at CERN is 27 km in length. Two experimental interaction halls are planned. One hall will be a high-energy hall and the other hall will be for lower-energy collisions. The two halls will be offset from each other by about 440 meters longitudinally and 20 meters transversely. The high-energy hall will be in a direct line with the main linacs which are not collinear, but are tilted at a very small 20-milliradian angle with respect to each other. Two alternates are planned for the configuration of the injector complexes. One will place the positron and electron injectors at opposite ends of the machine. The other will place all injectors near the center of the machine.

Electric power consumption will be less than 200 megawatts of metered demand, about equivalent to that used by a city of 200,000 people. Water consumption will be roughly 7 acre feet each day of operation or about what is used by a city of 28,000 people. Emissions of radiation from the accelerator will be contained underground within the tunnel housing, and exposures from the accelerator to human populations off-site will be much less than natural backgrounds. Similar accelerators are presently operated safely at laboratories in heavily populated areas at SLAC (California), Fermilab (Illinois), Hamburg (Germany), and Geneva (Switzerland).

The sections that follow describe preconceptual development and options for configurations, sites, injectors, main linacs, detectors and campuses.

## 3.2 Sites

### 3.2.1 Site Criteria

The NLC beam housings must be structurally stable, thermally stable, and be subjected to an absolute minimum of local noise and vibration [1]. To reduce rf microwave losses, the beam housing must be adjacent to a klystron gallery housing which is continuously accessible by personnel for maintenance. The klystron housing must be separated from the beam housing by at least 2.4 meters (8 feet) of concrete or rock shielding. The beam housing must be shielded from the general surface environment by at least 7.3 meters (24 feet) of earth and/or rock. Where the beam and klystron housings are in adjacent parallel bored tunnels, the required housing separation is greater than 2.4 meters (8 feet) to maintain adjacent tunnel structural stability. Slow drift of the beam housing floor may not exceed a maximum of ±1.5 mm (± 0.059 inches) during a nine-month run period, after which realignment smoothing can be done to return the remotely controlled movers on the beam-line components to the center of their working range. The allowed amount of motion is roughly twice that observed in the SLAC linac tunnel after construction and more than that observed at LEP. The diffusive motion of the floor may not exceed about 3 microns over 100 meters (328 feet) after a day. The motion measured at SLAC and in other tunnels built in competent rock is much less than this limit, so the stability should be achievable. To restrict the motion of components mounted on the girders, the temperature of the tunnel must be stabilized to a fraction of a degree, similar to what is typical for the SLAC linac.

The beam housing must be either deep underground or near the surface in a very quiet rural location to avoid local sources of noise and vibration. NLC utility-induced vibration in the beam housing floor directly below the beam-line magnet pedestals is limited to 3 nanometers at frequencies above 3 Hz. Various specific frequency amplitude peaks (for example 60 Hz) are evaluated on a total power spectrum basis. The beam housing cooling water system is limited to a low flow rate velocity to minimize mechanical vibration. Critical technical components inside the beam housing are cooled with low conductivity water supplied at 32°C, ± 0.17°C at 17°C rise (90°F, ± 0.3°F, at 30°F rise). The air temperature in the beam housing is close to 95°F during normal beam operation. Except for drainage sump motors, no utility motors are permitted inside the beam housings or in the adjacent klystron gallery and housings. Remote utility motor controllers are to be variable frequency drives and phase locked to the 120 hertz beam repetition rate. Low conductivity cooling water for the klystron and modulator rf systems is to be 90°F supply, ± 5°F, at 65°F rise. Sections that follow describe preconceptual development and options for configurations, sites, injectors, main linacs, detectors and campuses.

### 3.2.2 Illinois North-South

The Illinois North-South site for the NLC is centered on the 2,750 hectare (6,800 acre) Fermilab site and takes advantage of the favorable geology of the area. The alignment chosen seeks to minimize adverse impact to the surrounding community by aligning the off-site portions of the NLC complex within developed utility corridors and surrounding light industrial areas. Parallel tunnel construction, similar to transportation tunnels, allows greater distances between necessary points of egress, thus reducing off-site construction at grade.

The North-South orientation, shown in a section view in Fig. 3.1, provides consistently flat geological features with rock conditions proven to be favorable. The Chicago Deep Tunnel, the local Aurora Area Mine and the current MINOS project at Fermilab have provided extensive experience with the geologic strata of Northern Illinois. Further investigation and understanding of local ground motion is underway.

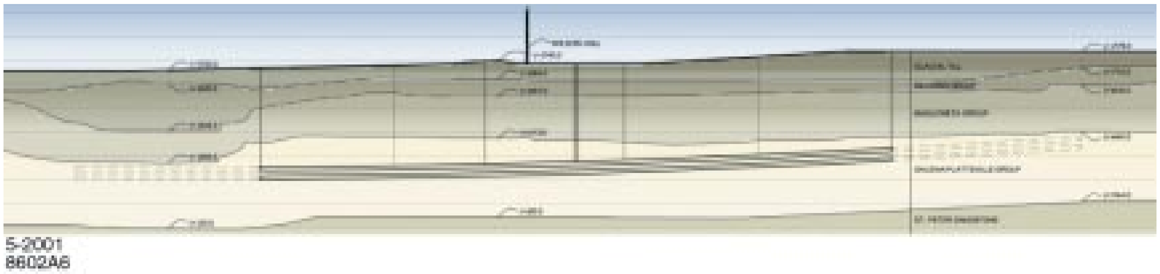

**Figure 3.1:** North-South Geologic Section View (galena / platteville in yellow)

### 3.2.3 California 135

The California sites for the NLC that have been investigated to date have been aligned to be parallel and close to both the west coast North-South electric power transmission corridor and the adjacent California aqueduct system that stores and distributes water along the Great Central Valley. Native California sandstone comes to the surface in long straight formations providing a stable competent rock base for the NLC.

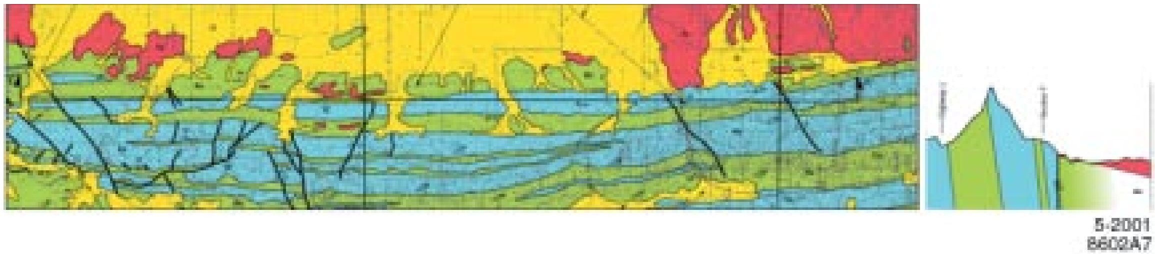

**Figure 3.2**: Site 135 Geologic Plan View (40 x 10 km) and Cross-section View (sandstone in blue)

The 135 site plan and cross section view is shown in Fig. 3.2. The rock formations are typical of the region and other sites are available with similar attributes. To obtain the best structural stability, the beam housing must be in a location where the bedrock is either at or very near the surface. A near-surface site must also be in a rural environment away from man-made cultural noise and vibration sources. These conditions exist along the eastern slope of the California coastal mountain range. There, the critical assets: geology, power, water, and quiet available land, are all in close proximity. There are possible sites which are straight and parallel and extend for several tens of kilometers to provide an attractive location for the NLC.

### 3.2.4 Site Development Work

A collaborative effort between the Facilities Engineering Services Section at Fermilab and the NLC Conventional Facilities group at SLAC is developing potential sites in both California and Illinois [2]. To expand and augment the R&D work, the NLC has employed a variety of consultants to evaluate and develop portions of the project. Technical areas investigated so far include geology, geotechnical engineering, tunnel construction costs, life safety, land use, mechanical cooling, electric power distribution, and electric power resource development. Firms contributing to these studies include: Anderson & Associates, Fluor Daniels, P. Frame & Associates, Gauge Babcock, Harza Engineers, Jacobs Associates, Knight Advanced Technology, and Patrick Engineering.

## 3.3 Injectors

The different solutions chosen for the Illinois and California sites also lead to a different optimization of the layout of the injector complexes. For the California site, the injectors are located at the far ends of the site at the low-energy ends of the main linacs. This minimizes the length of tunnel and transfer lines required between the injectors and the linacs. For the more densely populated Illinois site, the injectors are centrally located on the existing Fermilab campus.

### 3.3.1 Central Injectors

The North-South machine alignment at Fermilab is envisioned to have centralized injection complexes at or near the surface, with low-energy transport lines taking the beams to the remote ends of the machines. These complexes will be located on the existing Fermilab site, thus avoiding the need for land acquisition for the injectors at the far ends of the main linacs and allowing ease of access because of their central location. The central injector schematic is shown in Fig. 3.3. The electron and positron injectors are positioned in a central location adjacent to the interaction regions. A transfer line connects the injectors to their respective compression bends and main linacs. The centralized injection complexes will be configured to house several beam lines in common housings and will be located at or near grade level. Utilities to support the centralized injector complexes will come from the existing Fermilab central utility complex. The near-grade locations of the injection complexes are presumed to provide effective noise and vibration isolation between the injector complex and the final focus and experimental detector halls.

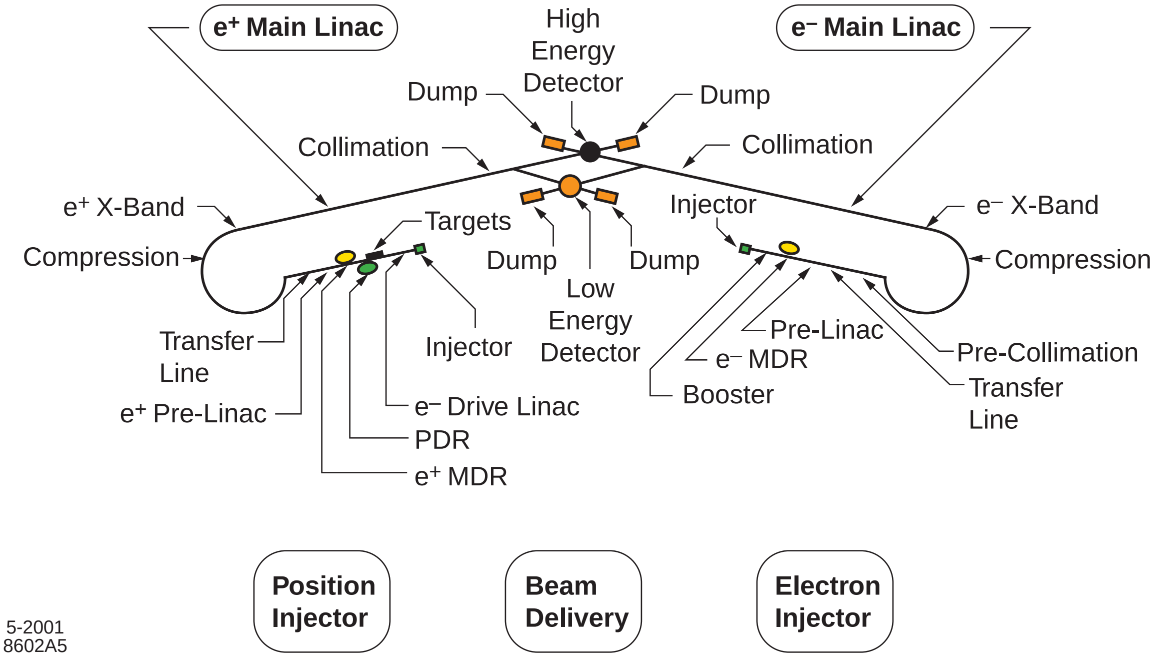

**Figure 3.3**: NLC Central Injector Schematic Overview

### 3.3.2 Remote Injectors

Functionally, the NLC has two independent injector complexes, one for electron beam production and one for positron beam production. As there are two main linacs in the NLC, separated by 30 kilometers (18 miles) at their far ends, the two injector complexes are naturally remote from each other and from the center of the site where the experimental halls are located. The NLC remote injector schematic is shown in Fig. 3.4. The electron and positron injectors are positioned immediately adjacent to the compression bend arc at the beginning of their respective main linacs. This configuration is the least expensive and is preferred for the California site 135 and any site where land costs at the ends of the linacs are not prohibitive. The remote injection complexes will be configured to house several beam lines in common housings and will be located at or near grade level. Utility equipment vibration and cultural noise associated with the remote injectors is isolated from the experimental halls by displacement dispersion of at least 15 kilometers (9 miles) each way. For the 135 site, each of the remote injector complexes is near an available access road and is at the same elevation as to the main linac, reducing complexity and cost. Remote injectors have only 180° of beam compression arc housing compared to 360° for the central injector, and they require no beam transport lines in the main linac housings.

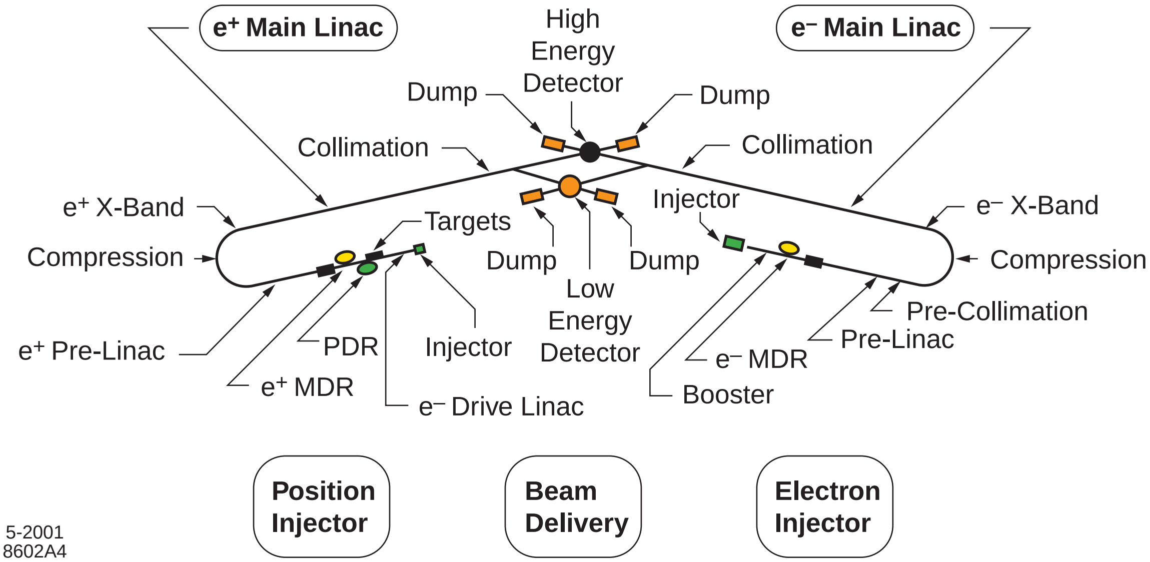

**Figure 3.4**: NLC Remote Injector Schematic Overview

## 3.4 Main Linacs

### 3.4.1 Parallel Deep-Bored Tunnel Configuration

The NLC parallel deep-bored tunnel configuration utilizes two tunnels bored through dolomitic rock at a depth of 30 to 90 meters (100 to 300 feet) below the surface. The optimal depth is a trade-off between tunneling costs and vibration isolation from surface noise sources. The parallel tunnel layout places klystrons and modulators as close as practical to beam-line components to minimize rf losses between them. Each tunnel provides personnel egress to the other tunnel to facilitate hazards management for deep underground occupancy. This scheme is used in most underground transportation tunnels worldwide. Fire separation doors between the tunnels are placed at intervals of 450 to 600 meters (1,500 to 2,000 feet). One tunnel is a support enclosure which houses klystrons, modulators, transformers and piping with continuous access for maintenance personnel.

The other tunnel, shown in Fig. 3.5, is called the beam-line tunnel. It is parallel but offset from the support tunnel by a distance sufficient to protect maintenance personnel from radiation during ‘beam on’ operations. Radiation shielding is provided by the rock between the tunnels. The beam line tunnel houses the DLDS rf distribution system and the beam line with its various technical components. The parallel tunnels are to be constructed with tunnel boring machines, which appears to be both feasible and cost effective. Small tunnel-tunnel penetrations are to be cored. Larger penetrations will be drilled and blasted as needed.

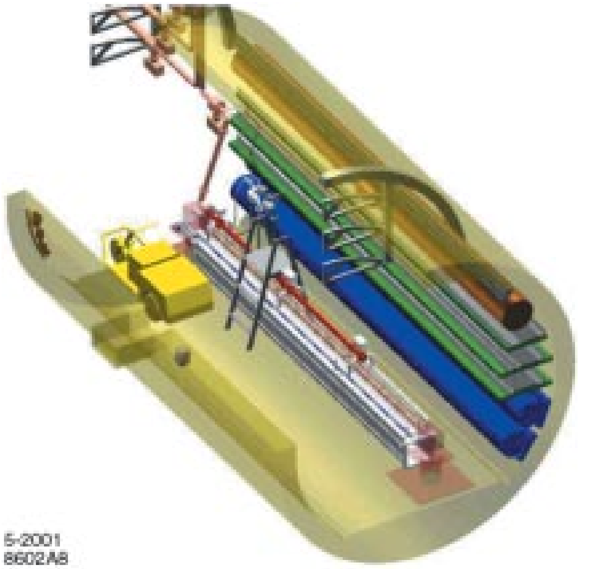

**Figure 3.5**: Parallel Deep Tunnel View – Beam Housing Tunnel Only

### 3.4.2 Near-Surface Precast Section Configuration

The NLC near-surface configuration is designed for a cut-and-cover construction technique with precast concrete sections similar to the one employed at FNAL for the Main Injector project. This configuration is shown in Fig. 3.6. Periodic ramps to the surface provide access for conventional surface vehicles along the length of the beam-line housing. The average depth underground of the precast section housings is 10 meters (33 feet), enough to provide radiation safety shielding and diurnal temperature isolation.

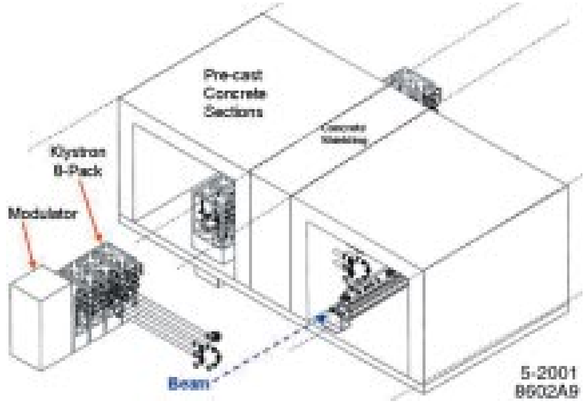

**Figure 3.6**: Near Surface Precast Section Configuration Line Drawing Section

## 3.5 Detectors

### 3.5.1 High and Low Energy Experimental Halls

Two experimental halls are planned for the NLC, one identified as ‘High Energy,’ and one identified as ‘Low Energy,’ which are similar in most respects. The two beams that intersect in the high energy hall cross at a 20-milliradian angle. This hall has a floor area of 2,280 square meters (24,500 square feet) with a bridge crane span of 30 meters (98 feet) and travel of 76 meters (249 feet). The Low Energy hall has a detector floor area of 1,080 square meters (11,600 square feet) with a bridge crane span of 20 meters (66 feet) and travel of 54 meters (177 feet). The low energy hall beams intersect and cross at a 30-milliradian angle. Both detector halls are in and on bedrock and, for the remote injector configuration, away from other areas of the NLC having concentrations of utility equipment and noise sources. Figure 3.7 shows the experimental hall with the detector.

**Figure 3.7:** Interaction Hall with Detector and Beam Housings

### 3.5.2 Deep and Near Surface Experimental Halls

The experimental hall detectors have a center bore that is critically aligned to the same elevation as the main linac beam. The main linac beam is planned to be in either near-surface or deep-tunnel housings depending on the NLC site selected and the construction technique used. The detector experimental halls will be at a matching elevation with the linac housing, either 10 meters (33 feet) below the surface or 100 meters (330 feet) below the surface for the two alternatives under consideration. As the total high-energy detector assembly weight is on the order of 11,000 metric tons, moving it, even in sections, will be quite different depending on the elevation differences and the lateral access space available. The near-surface experimental hall alternative offers a clear advantage for moving large, heavy detector components. A vehicle ramp between the detector floor and the surface would allow a single move from the transport vehicle using the detector hall bridge crane. Alternatively, an experimental hall at a deep tunnel elevation may not include a surface ramp as a practical option. A deep experimental hall would likely be more costly to construct and have additional functional complexity for detector assembly rigging operations. Offsetting these apparent shortcomings, a well-designed experimental hall at a deep tunnel elevation would likely have better isolation from surface sources of utility vibration and cultural noise.

## 3.6 Campus

### 3.6.1 Central Campus

A central campus on the existing 2,750 hectare (6,800 acre) Fermilab site in Illinois would function to support the NLC through all phases of development, using the laboratory facilities and staff. The preferred North-South site machine alignment would place the NLC immediately adjacent to existing laboratory space, available to be used for construction, testing, installation, operation and maintenance of the technical components. Most of the personnel working on the NLC would be located on the laboratory site.

The beam-delivery housings and the interaction halls would be constructed in bedrock deep beneath the existing site. The central injection complex and the various associated support facilities would be constructed in the glacial till near the surface. All of these facilities would be entirely within the Fermilab site boundaries. Technical support facilities, including machine shops, assembly halls, communication centers and utility control facilities, would be constructed at grade, near the center of the NLC complex. Surface transportation of equipment outside of the laboratory boundaries for installation and maintenance would be largely accomplished through direct tunnel access from the surface at the central campus.

The personnel and the site infrastructure to construct and operate the NLC project at Fermilab includes buildings for administrative and support staff, conference and meeting facilities, computing space, warehousing, machine and preassembly shops, roads, sewers and cooling ponds. Functional analysis of the facility requirements for the NLC has begun and is expected to provide additional planning tools for the design and construction of the conventional facilities.

### 3.6.2 Distributed Campus

A distributed campus in California would provide support for the NLC. The 135 accelerator site is envisioned to have a minimum of personnel who would be primarily responsible for site operations and maintenance. Operation of the accelerator would be from distributed control rooms, both at the site and in the other laboratories. Most of the personnel at work on the NLC would be located at the existing nearby laboratories in Northern California including SLAC, LLBL and LLNL. The existing laboratory infrastructures for fabrication, measurement, testing and other tasks will become a part of the distributed NLC campus. These laboratories would also provide administration and support staff, conference and meeting facilities, computing space and other functions. The largest single block of new space constructed at the NLC experimental site would be highly flexible warehousing with modular internal occupancies to adapt to the various needs of the NLC project, from planning, through construction, to operations.

## References

[1] Corvin, C., "NLC 2001 Configuration Documentation-Conventional Facilities," *http://www-project.slac.stanford.edu/lc/local/Reviews/Apr2001/Documentation.htm*, May 2001.

[2] Kuchler, V., Corvin, C., "NLC 2001 Conventional Facilities Configuration", U.S. NLC Collaboration Video Meeting, February 2001.

# Chapter 4

# Rf System Design

## 4.1 Introduction

### 4.1.1 Historical Perspective

The design of the NLC main linacs is based on the extensive experience gained from the design, construction, and 35 years of operation of the 3-km SLAC linac, which is powered at a frequency of 2.856 GHz. Since its initial operation in 1966, the SLAC linac has been continuously upgraded for higher energy, higher intensity, and lower emittance.

The initial gradient of the SLAC linac was 7 MV/m. The original design included an upgrade path in which the number of klystrons would be quadrupled. The upgrades that were eventually implemented involved replacing each of the initial 24-MW klystrons with a single higher-power klystron (first with 35-MW, XK-5 klystrons and, later on, with 65-MW, 5045 klystrons), and adding a SLED pulse compressor after each klystron to more than double the peak power. The SLAC linac is currently energized by 240 high-power S-band klystrons. The klystron peak power and pulse duration are, respectively, 65 MW and 3.5 μs. After pulse compression, the power from one klystron feeds four 3-m constant-gradient S-band accelerator structures operating in the $2\pi/3$ mode. The accelerator gradient has been tripled since 1966, to 21 MV/m, and the maximum beam energy is now 50 GeV.

### 4.1.2 NLC Rf System Overview

The NLC has two main linacs that accelerate electron and positron beams from 8 to 250 GeV in the initial configuration, and to 500 GeV or more after full installation. The 11.424-GHz radio frequency (rf) system used for this purpose is similar in character to that in the SLAC linac. The NLC system is illustrated in Fig. 4.1 and includes all the hardware through which energy flows, from the AC input to the beam-line accelerator structures. Electrical energy is transformed in several stages: the induction modulators convert AC power to high-voltage pulsed DC; the klystrons transform the pulsed DC to high-power rf; the Delay Line Distribution System (DLDS) combines the power from eight klystrons and routes it up-beam sequentially to eight sets of accelerator structures; and finally, the six structures in each set convert it to beam power. Because the power required to drive the accelerator structures is high, it is important that the conversion and transmission of energy at every stage of the rf system be efficient. Every effort must be made to maximize the pulse energy generation and handling capabilities of the subsystems to reduce the number of components, and thus the cost.

The primary technical choice for the rf system is the 11.424-GHz frequency (2.62-cm wavelength). This frequency, high in the X-band range (8.2 to 12.4 GHz), is exactly four times that of the SLAC 50-GeV linac. The choice of such a high frequency, relative to existing linacs, allows the same rf-to-beam efficiency for a given beam current to be achieved at a higher gradient (thus a shorter linac) with less rf energy per pulse (thus fewer rf components). On the downside, stronger transverse wakefields are generated by off-axis beams in higher frequency accelerator structures, which act to increase the beam emittances. The choice of 11.424 GHz gains the major cost benefits of a higher-frequency rf system while allowing achievable alignment tolerances associated with the stronger wakefields.

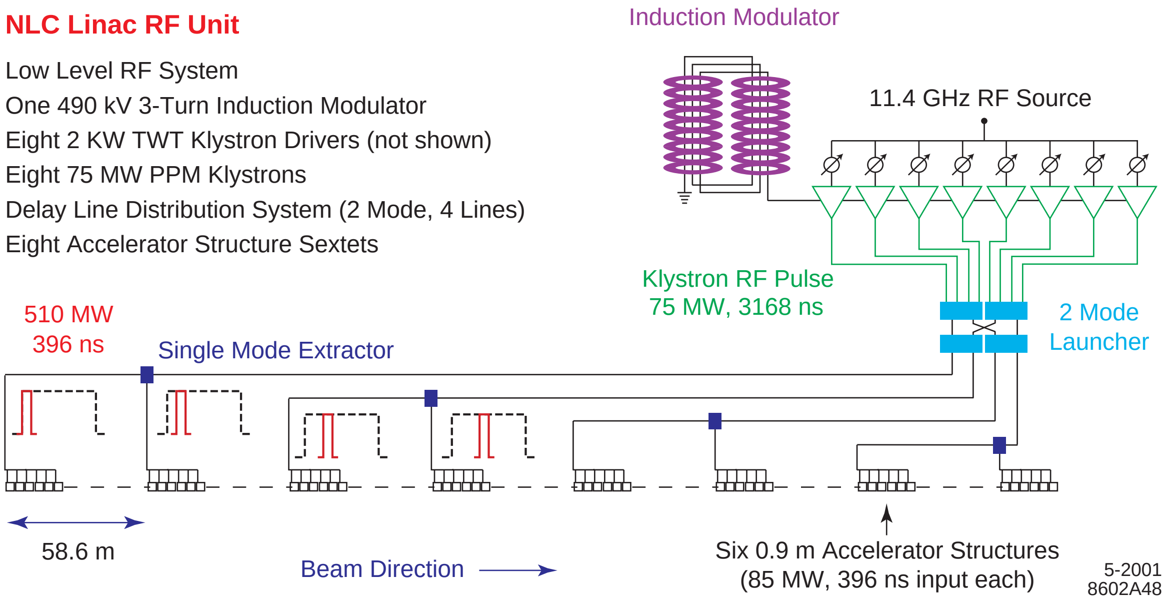

**Figure 4.1:** Schematic of a linac rf unit (one of 117 per linac).

Outstanding progress has been made in applying and extending the science and engineering of microwave power and acceleration systems from S-band, the enabling technology for the SLAC linac, to X-band, which can provide the significant performance improvements and cost reductions needed for a high-energy linear collider. New modulators, klystrons, microwave power distribution systems, and accelerator structures that can meet the challenging demands of the Next Linear Collider (NLC) are in the final stages of development. The R&D on these components has been pursued as a joint effort with the Japanese Linear Collider (JLC) project as part of the International Study Group (ISG) developing designs for an X-band linear collider.

The X-band rf components for the NLC are being tested in the NLC Test Accelerator (NLCTA). The NLCTA was constructed using the first versions of these components. It was commissioned in late 1996 and, in 1997, accelerated beam to 300 MeV at a gradient of 45-50 MV/m. The first iteration of the NLC rf system installed in the NLCTA could have been used to power a 500-GeV linear collider, but the system was inefficient and costly. Subsequent design changes have improved the electrical efficiency by roughly 50% and have reduced the expected cost by a similar factor. The current rf system being developed will form the basis for a 1-TeV linear collider.

High-power pulse modulators with increased efficiency and reliability have been developed. They are based on induction cells and relatively inexpensive IGBT switches, components made available by industrial markets of much greater volume and competitiveness than high energy physics. A small-scale version of the induction-based modulator has driven an S-band klystron in the SLAC Linac. A full-scale test version will soon drive four S-band klystrons and, in 2002, eight X-band klystrons.

Klystrons have been developed that efficiently amplify pulsed X-band rf to high power using a velocity-modulated electron beam vacuum tube, much like the S-band klystrons in the SLAC Linac. The beam in the X-band tubes, however, is focused by periodic permanent magnets (PPMs) instead of electromagnetic solenoids to reduce power consumption. This saves 47 MW relative to operation with a comparable number of solenoidal-focused klystrons. R&D versions of X-band PPM klystrons, designed for 50- and 75-MW peak power levels have been successfully operated at low pulse-repetition rates. The PPM klystron design is being improved to make it more robust, easier to manufacture, and operable at the nominal 120-Hz pulse rate. In addition, klystrons are being built with industrial participation to qualify potential vendors.

A dual-moded Delay Line Distribution System (DLDS) has been developed to transform the 3.2-μs 75-MW klystron pulses to the 0.4-μs 600-MW pulses needed by the accelerator structures. DLDS is a more cost-effective and efficient implementation of the low-loss waveguide technology first developed and used for high-power Binary Pulse Compression and SLED-II. The microwave properties of the most critical components have been demonstrated. Full power tests of the DLDS are planned in the next two years at the NLC Test Accelerator at SLAC, and later at an Engineering Test Facility (ETF) at Fermilab.

Accelerator structures for X-band have been developed and used to accelerate beams at gradients up to 70 MV/m in the NLCTA. The intense transverse wakefields created by the small apertures of the X-band structures have demanded new techniques for preservation of emittance and suppression of beam breakup. Solutions incorporating cavity detuning and damping have been developed and proven effective. Limitations on structure lifetime at these high gradients were encountered and a program to address this issue is being vigorously pursued. Recent results from this program suggest that a 0.9-meter rf structure with a low group velocity will meet the NLC requirements for accelerating gradient, reliability, and short-range transverse wakefields.

System integration testing of the rf components will be carried out in two stages. The essential elements of an NLC X-band linac rf unit will be tested with full power pulses at the NLCTA in two years. An Engineering Test Facility containing a full-size linac rf unit as shown in Fig. 4.1 will be built later at Fermilab. The ETF will use industrially produced versions of the components and allow studies of installation and maintenance procedures needed for the final engineering design of the collider. Acceleration of beam in the ETF will provide operational experience and a bottom-line demonstration of its performance. This facility could be completed in FY06/07, and would be a milestone on the road to completion of construction of the NLC.

The parameters of the NLC linac beam and the major rf subsystems (modulators, klystrons, rf distribution, and accelerator structures) are listed in Table 4.1. Of the rf parameters, the choice of acceleration gradient has the largest impact on the linac cost. The unloaded gradient ($G_U$) of 70 MV/m is close to optimal in the tradeoff between energy-related costs (e.g., modulators and klystrons), which scale roughly as $1/G_U$, and length-related costs (e.g., structures and beam-line tunnel), which scale roughly as $G_U$. However, the overall linac cost has a fairly weak dependence on unloaded gradient in the range of interest for the NLC (50 to 100 MV/m). The beam parameters were chosen as a tradeoff between increasing rf-to-beam efficiency and easing tolerances related to both short-range and long-range transverse wakefield effects. These beam-related choices are described in more detail in ref. [1] and are discussed in Chapter 2.

The upgrade to 500-GeV beam energy (1-TeV cms energy) will be accomplished by doubling the number of rf components while keeping the beam parameters the same. The linac housings will initially be sized for 1-TeV cms energy operation, but only the upstream half of each linac will have rf components installed. For the initial operation at 500-GeV cms energy, the beam will 'coast' through the downstream half of each linac housing.

A brief description of each major rf subsystem follows, including design choices and R&D progress. The section concludes with a description of the linac layout. Sections 4.2 through 4.5 describe the rf subsystems in greater detail.

**Table 4.1:** Linac Beam and Rf System Parameters.

| **BEAM PARAMETERS** | **VALUES** | **UNITS** |
|---|---|---|
| Nominal cms Energy | 0.5 | TeV |
| Initial Beam Energy | 8 | GeV |
| Final Beam Energy | 250.0 | GeV |
| Linac Pulse Rate | 120 | Hz |
| Number of Bunches per Pulse | 190 | |
| Number of Particles per Bunch | 0.75 | $10^{10}$ |
| Bunch Separation | 1.40 | ns |
| Beam Current | 0.86 | A |
| | | |
| **Rf SYSTEM** | | |
| Rf Units (8-Packs) per Sector | 9 | |
| Sectors with Rf per Linac | 13 | |
| AC Power for Modulators per Linac | 60.7 | MW |
| AC Power for Other Rf + Cooling RF System per Linac | 5.5 | MW |
| Total AC Power Related to Rf per Linac | 66.2 | MW |
| Beam Power per Linac | 6.6 | MW |
| AC-to-Beam Power Efficiency | 10.0 | % |
| | | |
| **MODULATORS** | | |
| Modulator Type | 1:3 Induction | |
| Modulator Efficiency | 80 | % |
| Number of RF Modulators per Rf Unit | 1 | |
| | | |
| **KLYSTRONS** | | |
| Klystron Type | PPM | |
| Output Power | 75.0 | MW |
| Number of Klystrons per Rf Unit | 8 | |
| Klystron Pulse Length | 3168 | ns |
| Klystron Efficiency | 55 | % |
| | | |
| **Rf DISTRIBUTION** | | % |
| Type | 4x2 DLDS | |
| Power Gain = Number of Feeds per Rf Unit | 8 | |
| Compression Efficiency | 85 | % |
| Switching Time | 10 | ns |
| Rf Pulse Length per Feed | 396 | ns |
| Rf Group Velocity in Delay Lines | 0.974 | c |
| Implied Sector Length | 468.6 | m |
| Implied Packing Fraction | 0.830 | |

**Table 4.1:** Linac Beam and Rf System Parameters (continued).

| **ACCELERATOR STRUCTURES** | | |
|---|---|---|
| Structure Type | TW | |
| Phase Advance per Cell | 150 | °/cell |
| Initial Group Velocity | 5.1 | % c |
| Structure Length | 0.90 | m |
| Field Attenuation Factor (tau) | 0.510 | |
| Number of Structures per Rf Feed | 6 | |
| Fill Time | 120 | ns |
| Acceleration Shunt Impedance | 81.2 | Mohm/m |
| Loading Shunt Impedance | 82.4 | Mohm/m |
| Peak Rf Power into Structure | 85.0 | MW |
| Unloaded Accelerator Gradient | 70.0 | MV/m |
| Normalized Current (IR/Gu) | 1.01 | |
| Beam loading | 21 | % |
| Multibunch Loading | 15.0 | MV/m |
| Single Bunch loading | 0.34 | MV/m |
| Loaded Accelerating Gradient | 54.7 | MV/m |
| Average Rf phase | 11.0 | degrees |
| Rf Overhead (3% BNS + 3% Failed + 2% FB) | 8 | % |
| Effective Gradient | 47.9 | MV/m |
| | | |
| **LENGTHS** | | |
| Length of Rf Sectors | 6.09 | km |
| Length of Non-Rf Sectors | 6.09 | km |
| Length of Diag. And Bypass Regions | 0.67 | km |
| Total Length of Each Linac Tunnel | 12.86 | km |

### 4.1.3 Klystrons

The X-band power required for the NLC has driven the development of klystrons much more powerful than those commercially available. The designs first considered were similar in concept to the solenoid-focused S-band klystrons used in the SLAC linac. The general design goal was to achieve the highest peak power and the longest pulses possible while minimizing the overall klystron cost for the NLC. As a first step, a robust design, the XL-4, achieved its target power of 50 MW. Ten of these XL-4s have been built. They are used as X-band rf sources for R&D at the SLAC Klystron Test Laboratory and the Next Linear Collider Test Accelerator (NLCTA). They reliably generate 1.5-µs, 50-MW pulses with a 43% beam-to-rf efficiency. In a brief test, one XL-4 klystron was run with 75-MW, 1.5-µs pulses, which were produced with 48% efficiency. The integrated running time of these klystrons is about 10,000 hours, during which time there have been no major failures. (The NLC lifetime goal is > 20,000 hours.)

When the XL-4 klystron was developed, it was known that it would not be practical for the NLC because the large solenoid magnet used to focus the klystron beam would consume too much power (about 25 kW, which is comparable to the average klystron output power). With the success of the XL-4, attention turned to developing a klystron beam-focusing system using permanent magnets, which consume no power. In the PPM design that resulted, about 40 magnet rings with alternating polarities are interleaved with iron pole pieces to generate a periodic axial field along the 0.5-m region between the gun anode and beam collector. The resulting focusing strength is proportional to the rms of this sinusoidal axial field. About 2 kG can be achieved practically, which is smaller than the 5-kG field in the solenoid-focused klystrons. The weaker PPM field has led to a klystron design with a higher voltage-to-current ratio, which reduces the space-charge defocusing. This higher ratio has the advantage of increasing efficiency through improved bunching, but the higher-voltage requirement makes the modulator more of a challenge to build.

The first PPM klystron was built to generate 50-MW pulses, like the XL-4s. It worked well, producing 1.5-μs, 50-MW pulses with an efficiency of 55%, close to the predicted performance. For the next klystron, the design goal was raised to 75 MW, which was achieved with similar efficiency after a number of design modifications. This klystron was eventually run with pulse lengths up to 3 μs. However, like the 50-MW PPM prototype, it was designed to run at a low repetition rate. Average power effects have yet to be tested at 120 Hz. Currently, a next-generation, 75-MW klystron called XP3 is nearing completion. It incorporates lessons learned from the first 75-MW prototype and is designed to improve manufacturability and operate at the full 120 Hz.

Based on initial success generating 75-MW, 3-μs pulses, the NLC rf system has been modified to use these parameters. The ultimate pulse-length limit of the PPM klystrons has not been measured because the existing SLAC modulators cannot produce pulses longer than 3 μs. An even longer pulse length for the NLC would be difficult due to limitations related to cooling, modulator size and pulse compression. Generating peak power greater than 75 MW with conventional klystrons is difficult due to the stronger space-charge defocusing, higher surface fields, higher beam voltage (> 500 kV) and the greater potential for oscillations.

### 4.1.4 Modulators

The 75-MW PPM klystrons require 500-kV, 270-A pulses to power them. Initially, conventional line-type modulators like those used in the SLAC Linac were considered for this purpose. These modulators contain pulse-forming networks composed of discrete inductors and capacitors that are slowly charged and then rapidly discharged, via a thyratron, through a step-up transformer to generate the high-voltage pulse. These modulators have several drawbacks including low efficiency. They also use thyratrons, which in general have relatively short lifetimes (10,000-20,000 hours) and require periodic tuning. As an alternative, the idea of a solid-state induction-type modulator was explored, based on recent advances in high-power, solid-state switches (Insulated Gate Bipolar Transistors or IGBTs) that are used primarily in the electric train industry. The concept is to sum many low-voltage sources (2-4 kV) inductively to yield the desired klystron voltage. This has been implemented by having each source drive a toroidal-shaped transformer made with a Metglas core. The cores are stacked so secondary windings, which sum the output voltages, can be threaded through them. Each source is essentially a capacitor that is slowly charged and then partially discharged (2%) through an IGBT switch to generate the pulse.

For cost reasons, it is preferable to drive as many klystrons per modulator as possible. For the induction modulator, there are practical limits on the number of induction cells per modulator and on the turns ratio. A reasonable choice given these limits and the current and voltage ratings of the IGBT switches, is to drive eight klystrons witη 3-μs pulses through a three-turn secondary. If a much-longer pulse length was required the optimization would change. It would be more cost-effective to drive fewer klystrons per modulator because of the increase required in the thickness of the induction cores and the size of the storage capacitors.

To develop the induction-modulator concept, a 10-core stack was built using two IGBTs per core running in parallel. With a single-turn secondary, the stack produced 20-kV, 6-kA pulses into a load. It is currently being used to power an S-band klystron in the SLAC Linac. A full-scale NLC prototype modulator with 76 cores is nearing completion. It will be tested first by powering four S-band klystrons in lieu of

PPM klystrons. Later it will be upgraded and moved to the NLCTA to be operated with a full complement of 75-MW klystrons for an rf system test.

### 4.1.5 Rf Distribution

Configuring the klystron output power to drive the accelerator structures is complicated by the different pulse-length requirements. While long klystron pulses are optimal from a klystron cost perspective, shorter pulses are needed to power the structures to minimize overall cost. For the structures, it is not cost effective to generate longer pulses than needed to achieve good rf-to-beam energy-transfer efficiency. The increased energy per pulse would require more rf components, and thus increase the machine cost. The efficiency depends on the ratio of the rf pulse length to the structure filling time (120 ns). This ratio should be greater than unity but not too large or it becomes more economical to increase the machine repetition rate rather than the pulse length. For the present configuration where 190 bunches with a 1.4-ns spacing are accelerated in each pulse, the ratio is 3.2, which yields a 76% fill-time efficiency.

In converting the long klystron pulses to the shorter rf pulses needed to power the structures, the goal is to make the transition efficiently with as little waveguide as possible. A Delay Line Distribution System (DLDS) proposed by KEK was chosen over other options. The SLED-II system is less efficient and the Binary Pulse Compression system more complex. Like all of these rf distribution systems, the DLDS is characterized by the ratio of the klystron to structure pulse length or compression ratio. Given the prototype PPM klystron pulse length results and the desired bunch-train length, a compression ratio of 8 was chosen. In this case, the power from 8 klystrons is combined and sequentially routed up-beam in 8 shorter pulses to feed 8 sets of accelerator structures. Each of these feed pulses is 1/8 the klystron pulse length but essentially 8 times the output power of each klystron. This compression ratio is the maximum possible with 8 klystrons since there is only one degree of freedom per klystron, the phase of the klystron drive rf, available to do the routing. A 10-ns period is allotted for each phase shift, making the total klystron pulse length needed to accelerate an NLC bunch train equal to 3.17 μs.

To achieve the factor of eight compression, a four-arm, two-mode version of DLDS will be used. It is based upon the two-mode ($TE_{10}$ and $TE_{20}$) planar waveguide components that have been developed for hybrid-like applications. Both the launcher and the extractors shown in Fig. 4.1 use these rectangular waveguide modes. The planar geometry allows the component heights to be increased easily to achieve low surface fields (< 40 MV/m) for the 600-MW power-transmission requirement (8 x 75 MW). Also, rectangular-to-circular mode converters have been developed to transform the planar modes to low-loss circular waveguide modes ($TE_{01}$ and $TE_{12}$) for transmission of the power in the long delay lines between the klystrons and structures (up to 470 m). Overall, the DLDS transmission efficiency is expected to be 85% with most of the losses occurring in the rectangular waveguide components.

All critical components for DLDS have been designed, and low-power versions of some of them have been built and tested successfully. A low-power transmission test of the two circular DLDS modes in a 55-m delay line was done to verify that the polarization of the $TE_{12}$ mode is preserved and to verify the expected power attenuation per unit length of the modes. The results confirm the viability of these modes for the DLDS system. At high power, extensive experience has been gained with operating $TE_{01}$ components in the SLED-II systems at NLCTA and the Klystron Test Laboratory. In one test, 500-MW, 150-ns pulses were generated in a SLED-II system upgraded with a launcher-like hybrid. This verified the power handling of the DLDS launcher system at NLC. Because of their close proximity to the klystrons, the 600-MW pulses in the launchers can be shut off within 100 ns if breakdown occurs. For the DLDS extractors, there is a greater concern about breakdown damage because they are far from the klystrons and can receive the full pulse energy (450 J) after breakdown. To demonstrate the extractor power handling capability, high power tests with up to 800-MW, 200-J pulses are planned at NLCTA in the next year. In two years, they will be operated at full power and energy as part of an rf system test.

### 4.1.6 Accelerator Structures

The number of accelerator structures per DLDS feed depends on the structure input-power requirements and hence on the structure design. Until recently, the design of choice was the Rounded Damped Detuned Structure (RDDS), which is a 206-cell, 1.8-m, traveling-wave structure. Its rf group velocity varies from 12% of the speed of light (c) at the upstream end to 3% c at the downstream end to achieve a nearly constant gradient along the structure. The basic parameters were defined primarily by the choice of average cell iris size, which determines the strength of the short-range (intrabunch) transverse wakefield. An average iris radius equal to 18% of the rf wavelength was chosen to limit the wakefield-related bunch emittance growth in the NLC linacs.

During about eight years of R&D, a number of refinements aimed at suppressing the long-range transverse (interbunch) wakefield were made to the structure design. The wakefield suppression was particularly challenging because a two order-of-magnitude reduction is needed for an interbunch spacing of 1.4 ns. The initial solution was to use detuning, where the frequency profile of the dominant deflecting mode of the cells along the structure is varied to produce an initial Gaussian-like decay of the wakefield amplitude. This approach works well to suppress the wakefield for about the first 30 ns, after which its amplitude increases due to a partial recoherence of the mode excitations. To offset this rise, weak mode damping with a Q of about 1,000 was introduced. The modes are coupled through slots to four parallel manifolds (terminated waveguides) that run along the structure at 90-degree azimuthal intervals.

Other changes were made to the structure design to improve efficiency. The original disk-shaped cell was changed to a rounded one (hence the 'R' in RDDS) that increased the gradient by about 6% for a given input power. During this design evolution, several prototype structures were built and their wakefields were measured in the ASSET facility in the SLAC Linac. The results from the first RDDS and earlier damped and detuned structures showed that the long-range wakefield can be suppressed to the levels required in the NLC and that the wakefield can be modeled with great accuracy.

After the wakefield measurements, the 1.8-m structures were processed to high gradients in the NLCTA or Klystron Test Laboratory at SLAC. During the past year, the testing capability at the NLCTA was increased significantly, allowing automated, around-the-clock, higher-power processing. Measurements made during this period revealed breakdown-related damage in the structures at gradients lower than had been expected. Shifts of the net structure phase advance by about 20 degrees per 1,000 hours of operation were observed at gradients as low as 50 MV/m. This was surprising since earlier tests had shown that gradients of more than 80 MV/m could be readily achieved in standing wave and short, low group velocity structures. Such designs had been used in earlier tests because high gradients could be achieved with the limited rf power available at the time.

A major clue as to the cause of this discrepancy was that most of the damage in the 1.8-m structures occurred in the upstream end where the group velocity is highest (12% to 5% c). No damage was seen in the downstream end where the group velocity is comparable to that in the early test structures (< 5% c). Subsequent tests of lower group velocity structures have confirmed that they indeed achieve higher gradients before the onset of damage. The damage threshold for structures with an initial group velocity of 5% c is 70-75 MV/m. Even lower group velocity structures (< 3% c) and standing-wave structures are currently being tested. These damage tests have been performed on simple, easily assembled structures. The next step will be to build and test NLC-compatible versions of the successful structures with better efficiency and an acceptable average iris radius (18% of the rf wavelength). In a parallel effort, designs are being developed which apply previous experience with damping and detuning techniques to address the long-range wakefield suppression requirement. It is expected that a basic high-gradient structure design will be finalized in a year. Tests of such a structure with wakefield suppression will require about another year.

For the current linac design, 0.9-m structures with initial group velocities of 5% c are assumed. Powering six of these structures per DLDS feed at 85 MW input power (600 MW x 0.85/6) yields a 70-MV/m unloaded accelerator gradient. This gradient minimizes overall rf system cost. In earlier designs with three 1.8-m structures per feed, the gradient was 5% higher. To power each structure, the rf will be tapped off from the DLDS feed via a series of hybrids whose designs are based on the two-mode planar waveguide components used in the DLDS.

The six structures will be supported on a common girder, which itself will sit on remotely controlled transverse movers. During NLC operation, beam-induced signals from the structure damping manifolds will be used to center the structures relative to the beam. Tests of this approach during the wakefield measurements of the 1.8-m structures showed that micron-level resolution can be achieved, well below the 10-µm alignment requirement for NLC.

As noted above, a system test will done in about two years that includes the four basic rf subsystems: a modulator, klystrons, DLDS and structures. Ideally, the test would be of a full linac rf unit as shown in Fig. 4.1. For it to be affordable and realizable on a two-year time scale, however, the DLDS and the number of structures will be reduced. Figure 4.2 shows the proposed test layout at the NLCTA, which allows a demonstration of the essential NLC performance goals. One DLDS arm will be long enough so that the extractor will witness the full pulse energy in the event of a breakdown (if it were shorter, the klystrons would be shut off by a reflected energy interlock system before the full pulse was launched). With this shortened DLDS configuration, two sets of six accelerator structures will be powered. The structure designs will be of the type being developed for high-gradient operation. The ultimate performance requirement for the NLC rf system will be to accelerate 0.86-A, 265-ns bunch trains at a 55-MV/m loaded gradient where the beam-loading variation along the train is compensated at the 0.1% level. To test this requirement, NLCTA bunch trains will be accelerated in the structures and the resulting beam properties measured.

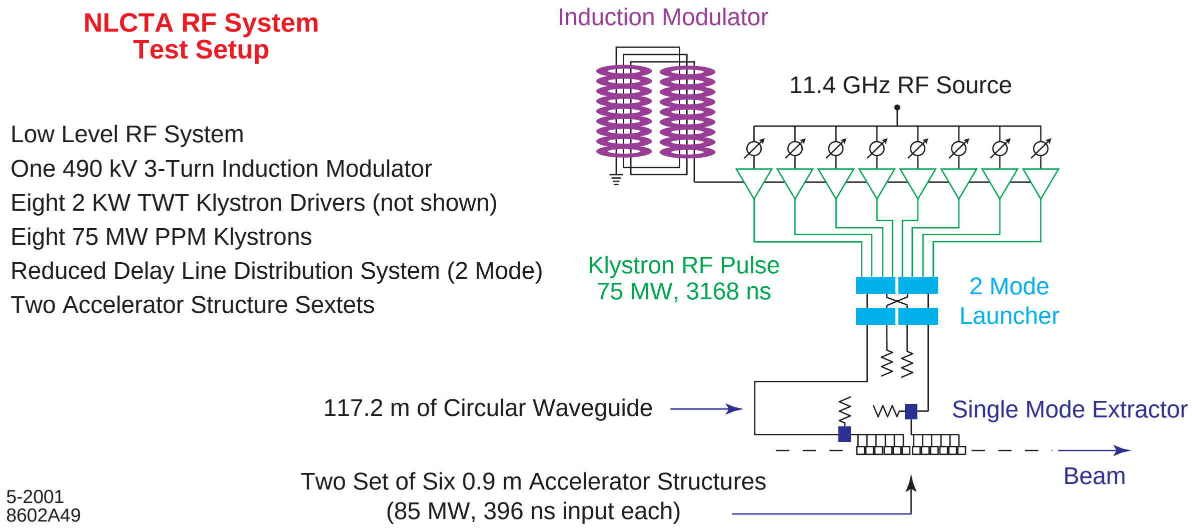

**Figure 4.2:** Schematic of rf system to be constructed at NLCTA to demonstrate essential performance goals of an NLC rf unit.

### 4.1.7 Linac Layout

The main NLC linacs are each 12.9 km and are divided logically into twenty-six 468-m sectors, plus three diagnostic regions and extraction sections that feed bypass lines (see Fig. 4.3). The first 13 sectors in each linac each contain nine interleaved rf units. Each rf unit contains one induction modulator, eight 75-MW klystrons, a four-arm, two-mode Delay Line Distribution System, and eight girders each supporting six 0.9-m accelerator structures. The 0.9-meter structures require a somewhat longer linac than the 1.8-m structures originally planned. The loaded gradient is about 5% smaller and another 4% in length is required to accommodate the longer structure fill time (120 ns compared to 104 ns for RDDS), which increases the distance between DLDS feeds. This extra space allows room for the additional structure input and output couplers.

These components are described more fully in the sections that follow. The linac beam-line enclosure contains the DLDS components and accelerator structures, and a parallel enclosure (klystron gallery) houses the klystrons and modulators. The gallery region containing the nine eight-packs of klystron is one-eighth the length of the sector. The klystron gallery is separated from the beam-line enclosure by at least 6 feet of concrete for shielding purposes and can be occupied during NLC operation for maintenance and repair of the rf equipment. This will enable high availability of the linacs. The last 13 sectors in each linac are drift sections that will eventually be filled with rf units to produce cms energies of 1 TeV or higher.

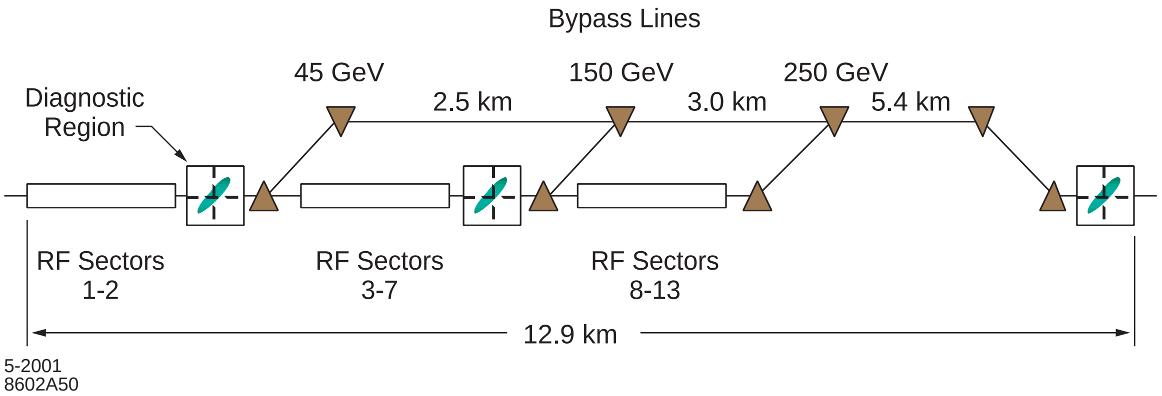

**Figure 4.3:** Linac beam-line layout.

The linac transport optics were chosen to minimize the net effect of dispersive and wakefield-related beam emittance growth. Quadrupole magnets in a FODO configuration are located after every (one, two, or three) girders at the (beginning, middle, or end) of each linac. The quadrupoles in the rf regions will have 12.7-mm-diameter apertures and vary in length from 0.32 m to 0.96 m. They will be permanent magnets with a 20% field strength adjustability. The girders and quadrupoles will be supported on movers that will be remotely adjusted during beam operation based on signals from the structure manifolds and beam position monitors in the quadrupole magnets. To monitor the beam emittance, diagnostic regions at three locations along the linac will allow for full beam phase-space analysis.

Bypass lines with transfer points located at 50, 150 and 250 GeV will allow extraction of the beam into a common transport line in each linac. Three transfer points are sufficient to provide a continuous range of cms energies at the IPs. These lines also serve to transport the beams through the second half of the linac housings.

## 4.2 Modulators

### 4.2.1 Introduction

The NLC modulators convert AC line power to the high-voltage, high-current pulses required by the klystrons. Like all of the major rf subsystems, the modulators need to be designed for the highest possible efficiency and reliability, and for the lowest possible cost. Initial R&D was aimed at using line-type modulators like those in the SLAC Linac, where the number of klystrons is about an order of magnitude smaller than for the current NLC design. In these modulators, a lumped transmission line (Pulse Forming Network, or PFN) is charged to a high voltage, then switched through a high-voltage, high-current thyratron into a step-up transformer. The line-type design had three main deficiencies for use in the NLC: 1) the thyratron switch tube requires frequent adjustment and has a relatively short lifetime; 2) the overall efficiency is only 50-60% due to losses in the various components including lumped line, switch tube and pulse transformer; and 3), the unit cost is high, which would make these modulators a dominant cost driver in the rf power system. Although R&D was directed at these issues, it soon became clear that significant improvements in this technology were not likely in the short term. After evaluating many options [1,2], a solid-state switching approach was adopted. This takes advantage of the emerging Insulated Gate Bipolar Transistor (IGBT) technology being developed for the electric train and motor drive industries [3]. The induction-style modulator design promises to be more reliable (no thyratrons), more efficient (> 80 %) and less expensive (< half the cost per joule) than the Line-type modulators. The design and development of these modulators are discussed below following a summary of their requirements.

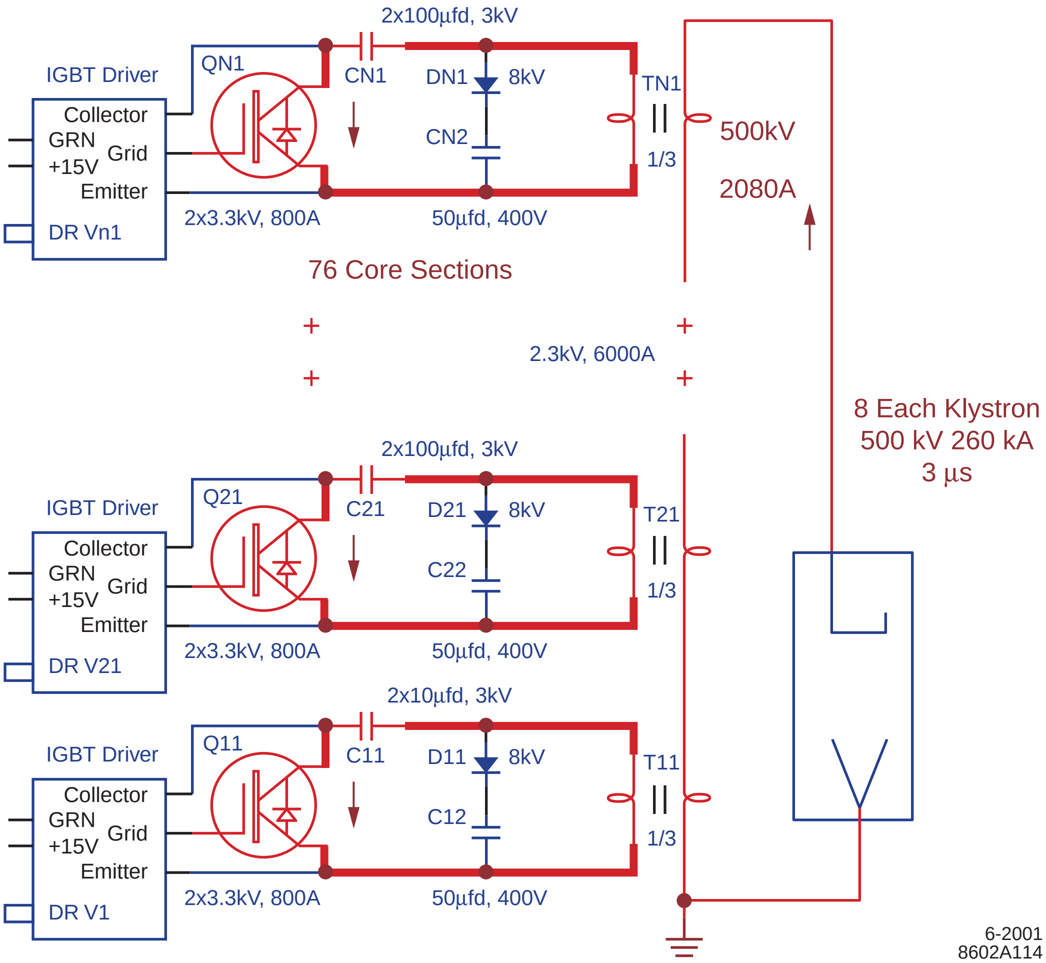

6-2001
8602A114

**Figure 4.4:** IGBT induction concept.

### 4.2.2 Modulator Requirements

The modulator design is closely linked to the manner in which rf power is produced and distributed in the NLC linacs. As shown in Fig. 4.1, the power from groups of eight klystrons is combined in the Delay Line Distribution System. Thus, a modulator design that powers eight klystrons was a logical choice. Table 4.2 shows the requirements for powering these 'eight-packs.'

**Table 4.2:** Main Linac 8-Pack Modulator Requirements

| | |
|---|---|
| Output Peak Voltage | 500 kV |
| Output Peak Current | 2120 A |
| Pulse Flat Top | 3.2 µs |
| Pulse Transformer | 1:3 Step-up from Induction Stack |
| Rise & Fall | 200 ns loaded |
| Droop/ Flatness | ±1% nominal |
| Pulse-Pulse Amplitude | ±0.1% nominal |
| Pulse-Pulse Jitter | ±10 ns |
| Pulse Repetition Rate | 120 Hz |
| Modulator Load | Eight 75-MW klystrons in parallel |
| Power Supply | 550 kW continuous for full load @ 120 Hz |
| Overall Efficiency | > 80% |
| Reliability | >10,000 hrs MTBF |

### 4.2.3 Solid-State Induction Modulator

The solid-state induction design was started at SLAC in 1998. It is based on an induction-linac principle in which the high voltage is developed by magnetically stacked cells driven at relatively low voltage (2-4 kV) by separate solid-state switches on printed circuit boards. A stack of N cells develops a voltage of $NV_{cell}$ in each turn of the secondary. Figure 4.4 shows the circuit concept, and Fig. 4.5 shows the full modulator-packaging concept. The enabling technology for this approach is high-speed, high-switching-power Insulated Gate Bipolar Transistors. Unlike the thyratron, which is a fast ON switch that takes a long time to turn back off, the IGBT is a fast ON-OFF switch that permits using a partial discharge of a large storage capacitor to produce the desired pulse of a few microseconds. This technique generates short pulses with excellent rise and fall times at much higher currents than the nominal maximum DC current rating of the IGBT. Since there is no impedance-matching issue as in a line-type modulator, it is straightforward to drive any number of klystrons, up to a maximum of eight in the NLC design. The same induction components will be scaled to power the NLC injection linacs, which use S- and L-band tubes of differing voltage and current requirements.

As an initial test of the concept, a stack of six Metglas cores was built. These are made of a very high permeability, low-loss, amorphous magnetic material. Each core was driven through a one-turn primary using a single IGBT to generate 12-kV secondary pulses [3]. This simple demonstration in 1998 spurred a major development program in 1999, in collaboration with LLNL and its mechanical engineering contractor, Bechtel-Nevada. Resources have been heavily concentrated on demonstration of a full prototype of the induction design.

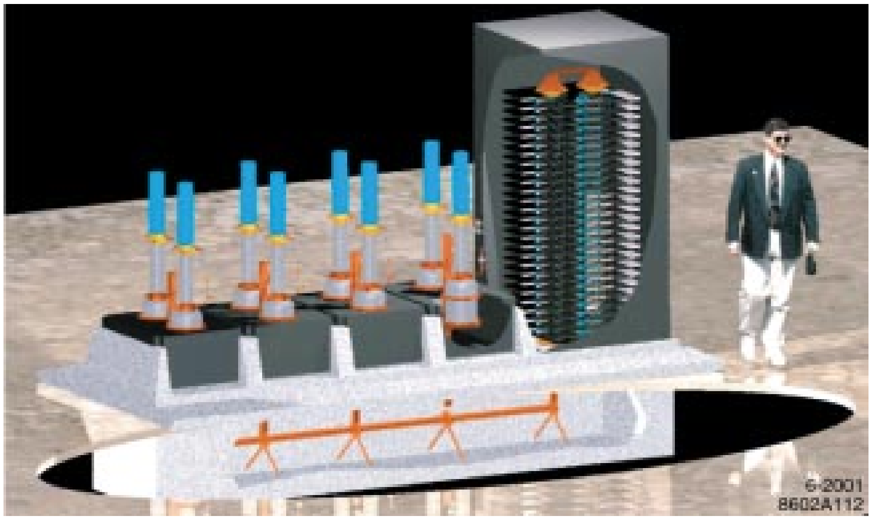

**Figure 4.5:** 8-Pack Packaging Concept.

**Figure 4.6:** Magnetic Core and Cell Prototype.

Several key technical challenges encountered in bringing the design from concept to working prototype include:

**Core Material:** The amorphous core materials are designed for very high performance, but there were problems with obtaining a coating on the tape that preserved the performance when wound. The mechanical assembly required potting the cores within a machined aluminum case, without voids or impregnation between layers of the cores. Finally, a low-inductance connector scheme was needed to mate the driver boards to the core, since the circuit requires tight control of inductance to achieve the fast rise and fall times that are basic to high waveform efficiency. The completed core and cell prototype designs are shown in Fig. 4.6. Driver boards connect through the flat slots on each side of the cell so that two drivers can pulse the same cell from opposite sides at 3,000 A each, via a flat rf contact-band connector soldered flat on the circuit board (see Fig. 4.7).

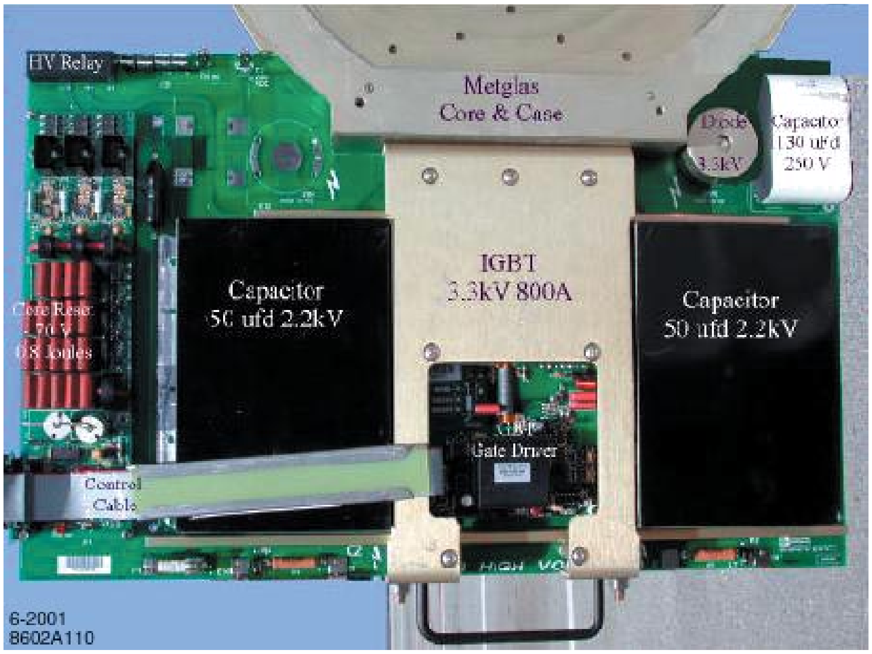

**Figure 4.7:** Induction cell driver board.

**Core and IGBT Cooling:** The inner region of the cores will carry insulating oil for the multiturn secondary of the transformer, shown conceptually in Fig. 4.8. However, this is not designed to provide primary cooling. The thermal path from the IGBT power device through its heat sink, then through the cell and magnetic core to its center, represents too high an impedance to the oil column. Instead, cooling is accomplished via a water jacket in the form of a band around the magnetic core, inside the aluminum case, which cools the core, cell and IGBT. This removes approximately 200 W per cell from boards and core at full rated operation with only a modest temperature rise. One drawback of the design is the large number of water connections required. Another concern is that the oil column is separated by O-rings between each cell, and a very tight seal at all locations may be problematical. The stack has been tested with vacuum but not yet with oil.

**IGBT Reliability:** For fast pulse performance, the IGBT drivers must be operated in a regime where they are not well modeled. The drivers are designed for locomotive traction, requiring very high power at a few kV, 600-800 A AC, continuous duty. The pulse-power requirements of the modulator are very high dI/dt, peak currents that nearly saturate the bipolar switch, high voltage lasting only for a few microseconds, and inductive connections through the drivers, cells and transformer secondary to capacitive loads (klystrons). After each pulse, the core has to be reset, and stored energy recovered. This must be done without producing transients on the gate of the IGBT sufficient to exceed its ratings and destroy the transistor. Finally, IGBTs have a known susceptibility to neutron radiation induced from cosmic rays, or accelerators, which can cause a Single Event Upset (SEU) that latches and destroys the bipolar transistor. Shielding solves this problem in the NLC application, but the failure mode is serious enough that, in locomotive applications, the device specifications are derated roughly 30% to prevent catastrophic failure. This derating has been applied in the NLC modulator design. Shielding from any radiation source is assumed to be equivalent to 3 meters of concrete.

**IGBT Protection:** Many studies have been conducted to develop circuits that will protect the IGBTs under conditions of a short circuit to the load and of core saturation [4]. The latter is the more difficult to protect. Even with proper sizing of the cores and a protection mechanism to assure that the pulse width never accidentally exceeds a programmed maximum, it is still important that the device not fail if this happens. The problem is complicated by the wiring layout of separate chips inside the IGBTs, but a successful protection system has been developed. Some layout changes have been made in the transistor itself to minimize unwanted transients. A second problem is to protect the stack if a single IGBT fails. The circuit developed for this assures that on failure, the device is shorted and disconnects its drive voltage from the cell primary single turn. Therefore, the stack suffers an incremental drop in voltage due to the loss of the one cell, which could be compensated by slightly raising the supply voltage on each cell. This fail-soft feature will enable longer periods of continuous operation without interruptions for maintenance. Intervention is required only when enough boards have failed that the voltage cannot be maintained at some minimum acceptable level.

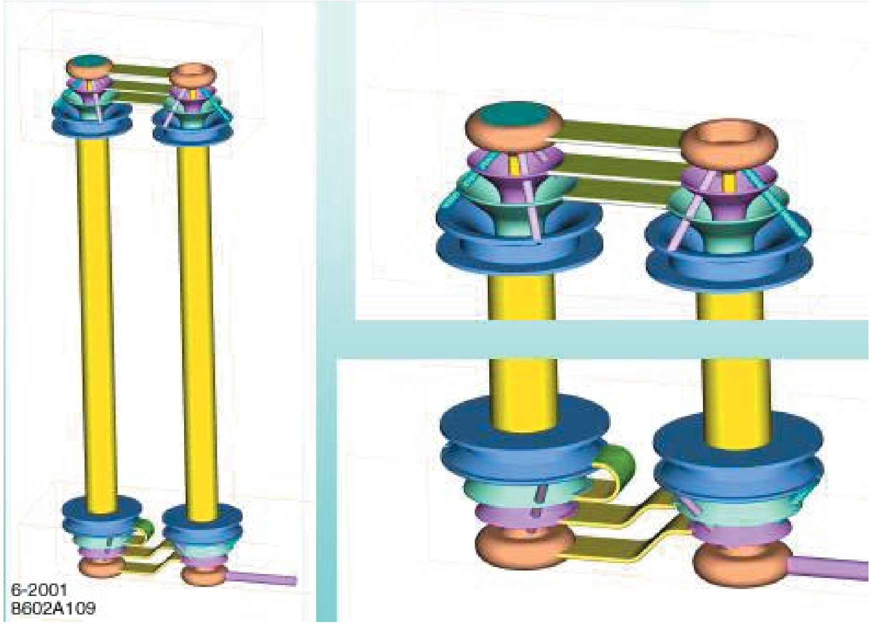

**Figure 4.8:** Three-turn transformer secondary.

**Klystron Protection:** One major worry is that if one tube arcs in an array of eight klystrons, it could draw all the stored energy from the other seven tubes and be destroyed. There are two approaches being adopted to prevent this. Passive inductance from the stack to each tube, and between tubes, is used to slow the transfer of charge to the faulting tube. In addition, the entire stack is designed to sense the fault and shut off in about 400 ns, drawing most of the load's stored charge and shunting it to ground. Klystron faults have been studied on pairs of X-band klystrons in NLCTA, so far with no apparent degradation. However, the statistics are small and one cannot assess damage without dissecting tubes. One major goal in the near-term testing program is to operate tubes as diodes to look for signs of arc damage under controlled faulting.

### 4.2.3 Development Program

As a first step to building a full-scale NLC prototype modulator, a stack of ten cells, as shown in Fig. 4.9, was operated. For an early practical demonstration, the 10-Stack was connected through a 1:15 step-up transformer to drive a single 5045 SLAC S-band modulator [5,6]. The 10-Stack develops 22 kV at up to 3 μs, which is then transformed to 330 kV, 360 A at the output. The output pulse has a slow rise and fall due to the large transformer drive line mismatch ratio (Fig. 4.10). The unit has operated in the SLAC klystron gallery for 200 hours. It reached about half its full power rating. The power was limited by circuit protection problems that have since been solved.

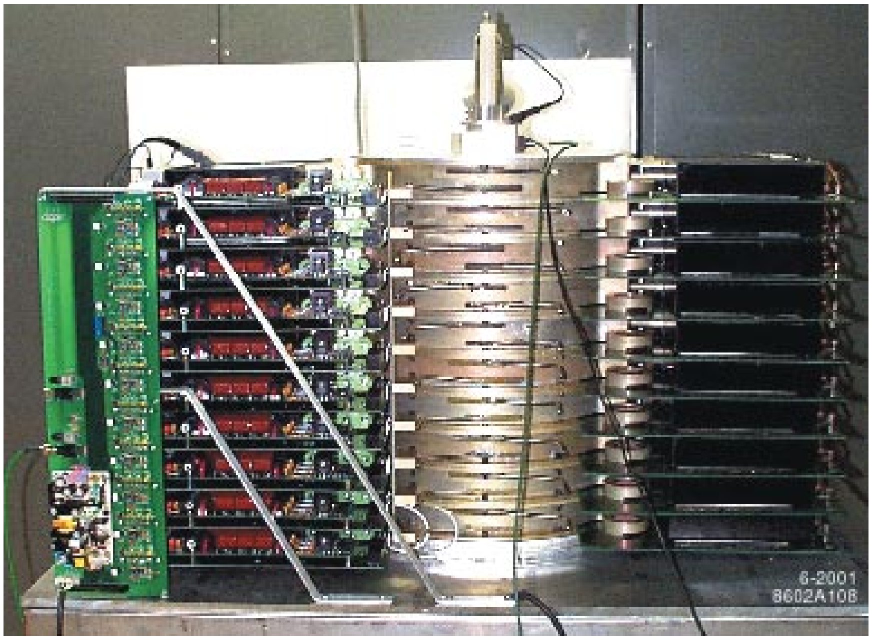

Figure 4.9: 10-stack induction modulator prototype.

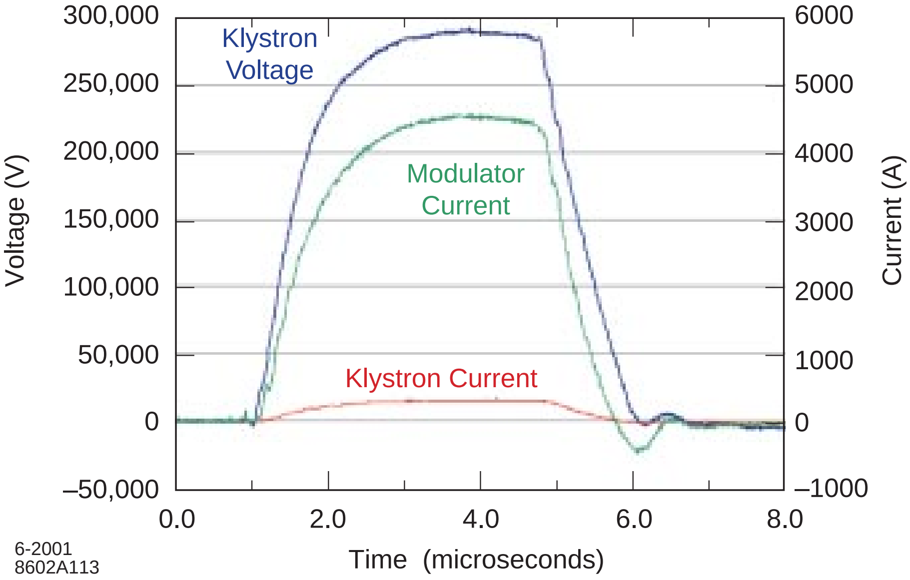

**Figure 4.10:** 10-stack pulses produced when driving a 5045 S-band klystron.

A full-scale induction modulator is being built that will be capable of producing the 500-kV, 2120-A, 3.2-µs, 120-Hz pulses required by the NLC (see Fig. 4.11) [7,8]. It will be tested to near full power, but less than full voltage, using four 5045 S-band klystrons operating as diodes. These klystrons are the only loads available that permit testing to near full power, but less than full voltage. The prototype is nearing completion and testing has started with 76 sections running at 2.2 kV, ultimately to develop 167 kV on the primary. To date, tests are limited to 75 kV in air. Installation of a 1:3 transformer in oil will later raise the output voltage to 500 kV. Figure 4.12 shows the output waveform at 75 kV, 1100 A into a water load in air. The rise time is slow because the circuit does not include the 1:3 step-up transformer and capacitive klystron loads. Sections of the core stack will be time-delayed to shape the pulse rise time and flattop.

**Figure 4.11:** Full-scale modulator prototype with drivers installed.

The current program goals are to complete the four 5045 S-band klystron unit and to operate it up to the rating of the klystron loads, which is 420 kV at 1800-A peak, 3.2 µs and 120 Hz. This unit will then be upgraded and moved to the NLCTA to power the 75-MW PPM klystrons as they become available. It will eventually power eight such klystrons for a system test that includes a scaled-down version of the DLDS, powering two sets of six accelerator structures. In the course of this program, the various technical issues will continue to be addressed and mitigated: cooling, reliability, circuit protection, klystron protection and overall efficiency. In addition, the design team will continue to work with industry partners and collaborators to improve manufacturability, robustness and cost.

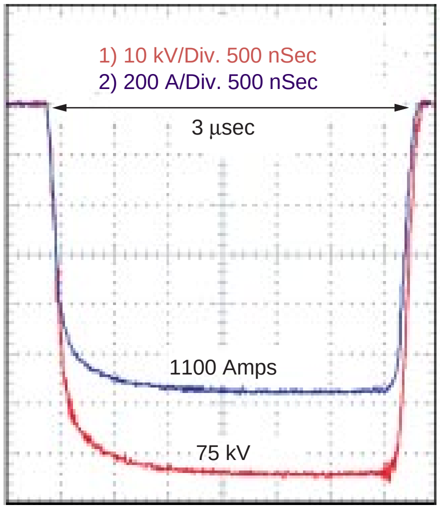

6-2001
8602A33

**Figure 4.12:** Full-scale prototype running at 75 kV with a water load.

## 4.3 Klystrons and Low-Level Rf

### 4.3.1 Introduction

Linear-beam microwave vacuum tubes called klystrons will be used in the NLC to produce the X-band power for the accelerator structures [9]. Klystrons and the low-level rf (LLRF) systems that drive them are well-established technology [10, 11] to provide high power, gain and efficiency with minimal pulse-to-pulse variation. The challenge is to provide the power in a cost-effective manner, both for acquisition and operation. This requires long klystron pulses, high peak and average powers, manageable voltages, energy-efficient klystron beam focusing, and long lifetimes (> 20,000 hours). The R&D work on the X-band klystron has been performed mainly at SLAC and KEK [12]. It has been very successful in systematically advancing the state of the art for microwave devices of this type. The X-band development has built upon the success of the SLAC 5045 S-band klystron [13] (65-MW peak power, 27-kW average power, 350-kV beam, 40,000-hour lifetime), which has been produced for the SLAC linac in quantities of a thousand (700 new, 500 rebuilds).

For the NLC, the basic S-band (2.856 GHz) design had to be scaled to X-band (11.424 GHz). To reduce average power consumption, the solenoids used for beam focusing had to be replaced by permanent magnets. Since there was little experience with either technology for high-power klystrons, the first step was to scale to X-band but maintain solenoid focusing. The initial goal for output power level was 100 MW, but this proved to be too difficult a first step. A robust 50-MW klystron, called XL-4, was built. The XL-4 reliably produces 1.5-µs pulses with 43% efficiency at the design power [14]. Ten of these klystrons have been built to date. They are being used at the NLCTA and the SLAC Klystron Test Laboratory with over 10,000 hours of operation at 60 Hz. The klystron has been run stably to produce 75-MW, 1.5-µs pulses at 120 Hz, but only for brief tests. It has also been operated at 2.4 µs and 50 MW without difficulty. At KEK, two similar klystrons at the 50 MW level (XB72K series) have been produced.

The second step in developing an NLC X-band klystron was to incorporate periodic permanent magnet (PPM) focusing. Like the solenoid klystron development, the initial goal was 50 MW [15, 16]. The first klystron was built at SLAC and produced 50 MW with pulse lengths up to 2.4 µs in excess of the design goal of 1.5 µs. For simplicity, the klystron was not designed for high rate operation, but it was tested briefly at the NLC pulse rate of 120 Hz at 50 MW. In addition to the klystron produced at SLAC, two have been built in industry as part of a program to develop potential vendors. The klystrons have recently been delivered to SLAC where they will be tested shortly. One klystron has already been successfully operated by the manufacturer at 50 MW with pulse lengths up to the 1-μs limit of their modulator. KEK has also produced a 50-MW PPM klystron in an industrial partnership.

**Figure 4.13:** Photo of PPM klystron.

The next phase of the NLC klystron program was to increase the output power level to 75 MW and to produce a robust design that lends itself to mass production [17, 18, 19, 20]. The first klystron produced in this effort, denoted XP1, was an extrapolation of the 50-MW PPM design. It eventually produced 3-μs pulses at 75 MW where the pulse length was limited by the modulator. Figure 4.13 is a photograph of a ppm klystron and Fig. 4.14 shows a power measurement. Like its predecessor, it was not designed for high-rate operation. The next prototype klystron (XP3) is nearing completion. It includes many modifications to improve manufacturability, and incorporates the lessons learned from the first 75-MW klystron. It is designed to run at 120 Hz with a 3-µs pulse length based on the success of the previous klystron. The initial test of this klystron should be completed by late Summer 2001. A klystron containing the magnet and rf output assembly produced by industry should follow in early 2002. At KEK, a 75-MW industrially produced klystron is under test. This klystron was designed for 150-Hz operation with a 1.5-µs pulse length. Additional klystrons will be produced by both laboratories to support the larger-scale rf system tests that are planned during the next three years.

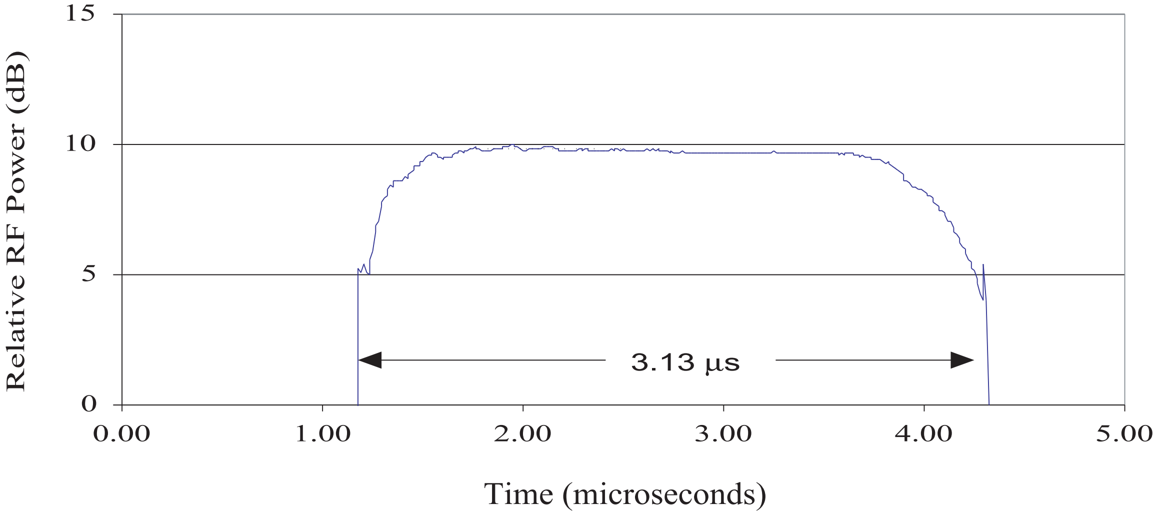

**Figure 4.14:** 84 MW peak output pulse from the XP1 klystron.

### 4.3.2 PPM Klystron Development at SLAC

Although the solenoid-focused XL-4 klystrons can deliver pulses close to those desired for the NLC, their efficiency is too low to be practical, especially when including the 25-kW solenoid power requirement. Using a superconducting solenoid would be too expensive, and while other more exotic, lower-power, warm solenoid approaches appear possible, they would require long-term R&D. Permanent magnets remain as the most viable option. A periodic permanent magnet stack design was chosen where the magnets are ring-shaped and the fields flip direction magnet-to-magnet. To achieve good efficiency (about 60%) with such a klystron and to reduce the beam-focusing strength requirements, which are harder to achieve with permanent magnets, a lower microperveance was chosen (0.60 for the 50-MW klystron and 0.75 for 75-MW klystron) than that of the XL-4s , which was 1.2. Thus, while the XL-4 produces 75 MW with 440-kV, 350-A high-voltage pulses, the 75-MW PPM design operates at 490 kV and 256 A with 60% efficiency.

The first SLAC PPM klystron was built in 1996 and was designed for 50-MW operation. Considerations of cathode life led to an electron gun design with an area convergence ratio of 144:1. Since this value is higher than previous SLAC klystrons, including the XL-4, a beam test diode was fabricated to prove the gun and drift region optics for the PPM design. The diode was tested successfully, demonstrating very stable operation up to a 2.8-µs pulse length at 120 Hz and 490 kV, where the average beam power was 42 kW and the beam transmission was 99.9%. These excellent results provided confidence that a magnet structure could be designed with no allowance for shunting or adjustment.

Initial testing of the 50-MW klystron showed evidence of multipactoring in the drift klystron, so the tube was coated with a titanium-nitride (TiN) layer roughly 100 angstroms thick. The klystron reached the full operational specification of 50 MW at 2 μs. The efficiency at 50 MW was well over 55%, and over 60% at 60 MW, based on calorimetric diagnostics. The intercepted beam power at 50 MW was about 1% of the total beam power, but about 7% of the beam current was lost while passing through the klystron, suggesting that the average energy of the intercepted electrons was approximately 66 keV. (This is caused by the high efficiency of the klystron, which draws the kinetic energy of many of the electrons down to very-low levels.) Recently the 50-MW klystron was retested to explore longer pulse operation. It reached 50 MW at 2.37 μs and 60 Hz with 55% efficiency.

The design and construction of a 75-MW PPM klystron was begun in 1997. In comparison with the 50-MW klystron, a number of major changes were made in the design, including higher microperveance (0.75), an enlarged stainless-steel drift tube for higher beam current and the elimination of the gun focus coils. Opening the beam tunnel by 13% to 0.425 inches reduced the efficiency of the beam-cavity interaction and thereby forced the inclusion of an extra gain cavity. This also allows more modes to propagate within the drift tube, including the second-harmonic TM mode. The construction of the 75-MW PPM magnetic circuit differed in that the drift tube is a semicontinuous stainless-steel structure interrupted by the cavities, with the iron pole pieces and nonmagnetic spacers placed outside the vacuum envelope (see Fig. 4.15). This design change addressed three separate issues: avoiding the multipactoring seen in the 50-MW klystron; taking a step toward the eventual low-cost design of a production klystron using a clamp-on magnetic circuit; and adding loss in the drift tube to increase the start-oscillation currents of the various parasitic modes which may arise.

The 75-MW design used neodymium-iron-boride (NdFeB) magnets which have a higher energy product, are easier to machine and are less brittle, but have a lower Curie temperature and are more sensitive to radiation damage. However, at 500-keV X-ray levels, the radiation effects do not seem to be a limitation given the projected lifetime of the magnets. Furthermore, NdFeB magnets are less expensive than samarium cobalt ($Sm_2Co_{17}$) in bulk quantities.

Several problems were encountered in early testing of the klystron and eventually solved. Most of the magnets failed to meet specification as delivered and they had to be adjusted to achieve a more desirable field profile. A 20-GHz oscillation was seen at the end of the beam pulse, and a replacement transition from the output cavity to collector was designed to damp the rf energy in the 20-GHz range. A strong 1.5-GHz gun oscillation was seen, which was confirmed with SUPERFISH analysis of the gun geometry. A lossy collar of silicon-carbide-loaded beryllium oxide (BeO-SiC) ceramic was designed and fabricated along with a set of screens to isolate the potential cavities formed in the gun structure. After modification, the klystron operated at a peak voltage to 463 kV and delivered over 90 MW in a 3-μs pulse length and 72 MW at 3.13 μs. The gain was found to be between 55 and 60 dB with 60% efficiency at 70-MW saturated output power. This latest operation was limited to 1-Hz repetition rate due to heating of the uncooled magnet stack.

A lower-cost design of a 75-MW klystron, known as the Design For Manufacture (DFM) klystron or the XP3, has been developed over the past three years. This design seeks to minimize parts count, decrease complexity, and reduce construction labor, while increasing the reliability of the klystron. The main modifications are a smaller gun and collector, better output waveguide hardware such as mode converters and windows, and a simplified drift tube and magnet structure. In addition, the pulse width was doubled from the 1.5 μs required of the first 75-MW klystron to 3 μs, and this resulted in a rigorous examination of the thermal characteristics of the klystron and its mechanical design. Modeling shows that 1580 watts can be absorbed in the drift section and 770 watts in the buncher section without affecting the magnet fields significantly. Of all the possible problems on microwave klystrons, thermal problems are the most tractable due to the availability of analytical tools and the variety of mechanical solutions possible.

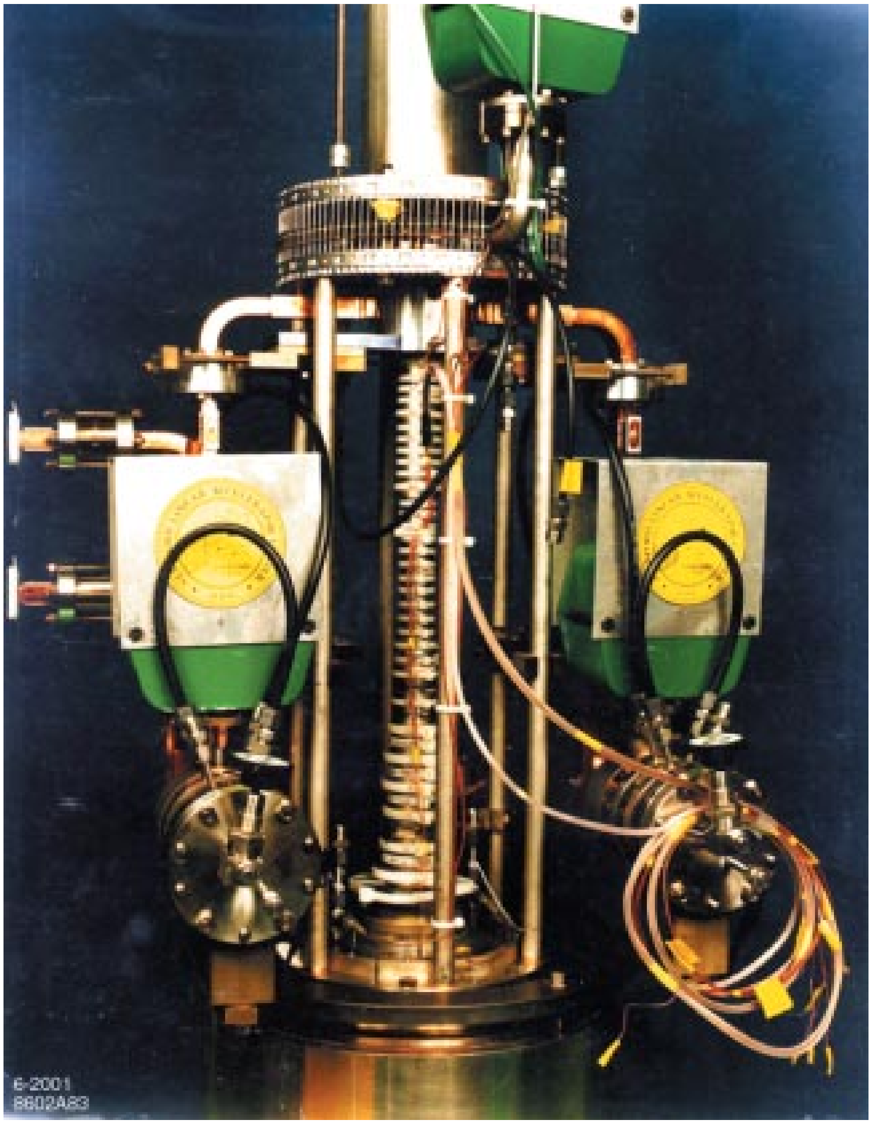

**Figure 4.15:** XP1 PPM stack.

Since there were changes from the first 75-MW klystron, a diode (similar to the diode for the 50-MW klystron) was constructed and is now in electrical test. Like the first 75-MW klystron, this diode showed a different spurious oscillation in the gun region. A similar suppression mechanism was adopted for the diode and the second 75-MW klystron.

The rf design is very similar to the design of the first 75-MW klystron with modifications to allow for a smaller drift-tube diameter throughout the gain section of the klystron. The klystron will use the smaller gun and collector utilized in the diode as well as a clamp-on magnetic circuit. The output is through dual $TE_{01}$ windows. A dual directional coupler will be installed between the output cavity and one output window of the klystron for diagnostic purposes. An adjustable gun-coil/anode-coil assembly will be used to allow tuning of the entrance magnetic field into the PPM stack. Once the klystron behavior is well characterized, this assembly can be replaced with fewer, smaller coils for the production version of the klystron.

### 4.3.3 Low-level Rf

The low-level rf drive system [21] in the main linacs generates the rf that is amplified by the klystrons to power the accelerator structures. Rf amplitude and phase are modulated at the milliwatt level for each klystron in the linacs. The low-level rf reference signal used for this purpose is generated by frequency multiplication of the master timing signal (714 MHz) sent to each sector through fiber-optic links. After modulation, the rf power is increased to the 1-kW level by a traveling-wave-tube (TWT) amplifier driving each PPM klystron. Both the TWT amplifier and klystron are operated near saturation to improve stability and efficiency.

During each pulse, the relative phase of the rf input going to each klystron is modulated as required for the DLDS (Section 4.4) to route the combined power of eight klystrons to the accelerator structures in the proper sequence, synchronous with the beam. Modulation of the phases of pairs of klystrons, in quadrature, compensates for the beam loading by creating a 120-ns initial ramp on the pulse that accelerates the beam. This shape 'preloads' the structures so the field profile witnessed by the first bunch is the same as that in steady-state loading.

Rf detectors on the structure outputs will be used to monitor the rf-to-beam phase. To improve sensitivity, the phase of the beam-induced rf will be measured on dedicated pulses where the klystron power is absent. This information will be used to phase optimally the rf going to each of the eight DLDS feeds. Any steady-state phase variations during the pulses can also be compensated, in particular, those resulting from voltage ripple on the modulator pulse. The goal is to achieve a 1° rf-to-bunch setting accuracy and a 1° pulse-to-pulse stability. The rf amplitude stability is expected to be better than 1%. The bandwidth of the system will allow the power routing to be changed in about 10 ns. This switching time, which represents a loss in efficiency, has been taken into account in the design parameters.

For rf modulation and demodulation, a programmable digital IF solution is planned, rather than an I/Q approach currently being used at NLCTA. Prototype studies have begun using a Direct Digital Synthesizer, a new commercial component that promises 12-bit vertical resolution, 300-MHz update rate, 100-MHz bandwidth, and low cost. The system would use an 89.75-MHz sub-IF that would be frequency multiplied by a factor of 8 and mixed up to 11.424 GHz.

The 1-kW amplifier needed for each klystron has such low average power (a few watts), that it can be designed to maximize lifetime without causing unacceptable thermal problems. The TWT amplifier portion of this system is being developed through the use of High Energy Physics SBIR funding from the Department of Energy. Prototype units have been made available to SLAC and integrated with traditional power supplies. These units are in operation but do not yet contain the desired long-life features. A prototype of an inexpensive Marx-style power supply is being developed and will be tested soon.

## 4.4 Rf Distribution

### 4.4.1 Introduction

The rf distribution system for the NLC transports the klystron output power to the accelerator structures. This task is complicated by the fact that the klystron pulse length and peak power, which were chosen to minimize klystron costs, are not optimal for powering the structures. Thus, a simple one-to-one connection between the two is not practical. To transform the relatively long, low-power NLC klystron pulses to the short, high-power pulses needed for the structures, several methods were considered during the past decade. They are generally referred to as pulse-compression systems since the pulse length is shortened in order to increase peak power. Most of the practical experience with pulse compression has come from the development of SLED-II [22], which is a delay-line version of the SLAC Linac Energy Doubler (SLED). In its implementation in the NLCTA, a 'magic T' splits the klystron power equally to fill two 40-m , 12.1-

cm-diameter delay lines (circular waveguides). These lines are shorted at the far ends and have irises at the near ends that partially reflect the rf. In operation, the lines are resonantly filled during the first 5/6 of the 1.5-µs-long klystron pulse, and then essentially discharged through the remaining hybrid port by a 180° reversal of the klystron phase during the last 1/6 of the pulse. This yields a shorter (1/6 as long), higher-power pulse that is used to power NLCTA accelerator structures. Although it works well, it is not particularly efficient. Only about 65% of the input power ends up in the compressed pulse, so the power gain is about four.

An intrinsically more efficient scheme of pulse compression called the Delay Line Distribution System (DLDS) was proposed by KEK and has been adopted for NLC [23]. It reduces costs, eliminates the need for resonant rf storage, and utilizes the time-of-flight of the beams to decrease the required length of delay line. In this latter respect, it is superior to an early SLAC proposal called Binary Pulse Compression (BPC), which also had high intrinsic efficiency [24]. As initially conceived, power in the DLDS delay lines was transported in a single mode. To further reduce the amount of waveguide, multimoded DLDS [25] was introduced with two modes transported in each delay line.

Figure 4.16 shows a schematic of an NLC linac rf unit featuring the dual-moded DLDS components. During operation, the 3.2-µs pulses from the eight 75-MW klystrons are combined and then sent upstream (opposite the beam direction) in eight sequential, 396-ns pulses. The power routing in the ‘launcher’ is controlled via the phase of the rf drive to the individual klystrons. The shorter pulses are transported in two circular-waveguide modes (TE$_{01}$ and TE$_{12}$) in the delay lines. In each line, the TE$_{12}$ pulse is extracted to feed a nearby set of structures. The TE$_{01}$ pulse passes through the ‘extractor’ to feed a set further upstream. At the end of each feed, the power is split evenly among a set of six 0.9-meter structures. The feeds are spaced so that the same beam-to-rf arrival time is achieved in each set of structures. Nine such rf units are interleaved to power a contiguous set of structures in each rf sector of the NLC linacs.

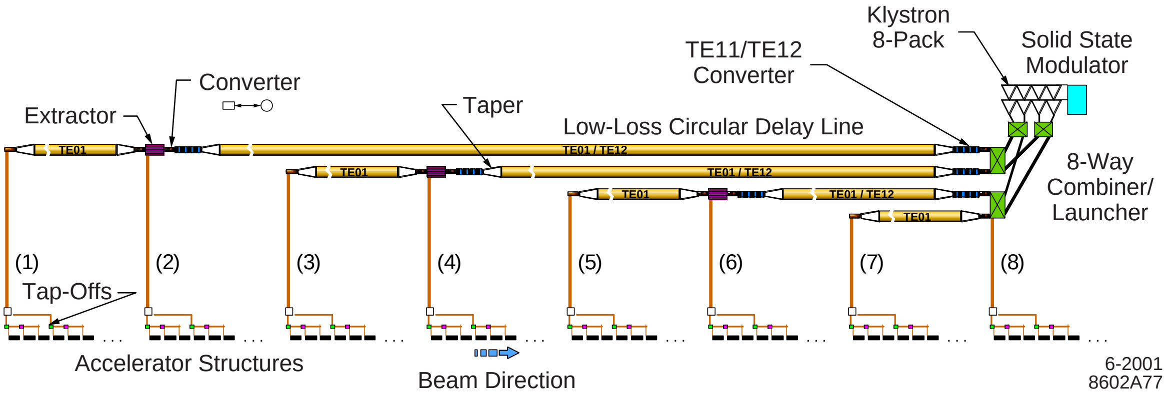

**Figure 4.16:** Schematic of the four-arm, dual-moded DLDS with eight accelerator feeds. The feeds are numbered by the order in which power is received.

Because the DLDS must transport high peak power (600 MW), design efforts have concentrated on reducing surface field levels in all components other than the circular waveguides, where this is not an issue. The use of moderately overmoded, rectangular waveguide to manipulate the rf was chosen for this purpose. Transitioning to and from the highly overmoded circular delay line waveguide is done through special mode-order-preserving tapers. Component designs exploit planar symmetry, which makes it easier to manipulate the modes and allows the waveguide height to be arbitrarily increased to reduce surface fields. The goal has been to keep the electric field below 40 MV/m while aiming for compactness to minimize ohmic losses.

In the following sections, the major components of the NLC DLDS are described.

### 4.4.2 Delay Lines

For low-loss transmission of rf power, the circular $TE_{01}$ mode is ideal since its attenuation is very small with reasonable waveguide diameters. Much experience has been gained in the past decade in transporting hundreds of megawatts of X-band power in this mode [26]. At the waveguide diameter being considered for the NLC, the next lowest-loss mode is $TE_{02}$, although $TE_{12}$ is very close. Since $TE_{12}$ simplifies the design of launcher and extractor, as will be discussed below, it was chosen as the second transport mode. The feasibility of using $TE_{12}$ was demonstrated in recent transmission experiments in 55-m circular waveguide where no coupling between cross polarizations was detected [27]. The average transmission efficiency in the DLDS delay lines versus the delay-line diameter is shown in Fig. 4.17. A waveguide diameter of 17.1 cm was chosen since it yields a good transmission efficiency (> 97%) and it is centered in the widest gap in the distribution of nearby higher-order mode cut-off diameters so coupling to other modes in minimized.

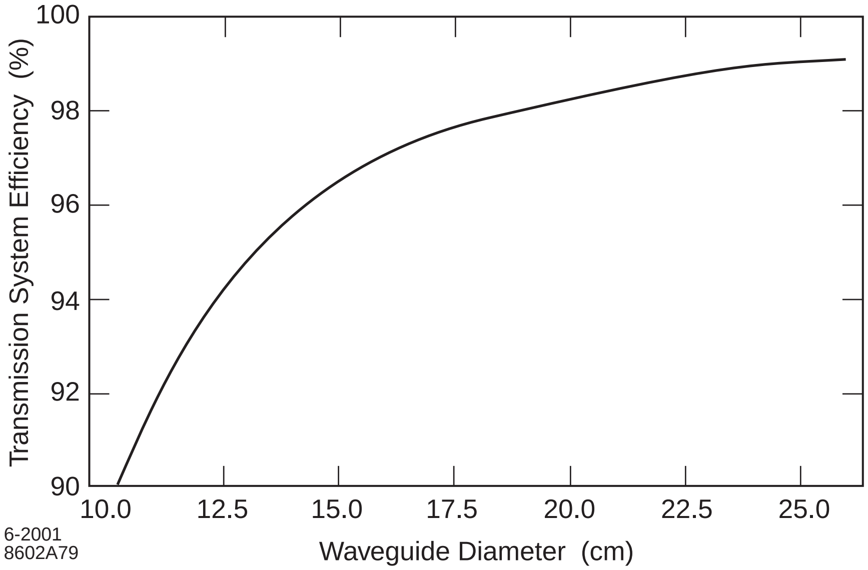

**Figure 4.17:** Average transmission losses in the DLDS delay lines versus delay line diameter.

Because the long delay lines must be built in sections, a flange design is needed that allows both modes to pass through unperturbed. The $TE_{01}$ mode is insensitive to small gaps because it has no longitudinal field [26,27]. The longitudinal current component for the $TE_{12}$ mode decreases rapidly with increasing waveguide radius. With proper gap dimensions, the effect of a discontinuity at the waveguide diameter on this mode can be reduced to negligible levels as shown in Fig. 4.18

### 4.4.3 Rectangular-to-Circular Mode Converter

The rectangular waveguide modes used to route power are $TE_{10}$ and $TE_{20}$. To make the transition from them to the $TE_{01}$ and $TE_{12}$ circular waveguide modes, it is easier to first convert to $TE_{01}$ and $TE_{11}$ and then to use an adiabatically corrugated circular waveguide to convert $TE_{11}$ to $TE_{12}$ while passing $TE_{01}$ unperturbed. To launch $TE_{01}$ and $TE_{11}$ in circular waveguide from the rectangular launcher, the transition between the two cross sections was constructed in such a way that a one-to-one correspondence was achieved for the respective operating modes. An adiabatic cross-section taper naturally converts $TE_{10}$ to

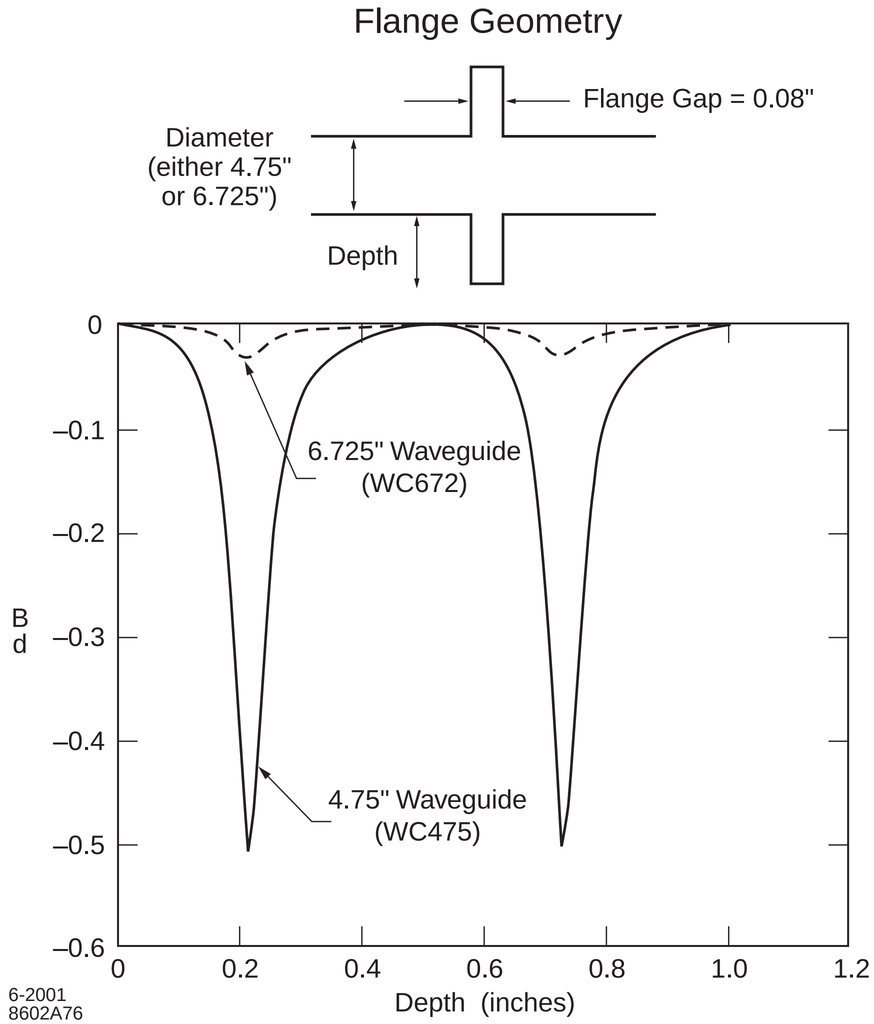

**Figure 4.18:** Mode-matching simulation of $S_{12}$ for the $TE_{12}$ mode through eleven cascaded flanges.

$TE_{11}$. For $TE_{20}$, however, it tends to produce a combination of the circular modes $TE_{21}$ and $TE_{01}$. The cross-section deformation had to be done in two properly designed and spaced taper sections to yield a pure $TE_{01}$ wave [28]. This was accomplished within a length of several centimeters without compromising the $TE_{11}$ conversion. The design is illustrated in Fig. 4.19 [29]. In DLDS, the output of this converter, which is 4.1 cm in diameter, is connected to a specially corrugated waveguide to convert to $TE_{11}$ to $TE_{12}$. A transition to the 17.1-cm-diameter circular waveguide is then made through a special taper [30] that preserves both $TE_{01}$ and $TE_{12}$.

### 4.4.4 Launcher

The use of rectangular waveguide components in which planar symmetry is exploited to allow arbitrary waveguide height began with the design of a planar hybrid [31] to replace the ‘magic T’s in the SLAC Klystron Test Laboratory SLED-II system. The Ts had exhibited rf breakdown problems above 200 MW, particularly at the mouth of the E-plane port. One novel hybrid design has an ‘H’ geometry. Its central guide is wide enough to support two TE modes and, at its junctions, triangular wall protrusions produce essentially double mitered bends. Prototypes have been built and successfully operated at peak power levels of roughly 500 MW.

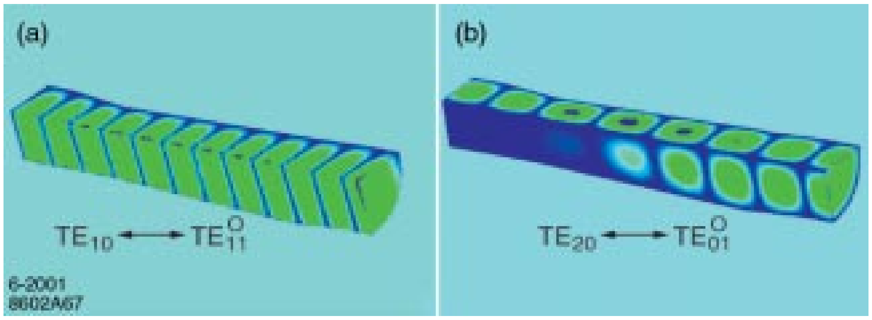

**Figure 4.19:** Rectangular-to-circular mode converter (¼ geometry shown) with field patterns illustrating conversion between a) rectangular TE$_{10}$ and circular TE$_{11}$ and b) rectangular TE$_{20}$ and circular TE$_{01}$.

If two such ‘magic H’ hybrids, with ports half the width of the central guide, are placed side-by-side and their common wall removed, the resulting oversized ports have the same cross section as the central guide. If these are split again with Ts at the proper distance, the symmetry is completed, and an eight-port device in the shape of a cross potent (cross with a cross bar at each extremity) results [32]. This ‘cross-potent super hybrid’ can be used to combine power from four input ports into any one of four output ports, by proper phasing of the input rf. Opposite pairs of cross arms are isolated. A prototype has been built and its scattering parameters measured with a network analyzer. The performance was as expected.

To use this design to launch circular modes, the T split on one or more of the arms can be left off, substituting posts for matching. The TE$_{10}$ and TE$_{20}$ modes are then transformed to the circular modes via the rectangular-to-circular mode converter described above. A one-arm launcher configuration is illustrated in Fig. 4.20. The wide dimension of the launcher arm is 3.7 cm, and the height can be chosen to accommodate the mode converter.

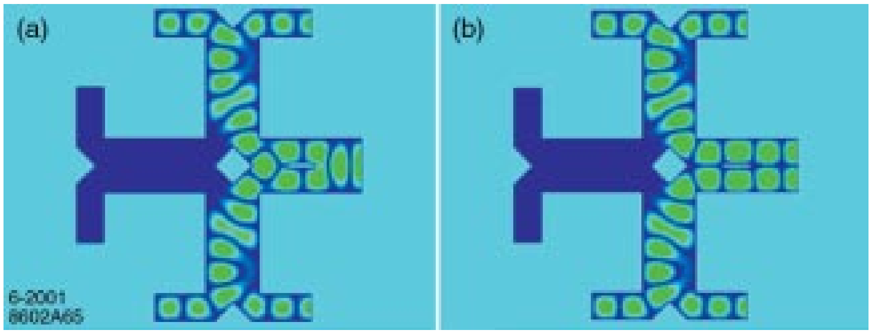

**Figure 4.20:** Cross-potent launcher with electric field patterns illustrating launching a) TE$_{10}$ and b) TE$_{20}$ in the right overmoded rectangular port with the indicated relative phases for four equal amplitude inputs. Alternate phasing of the inputs sends the power to either of the left ports.

The DLDS launcher circuit, which uses four cross-potent super hybrids, is illustrated in Fig. 4.21. At the input portion of the circuit, two hybrids each combine the power from four klystrons and direct it to one of two circular waveguides in one of two modes (in the figure, the circular waveguides are either the right two or left two). These circular waveguides transport the power from the klystron galleries in the NLC through a shielding wall to the beam-line tunnel, which houses the DLDS delay lines. At the output portion of the circuit, two hybrids are used to combine and direct the power from the two circular waveguides to one delay line in one mode. As discussed above, the four output ports are connected to $TE_{11}$ to $TE_{12}$ converters and then tapered up to the 17.1-cm diameter delay lines.

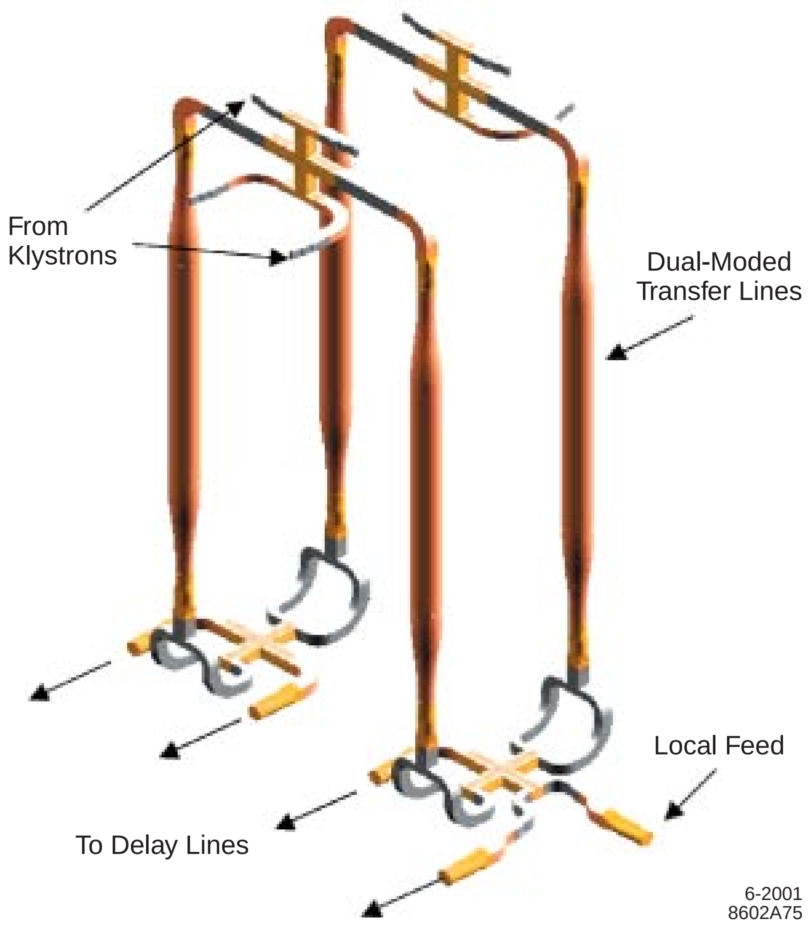

**Figure 4.21:** DLDS launcher circuit.

### 4.4.5 Extractor

In each delay line, a section is added that extracts one mode and transmits the other. This extractor uses the same rectangular modes as in the launcher. As input, the circular modes are converted back to rectangular modes in the reverse manner in which they were launched. Thus the extractor input has the same rectangular dimensions as the launcher output. A 45° H-plane bend with an inner-wall radius-of-curvature of 2.7 cm then mixes the two rectangular guide modes, converting them into an equal combination of $TE_{10}$ and $TE_{20}$ (see Fig. 4.22). A short, straight section is used to achieve the proper relative phase. Then a doubly matched T split, at which the $TE_{10}$ field adds constructively to one lobe of $TE_{20}$ and destructively to the other, sends all the power one way for a given extractor input mode and all the power the other way for the other input mode. Since the two input modes result in combinations with opposite relative phases, they excite opposite ports at the split. The rectangular $TE_{10}$ mode was selected for extraction because it corresponds to the circular mode with the larger attenuation.

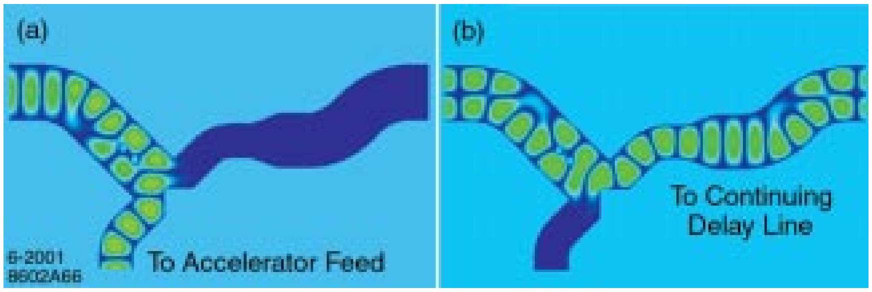

**Figure 4.22:** Extractor with electric field patterns illustrating a) extraction of the $TE_{10}$ mode and b) passing the $TE_{20}$ mode.

Single-moded 45° H-plane bends orient the extraction port waveguide perpendicular to the delay line and the through port waveguide parallel to it, albeit offset. The latter waveguide is then tapered to full width and sent through a dogleg or 'jog converter,' which simultaneously brings the port back in line with the delay-line axis and restores the $TE_{20}$ mode. An identical mode converter is appended to the extraction port. Using the same rectangular-to-circular transitions employed after the launcher, both the transmitted and extracted $TE_{20}$ mode are converted to the low-loss circular $TE_{01}$ mode for further transport. The extracted power is sent to a set of accelerator structures a few meters away while the transmitted power is sent 59 meters upstream to the next structure set.

### 4.4.6 Tap-offs

Each DLDS feed must deliver close to 600 MW of power split evenly among six adjacent accelerator structures. This is accomplished by first dividing the power in half through a 'magic H' hybrid such as discussed earlier. Each of the two outputs runs parallel to three of the six structures. For the first structure in each triplet of structures, one third of the power is tapped off, and for the second, half the remaining power is tapped off before the waveguide terminates in the third structure.

To isolate the structures in case of rf breakdown, a directional coupler-like layout is used for the tap-offs. The 'magic H' serves as the second tap-off as illustrated in Fig. 4.23. For the first tap-off, the modified hybrid design is used to give the proper 1/3-to-2/3 split. This is achieved by adjusting the differential phase length of the coupling section in the 3-dB design while maintaining the match. Any reflected power from the structures travels back through the waveguide system or ends up in the fourth ports of the hybrids, which are connected to high-power loads. Since the structure inputs are only about a meter apart, the power is transported between them in rectangular waveguide.

**Figure 4.23:** A 3-dB tap-off made with a 'magic H' hybrid and jog converters. Electric field patterns are shown for power flow from left to right.

## 4.5 Accelerator Structures

### 4.5.1 Introduction

The NLC linacs will each contain about 5 km of X-band accelerator structures to increase the beam energy from the 8 GeV at injection to 250 GeV for collisions at the IP. There are three basic requirements on the structure design: it must transfer the rf energy to the beam efficiently to keep the machine cost low; it must be optimized to reduce the short-range wakefields which depend on the average iris radius; and it must suppress the long-range transverse wakefield to prevent multibunch beam breakup (the resonant amplification of bunch betatron motion by the bunch-to-bunch transverse wakefield coupling).

### 4.5.2 Structure Design Considerations

The primary issue for the basic structure parameters is the tradeoff between high rf-to-beam efficiency and low wakefield-related emittance growth. The emittance growth is caused by the head-to-tail transverse wakefield deflections generated when the bunches travel off-axis through the structures. Resonant head-to-tail amplification is suppressed by introducing a correlated energy spread along each bunch (so called BNS damping, Section 7.4.1). The size of the remaining nonresonant growth depends on a number of factors including the average iris radius, the bunch charge and the achievable beam-to-structure alignment (the goal is about 10 μm). The average iris radius and the bunch charge also affect the rf-to-beam energy transfer efficiency. Higher efficiency comes at the expense of increased emittance growth. As a result of this basic tradeoff and the constraints on a number of related parameters, an average structure iris radius of 18% of the X-band wavelength was chosen for the linac design [33].

Defining the structure parameters required a number of other design choices. A traveling-wave structure was selected because standing-wave designs are generally more expensive. A disk-loaded waveguide geometry was used since disk-shaped cells are easy to manufacture. The gradient and iris surface field along the structure were held roughly constant to avoid having one region of the structure limit the gradient because of rf breakdown. The gradient profile was shaped by varying the rf group velocity along the structure, a common method for achieving a constant gradient. The phase advance was chosen to be 120 degrees per cell, the same as in the SLAC S-band structure. This value gives a high shunt impedance per unit length which improves efficiency. (The shunt impedance is the ratio of the square of the unloaded gradient to the power dissipated per unit length in the copper cells.) The structure filling time was chosen to maximize the rf-to-beam energy transfer efficiency, taking into account the length of the NLC bunch train. These choices constrained the basic structure geometry, and resulted in a 206-cell, 1.8-m long structure with a group velocity varying from about 12% to 3% c.

Once the basic design had been selected, a method for suppressing the long-range transverse wakefield had to be developed. A final design with acceptable wakefield properties was achieved by using two techniques. "Detuning" requires that each cell of the rf structure have a slightly different dipole frequency, such that the wakefields from the different cells have decohered by the time the second bunch arrives. "Damping" requires that the cells be engineered to reduce the *e*-folding time for the wakefields, effectively causing the dipole wakefield power to be dissipated more rapidly in the structure. This achievement required major advances on two fronts. One was the accurate modeling of wakefield generation in structures whose geometry varies from cell to cell. This was achieved using 3D finite-element calculations to obtain parameters for an equivalent circuit model of the cells. Another key advance was in the precision machining of the cell shapes to produce the desired acceleration and dipole mode frequencies. The result of these two efforts produced structures with frequencies that matched design to better than 1 MHz. The precision fabrication methods also result in structure straightness better than the NLC requirements. The wakefield suppression methods are described in the next section, followed by a discussion of the structure fabrication and testing procedures in Section 4.5.4.

In parallel with the structure design effort, upgrades to the NLCTA were made to allow for systematic studies of the structure long-term, high-gradient performance. During this program, evidence for rf breakdown-related damage was seen. The NLC group, in collaboration with KEK and LLNL, immediately began an intensive program to understand the damage mechanism and find a structure design that will support the full gradient. This program is described in Section 4.5.5. Preliminary results indicate that a shorter 0.9-m structure design will reach 70 MV/m gradient reliably.

### 4.5.3 Long-Range Wakefield Suppression

In order to deliver the desired luminosity, the NLC will operate with a train of 190 bunches. A major concern is that the long-range transverse wakefields generated as the beams traverse the accelerator structures can strongly couple the motion of the bunches. This coupling will resonantly amplify any betatron motion of the train, unless the transverse wakefield is reduced by about two orders of magnitude during the 1.4 ns between bunches. This difficult goal was met by using a combination of cell detuning and damping [34]. These methods are described below in the context of the most recently built 1.8-m structure, the first Rounded Damped Detuned Structure (RDDS1). Figure 4.24 shows cutaway views of the structure and one of its cells. ‘Rounded’ in the name refers to the fact that it has cells with a rounded shape instead of the disk-like ones of previous Damped and Detuned Structures (DDSs). This change in geometry increased the shunt impedance by roughly 15%, which improved the rf-to-beam efficiency by about 6%.

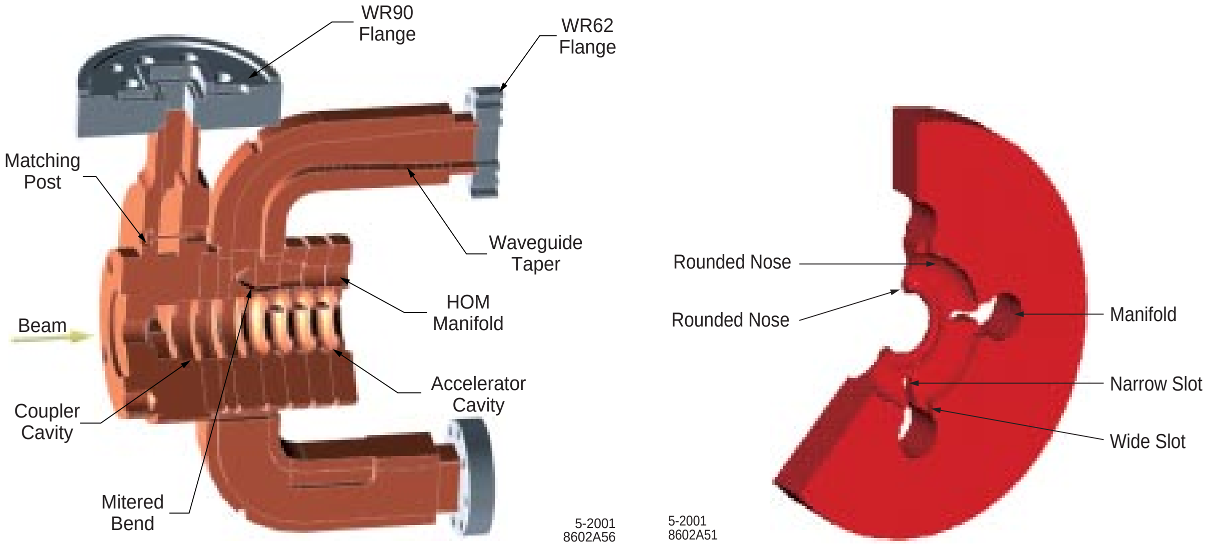

(a) (b)

**Figure 4.24:** Cutaway view of (a) upstream end of RDDS1 and (b) RDDS1 cell.

The first technique to be developed was mode detuning. The frequencies of the lowest (and strongest) band of dipole modes are varied so that the modes excited by an off-axis bunch do not add constructively. For RDDS, the variation is systematic along the 206-cell structure to produce a Gaussian distribution in the product of the mode density and the mode coupling strength to the beam. This detuning produces an approximately Gaussian falloff in the net wakefield generated by each bunch. Detuning works well to suppress the wakefield for about the first 30 ns, after which the amplitude increases due to a partial recoherence of the mode excitations. To offset this rise, weak mode damping was introduced. The damping is achieved by coupling each cell through a longitudinal slot to four TE$_{11}$ circular waveguides that run parallel to the structure. Two of the circular waveguide manifolds are in the horizontal plane and couple to the vertically deflecting dipole modes. Two are in the vertical plane and couple to the horizontally deflecting modes.

The manifold damping works because the phase velocity of the manifold mode is greater than c and the detuning results in localized dipole modes in the structure that each have a phase velocity profile that varies from near c at one end of the mode (the π-mode-like end) to infinity at the other end (the 0-mode-like end). Thus a near-speed-of-light beam excites the dipoles modes near their π-mode end. The energy propagates at the local group velocity until it reaches the region of the mode where the phase velocity matches that of the manifold mode, at which point it couples to the manifold. The damping is optimized when the coupling is adjusted so 100% of the dipole energy flows directly into the manifolds, as if it were a perfectly terminated traveling wave.

At the ends of the structures, the circular manifold waveguide makes a transition to rectangular waveguide, which transports the power out of the structure. It is sent either to matched loads or to processing electronics so the signals can be used for beam position monitoring. If the power is extracted without any reflections, the manifolds reduce the dipole mode Qs from about 6,000 to 1,000, enough to keep the wakefield from significantly recohering. However, a surprisingly small mismatch (voltage standing-wave ratio of 1.05) at the output ends of the manifolds can significantly degrade the long-range wakefield suppression. Such a mismatch can double the average value of the wakefield in the region from about 30 to 60 ns behind the driving bunch.

The process of designing the damped and detuned structures is quite complex [35]. It has been simplified somewhat by treating short regions of the structure as if they were part of a periodic (constant geometry) structure. Such an approximation makes the calculations easier and is accurate because the cell geometry varies slowly through the structure. In this regard, an n cell structure is initially treated as n periodic structures, each with a unique synchronous dipole mode frequency (a synchronous mode in a periodic structure is one with speed-of-light phase velocity).

The first step of the design process is to choose a set of synchronous dipole mode frequencies that has a truncated Gaussian distribution when weighted by the amplitude of the mode excitation per unit beam offset, referred to as the kick factor. Figure 4.25 shows the distribution of the 206 dipole modes for RDDS1, both weighted and unweighted. The weighted distribution has a mean frequency of 15.2 GHz and a frequency spread of 11.25%. It is truncated at 4.75 σ. These values produce more than a factor of 100 falloff of the wakefield within one bunch spacing (1.4 ns). The resulting wakefield is essentially the inverse Fourier transform of the weighted frequency distribution, and is approximately Gaussian.

The second design step is to compute the cell parameters for each dipole frequency using a 2D field solver. Since this alone does not uniquely define the cell parameters, the extra degrees of freedom are used to selectively detune the weaker dipole modes in the third and sixth band. For the third band, the iris thickness is varied, while maintaining a minimum thickness of 0.75 mm for mechanical considerations. For the sixth dipole band, the iris bulging radius is changed. To match the desired frequencies in the first band, the iris radii are varied with the constraint that their average equals 18% of the rf wavelength as discussed earlier. The remaining cell parameter, the cavity radius, is adjusted to obtain 11.424 GHz for the fundamental mode. The manifold slot parameters are set somewhat empirically by iterating the sizes until a ‘good’ wakefield is achieved (see below).

The third step is to construct an equivalent circuit to model the wakefields in a damped and detuned structure [36]. The schematic is shown in Fig. 4.26 where the LC circuits represent the TE and TM components of the dipole field of the individual cells. Each component is magnetically coupled to both components of the adjacent cells. The beam excitation of the cavity is modeled by the input currents to each of the TM cells. The manifold structure is modeled by the uppermost sequence of transmission line sections each carrying a $TE_{11}$ waveguide mode and shunted by an LC circuit at the junction of adjacent transmission lines. Coupling of the accelerator cells to the manifolds is represented by a coupling between the shunt capacitance of the manifold and the capacitance of the TE component of the corresponding accelerator cell.

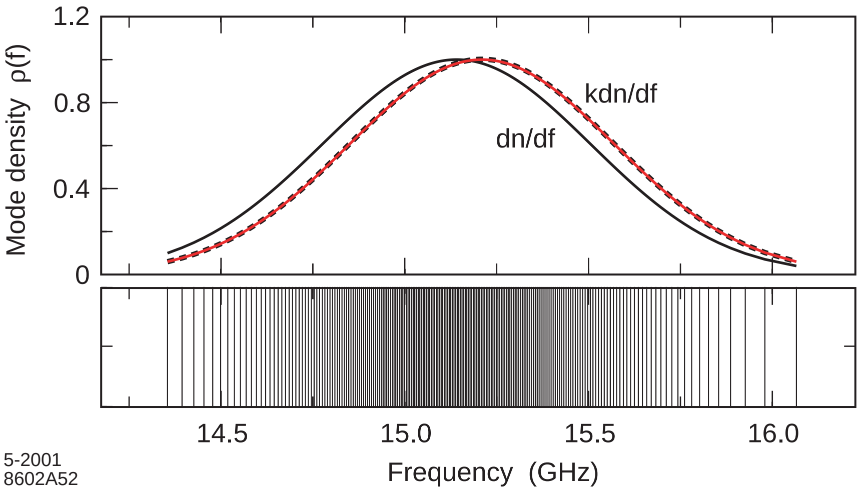

**Figure 4.25:** RDDS1 dipole mode frequency distributions: dn/d*f* is the mode density and *k*dn/d*f* is the density weighted by the mode kick factors (*k*).

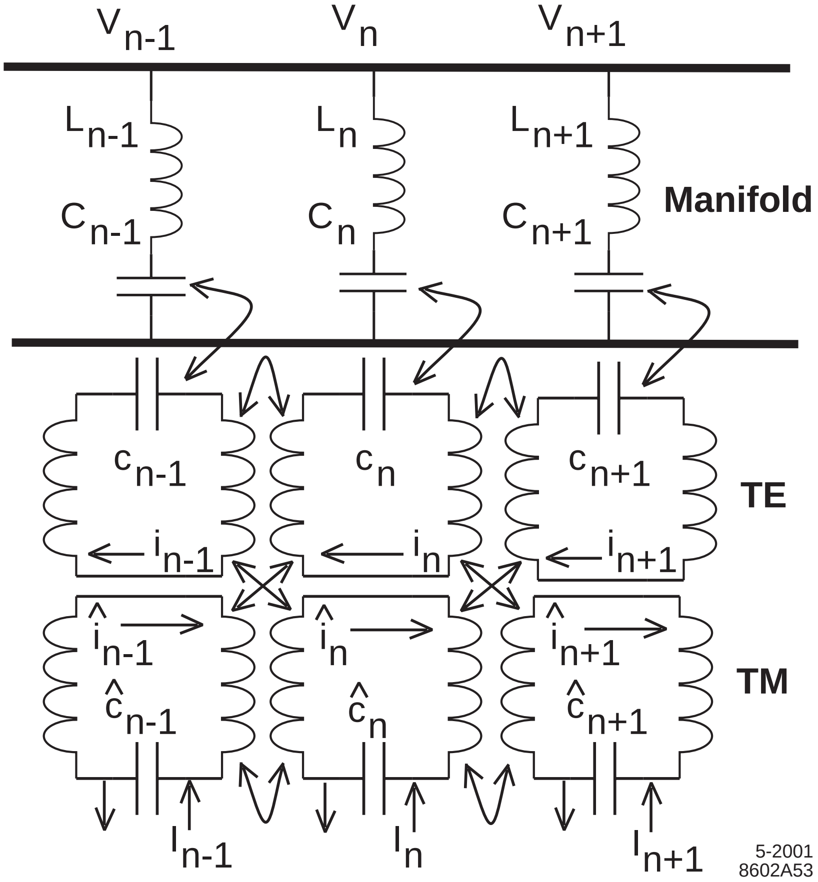

**Figure 4.26:** Equivalent circuit for the damped, detuned structure.

In this model, there are nine parameters per cell. The cell dimensions are determined for a representative set of seven cells. The periodic circuit predictions are fitted to computed dispersion curves for three modes, the two lowest dipole modes of periodic structures having the dimensions of the selected cells, and the lowest mode of the manifold. The circuit parameters for the other cells are determined by interpolation from these results. A newly developed 3D finite-element, parallel-processing code (Omega3P) was used to compute the dispersion curves for RDDS1. To verify the accuracy of the code, five sets of test disks were carefully measured mechanically with a coordinate measuring machine (CCM). These mechanical data were then used to predict the disk properties. Excellent agreement (< 1 MHz) was obtained between electrical measurements with a network analyzer and the finite-element predictions.

In the final step of the design process, the long-range wakefield is computed and the results evaluated. First, the equivalent circuit is used to compute the dipole impedance as a function of frequency over the bandwidth of interest (about 15% of the mean frequency). The results are then inverse Fourier transformed to obtain the time dependence of the wakefield. If the wake suppression is at the level desired, the wake function is used as input to simulations of linac beam transport to determine its effect on betatron motion and emittance growth. If acceptable levels are not found, the procedure is iterated, varying the structure parameters, in particular the detuning width and sigma and the damping slot sizes.

### 4.5.4 Structure Fabrication and Testing

To build a structure, disks and cells are first rough-machined using regular lathes and milling machines [37,38]. At this stage, more than 40 μm of extra copper are left on all surfaces except the coupling slots and manifolds. Final machining is done to micron accuracy and 50 nm surface finish using single crystal diamond turning. The cells are carefully cleaned and rinsed with ozonized water, and then stacked in the V-block of a special fixture. The whole stack is pre-diffusion bonded at 180°C and final-diffusion bonded at 890°C. The final assembly including flanges, vacuum ports, WR90 waveguides for the fundamental mode, and WR62 waveguides for the dipole modes are brazed in a hydrogen furnace at 1,020°C. The brazed section is then installed on a strongback for final mechanical measurement and straightening in a CMM. This procedure has produced structures with straightness over the 1.8-m length that is well within the NLC requirement of 10 μm rms.

During the assembly process, microwave quality control is used to evaluate the cell and structure properties at several steps [39,40]. This is particularly important since the cells are not designed to be tuned. As the cells are fabricated, the fundamental and dipole modes are measured to look for significant cell-to-cell deviations. Stacks of cells are also measured to verify that the phase advance is correct at 11.424 GHz. If the net phase error deviates by more than several degrees, the dimensions of subsequent cells are modified to compensate the phase shift. After the structure is assembled, a semiautomated bead pull system is used to measure the field phase and amplitude along the structure. Phase deviations of less than 20 degrees are generally achieved, within the NLC specifications.

To determine if the long-range wakefield of the structure is as predicted, the wakefield is measured in the Accelerator Structure SETup (ASSET) facility in the SLAC Linac. The positron beam passes first through the structure and induces a wakefield, the effects of which are then observed with the trailing electron beam. For RDDS1, a comparison of the measurements and prediction is shown in Fig. 4.27. Although the agreement is excellent, the wakefield is larger than originally designed and is not acceptable for NLC. This is due to a defect in the final assembly procedure. Several cells of the structure were distorted by a support ring during the final braze of the vacuum manifolds onto the outside of the structure. This changed their frequencies by about 30 MHz. To estimate the effect of this error, the phase advance of the fundamental mode was measured after assembly. A corresponding change in the dipole frequencies was then included in the wakefield prediction. Despite this defect, the random dipole frequency errors are less than 1 MHz, which is demonstrated by the fact the wakefield dips to the 0.1-V/pC/m/mm level at about 25 ns. In an earlier structure (DDS1), a smaller wakefield was achieved, but a mismatch in the manifold vacuum windows also caused it to be larger than designed.

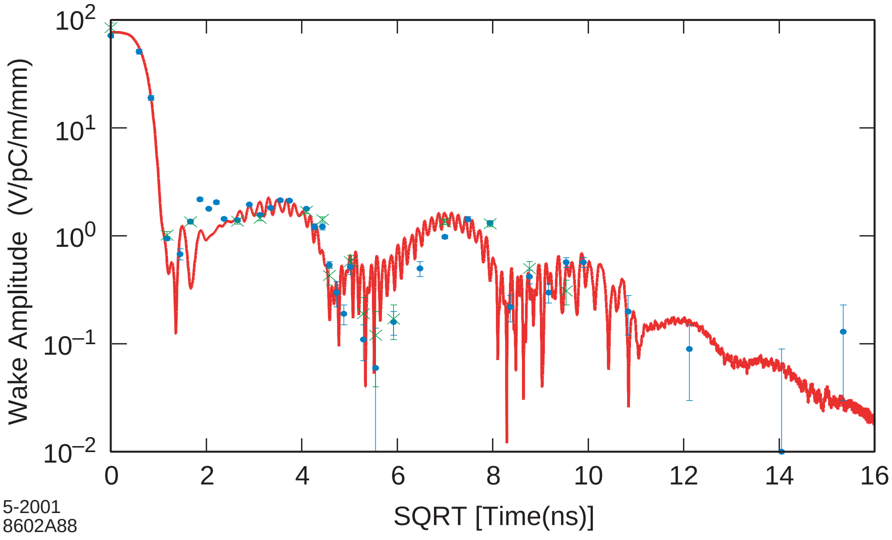

**Figure 4.27:** RDDS1 vertical (circles) and horizontal (crosses) wakefield measurements and prediction (solid line).

Centering tests were also performed in ASSET using the dipole signals from the manifolds as a guide to position the positron beam. Measurements of the resulting short-range wakefield (< 300 ps) indicated that the beam had been centered to less than 20 µm in the structure, which is close to the requirement during NLC operation.

In summary, the techniques for suppressing the long-range transverse wakefield are well developed and structures with wakefields that are close to meeting the NLC requirements have been fabricated. The modeling tools needed for the design, and the fabrication methods needed for construction, are well advanced and are being applied to the high-gradient designs that are being developed (see below). Activity has begun to prepare for eventual production of these structures by industry, which will help to reduce the uncertainty in the cost for mass producing the structures.

### 4.5.5 High Gradient Development

During the period when the long-range wakefield-suppression techniques were being developed, there was little concern about the feasibility of operating the 1.8-m structures at unloaded gradients in the 50-80 MV/m range. Earlier rf power tests with standing-wave cavities and short, low group velocity structures had achieved gradients that far exceeded the NLC goal. These first tests were limited to cavities and short structures because of the limited rf power available at the time, which was insufficient for a long structure. Some pitting was seen on the cell irises of these structures after high power operation. This pitting was clearly associated with the rf breakdown that occurred during processing. At that time, it was generally thought that this damage occurred only at the highest gradients, or only during the initial processing to a high gradient. Facilities were not available to study the long-term effects of high-gradient operation, and the effect of the pitting on the structure performance was not measured.

High-power testing of NLC and JLC prototype structures only began in earnest when higher-power X-band sources became available and facilities for doing more extensive studies came into operation. Four of the 1.8-m structures that had been developed for the wakefield suppression studies were installed in the

NLCTA. They were initially intended to operate at 50 MV/m with 240-ns pulses, which was the maximum pulse length possible in the NLCTA. It took a few hundred hours to process the fields to the desired level, but the 50-MV/m gradients were eventually achieved.

During this time, a 1.3-m JLC structure was tested at the Klystron Test Laboratory at SLAC, which achieved gradients up to 85 MV/m with 150-ns pulses [41]. A new bead-pull technique was used to compare the phase profiles before and after processing of the JLC structure. It showed the surprising result that the net phase shift through the structure had changed by 25 degrees. This shift occurred only in the upstream two-thirds of the structure.

A similar pattern of damage was later observed when processing one of the damped, detuned structures to 70 MV/m with 240-ns pulses in the NLCTA. This measurement used an in-situ beam technique. During about 1,000 hours of operation at high gradient, the net phase shift increased by 90 degrees. Once this continued degradation was seen, bead-pull measurements were made on the remaining three1.8-m structures. All of these had about 500 hours of operation at gradients less than 55 MV/m. The same pattern of damage was observed [42].

Based on these results and those from the early structure tests, it was hypothesized that the damage was related to the higher group velocity at the upstream end of the structures. This relation was proposed in part because the rf power required to achieve a given gradient increases with group velocity. In addition, if the structure is viewed as a transmission line and rf breakdown as a load impedance, the fraction of incident power absorbed during breakdown increases with group velocity. If damage relates directly to absorbed power, these two effects combined predict that the gradient at which a given level of damage occurs is inversely proportional to the group velocity.

Another possible explanation for the greater upstream damage is that reflected rf energy from a breakdown causes an overvoltage upstream that initiates further breakdown within the same rf pulse. Such events have been observed, and this mechanism would increase the number of upstream breakdowns. Contrary evidence is that more than 70% of breakdowns appear to occur in one location.

A series of structures with different lengths and group velocities was built to study the factors contributing to the damage. In addition, various improvements were made to the structure cleaning, handling and processing procedures to determine their impact on high gradient performance. The first structure tested in this program was made by cutting off the last 52 cells of one of the 1.8-m structures that had been run in NLCTA. This portion was chosen because it showed no discernible phase shift from the previous operation at less than 50 MV/m. The shortened structure was operated for about 1,700 hours with 240-ns square pulses at gradients up to 73 MV/m. Although the structure incurred some damage, as indicated by a 5-degree phase shift, the breakdown rates at the end of the experiment the were fairly low, about 1 per hour at 70 MV/m and 0.25 per hour at 65 MV/m. The value at 65 MV/m is almost acceptable for NLC operation.

The goal of the next test was to compare the relative breakdown rate in two structures with a common group velocity profile but different length. For this purpose, two new structures were fabricated at KEK with initial group velocities of 5% c. One was 20-cm long (23 cells) and the other 105-cm long (120 cells) with the first 23 cells identical to those in the shorter structure. The iris surface fields were held constant along the structure to eliminate field-strength differences and both were powered equally. The shorter structure was found to have an internal overvoltage of roughly 10% due to a reflection from the loads, which had to be taken into account in the measurements. Both structures behaved similarly. At lower gradients, the breakdown occurred mainly near the input or output couplers so the effect of length was unclear. At the highest gradients, the coupler regions were not the dominant breakdown locations and the breakdown rates were comparable. In general, the breakdown rates were similar to those measured in the previous test but the damage was less (< 2 degrees of phase shift). This reduction may be the result of the improvements made in the way the structure was prepared, with better degassing, and rf processed, with a reduced rf trip threshold.

In a parallel program to the tests discussed above, a 1.8-m prototype NLC/JLC structure that had not previously been powered was tested to determine the gradient at which damage begins to occur. Like the previous prototype structures operated in the NLCTA, this structure has an initial group velocity of 12% c. A 'less aggressive' processing protocol was used to prevent the breakdown from continuing for several pulses and to allow a longer time for outgassing after a trip. In spite of these changes, the damage threshold was found to be 45-50 MV/m, consistent with the earlier 1.8-m structure results. Clearly, the lower group velocity structures were able to reach much higher gradients before damage, 70-75 MV/m. The low group velocity structures also reached gradients of 50-60 MV/m before the breakdown rate exceeded several per hour. This occurred much earlier, at 30-40 MV/m, for the higher group velocity 1.8-m structure. This dependence is very evident in Fig. 4.28.

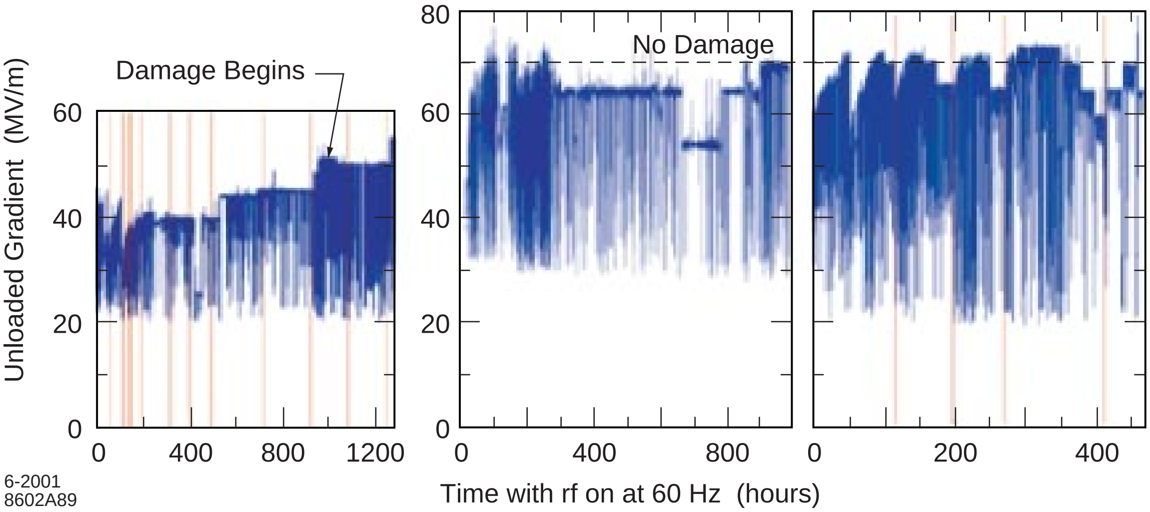

**Figure 4.28:** Operational Histories of Three Accelerator Structures as they are processed to high gradients. (a) A 1.8-meter-long NLCTA structure with group velocity 12% the speed of light at the input end. (b) A 0.5-meter-long test structure with group velocity 5% the speed of light at the input end. (c) A 1.0-meter-long test structure with group velocity 5% the speed of light at the input end. The data are unselected and correspond to a range of operational conditions.

Much has also been learned during the structure processing from measurements of various emission signals (rf, light, X-rays, sound, vacuum pressure and electron currents) before, during, and after breakdown. In addition, the cell irises have been examined after processing to look for contaminants. Some of the general conclusions are listed below:

- No consistent precursors to breakdown have been found.
- No definitive evidence has been found as to what triggers breakdown.
- After a breakdown begins, up to about 80% of the incident rf energy is absorbed. The transmitted power falls to zero in about 100 ns.
- Rf transmission fully recovers after the main rf pulse has been off for several microseconds, even if there has been a large gas burst.

- Vacuum pressures up to $10^{-7}$ torr do not seem to affect the breakdown rate.
- When running at a fixed gradient, the breakdown rate decreases slowly. A more rapid reduction is seen after processing first to a higher gradient.

Perhaps the most important observation is that, for the longest pulse operation at the highest gradients, the breakdown events tend to be clustered in time and localized in regions of the structure. These events suggest that a breakdown can cause secondary damage that lowers the breakdown threshold on subsequent pulses. Evidence for such secondary damage has been seen on irises inspected after processing. The number of pits observed can be 100 times larger than the number of rf trips that occurred during processing. This collateral damage mechanism would explain why a given cell iris behaves differently in a high group velocity structure rather than a low group velocity structure (i.e., it breaks down more in one case than the other for the same surface field). It is the larger secondary damage that causes the continued breakdown.

The principal focus of the NLCTA program this year will be to gain greater understanding the gradient limits in X-band accelerator structures. In the next set of tests, two structures of the same length (53 cm) but different initial group velocity (5% and 3% c) will be operated to assess the dependence on group velocity. In parallel, two 15-cell standing-wave structures will be tested. The standing-wave approach was chosen because it is difficult to lower the group velocity of a traveling-wave structure below 3% c without reducing the average iris radius or losing efficiency. The standing-wave structures are efficient and the group velocity with respect to breakdown should effectively be less than 1% c.

For later tests, several types of standing wave structures and low group velocity traveling-wave structures will be built. The low-velocity structures built for the current tests could not be used for NLC because they have small-diameter irises that would produce stronger wakefields. The newer structures will have a higher phase advance per cell (150° instead of 120°) to achieve both acceptable iris sizes and low group velocities. Three designs are being developed, one that is 0.9-m long with an initial group velocity of 5.1% c and two that are 0.9-m and 0.6-m long with initial group velocities of 3.2% c. These prototypes are scheduled for high power testing by the end of the year. Various methods of pretreating the structures will also be tried, including glow discharge cleaning.

The structure design chosen for the current NLC configuration is a 0.9-m long traveling-wave structure with a 5.1% c initial group velocity and a phase advance of 150 degrees per cell. The higher phase advance allows an average iris radius that is 0.18 of the rf wavelength, which is necessary to attain the desired short-range wakefield performance. The structure is similar to one of the test structures to be studied this fall in the NLCTA. The recent results from the NLCTA high-gradient program suggest that this structure will meet the NLC requirements on accelerating gradient, reliability, and short-range wakefields. Preliminary damped and detuned parameter sets have been developed for the structure that produce acceptable long-range wakefields. The proper wakefield suppression will be added using the same techniques that were successful with the earlier structures. A full prototype structure, meeting all of the performance requirements, will be developed and tested late next year.

## References

[1] Adolphsen, C., *et al.*, "International Study Group Progress Report on Linear Collider Development," *International Study Group and High-Energy Accelerator Organization*, April 2000. 286pp, SLAC-0559, KEK-REPORT-2000-7, LCC-0042.

[2] Larsen, R.S., "NLC Klystron Modulators R&D Plan Overview," *1999 NLC Klystron Modulator Workshop*, SLAC, June 1999. www-project.slac.stanford.edu/lc/local/Reviews/modulators/workshop/Mod%20WS99R1.pdf

[3] Cassel, R.L., Pappas, G.C., Nguyen, M.N.,. DeLamare, J.E, "A Solid State Induction Modulator for the NLC," *Proc. of the 1999 Particle Accelerator Conference (PAC99)*, New York, New York, March 1999.

[4] Cassel, R.L., Nguyen, M.N., "A New Type Of Short Circuit Failures Of High Power IGBTs," *IEEE 2001 Pulsed Power Conference*, Las Vegas, Nevada, June 2001.

[5] Cassel, R.L., de Lamare, J.E., Nguyen, M.N., Pappas, G.C., "Solid State Induction Modulator Replacement for the Conventional SLAC 5045 Klystron Modulator," *20th International Linac Conference (Linac 2000)*, Monterey, California, August 2000. SLAC-PUB-8704, LINAC2000-THA13, November 2000, 3pp.

[6] Cassel, R.L., Delamare, J.E., Nguyen, M.N., Pappas, G.C., "Solid State Induction Modulator Replacement for SLAC Klystron Modulators," *24th International Power Modulator Symposium*, Norfolk, Virginia, June 2000.

[7] Cassel, R.L., "A Long Pulse Solid State Induction Modulator," Presented at the *5th Modulator-Klystron Workshop for Future Linear Colliders*, CERN, PS Division, Geneva, Switzerland, April 2001.

[8] Cassel, R.L., Delamare, J.E., Nguyen, M.N., Pappas, G.C., Cook, E., Sullivan, J., Brooksby, C., the "Prototype Solid State Induction Modulator For SLAC NLC," *PAC 2001*, Chicago, Illinois, June 2001.

[9] Chapter 5 in reference [1].

[10] Caryotakis, G., "The Klystron: A Microwave Source Of Surprising Range And Endurance," Invited review paper given at 39th Annual Meeting of the Division of Plasma Physics of the American Physical Society (DDP 97), Pittsburgh, Pennsylvania, November 1997. SLAC-PUB-7731, January 1998, 13pp. Revised version, 4/98.

[11] Bohlen, H. P., "Advanced High-Power Microwave Vacuum Electron Device Development," *Proceedings of the 1999 Particle Accelerator Conference*, New York, New York, March 1999.

[12] Chin, Y.H., Takata, K., Fukuda, S., Mizuno, H., Michizono, S., Yamaguchi, S., Matsumoto, S., Tokumoto, S., Tsutsui, H., (KEK, Tsukuba), Kazakov, S., (Novosibirsk, IYF), "The 120-Mw X Band Klystron Development At KEK," *6th European Particle Accelerator Conference (EPAC 98)*, Stockholm, Sweden, June 1998. KEK-PREPRINT-98-118, August 1998, 4pp.

[13] Koontz, R.F., Lee, T.G., Pearson, C., Vlieks, A.E., "Recent Performance, Lifetime, And Failure Modes of the 5045 Klystron Population At SLAC," *Proc. LINAC 92*, Ottawa, Canada, August 1992. SLAC-PUB-5890, Aug 1992, 3pp.

[14] Caryotakis, G., "The X-Band Klystron Program At SLAC," *Proc. 3rd International Workshop on RF Pulsed Power Sources for Linear Colliders (RF 96)*, Hayama, Japan, April 1996. SLAC-PUB-7146, April 1996, 9pp.

[15] Sprehn, D., Caryotakis, G., Eppley, K., Phillips, R.M., "PPM Focused X-Band Klystron Development at the Stanford Linear Accelerator Center," *Proc. 3rd International Workshop on RF Pulsed Power Sources for Linear Colliders (RF 96)*, Hayama, Japan, April 1996, SLAC-PUB-7231, July 1996, 9pp.

[16] Wright, E., Callin, R., Caryotakis, G., Eppley, K., Fant, K., Fowkes, R., Gold, S., Koontz, R., Miller, R., Pearson, C., Phillips, R.M., Tantawi, S.G., Vlieks, A.E., "Design Of A 50-MW Klystron At X-Band," Pulsed RF Sources for Linear Colliders, Montauk, New York, October 1994. *RF 1994:0058-66* (QCD183:I796:1994), SLAC-PUB-6676, July 1995, 12pp.

[17] Jongewaard, E., Caryotakis, G., Pearson, C., Phillips, R.M., Sprehn, D., Vlieks, A.E., "The Next Linear Collider Klystron Development Program," *7th European Particle Accelerator Conferences (EPAC 2000)*, Vienna, Austria, June 2000 and *20th International Linac Conference (Linac 2000)*, Monterey, California, August 2000, SLAC-PUB-8478, June 2000, 4pp.

[18] Sprehn, D., Caryotakis, G., Jongewaard, E., Phillips, R.M., Vlieks, A.E., " X-Band Klystron Development at the Stanford Linear Accelerator Center," 7th SPIE Microwave Intense Pulses, Orlando, Florida, April 2000. *Proc. SPIE Int. Soc. Opt. Eng.*, **4031**:132-143, 2000, SLAC-PUB-8346, March 2000, 13pp.

[19] Sprehn, D., Caryotakis, G., Jongewaard, E., Phillips, R.M., "Periodic Permanent Magnet Development for Linear Collider X-Band Klystrons," *19th International Linear Accelerator Conference (Linac 98)*, Chicago, Illinois, August 1998 and AIP Conf. Proc. 474:31-40, 1999, SLAC-PUB-7925, September 1998, 6pp.

[20] Caryotakis, G., "Development of X-Band Klystron Technology At SLAC," *17th IEEE Particle Accelerator Conference (PAC 97)*: Accelerator Science, Technology and Applications, Vancouver, Canada, May 1997. Also SLAC-PUB-7548, May 1997, 5pp.

[21] Corredoura, P. and Adolphsen, C., "The Proposed NLC Linac LLRF System," *7th European Particle Accelerator Conferences (EPAC 2000)*, Vienna, Austria, June 2000, SLAC-PUB-8497, July 2000, 3pp.

[22] Nantista, C., *et al.*, "High-Power RF Pulse Compression With SLED-II at SLAC," *IEEE Particle Accelerator Conference*, Washington, D.C., 1993; SLAC-PUB-6145.

[23] Mizuno, H., Otake, Y., "A New RF Power Distribution System for X Band Linac Equivalent to an RF Pulse Compression Scheme of Factor $2^N$," *17th International Linac Conference (LINAC 94)*, Tsukuba Japan, August 1994.

[24] Lavine, T.L., *et al.*, "High-Power Radio-Frequency Binary Pulse-Compression Experiment at SLAC," *IEEE Particle Accelerator Conference*, San Francisco, CA, May 1991, SLAC-PUB-5451.

[25] Tantawi, S.G., *et al.*, "A Multi-Moded RF Delay Line Distribution System for the Next Linear Collider," *Proc. of the Advanced Accelerator Concepts Workshop*, Baltimore, Maryland, July 1998.

[26] Tantawi, S.G., *et al.*, "The Generation of 400-MW RF Pulses at X Band Using Resonant Delay Lines," *IEEE Trans. Microwave Theory Tech.*, **47**(12): 2539-2546, December 1999, SLAC-PUB-8074.

[27] Tantawi, S.G., *et al.*, "Evaluation of the $TE_{12}$ Mode in Circular Waveguide for Low-Loss, High-Power RF Transmission," *Phys. Rev. ST Accel. Beams*, 3, 2000.

[28] Tantawi, S.G., *et al.*, "RF Components Using Over-Moded Rectangular Waveguides for the Next Linear Collider Multi-Moded Delay Line RF Distribution System," *18th Particle Accelerator Conference*, New York, New York, March 1999.

[29] *HP High Frequency Structure Simulator*, Version 5.4, Copyright 1996-1999 Hewlett-Packard Co.

[30] *Calabazas Creek Research, Inc., 20937 Comer Dr., Saratoga, CA 95070.*

[31] Nantista, C.D., *et al*., "Planar Waveguide Hybrids for Very High Power RF," *1999 Particle Accelerator Conference*, New York, New York, March 1999, SLAC-PUB-8142.

[32] Nantista, C.D., Tantawi, S.G., "A Compact, Planar, Eight-Port Waveguide Power Divider/Combiner: The Cross Potent Superhybrid," *IEEE Microwave and Guided Wave Letters*, **10**:520-522, December, 2000.

[33] Chapter 7 in reference [1].

34] Miller, R.H., "Accelerator Structures for Linear Colliders," SLAC-PUB-8621, September 2000.

[35] Li, Z., *et al*., "RDDS Cell Design and Optimization for the Linear Collider Linacs," SLAC-PUB-8244, May 1999.

[36] Jones, R.M., *et al*., "Equivalent Circuit Analysis of the SLAC Damped Detuned Structure," SLAC-PUB-7187, June 1996.

[37] Wang, J.W., *et al*., "Accelerator Structure R&D for Linear Colliders," SLAC-PUB-8394," June 1999.

[38] Higashi, Y., *et al*., "Studies of High-Precision Machining of Acclerator Disks of X-band Structure f r Linear Collider," KEK Report 2000-1, April 2000.

[39] Wang, J.W., *et al*., "Design Fabrication and Measurement of the First Rounded Damped Detuned Accelerator Structure (RDDS1)," SLAC-PUB-8583, September 2000.

[40] Miller, R.H., *et al*., "Microwave Quality Assurance for Single Cells of the NLC," SLAC-PUB-8620, September 2000.

[41] Loewen, R., *et al*., "SLAC High Gradient Testing of a KEK X-Band Accelerating Structure," SLAC-PUB-8399, March 2000.

[42] Adolphsen, C., *et al*., "RF Processing of X Band Accelerator Structures at the NLCTA," SLAC-PUB-8573, August 2000.

# Chapter 5

# Injector Systems

## 5.1 Introduction

The Next Linear Collider Injector System is designed to produce low emittance, 8-GeV electron and positron beams at 120 hertz for injection into the NLC main linacs. Each beam consists of a train of 190 bunches spaced by 1.4 ns; each bunch has a population of $0.75\text{x}10^{10}$ particles. The emittances at injection into the main linacs are $\gamma\varepsilon_x = 3\text{x}10^{-6}$ m-rad in the horizontal and $\gamma\varepsilon_y = 2\text{x}10^{-8}$ m-rad in the vertical, and the bunch length is in the range of 90-140 µm. Electron polarization of greater than 80% is required. Electron and positron beams are generated in separate accelerator complexes, each of which contains the source, damping ring systems, L-band, S-band, and X-band linacs, bunch length compressors, and collimation regions.

The need for low technical risk, reliable injector subsystems has been a major consideration in the design effort. Technologies chosen for the design of the NLC injector systems are solidly based on experience with previously built and operated high-energy colliders and with third-generation synchrotron light sources. Polarized electrons are produced using a dc photocathode gun which is very similar to the successful SLC polarized source [1]. Unpolarized positrons are generated using multiplexed target systems which will be run in parallel; the peak energy deposition in each target assembly is designed to be identical to that of the SLC positron system which ran for more than 5 years without trouble [2]. The parameters of the two main damping rings are similar to the present generation of synchrotron light sources and the B-Factory colliders in that they must store high-current beams (~ 1 A) while attaining small normalized emittances. The acceleration gradient in the injector S-band linacs [3] is only modestly higher than the gradient in the SLC linac and the S-band klystrons are based on the 65-MW SLAC 5045 [4] klystrons. Injector L-band linacs [3] have been designed with low gradients to avoid problems associated with high fields in the structures or ancillary rf distribution systems. The X-band rf for the bunch length compressors is adapted from the NLC main linac rf development.

Descriptions of the choice of injector layouts, the polarized electron source, the positron system, damping ring systems, and bunch length compression systems follow. The possibility of polarized positrons is followed by a discussion of present and future injector system activities. An explicit description of the 6-GeV injector prelinacs has not been included. While key to the functioning of the injector systems, the prelinacs are not seen to be fundamentally difficult. The designs of the prelinacs are based on proven S-band technologies for which performance is well demonstrated and understood in the operating range of the NLC injector design.

## 5.2 Injector Layout Choices

The present NLC configuration includes two injector-system layouts: a remote, near-surface cut-and-cover design for the California 135 site and a centralized deep-bored-tunnel design for the North-South Fermilab site. A design requirement for both is that technical components are not shared among electron and positron generation, damping, and initial acceleration systems. Cost optimization leads to separate electron and positron injector complexes. Figures 5.1a and 5.1b show the layout of the electron and positron injector complexes for the near-surface scenario. Figures 5.2a and 5.2b show the layout of the electron and positron injector complexes for the deep- bored-tunnel scenario.

In the near-surface cut-and-cover configuration, the electron and positron systems are located in separate complexes at the upstream ends of the respective main linacs, separated by about 30 km. Whereas it is reasonable to consider combining the two injector complexes at a central location, such a layout requires the addition of lengthy and costly low emittance-preserving transport lines. With no obvious cost or operational advantage for the combined complexes, it has been decided to adopt the remote and separated injectors for their low cost. As depicted in Figs. 5.1a and 5.1b, cost savings are taken wherever possible through the sharing of accelerator housings and klystron galleries among injector subsystems (e.g., in Fig. 5.1b, the $e^-$ drive linac, $e^+$ targets and $e^+$ booster linac share a common accelerator tunnel and equipment support housing with the $e^+$ prelinac; in Fig. 5.1a, the $e^-$ booster and $e^-$ prelinac share a common accelerator tunnel and support housing ).

The layout for the deep-bored-tunnel design is quite similar, except that the separate electron and positron injector complexes are placed closer to the center for the purpose of placing them on the Fermilab site and utilizing its existing facilities. The two injectors are separated by about 5 km and have separate housings for each beam line. Each injector has approximately 20 km of low-emittance-preserving transport lines and turnout beam lines at their ends for the purpose of connecting into the 180° bunch compressor arcs at the entrances to the main linacs.

A fully centralized injector is under consideration for the Fermilab site. This compact layout is located on or near the surface. Beam lines are required to drop the damped injector beams down to the long-haul transport lines placed in the main linac tunnel. The accelerator components for both electron and positron injectors are located in a common housing with shared equipment galleries and facility infrastructure.

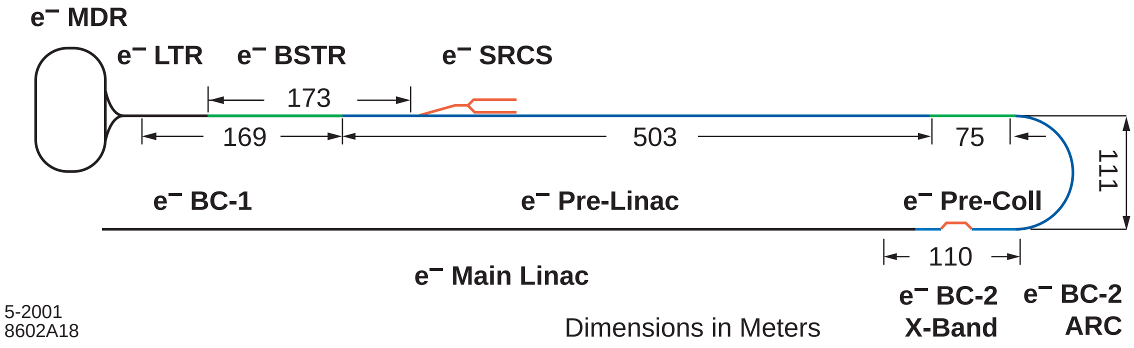

**Figure 5.1a:** Electron injector complex layout for the near surface cut-and-cover design. $e^-$ SRCS is a pair of electron sources; $e^-$ BSTR is the 2-GeV, S-band booster linac; $e^-$ LTR is the linac-to-ring transport line; $e^-$ MDR is the electron main damping ring; $e^-$ BC-1 is the first stage bunch length compressor; $e^-$ PreLinac is the 6-GeV S-band prelinac; $e^-$ Pre-Coll is the $e^-$ precollimation region; $e^-$ BC-2 Arc is the second stage bunch length compressor arc; and $e^-$ BC-2 X-band denotes the second compressor stage X-band rf section and magnet chicane.

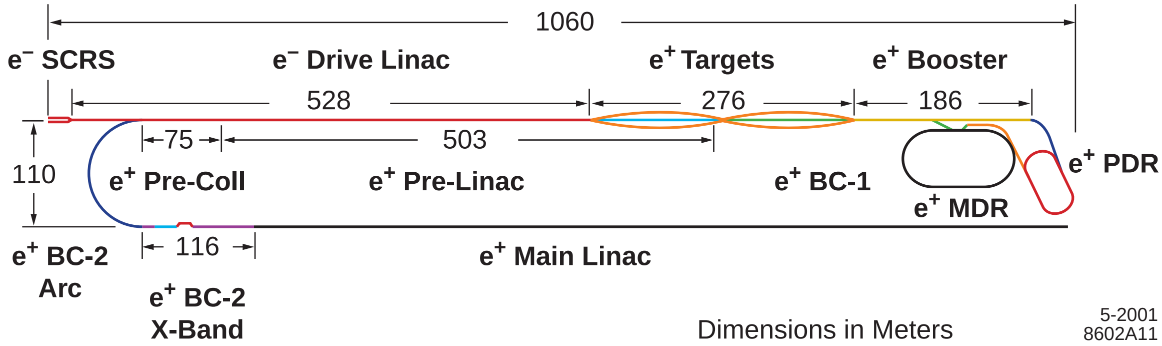

**Figure 5.1b:** Positron injector complex layout for the near-surface, cut-and-cover design. $e^-$ SRCS is a pair of nonpolarized electron sources; $e^-$ Drive Linac is a 6-GeV, S-band linac; the $e^+$ Targets region contains 4 identical target/capture stations of which 3 are required for normal NLC $e^+$ operations; $e^+$ BSTR is the 2-GeV, L-band booster linac; $e^+$ PDR is the positron predamping ring; $e^+$ MDR is the positron main damping ring; $e^+$ BC-1 is the first stage bunch length compressor; $e^+$ PreLinac is the 6-GeV S-band prelinac; $e^+$ Pre-Coll is the $e^+$ precollimation region; $e^+$ BC-2 Arc is the second stage bunch length compressor arc; and $e^+$ BC-2 X-band denotes the second compressor stage X-band rf section and magnet chicane.

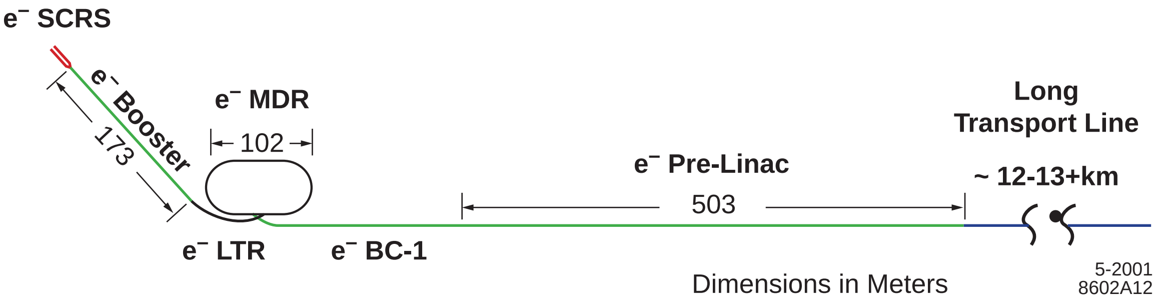

**Figure 5.2a:** Electron injector complex layout for the deep-bored-tunnel design. $e^-$ SRCS is a pair of electron sources; $e^-$ BSTR is the 2-GeV, S-band booster linac; $e^-$ LTR is the linac-to-ring transport line; $e^-$ MDR is the electron main damping ring; $e^-$ BC-1 is the first stage bunch length compressor; $e^-$ PreLinac is the 6-GeV S-band prelinac; the $e^-$ precollimation region, the second stage bunch length compressor arc and the second compressor stage X-band rf section and magnet chicane are located at the end of the Long Transport Line and are not shown in this view.

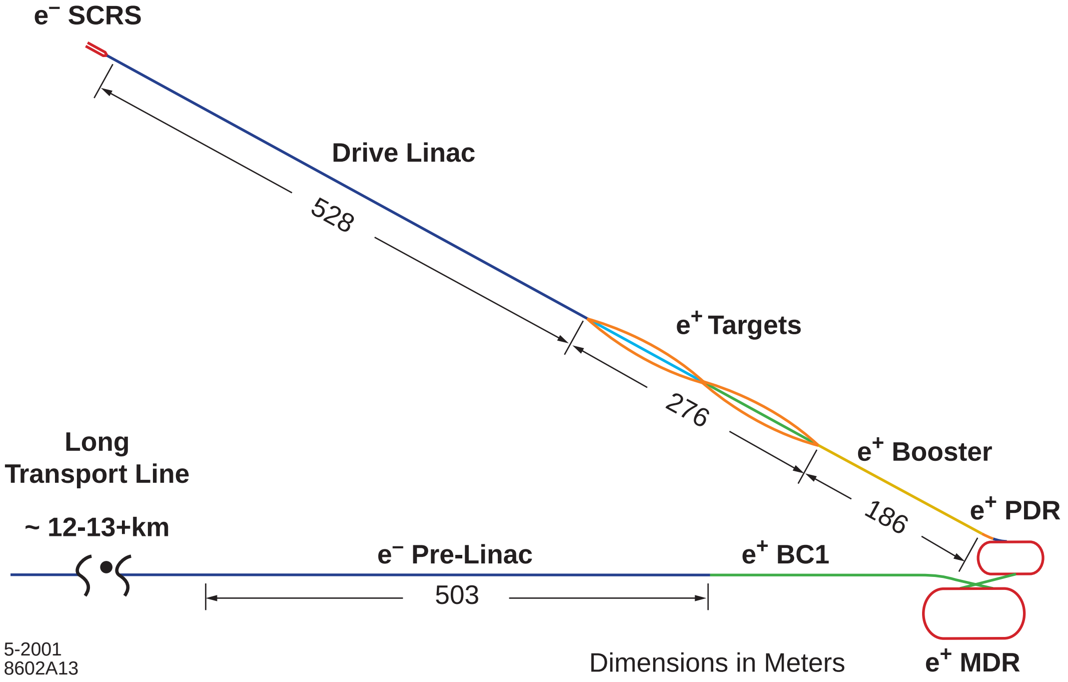

**Figure 5.2b**: Positron injector complex layout for deep-bored-tunnel design. $e^-$ SRCS is a pair of nonpolarized electron sources; $e^-$ Drive Linac is a 6-GeV, S-band linac; the $e^+$ Targets region contains 4 identical target/capture stations of which 3 are required for normal NLC $e^+$ operations; $e^+$ BSTR is the 2-GeV, L-band booster linac; $e^+$ PDR is the positron predamping ring; $e^+$ MDR is the positron main damping ring; $e^+$ BC-1 is the first stage bunch length compressor; $e^+$ PreLinac is the 6-GeV S-band prelinac; the $e^+$ precollimation region, the second stage bunch length compressor arc and the second compressor stage X-band rf section and magnet chicane are located at the end of the Long Transport Line and are not shown in this view.

## 5.3 Polarized Electron Source

The NLC injector electron source system creates polarized electron beams of the required energy and emittance for injection into the electron damping ring system. The polarized electron beams are produced with a photocathode electron gun, bunched in a subharmonic rf system and accelerated in an S-band linac to 1.98-GeV, the energy of the damping ring. Each beam consists of a bunch train of 190 bunches with $0.8\mathrm{x}10^{10}$ particles per bunch that are spaced by 1.4 ns (or 95 bunches with $1.6\mathrm{x}10^{10}$ particles per bunch that are spaced by 2.8 ns). The electrons at the end of the source booster linac have an emittance of $100\mathrm{x}10^{-6}$ m-rad and spin polarization of 80%. A summary of the design parameters is given in Table 5.1.

The polarized electron source consists of a polarized high-power laser and a high-voltage dc gun with a semiconductor photocathode. Many of the performance requirements for the NLC injector are similar to those in the SLC and the design of the NLC injector is based on the successful SLC injector. The main difference is that, while the SLC polarized electron injector produced one pair of electron bunches separated by 60 ns at 120 Hz repetition rate, the NLC injector must produce 265-ns-long trains of 190 bunches separated by 1.4 ns. Individual bunch populations for the NLC are down by a factor of about 6 from the

SLC but the peak current is comparable due to the higher bunching frequency. The NLC design uses 714 MHz rf for the subharmonic bunching systems to permit the generation of beams with either 1.4 ns or 2.8 ns separation.

**Table 5.1:** Beam parameters as delivered by the electron source system to the electron main damping ring system for the 1.4 and 2.8 ns bunch spacing options.

| PARAMETER NAME | SYMBOL | VALUE | UNITS |
|---|---|---|---|
| Bunch Spacing | $T_b$ | 1.4 (2.8) | ns |
| Energy | E | 1.98 | GeV |
| Energy Adjustability | $\Delta E$ | ±5 | % |
| Bunch Energy Variation | $\delta E/E$ | 1 | % Full Width |
| Single Bunch Energy Spread | $\sigma_{\Delta E/E}$ | 1 | % Full Width |
| Emittance (norm. rms) | $\gamma\varepsilon_{x,y}$ | 100.0 | $10^{-6}$ m-rad |
| Bunch Length | $\sigma_z$ | <10 | mm |
| Particles/Bunch | $n_B$ | 0.8 (1.6) | $10^{10}$ particles |
| Train Population Uniformity | $\Delta n_T/n_T$ | 1 | % Full Width |
| Bunch-to-Bunch Pop. Uniformity | $\Delta n_B/n_B$ | 2 | % rms |
| Number of Bunches | $N_b$ | 190 (95) | # |
| Repetition Rate | f | 120 | Hz |
| Horizontal Beam Jitter | $\Delta\gamma J_x$ | 50 | $10^{-6}$ m-rad |
| Vertical Beam Jitter | $\Delta\gamma J_y$ | 50 | $10^{-6}$ m-rad |
| Polarization | $P_e$ | 80 | % |
| Beam Power | $P_b$ | 58 | kW |

The SLC polarized source generated 80% beam polarization. As long as ultra-high vacuum conditions were maintained, cathode lifetimes exceeded thousands of hours. System availability approached 99%. The basic technologies of the SLC injector will be utilized for the NLC. The most notable differences in the design are the increase in gun high voltage from the SLC value of 120 kV to 175-200 kV and the use of 714 MHz rf for subharmonic bunching. A 200 kV polarized electron gun is being developed at Nagoya University for the JLC [5]. Initial high voltage testing of this system has begun.

Improvement of the SLC photocathodes is required for NLC operation due to the higher pulse charge requirements. Efforts at SLAC [6] and at Nagoya University [7] are concentrating on developing cathodes with a highly doped surface layer to permit rapid dissipation of surface charge that builds up as beam is extracted. Recent tests [8] using a strained layer cathode with a 75 Å surface layer are extremely promising. Operating at 120 kV, up to 8 x $10^{11}$ electrons have been extracted by illuminating a 1-cm radius spot on the cathode. The polarization of the electrons was measured to be about 78% and no evidence of surface charge limit was observed. The maximum charge extracted was limited by available laser energy. Reduction of the laser spot to 0.5-cm radius still resulted in a maximum extracted charge of 8 x $10^{11}$. Extrapolating back to 1-cm radius spots, one would expect to extract 4 times the charge, 3.2 x $10^{12}$ electrons. The NLC charge requirement is 2 x $10^{12}$ electrons in 265 ns from the cathode. While very encouraging, work continues aimed at an explicit demonstration of the full NLC charge, current and polarization.

Significant development is required for the NLC polarized source laser system. Table 5.2 lists the source laser requirements. In Table 5.2, the range in laser wavelength reflects uncertainty in the choice of specific cathode material to be used. The most challenging aspects of the source laser are the requirements on parameter stability and the need for high availability. Both of these criteria were met for the SLC. Functional specifications for the source laser are being discussed and reviewed with the aim of assessing the technical difficulty of the laser and ultimately determining the level of resources (people, money, and time) which will be required for laser development. Although it is a difficult problem, it is not thought to be impossible.

**Table 5.2:** Polarized electron source laser system parameters

| PARAMETER NAME | SYMBOL | VALUE | UNITS |
|---|---|---|---|
| Bunch Spacing | $T_b$ | 1.4 (2.8) | ns |
| Wavelength | $\lambda$ | 740 - 850 | nm |
| Bandwidth | $\delta\lambda$ | 3 | nm |
| Bunch Length | $\Delta t$ | 0.5 | ns |
| Energy/Bunch | $E_b$ | 4.2 (8.4) | μJ |
| Energy. Uniformity | $\Delta n_B/n_B$ | <0.5 | % |
| Energy Uniformity along train | | 2 | % |
| Number of Bunches | $N_b$ | 190 (95) | # |
| Repetition Rate | f | 120 | Hz |
| Polarization | $P_\gamma$ | 99.9 | % |

An S-band linac is used to accelerate the captured electrons up to the damping ring energy of 1.98-GeV. The loaded gradient of the linac is 17-MeV/m. This linac will use KEK-style SLED systems for rf pulse compression [9] that have been designed and operated at higher field levels than the original SLAC SLED systems. Beam emittance growth through the booster linac is not a problem due to the low charge per bunch (in comparison with SLC operation) and because of the relatively large damping-ring design acceptance. Standard quadrupole focusing elements are employed along with discrete steering dipoles along the length of the booster linac. Multibunch beam loading in the linac is compensated using the $\Delta T$ method in which the beam is injected into the accelerator before the rf has fully filled the structures. Fine tuning of the amplitude of the rf in a prescribed fashion after the beam has been injected provides additional control over the energy spread. An energy compression system has been included in the transport line that leads from the end of the linac to the main damping ring to further stabilize the energy and energy spread of injected bunches.

To preserve electron helicity, the spin must be rotated into the vertical direction prior to injection into the damping ring. This is accomplished using superconducting solenoids located in the transport line leading from the end of the booster linac to the entrance of the damping ring. The solenoids are based on those developed for the SLC [10]. Spin rotation is also required after extraction from the damping rings. Emittance dilution due to beam rotation through the solenoids is compensated in the optics design and is therefore not a concern [11].

Development of a polarized rf gun is being pursued at several locations around the world [12,13]. A polarized rf gun offers the promise of improved operations through the reduction in the emittance of beams injected into the $e^-$ main damping ring and simplification of the initial bunching and capture. Such guns may generate less beam halo and subsequently reduce the radiation load at the output of the booster linac and in the damping-ring complex. It is unlikely, however, that a polarized rf gun which meets NLC performance and operational requirements will be demonstrated successfully prior to construction. Once developed, a polarized rf gun could be substituted for the SLC style source of the present design.

## 5.4 Positron Source

The injector positron-source system creates positron beams of the required energy and emittance for injection into the positron damping rings. Positrons are produced by colliding 6.2-GeV electrons into three separate high-Z material targets, capturing the resulting positrons, and accelerating them to the 1.98-GeV energy of the predamping-ring system. Each beam consists of a bunch train of 190 bunches with 0.9 x $10^{10}$ particles that are spaced by 1.4 ns (or 95 bunches with 1.8 x $10^{10}$ particles that are spaced by 2.8 ns). The positrons have an edge emittance of 0.03 m-rad as required by the predamping ring acceptance. Table 5.3 lists the positron beam parameters required for injection into the predamping ring system.

The design of the NLC positron system is based on the system used for the SLC [14], which demonstrated excellent reliability over many years of operation. The total number of positrons required for the NLC bunch train is almost two orders of magnitude greater than the number of positrons in the single SLC bunch. The NLC design goal is to build a target system which is expected to survive a 9-month run (120 Hz, 24 hours per day, 7 days per week, with no scheduled outages for maintenance). Targets can be replaced/repaired annually in a scheduled 3-month maintenance period.

**Table 5.3:** Beam parameters delivered by the positron source system to the positron predamping ring system for the 1.4 and 2.8 ns bunch spacing options.

| PARAMETER NAME | SYMBOL | VALUE | UNITS |
|---|---|---|---|
| Bunch Spacing | $T_b$ | 1.4 (2.8) | ns |
| Energy | E | 1.98 | GeV |
| Energy Adjustability | $\Delta E$ | ±5 | % |
| Bunch Energy Variation | $\delta E/E$ | 1 | % Full Width |
| Single Bunch Energy Spread | $\sigma_{\Delta E/E}$ | 2 | % Full Width |
| Emittance (norm. edge) | $\gamma\varepsilon_{x,y}$ | 0.03 | m-rad |
| Bunch Length | $\sigma_z$ | <10 | mm |
| Particles/Bunch | $n_B$ | 0.9 (1.8) | $10^{10}$ particles |
| Train Population Uniformity | $\Delta n_T/n_T$ | 1 | % Full Width |
| Bunch-to-Bunch Pop. Uniformity | $\Delta n_B/n_B$ | 2 | % rms |
| Number of Bunches | $N_b$ | 190 (95) | # |
| Repetition Rate | f | 120 | Hz |
| Horizontal Beam Jitter | $\Delta\gamma J_x$ | 0.015 | m-rad |
| Vertical Beam Jitter | $\Delta\gamma J_y$ | 0.015 | m-rad |
| Beam Power | $P_b$ | 65 | kW |

Positrons are produced by targeting a 6-GeV electron beam onto tungsten-rhenium (WRe) alloy to create an electromagnetic shower. The positrons produced in the shower are collected using a 5.8-tesla magnetic flux concentrator, accelerated to 250 MeV in structures encased in a 0.5-tesla solenoidal magnetic field, and then injected into an L-band linac and accelerated to 1.98-GeV. The average deposited power is handled by rotating the target and removing the excess heat through water cooling. Of critical concern for target damage is the nearly instantaneous energy deposition per unit volume.

After approximately 1,000 days of operation (~5 calendar years), the SLC positron system failed due to a combination of arcing in the initial rf capture section and increased vacuum activity in the target chamber. Upon examination it was found that a water-to-vacuum leak had occurred in one of the target cooling tubes. In addition, cracking and material ejection were found on the exit face of the target. Analysis of the damaged target was conducted at the CMR hot cell facilities at LANL [15]; thermal hydrodynamic [16] and beam-induced radiation damage simulations [17] have been made for the SLC target operating conditions.

The peak energy deposition in the SLC target was about 35 J/g under the conditions at which the target failed. This level produces a mechanical shock in the WRe target material which is about a factor of two below the expected ultimate tensile strength of pristine material. Material hardening of a factor of about 2 from target entrance to target exit was measured along the beam path. The calculated radiation damage to the material is in excess of 3 dpa (displacements per atom). Target embrittlement and subsequent loss of material integrity are consistent with the calculated exposure level. Aged WRe is expected to fail at the SLC energy deposition level.

Because of the consistency of the observed damage with expectations from the simulations, it has been decided to limit the shock in the NLC targets to that of the SLC system. In particular, the peak energy deposition and irradiation fluences will be kept by design to less than 35 J/g and 1 dpa. Investigations into the connection between radiation damage due to electrons with that from neutron/proton exposure are continuing. It is useful to tap into the data on material property degradation due to neutron/proton damage since the database of electron-induced damage is comparatively limited. Beam tests at SLAC are underway to determine the threshold for material damage and a model of the expected damage is being developed. To date, samples of Ti, Cu, GlidCop, Ni, Ta, W, and WRe have been irradiated in the FFTB area at SLAC. Additional studies will be aimed at developing an optimized target material [18]. Induced damage to candidate target materials will be studied using the E158 beam at SLAC ($5 \times 10^{11} e^{-}$/pulse at 45-GeV, 200-300 ns pulse width, and focusable to small spots).

Positron yield is defined as the number of positrons captured in the predamping ring divided by the number of electrons incident on the target. The NLC has adopted the use of L-band (1.4 GHz) for both the initial 250-MeV capture and 1.75-GeV booster linacs. The larger aperture and longer wavelength of the L-band affords a factor of about 30 increase in acceptance over an S-band system. The design acceptance goal of the combined capture, booster, and predamping-ring systems has been set to 0.03 m-rad. Yield into this acceptance is calculated based on the initial $e^{+}$ distribution, generated using EGS4. In order to keep the peak shock stress in the target below the threshold for damage, three $e^{+}$ targets operating in parallel are required to produce the NLC beam. To assure overall system availability, a layout has been adopted where there are four target/capture modules, three of which are operating at any one time. Access is possible to the fourth target/capture module for maintenance and repair while the other 3 modules are in operation.

A schematic layout of the general features of the 3x4 NLC positron target system is shown in Fig. 5.3. Using an rf deflector, 6.2-GeV electron bunches, incident from the left-hand side of the figure, are separated into three trains . The three trains are directed onto three of the four $e^{+}$ target/capture modules. Each module contains a rotating, water-cooled target and flux concentrator [19] assembly, followed by a 250-MeV L-band linac for capture and initial acceleration. The three streams of 250-MeV positron bunches are combined into the standard NLC bunch format using another rf deflector section. The 250-MeV full bunch train is then accelerated to 1.98 GeV in an L-band linac, situated off the right-hand side of the figure. Shielding of the target vaults is required to permit access to the fourth target region while the other three are in operation. Several different layouts of the 3x4 positron scheme are being considered to optimize both operational efficacy and initial cost. They are all functionally identical. Table 5.4 lists the single target and capture section parameters.

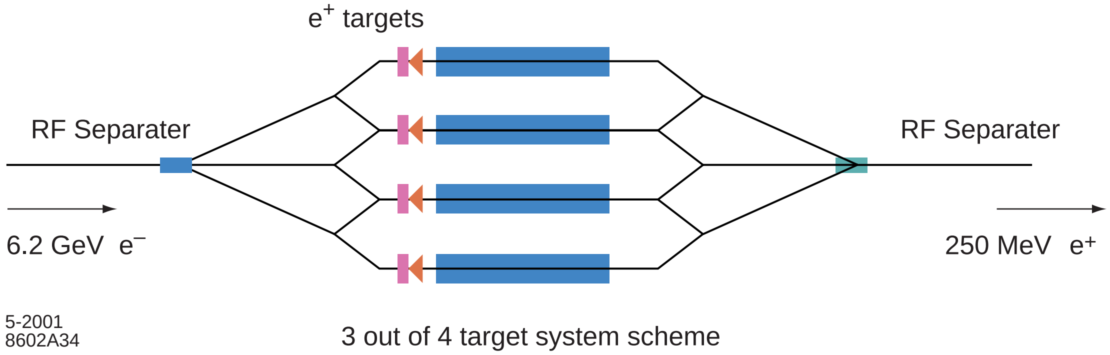

**Figure 5.3:** Schematic of the 3x4 NLC positron target system

**Table 5.4:** NLC Positron Source Parameters of the individual targets, 3 are operated in parallel, for case of 1.4 and 2.8 ns bunch spacing.

| PARAMETER NAME | SYMBOL | VALUE | UNITS |
|---|---|---|---|
| Bunch Spacing | $T_B$ | 1.4 (2.8) | ns |
| | | | |
| **TARGET** | | | |
| Drive Beam Energy | E | 6.2 | GeV |
| Drive Beam Energy Spread | $\Delta E$ | 1 | % full width |
| Electrons/Bunch on Target | $n_B$ | 1.5 (3) | $10^{10}$ particles |
| $e^-$ Bunch-to-Bunch Pop. Uni. | $\Delta n_B/n_B$ | <0.5 | % rms |
| Number of Bunches | $N_B$ | 63 (32) | # |
| Incident Beam Radius | $\sigma_r$ | 1.6 | mm rms |
| Repetition Rate | f | 120 | Hz |
| Drive | $P_b$ | 113 | kW |
| Target Material | | $W_{75}Re_{25}$ | |
| Target Thickness | $L_T$ | 4 | Rad. Length |
| Peak Energy Deposition | $\Delta E/\Delta vol$ | 35 | J/g |
| Absorbed Target Power | $P_T$ | 16 | kW |
| | | | |
| **POSITRON CAPTURE** | | | |
| RF Frequency | $f_{rf}$ | 1428 | MHz |
| Bunch Length | $\Delta T$ | 60 | ps full width |
| Capture Energy | $E_C$ | 250 | MeV |
| Capture Emittance (norm. edge) | $\gamma\varepsilon_{x,y}$ | 0.03 | m-rad |
| Pre-DR Acceptance (norm.) | $\gamma A$ | 0.045 | m-rad |
| Yield@ 250 MeV | $Y_C$ | 1.4 | $e^+/e^-$ |
| Yield@ 1.98 GeV into $\gamma A = 0.03$ m-rad | $Y_{PDR}$ | 0.6 | $e^+/e^-$ |

A 6.2-GeV electron drive beam is used to create the positrons. This system is based on S-band technology. Because of the need to use three quasi-independent target/capture sections for positron production, the electrons will be generated using a photocathode-based source. Fine tuning of the individual electron bunch populations within the drive train is possible through bunch-to-bunch intensity adjustments at the source laser. The unpolarized electron source system is essentially identical to the polarized electron source with the exception that shorter laser wavelengths and photocathodes with higher quantum yields will be used. The parameters of the electron drive beam are listed in Table 5.5.

**Table 5.5:** Drive Linac Electron Beam Parameters

| PARAMETER NAME | SYMBOL | VALUE | UNITS |
|---|---|---|---|
| Bunch Spacing | $T_b$ | 1.4 (2.8) | ns |
| Energy | $E$ | 6.2 | GeV |
| Bunch Energy Variation | $\delta E/E$ | 1 | % Full Width |
| Single Bunch Energy Spread | $\sigma_{\Delta E/E}$ | 1 | % Full Width |
| Emittance (norm. rms) | $\gamma\varepsilon_{x,y}$ | 100.0 | $10^{-6}$ m-rad |
| Bunch Length | $\sigma_z$ | 1.6 | mm |
| Particles/Bunch | $n_B$ | 1.5 (3) | $10^{10}$ particles |
| Train Population Uniformity | $\Delta n_T/n_T$ | 1 | % Full Width |
| Bunch-to-Bunch Pop. Uniformity | $\Delta n_B/n_B$ | 2 | % rms |
| Number of Bunches | $N_b$ | 190 (95) | # |
| Repetition Rate | $f$ | 120 | Hz |
| Horizontal Beam Jitter | $X/\sigma_x$ | 10 | % |
| Vertical Beam Jitter | $Y/\sigma_y$ | 10 | % |
| Beam Power | $P_b$ | 340 | kW |

The present design is a conventional, reasonably well-understood methodology for producing positrons which can be expected to work if properly designed. As discussed in section 5.7, the production of polarized positrons is also being investigated. One outgrowth of these studies will be the development of an alternative unpolarized positron source based on a planar wiggler, similar to the TESLA design, but designed to meet the NLC performance requirements. The initial design will then be compared to the conventional design in regards to the usual metrics of cost, risk, and technical feasibility. A wiggler-based system should eliminate the need for multiple targets, may ease the requirements on the predamping ring, obviates the 6-GeV drive linac, and provides a straightforward upgrade path to polarized positrons. Of principal concern are the logistical issues associated with providing a high-energy electron beam (~150 GeV) and developing an injector commissioning strategy in which initial positron production must await significant progress in the operation of the electron injector and main linac. The installation and commissioning of the conventional positron source are independent of the schedule of the electron systems.

## 5.5 Damping Rings

The NLC damping rings are designed to damp the incoming electron and positron beams to the small emittances needed for collisions. The rings have three purposes: (1) damping the incoming emittances in all three planes; (2) damping incoming transients and providing a stable platform for the downstream portion of the accelerator; and (3), delaying the bunches so that feedforward systems can be used to compensate for charge fluctuations. To meet these goals, three damping rings have been designed: two identical main damping rings, one for the electrons and one for the positrons, and a predamping ring for the positrons [21,22]. The predamping ring is needed because the emittance of the incoming positrons is much larger than that of the electrons. Each damping ring will store multiple trains of bunches at once. At every machine cycle, a single fully damped bunch train is extracted from the ring while a new bunch train is injected. In this manner, each bunch train can be damped for many machine cycles.

The parameters of the two main damping rings are similar to the present generation of synchrotron light sources and the B-Factory colliders in that they must store high-current beams (~ 1 A) while attaining small normalized emittances. Table 5.6 compares the NLC ring parameters with those of the SLAC B-Factory Low-Energy Ring (PEP-II LER), the Advanced Light Source (ALS) at Lawrence Berkeley National Laboratory, and the Accelerator Test Facility (ATF) damping ring at KEK in Japan, which was built to verify many of the damping-ring design concepts. In particular, the stored beam currents are less than half of what the PEP-II LER has achieved, while the emittance, energy, and size of the rings are similar to those of the ALS and the ATF. These other rings have been largely successful in meeting their design parameters, and have been able to test and verify many of the accelerator physics and technology issues that will arise in the NLC damping rings.

**Table 5.6:** Comparison of NLC main damping rings with design parameters of other rings.

| PARAMETER NAME | NLC MDR | PEP-II LER | LBNL ALS | KEK ATF |
|---|---|---|---|---|
| Energy (GeV) | 1.98 | 3.1 | 1.5 | 1.54 |
| Circumference (m) | 300 | 2200 | 197 | 139 |
| Current (A) | 0.8 | 2.16 | 0.4 | 0.6 |
| $\gamma\varepsilon_{x,\text{ equilib.}}$ ($10^{-6}$ m-rad) | 2.17 | 400 | 12 | 4.3 |
| $\gamma\varepsilon_{y,\text{ equilib.}}$ ($10^{-6}$ m-rad) | 0.014 | 12 | 0.12 | 0.03 |

Strong coupled-bunch instabilities have been studied in the high-current B-factories, and have been successfully controlled using broadband, bunch-by-bunch feedback systems. Rapid damping of coupled-bunch motion has been demonstrated in the presence of these feedback systems at the ALS and B-factories, and damping rates in excess of $10^4$ $s^{-1}$ have been observed [23,24,25].

Issues associated with the very small beam emittances, such as intrabeam scattering and ion trapping, continue to be studied in the ALS and ATF [26,27]. A summary of measured parameters for the ATF is shown in Table 5.7, and work continues to improve the performance and diagnostics of that machine. The ATF has achieved a vertical emittance close to that desired in the main damping rings. Experiments have also been performed at low energy (1 GeV) in the ALS, where the measured emittances at 1 x $10^9$ particles are $\gamma\varepsilon_x = 4 \times 10^{-6}$ m-rad and $\gamma\varepsilon_y = 0.07 \times 10^{-6}$ m-rad. These measurements, combined with theoretical modeling, are designed to improve the understanding of the process of intrabeam scattering in electron storage rings, and increase confidence in the predictions for the NLC damping rings.

**Table 5.7:** Achieved beam parameters at the ATF.

| PARAMETER NAME | ACHIEVED |
|---|---|
| Energy (GeV) | 1.28 |
| Bunch population | 1.2 x $10^{10}$ |
| $\gamma\varepsilon_x$ ($10^{-6}$ m-rad) | 3.5 ± 0.75 |
| $\gamma\varepsilon_y$ ($10^{-6}$ m-rad) | 0.038 ± 0.006 |

In addition, the PEP-II LER at SLAC, the KEK-B LER at KEK, and the Advanced Photon Source (APS) at Argonne have studied the photoelectron-positron instability and have had success in controlling and understanding the phenomenon [28]. Simulations based on a simple circular vacuum chamber predict that the threshold for multipactoring occurs at several times the NLC bunch current, and growth times of transverse instabilities driven by the electron cloud are greater than 100 μs and can be controlled with a broadband feedback system. The NLC vacuum-system design includes an antechamber in which synchrotron radiation is absorbed, significantly reducing the number of photoelectrons in the beam duct and further reducing the effects predicted for a simple circular cross section. At this stage it appears unnecessary to coat the aluminum vacuum chambers with low secondary-emission yield materials such as TiN.

The similarities with other rings have also simplified the design process for NLC, and experience at these other accelerators will continue to be applied to benefit the damping-ring designs. For example, the damping ring rf system is based on the higher-order-mode damped cavity designs successfully operating at the SLAC B-Factory and the ATF damping ring; the multibunch feedback systems are based upon the feedback systems successfully verified at the SLAC B-Factory and the ALS, and the vacuum system is similar to that used by the ALS [24,29,30]. Furthermore, the design uses ‘C’ quadrupole and sextupole magnets similar to those used at the ALS and the APS, a high-field permanent-magnet wiggler similar to those in use at third-generation light sources, and a double kicker system for extraction similar to one operational in the ATF. The successful demonstration of these and other systems and components allows a high degree of confidence in achieving the NLC damping-ring parameters.

The NLC damping-ring complex is designed to operate with the parameters listed in Table 5.8. These design parameters exceed the requirements of all presently considered NLC upgrades. The rings produce extracted electron and positron beams with emittances $\gamma\varepsilon_x = 3\text{x}10^{-6}$ m-rad and $\gamma\varepsilon_y = 2\text{x}10^{-8}$ m-rad, at a repetition rate of 120 Hz. Designs have also been developed which allow repetition rates as high as 180 Hz, however in this case the use of two main damping rings per complex is proposed [31]. The beams in the damping rings consist of multiple trains of 190 bunches with an injected single bunch charge of $0.8\text{x}10^{10}$. To provide operational flexibility, the rings have been designed also to accommodate trains of 95 bunches spaced by 2.8 ns with maximum single bunch charge of $1.6\text{x}10^{10}$ in the main rings ($1.8 \text{ x } 10^{10}$ in the predamping ring), and to operate with a peak current roughly 15% higher than the nominal peak current. In addition, the rings have been designed to operate at 1.98-GeV, with an energy range of ±5 %. This will allow the damping rate to be adjusted if necessary.

**Table 5.8:** Requirements for NLC Main Damping Rings.

| **PARAMETER NAME** | **VALUE** |
|---|---|
| $\gamma\varepsilon_{x\ \text{equilib.}}/\gamma\varepsilon_{x\ \text{extract.}}$ ($10^{-6}$ m-rad) | 3.0 / 3.0 |
| $\gamma\varepsilon_{y\ \text{equilib.}}/\gamma\varepsilon_{y\ \text{extract.}}$ ($10^{-6}$ m-rad) | 0.014 / 0.020 |
| Bunches per train | 190 / 95 |
| Bunch spacing (ns) | 1.4 / 2.8 |
| Bunch population | $0.8 \text{ x } 10^{10}$ / $1.6 \text{ x } 10^{10}$ |
| Repetition rate (Hz) | 120 |

At present, most of the studies have concentrated on the main damping rings. Engineering studies have been performed for key systems such as vacuum, damping wigglers, and rf systems, and a good outline of the design and the expected problems has been developed [21]. In particular, the most difficult issues have been identified and solutions described: these are the dynamic aperture, the vertical emittance, the impedance and instabilities, and the stability and jitter in both longitudinal and transverse phase space. As stated, much of the design rests on work performed for operational facilities including the B-factories and the ATF. In most aspects, the predamping ring has relatively loose requirements. The emittance, damping time and beam stability requirements are not severe. The two main challenges are the large dynamic aperture needed and the injection/extraction kicker systems. The design is still in a preliminary stage but these challenges have been addressed.

### 5.5.1 Main Damping Rings

The NLC main damping rings are roughly 300 m in circumference and measure 60 m by 100 m with a nominal energy of 1.98-GeV. The rings are designed in a racetrack form with two arcs separated by straight sections; the layout is illustrated in Fig. 5.4 [32]. The main damping rings are designed to damp beams with injected emittances $\gamma\varepsilon_{x,y} = 1.5\text{x}10^{-4}$ m-rad to extracted beam emittances of $\gamma\varepsilon_x = 3\text{x}10^{-6}$ m-rad and $\gamma\varepsilon_y = 2\text{x}10^{-8}$ m-rad. The rings will operate at 120 Hz. They provide sufficient damping to decrease the injected emittance by four orders of magnitude. These parameters are summarized in Table 5.9 for the main damping rings (MDR), and the positron predamping ring (PPDR). The main damping- ring lattice is based on detuned Theoretical Minimum Emittance (TME) cells utilizing combined-function bending magnets. This lattice type was chosen because of efficiency in generating low emittance and eased requirements on the combined-function bending magnets. The chromaticity is corrected with two families of sextupoles and the dynamic aperture is more than sufficient. The damping is performed using both high-field bending magnets and ten 4.6-meter sections of damping wiggler.

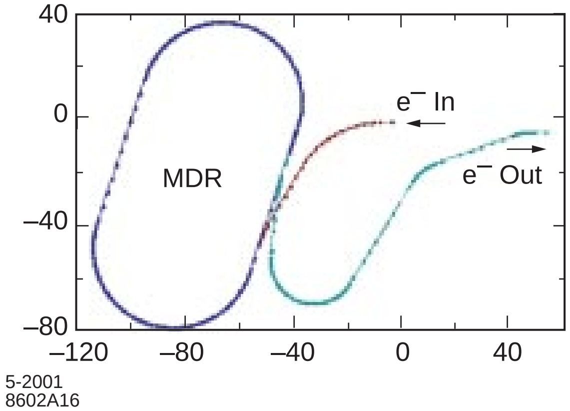

**Figure 5.4:** Layout of main damping ring.

The dynamic aperture is predicted to be in excess of 15 $\sigma_{\text{injected}}$, including effects of errors [32]. Figure 5.5 shows beam survival tracked over 500 turns, including in (b) systematic errors in dipoles, quadrupoles, and sextupoles. Potential limitations due to the contribution from the 46 meters of wiggler magnet have been studied. Analytical expressions of arbitrary three-dimensional wiggler fields have been developed, and tracking including the nonlinear components of the wiggler field will be used to determine the minimum pole width requirement for the 2.15 T hybrid wiggler magnet [33]. Preliminary analysis indicates that the wiggler with a magnet pole width of 11 cm does not seriously degrade the dynamic aperture.

The rings operate with three trains of 190 bunches. The bunch trains are injected onto and extracted from the closed orbit using pulsed kickers and DC septa. To avoid coupled-bunch instabilities, the rf cavities are higher-order-mode damped based on those of the PEP-II B-Factory and a transverse bunch-by-bunch feedback system is used. As stated, the rings are designed to operate with maximum bunch charges of $1.6\text{x}10^{10}$ particles; this is roughly 10% more than the maximum needed at the IP. In addition, the electron source has been designed to provide additional charge to allow for at least 10% losses during injection into the electron damping ring. Similarly, the positron source has been designed to produce at least 20% additional charge to provide for losses during injection into the predamping ring [34].

**Table 5.9:** Parameters for Main Damping Rings and the Predamping Ring.

| **PARAMETER NAME** | **MDR** | **PPDR** |
|---|---|---|
| Circumference (m) | 299.792 | 218.336 |
| Energy (GeV) | 1.98 | 1.98 |
| Max. Current (A) | 0.8 | 0.75 |
| Max. Rep. Rate (Hz) | 120 | 120 |
| Bunch trains x Bunches per train | 3 x 190 | 2 x 190 |
| Train / Bunch separation (ns) | 65 / 1.4 | 65 / 1.4 |
| $\nu_x$, $\nu_y$, $\nu_s$ | 27.26, 11.14, 0.0035 | 8.91, 7.24, 0.031 |
| $\gamma\epsilon_{x\ \mathrm{equilib.}}$ (m-rad) | 2.17 x $10^{-6}$ | 103 x $10^{-6}$ |
| $\gamma\epsilon_{x\ \mathrm{extract.}}$ , $\gamma\epsilon_{y\ \mathrm{extract.}}$ (m-rad) | 2.18 x $10^{-6}$, 0.02 x $10^{-6}$ | 114 x $10^{-6}$, 69 x $10^{-6}$ |
| $\sigma_{\Delta E/E}$, $\sigma_z$ | 0.09 %, 3.6 mm | 0.09 %, 7.2 mm |
| $\xi_{x\ \mathrm{uncorr.}}$, $\xi_{y\ \mathrm{uncorr}}$ | -37.12, -28.24 | -10.39, -12.23 |
| $\tau_x$, $\tau_y$, $\tau_\epsilon$ (ms) | 4.85, 5.09, 2.61 | 4.24, 5.13, 2.87 |
| $U_{sr}$ (kV/turn) | 777 | 561 |
| $\alpha_p$ | 2.95 x $10^{-4}$ | 7.05 x $10^{-3}$ |
| $V_{RF}$, Frequency | 1.07 MV, 714 MHz | 3.4 MV, 714 MHz |
| Lattice | 36 TME cells | 16 TME cells |

Finally, because the rings must generate extremely small beam emittances, there are tight jitter and alignment tolerances. Extensive effort has been made to include cancellations and tuning procedures in the design that will ease the tolerances to reasonable levels. Skew quadrupole windings will be incorporated in sextupole magnets to facilitate coupling correction. Quadrupoles and sextupoles will have independent trim control, and magnet movers will be used to facilitate beam-based alignment .

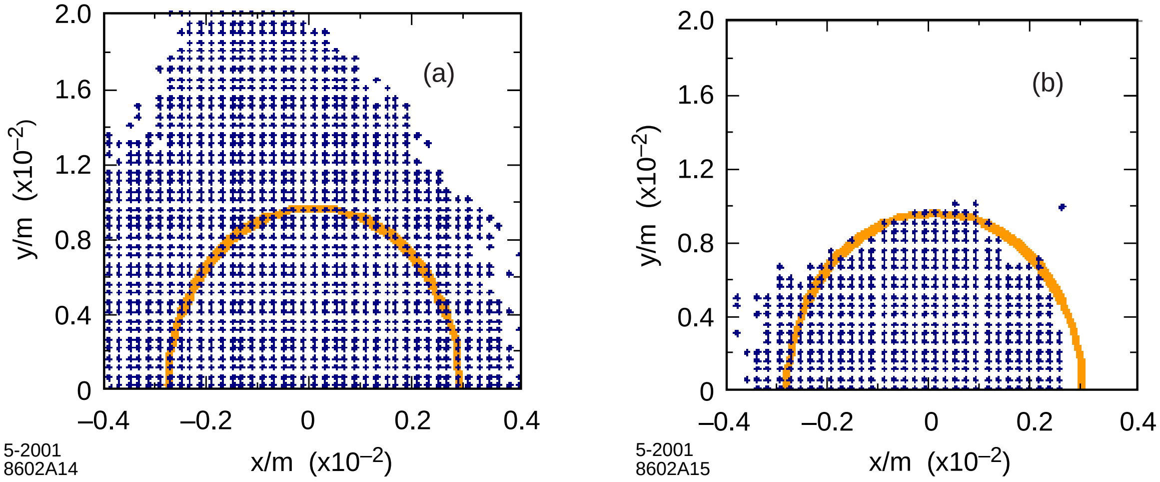

**Figure 5.5:** Dynamic aperture plots a) without errors, b) with combined systematic errors in dipoles, quadrupoles, and sextupoles. The half ellipse shows 15 times the injected beam size.

## 5.5.2 Positron Predamping Ring

The predamping ring has a racetrack form with dispersion-free straight sections for injection and extraction, and damping wigglers of total length roughly 25 m. The ring is roughly 60 meters by 40 meters and is illustrated schematically in Fig. 5.6. In the design, the injection and extraction regions are in the straight sections on opposite sides of the ring. To reduce the requirements on these components, the systems are designed to occupy most of these regions. To minimize rf transients during injection and extraction, a new bunch train will be injected one half turn after a train is extracted. In addition, the rf cavities are placed downstream of the injection kicker and upstream of the extraction kicker so that the injection/extraction process will not interrupt the beam current seen by the cavities.

The positron predamping ring is designed to damp the large emittance beam from the positron source to an emittance of roughly $\gamma\varepsilon_{x,y} = 1.5\text{x}10^{-4}$ m-rad; these parameters are summarized in Table 5.9. The extracted positrons are then injected into the main damping ring where they are damped to the desired final emittances. The predamping ring allows the large aperture requirements for the incoming positron beams to be decoupled from the final emittance requirements of the linear collider. The predamping ring does not need to produce flat beams, so to maximize the damping of the transverse phase space, the ring may operate on the coupling difference resonance. This increases the damping in both the horizontal and vertical planes. Like the main damping ring, the ring damps multiple trains of bunches at once.

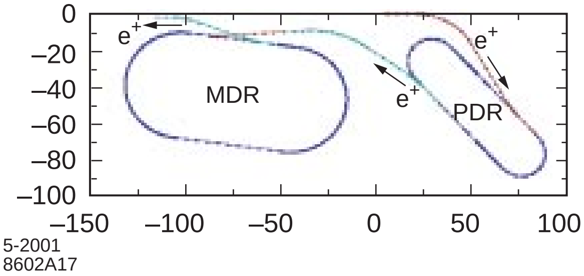

**Figure 5.6:** Layout of the positron damping ring and predamping ring.

The magnets and vacuum systems are designed to provide sufficient aperture to accept a 2-GeV beam with an edge emittance of $\gamma\varepsilon_{x,y} = 0.03$ m-rad and momentum spread of $|\delta p/p| = 1.5\%$ plus betatron-action jitter of $\Delta\gamma\varepsilon_{x,y} = 0.015$ m-rad for misalignments and missteering. Given the nominal injected edge emittance of $\gamma\varepsilon_{x,y} = 0.03$ m-rad, this provides a substantial margin for injection and internal mismatches. In addition, the injector specifications allow significant overhead for injection losses into the predamping ring [34]. The predamping ring is designed to operate with a maximum bunch charge that is roughly 10% greater than the maximum required at the IP. Like the main damping rings, quadrupoles and sextupoles will have independent trim control, and magnet movers will be used to facilitate beam-based alignment as well as matching of the lattice functions, which is especially important in the predamping ring because of the limited aperture.

## 5.5.3 Outstanding issues

Measurements of intrabeam scattering and minimum achievable emittance within the parameter range of the NLC damping rings will continue at the ATF, ALS and other machines. These measurements, combined with theoretical modeling, will improve our understanding of the process of intrabeam scattering, and confidence in predictions for the damping rings. Modifying the electron cloud simulations to include an antechamber will allow an improved estimate of the effect in the positron rings, and ion effects in the electron ring will be studied. Tracking studies using realistic wiggler fields will allow better definition of the pole width requirements to maintain sufficient dynamic aperture in the machine.

A residual vacuum pressure of $10^{-9}$ torr is required to alleviate ion effects. In the arcs, adequate pumping is expected from large ion pumps located directly under discrete photon stops in the antechamber. In the wiggler vacuum chamber, however, distributed pumping may be required to accommodate thermal outgassing in the vacuum chamber which has a large surface area and low conductance at the beam duct. While a design for such a distributed pumping scheme has been developed, improved methods of vacuum chamber fabrication are also being investigated to reduce the surface outgassing rate and avoid the necessity of distributed pumping. Various machining and cleaning techniques are under investigation, and accurate outgassing measurements of samples are being made using apparatus capable of measuring $10^{-12}$ torr l $s^{-1}$ $cm^{-2}$.

## 5.6 Bunch Length Compressors

The NLC bunch compressors [35] must reduce the ~4 mm rms length of the bunches extracted from the damping rings to the 90-140 μm bunch length required for the main linacs and final-focus systems. A two-stage compressor system has been designed where the first stage follows the damping ring and the second stage is at the exit of the S-band prelinac at a beam energy of 8-GeV. Electron and positron bunch-compression systems are identical. The bunch-compressor system has been designed to meet the following additional goals: (1) Expected multibunch phase variations in the damping ring of up to ±5 mm should not produce relative energy variations that are much larger than ±0.1 % in the final-focus systems. (2) The system should include a 180° turn-around arc to permit future main-linac extensions and to allow beam abort and feedforward systems. (3) The transverse emittances must be preserved to within a reasonable budget with diagnostics and correction elements included in the design. (4) The compression systems should not depolarize the beams.

The two-stage system has a number of advantages over a single-stage compressor. In particular, it keeps the rms energy spread less than about 2%; it is optically more straightforward; and the bunch length is more naturally matched to the acceleration rf frequency so that energy spread due to the longitudinal wakefields can be cancelled locally. The disadvantage of the two-stage design is that it is more complex and lengthy than a single-stage compressor. The first stage rotates the longitudinal phase by $\pi/2$ while the second stage performs a $2\pi$ rotation. In this manner, phase errors due to the beam loading in the damping rings and energy errors due to imperfect multibunch energy compensation in the 6-GeV S-band prelinacs do not affect the beam phase at injection into the main linac.

Assuming an rms energy spread of $\sigma_{\Delta E/E} = 1\text{x}10^{-3}$ and rms bunch length of $\sigma_z = 5$ mm, the first stage compresses the damping ring beam to a bunch length of about 500 μm. This stage consists of a 140-MeV L-band (1.4-GHz) rf section followed by a long-period wiggler which generates the momentum compaction, $R_{56}$, needed for the bunch compression. The second bunch-compression stage follows the prelinac. Assuming an rms bunch length of $\sigma_z = 500$ μm, it compresses the beam to a bunch length of 90 μm. This compressor is a telescope in longitudinal phase space which rotates the phase space by $2\pi$. It consists of a 180° arc which is followed by a 600-MeV X-band (11.4-GHz) rf section and a chicane. Adjustments to the low energy compressor rf voltage and wiggler strength permit control of the final bunch length over the specified range of 90-140 μm for fixed settings of the high energy compressor. Figure 5.7 illustrates the layout of the NLC bunch compression system. Beam parameters are listed in Table 5.10.

One of the driving philosophies behind the NLC compressor design has been to utilize naturally achromatic magnetic lattices wherever the beam energy spread is large. In particular, the optics is chosen so that quadrupoles are not placed in regions of large dispersion and strong sextupoles are not needed. This choice arises from experience with the SLC bunch compressors [36] which were based on second-order achromats in which quadrupoles are located in dispersive regions and strong sextupoles are used to cancel the chromatic aberrations. Unfortunately, the SLC design was difficult to operate and tune because of large nonlinearities and sensitivity to multipole errors in the quadrupoles; over the years, additional nonlinear elements were added (skew sextupoles and octupoles) to help cancel the residual aberrations but tuning remained problematic. To facilitate tuning, orthogonal tuning controls and diagnostics have been explicitly designed into the NLC system, making the system relatively straightforward to operate.

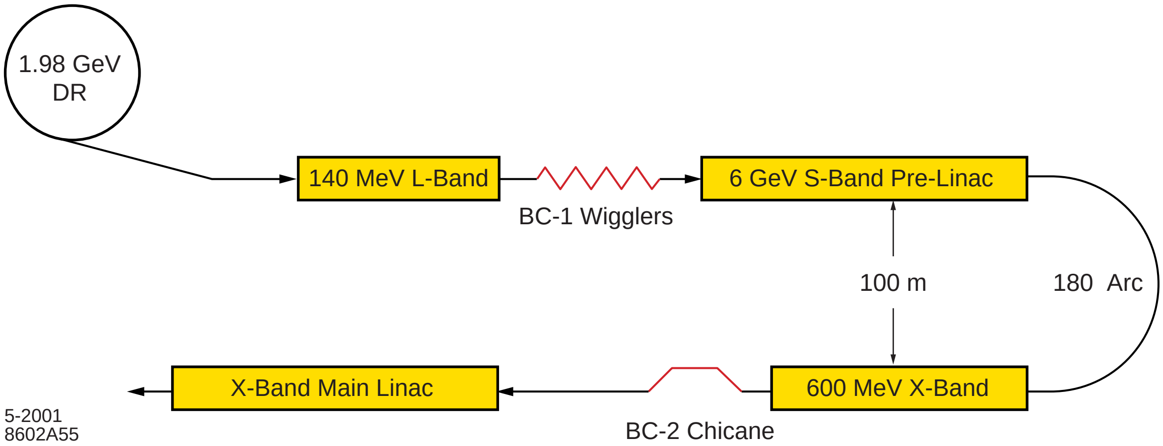

**Figure 5.7:** The NLC two-stage bunch length compression system. The first stage of compression consists of an L-band rf section followed by a dipole wiggler, operating and 1.98- GeV. The second stage of compression includes the 6-GeV prelinac, 180° turn-around arc, a 600-MeV X-band rf section and a dipole chicane. Beam diagnostics are included to permit full tune-up and control.

As discussed, the rf acceleration in the first-stage compressor system is performed with relatively low frequency L-band rf (1.4 GHz). Although this system is, in general, more expensive than higher frequency rf, it has a larger acceptance which is needed at the lower beam energy. In particular, the system has been designed to have small beam loading and relatively loose alignment tolerances. This is important to provide the desired reliability and stability. Finally, although the tolerances on components in the bunch compressor systems are not nearly as tight as in the main linacs or the final-focus systems, the same methods of beam-based alignment and tuning have been adopted. In particular, to ease the alignment procedures, all of the quadrupoles will be mounted on magnet movers. In addition, each quadrupole will contain a BPM with a resolution of 1 μm. Similarly, all of the accelerator structures will be instrumented with rf BPMs to measure the induced dipole modes and each girder will be remotely movable for minimization of wakefields.

**Table 5.10:** Input and Output Beam Parameters of the BC-1 and BC-2 Systems.

| PARAMETER NAME | SYMBOL | INPUT | VALUE | UNIT |
|---|---|---|---|---|
| | | | | |
| **BUNCH COMPRESSOR 1** | | | | |
| Energy | E | 1.98 | 1.98 | GeV |
| Single Bunch Energy Spread | $\sigma_{\Delta E/E}$ | 0.2 | 2 | % Full Width |
| Bunch Length | $\sigma_z$ | 5 | 0.5 | mm, rms |
| | | | | |
| **BUNCH COMPRESSOR 2** | | | | |
| Energy | E | 8 | 8 | GeV |
| Single Bunch Energy Spread | $\sigma_{\Delta E/E}$ | 0.5 | 3.2 | % Full Width |
| Bunch Length | $\sigma_z$ | 500 | 90-150 | μm, rms |

As noted in section 5.2, there are presently two layout scenarios under consideration for the NLC injector systems. Concerning the issue of bunch length compression, it should be noted that a centralized injector requires more bending through the beam turn-arounds than a remote injector. Since arc momentum compaction and synchrotron radiation emittance dilution depend on the absolute value of the net bend angle, the arc cell design has a different optimal configuration [35]. A methodology has been developed to minimize overall system costs while meeting the design goals. Designs for both layouts meet the NLC bunch-compression requirements.

## 5.7 Polarized Positrons

The only practical way to produce polarized positrons for a linear collider is through pair creation using circularly polarized photons. In principle, positrons can be polarized in a storage ring but the rate of polarization build-up is relatively low, making the storage time required prohibitively long. For pair creation, the required energy of the photons falls in the range of 10-60 MeV. There are three candidate methods for producing circularly polarized photons, generation through bremsstrahlung from polarized electrons [37], production from Compton backscattering of polarized laser photons off an unpolarized electron beam [38], and emission of polarized photons from a high-energy electron beam in a helical undulator [39]. The first method has low estimated conversion efficiencies and is not a primary candidate. The remaining two methods, Compton based and undulator based, both have significant technical issues to be resolved.

For Compton generation of polarized photons, extremely intense laser beams are required. On the other hand, the requirements on the electron beams are relatively modest; the energy of the electrons is in the range of several GeV. Furthermore, the helicity of the positrons is easily flipped on a pulse-to-pulse basis by switching the sign of the incident laser photon polarization. This ability to randomly and rapidly change the positron helicity is of significant interest to the experimenters. For undulator-based photon generation, present designs require high-energy, low-emittance electrons. The emittance requirements prevent the utilization of the post-collision, disrupted electron beam. The energy of the electron drive beam is 150 GeV or above for undulator periods in the range of a centimeter. Use of the undulator precludes rapid changes in the helicity of the positrons. The JLC has developed a design for polarized positrons based on Compton production [40]. TESLA has developed a design which uses an undulator [20]. Requirements for the photon conversion to polarized positrons and subsequent selective collection of the most energetic positrons for maximum polarization are essentially the same in both designs.

NLC is presently studying both options, which would ultimately lead to a design similar to one of the existing design proposals. The present plan for the NLC efforts are to reproduce the existing JLC and TESLA design studies as a means of developing the necessary tools and expertise. This effort is initially concentrated on understanding the conversion and collection of positrons. This will result in a projection of photon-to-polarized- positron yield captured by a predamping ring. The yield calculation allows the specification of the required number of incident photons, which drives the requirements on the methods of photon production. Figure 5.8 shows a possible layout for an NLC polarized positron system which is based on a helical undulator. In Fig. 5.8, a dedicated electron beam for photon production is produced through doubling the repetition rate of the first part of the electron main linac and sending it through an undulator. Possible alternatives include using the colliding electron beam which could be extracted from the main linac at an energy of about 150 GeV, passed through an undulator and reinjected into the main linac for further acceleration and transport to the IP.

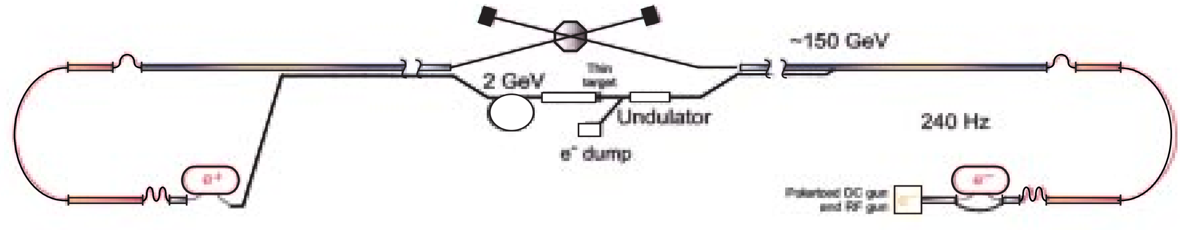

**Figure 5.8:** An undulator-based source of polarized positrons using a separate high energy electron beam.

## 5.8 Present Activities and Future Plans

The thrust of the present R&D and design activities fall into three broad categories: (1) improving the technical foundation of the NLC injector systems design through feasibility demonstrations, technology reviews, and augmented system simulations; (2) developing alternate schemes to assure the realizability of the designs; and (3), investigating the feasibility of novel options which improve either the operability or capability of the overall design. As discussed above, it is a goal of the R&D effort to demonstrate the full NLC polarized electron charge and current density. It is important to determine the maximum, survivable energy deposition in an NLC positron target. Demonstration of the NLC damped beam emittances and improved experimental understanding of damping-ring collective effects are priorities.

The present design of the positron generation system is based on limiting the peak energy deposition and integrated fluences in the targets to the level of the SLC positron target. Ongoing research is aimed at developing better target material and at improving the understanding of fatigue and radiation damage in a positron target. Although not presently included in the injector design, considerable thought and effort are going into the studies on the feasibility and efficacy of polarized rf guns and sources of polarized positrons. Because of the considerable work to be done in the development of both of these systems, neither are presently included as part of the present design configuration. The current design does not preclude the future adoption of either or both systems into the NLC complex at a later time.

Many of the requirements and systems needed to achieve the NLC damping-ring parameters have been demonstrated in other rings, such as the B-factories, the ALS, and the ATF. Additional experiments and theoretical studies are planned to further understand and predict behavior in the damping rings and through the extraction system. Investigations are focused on intrabeam scattering, electron cloud and ion driven instabilities, dynamic aperture limitations, extraction system stability, and vacuum systems technologies.

## References

[1] Alley, R., et al., “The Stanford Linear Accelerator Polarized Electron Source,” *Nucl. Instr. and Meth.*, **A365**:1-27, 1995 (also SLAC-PUB-6489, March 1995).

[2] Krejcik, P., et al., ‘Recent Improvements in the SLC Positron System Performance,” *Proc. 3rd EPAC*, Berlin, 1992 (also SLAC-PUB-5786, March 1992).

[3] Bane, K. and Li, Z., “Dipole Detuning in the Injector Linacs of the NLC,” LCC-0043, July 2000.

[4] Allen M.A., et al., “Performance of the SLAC Linear Collider Klystrons,” Proc. PAC 1987, Washington, D.C., 1987 (also SLAC-PUB-4262, March 1987).

[5] Nakanishi, T., et al., “Highly Polarized Electron Source Development in Japan,” *1st APAC 1998*, Tsukuba, Japan, March 1998.

[6] Mulhollan, G.A., et al*.*, “Photovoltage Effects in Photoemission from Thin GaAS Layers,” *Phys. Lett*. **A282**:309-318, 2001 (also SLAC-PUB-8753, Mar 2001).

[7] Togawa, T., et al., “Production of Polarized Electron Beam with Sub-nanosecond Multibunch Structure from Superlattice Photocathode,” *Nucl. Instr. and Meth.* **A455** 118, 2000.

[8] PPRC Private Communication, May 2001.

[9] Matsumoto, H., et al*.*, “High Power Test of a SLED System with Dual Side Wall Coupling Irises for Linear Colliders,” *Nucl. Instr. and Meth*. **A330** 1, 1993 ( also KEK-PREPRINT-92-179, January 1993).

[10] Blockus, D., et al., “Proposal for Polarization at the SLC,” SLAC-PROPOSAL-SLC-UPGRADE-01 (1986).

[11] Emma, P., “A Spin Rotator System for the NLC,” NLC-Note-7, December 1994.

[12] Aleksandrov, A.V., et al., “Experimental Study of GaAs Photocathode Performance in RF Gun,” *Proc. PAC 1999*, New York, N.Y. 1999.

[13] Aulenbacher, K., et al., “RF Guns and the Production of Polarized Electrons,” CERN-CLIC-NOTE-303, SLAC-NLC-NOTE-20, May 1996.

[14] Krejcik, P., et al., ‘Recent Improvements in the SLC Positron System Performance,” *Proc. 3rd EPAC*, Berlin, 1992 (also SLAC-PUB-5786, March 1992).

[15] Maloy, S., et al., “SLC Target Analysis,” LANL LA-UR-01-1913, June 2001.

[16] Stein, W., *“*Thermal Shock Structural Analyses of the SLC Positron Target,*”* Lawrence Livermore National Laboratory, Livermore, California, UCRL-PRES-142893, April 24, 2001.

[17] Caturla, M., Private Communication, May 2001.

[18] Sunwoo, A., et al., “Characterization of Virgin W-Re Material,” Lawrence Livermore National Laboratory, UCRL-PRES143841, April 24, 2001.

[19] Kulikov, A.V., et al., “SLC Positron Source Pulsed Flux Concentrator,” *Proc. PAC 1991*, San Francisco, CA, 1991 (also SLAC-PUB-5473 June 1991).

[20] Bialowons, W., et al., “Conceptual Design of a 500 GeV e+e- Linear Collider with Integrated X-ray Laser Facility (Tesla Design Report),” DESY 1997-048, May 1997, 416 ff.

[21] Corlett, J.N., et al., “The Next Linear Collider Damping Ring Complex,” *Proc. PAC 2001*, Chicago, 2001.

[22] Wolski, A. and Corlett, J.N., "The Next Linear Collider Damping Ring Lattices," *Proc. PAC 2001*, Chicago, 2001.

[23] Fox, J., et al., "Multi-bunch Instability Diagnostics via Digital Feedback Systems at PEP-II, DAFNE, ALS, and SPEAR," *Proc. PAC 1999*, New York, 1999.

[24] Barry, W., et al., "Operational Experience with the PEP-II Transverse Coupled-Bunch Feedback Systems," *Proc. PAC 1999*, New York, 1999.

[25] Byrd, J.M. and Barry, W., "Controlling the Vertical Mode Coupling Instability with Feedback in the Advanced Light Source," *Proc. PAC 1997*, Vancouver, 1997.

[26] Urakawa, J., et al., "Experimental Results and Technical Research and Development at ATF (KEK)," *Proc. EPAC 2000*, Vienna, Austria, 2000.

[27] Corlett, J.N., et al., "Measurements of Intra-Beam Scattering at Low Emittance in the Advanced Light Source," *Proc. HEACC 2001*, Tsukuba, Japan, 2001.

[28] Furman, M., et al., "Electron-Cloud Measurements and Simulations for the APS," *Proc. PAC 2001*, Chicago, 2001.

[29] Rimmer, R.A., et al., "RF cavity R&D at LBNL for the NLC Damping Rings, FY1999," CBP Tech Note 196, LCC-0033, LBNL, Berkeley, November 1999.

[30] "1-2 GeV Synchrotron Radiation Source," PUB-5172, LBNL, Berkeley, 1986.

[31] Wolski, A., "Improved Dynamics in the 180 Hz NLC Damping Rings," CBP Tech Note 223, LCC-0055, LBNL, Berkeley, 2001.

[32] Wolski, A., "Lattice Description for NLC Main Damping Rings at 120 Hz," CBP Tech Note 227, LCC-0061, LBNL, Berkeley, 2001.

[33] Wolski, A., "Symplectic Integrators for Nonlinear Wiggler Fields," CBP Tech Note 228, LCC-0062, LBNL, Berkeley, 2001.

[34] Sheppard, J.C., et al., "Update on the NLC Injector System Design," *Proc. PAC 2001*, Chicago, 2001.

[35] Emma, P., "Cost and Performance Optimization of the NLC Bunch Compressor Systems," LCC-0021, August 1999.

[36] Adolphsen, C. et al., "Chromatic Correction in the SLC Bunch Compressors," *Proc. PAC 1991*, 503-505, May 1991 (also SLAC-PUB-5584, June 1991).

[37] Potylitsin, A.P., "Production of Polarized Positrons through Interaction of Longitudinally Polarized Electrons with Thin Targets," *Nucl. Inst. and Meth.* **A398,** 395, 1997.

[38] Hirose, T., et al., "Generation of Polarized Positrons via Laser-Compton Scattering at the KEK Damping Ring," *1st APAC 1998*, Tsukuba, Japan, March 1998.

[39] Mikhailichenko, A.A., "Use of Undulators at High Energy to Produce Polarized Positrons, *Proc. Workshop on New Kinds of Positron Sources for Linear Colliders*, SLAC Report 502, 1997.

[40] Hirose, T., et al., "Polarized Positron Source for a Linear Collider, JLC," *Nucl. Instr. and Meth.* **A455**, 2000.

# Chapter 6

## The Beam Delivery System

### 6.1 Introduction

At the end of the NLC main linacs, the electron and positron beams have reached their final energy and have typical RMS sizes of 10 μm by 1 μm. The purpose of the beam delivery system (BDS) is to reduce the beams to the sizes required to produce luminosity, remove any particles that are far enough from the beam core to produce unacceptable detector backgrounds, and ensure that the extremely small beams do in fact, collide at the IP. In addition, the BDS must provide protection for the detector and beamline components against missteered beams emerging from the main linacs, and must safely transport the collided beams to water-cooled dumps which can absorb the high beam power density without damage. Finally, the BDS must provide instrumentation that can monitor the parameters of the collided beams, such as the energy spread and polarization after collision, which are required by the particle physics experiments. The four main subsystems of the beam delivery, in order from upstream to downstream, are: the collimation system, which provides protection from errant beams and removes particles which might cause backgrounds; the final focus (FF), which reduces the beam size; the interaction region (IR), which provides detector masking and specialized supports for the final doublet quadrupoles of the final focus; and the extraction line, which transports the spent beams to their respective dumps and provides the post-collision beam measurements.

The beam delivery system is conceptually similar to the low-beta insertion of a colliding-beam storage ring. Because the BDS pushes many of the parameters of a low-beta region to an extreme, its design and implementation are extremely challenging. The horizontal and vertical betatron functions at the IP ($\beta^*_{xy}$ = 8 x 0.1 mm for 500-GeV cms) are much smaller than those in a storage ring (for example, the PEP-II design betatron functions are 500 x 20 mm). Because the $\beta^*$ values are so small, the variation of focusing strength with particle momentum, or *chromaticity*, is much larger than in a storage ring and the cancellation of the chromaticity with nonlinear elements must be accomplished with much greater precision. The strong sextupoles which are used to cancel the chromaticity introduce additional high-order aberrations which would enlarge the beam size or reduce the bandwidth of the BDS if not addressed.

Several other issues constrain the design of the BDS. Because the beams at the interaction point (IP) are extremely small, $\sigma^*_{x,y}$ = 245 x 2.7 nm, the beams must collide head-on to within a few nanometers to maintain adequate luminosity. This in turn implies that any source of beam-beam jitter must be strictly limited. The beam-beam focusing at the IP is extremely intense because of the high charge density, which causes the quality of the spent beams to be poor. The energy spread and angular divergence of the outgoing beams at the IP are both large, and a significant fraction of the beam power is converted to photons in the collision. The number of particles in the beam 'halo' which are far from the core and can cause backgrounds can potentially be quite large in a linear collider. Collimators placed near the beam to intercept the halo particles can be damaged or destroyed by the high beam power density of the core if the beam is inadvertently steered onto a collimator.

Although the parameters of the NLC BDS are far beyond anything that has been achieved in a storage ring, the Stanford Linear Collider (SLC) [1] demonstrated the viability of a fully-integrated linear collider beam delivery system with millimeter-sized betatron functions and routine collision of beams with rms sizes of under 1 μm. The Final Focus Test Beam (FFTB) [2] at SLAC was a single-beam demonstration of a linear-collider beam delivery system with IP betatron functions comparable to the NLC; vertical beam sizes of 70 nm were routinely achieved. The NLC BDS design is based upon experience from these two facilities. In addition, a vigorous R&D program on passive and active magnet position stabilization, ground motion, materials damage thresholds, and instabilities driven by collimators close to the beam have all yielded insights which have been incorporated into the design of the system. In all particulars, therefore, the NLC BDS design is based upon the performance of previous accelerator systems or the results of R&D.

In the remainder of this chapter, the design of the NLC Final Focus and the SLC and FFTB results relevant to the Final Focus are presented, followed by the status of the collimation system design, the chosen layout for incorporation of all the components, and the possibility of constructing a beam delivery system engineering test facility.

## 6.2 Final Focus

As described in the Introduction, the role of the final focus is to reduce the size of the beam at the IP sufficiently to provide the required luminosity. Because of the relatively low collision rate of the NLC – one bunch train each of electrons and positrons is delivered every 8.3 milliseconds – the beams must be reduced to extraordinarily small sizes. RMS beam sizes at the IP of 245 nm (x) by 2.7 nm (y) are required to achieve luminosity of $2 \times 10^{34}$ $cm^{-2}s^{-1}$ at 500-GeV cms. The small beam sizes are achieved by generating beams with small normalized emittances – 3.0 x 0.02 mm-mrad – which are preserved throughout the injector, main linac, and BDS regions, and by using strong quadrupole magnets at the end of the final focus to reduce $\beta^*_{xy}$ to 8 x 0.1 mm.

The challenges for the final-focus design are fourfold. First, the final focus, like other parts of the NLC, must minimize emittance dilution due to misalignments, errors of beam line components, and synchrotron radiation. Second, the final doublet quadrupoles which generate the small $\beta^*$ values introduce a large energy-dependent focusing, or chromaticity, which must be corrected. Otherwise, the finite energy spread of the beam would cause the beam size at the IP to be much larger than that expected, given the emittances and betatron functions. Third, the aberrations that are typically introduced by the nonlinear elements that correct the chromaticity must be minimized. Fourth, the very small beams at the IP must be kept in collision with one another; a motion of one beam relative to the other of a few nanometers is sufficient to measurably reduce the luminosity.

### 6.2.1 Correcting the Chromaticity

Correcting the chromaticity of the final doublet is the issue that drives the rest of the design. In the final-focus systems used at the SLC and the FFTB, which were also the basis of the 1996 ZDR final-focus design, the chromaticity correction was accomplished in dedicated ‘chromaticity correction sections.’ In these sections, a combination of bend magnets and sextupoles generated a chromaticity equal-and-opposite to that of the final doublet. The primary design limitation in these systems was that the energy loss from synchrotron radiation between the last sextupole and the IP had to be minimized, to avoid causing a breakdown of the chromaticity correction. Because of this requirement the bending magnets were weak, and the final focus was correspondingly long.

The ZDR design called for a 1.8-km-long final focus that was capable of handling up to 750-GeV beams, but that would need to be over 3 km long for 2500-GeV beams. In the present design [3], this limitation is addressed by interleaving the chromatic correction sextupoles with the final doublet quadrupoles. This configuration requires a horizontal dispersion through the final doublet, which is tuned to be exactly zero at the IP; the large dispersion in the strong doublet quads introduces additional aberrations that must be cancelled. Nonetheless, the resulting configuration is both simpler and shorter than previous final-focus systems: less than 0.4 km is required for 750-GeV beams and 0.8 km will handle 2500-GeV beams. A schematic of the present design concept is shown in Fig. 6.1, and a plot of the optical functions is shown in Fig. 6.2. The energy reach of the final focus is shown in Fig. 6.3.

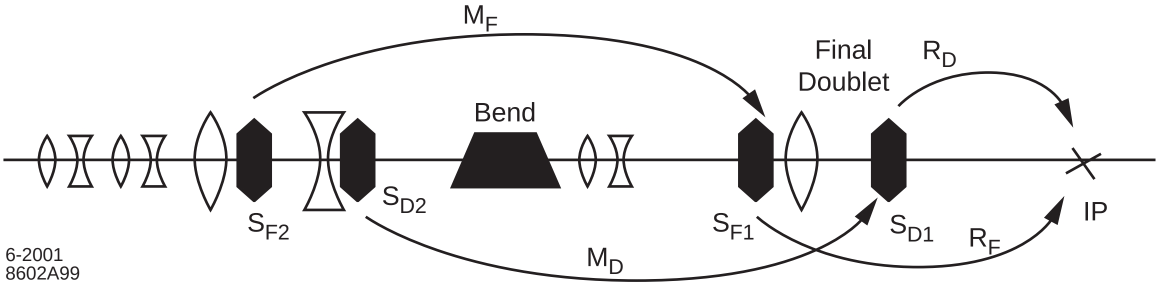

**Figure 6.1:** Schematic design of the current NLC FF.

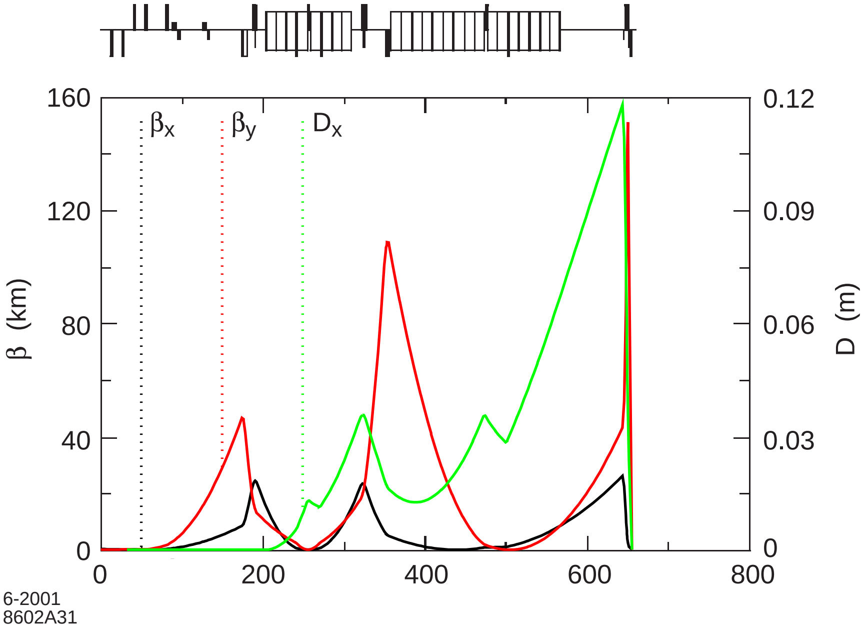

**Figure 6.2:** Optics of the NLC FF.

### 6.2.2 Additional Aberrations

Once the chromaticity of the final focus is corrected, the principal aberration to be cancelled is generated by the sextupoles that are required for chromaticity correction. This is accomplished by placing additional sextupoles in the beamline, with optical transformations between sextupoles which cause the geometric aberrations of the sextupoles to cancel while the chromatic aberrations remain, as shown in Fig. 6.1. In the SLC and FFTB, each of the sextupoles in a matched pair contributed 50% of the chromaticity correction. The combined effect of the chromaticities of the sextupoles, the quads between the sextupoles, the quads between the last sextupole and the final doublet, and the doublet chromaticity caused these designs to provide correct focusing for only a narrow range of particle energies. A more recent design by Oide [4] ameliorated this limitation by generating as much of the chromaticity correction as possible in the sextupoles closest to the IP, rather than splitting it equally among the pairs of sextupoles in a given family. The present design of the NLC final focus combines an extreme form of Oide's asymmetric-chromaticity solution with placing the chromaticity correction sextupoles in the final doublet itself. The combination of these features minimizes the chromatic aberrations of traditional final-focus systems. Fig. 6.4 shows the luminosity as a function of fractional energy error for the ZDR and present NLC final-focus designs. The performance of the two is comparable, but the new system's performance is a smoother function of energy, indicating weaker chromatic aberrations. Another valuable attribute of the system is that off-energy particles tend to have small amplitudes in the final doublet magnet, whereas traditional final-focus systems tend to drive off-energy particles to very large amplitudes in the final doublet. This is shown in Fig. 6.5.

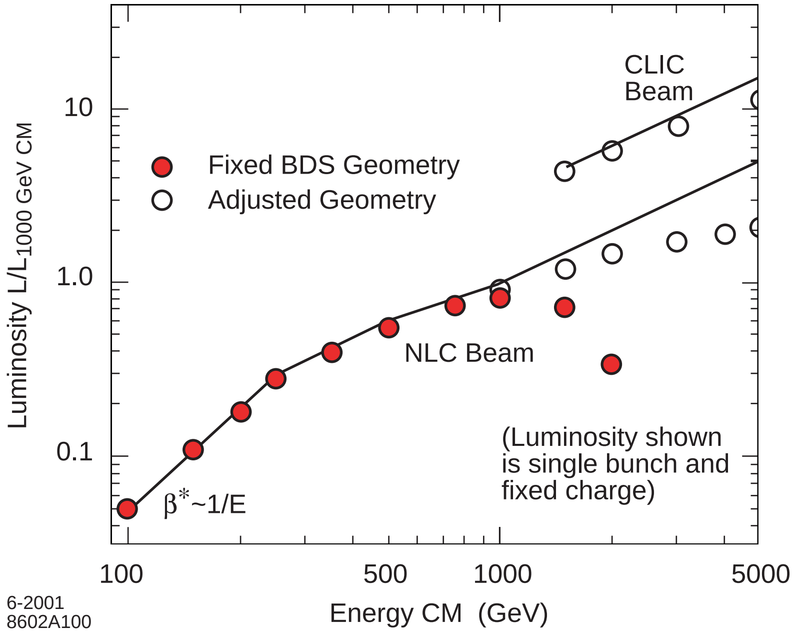

**Figure 6.3:** Energy reach of the NLC final focus. The present system, with under 1 km total length per side, can accommodate center-of-mass energies up to 5 TeV. Because of synchrotron radiation effects, the bending angles in the final focus must be reduced for CM energies above 1 TeV. Also shown is the luminosity if the normalized emittance delivered by the injector can be reduced at higher energies, as assumed in some studies of multi-TeV linear colliders.

### 6.2.3 Jitter and Emittance Dilution Tolerances

A critical issue for all NLC beamlines is whether or not the tolerances that must be kept are realistic. The most severe tolerances are magnet alignment and position stability. Magnet field quality and power supply stability tolerances are also important, but in general these tolerances are comparable to those achieved at the FFTB. Figure 6.6 shows the magnet position drift and position jitter tolerances for the NLC FF. The difference between 'drift' and 'jitter' is one of effect: drift tolerances are the tolerances which must be held to maintain small beam spots, while jitter tolerances are the ones which relate to maintaining collisions of the very small beams at the IP. Although the tolerances in Fig. 6.6 are small, it is important to note that these are so-called 'bare' tolerances – tolerances in the absence of feedback systems or other noninvasive correction algorithms which can stabilize accelerator performance. Understanding the real performance of the final focus requires simulation studies that include the planned diagnostic and correction systems, and their algorithms. This is discussed in greater detail in Chapter 7, but a few key examples are considered here.

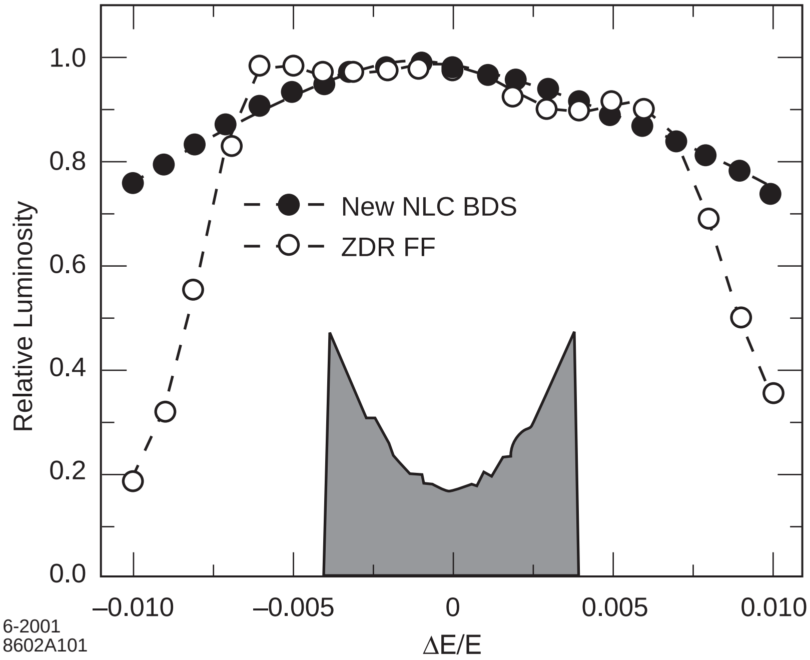

**Figure 6.4:** Energy bandwidth of the FF at the IP. Both ZDR-era and present final focus designs are shown. The natural energy distribution of the beam from the NLC main linac is also shown.

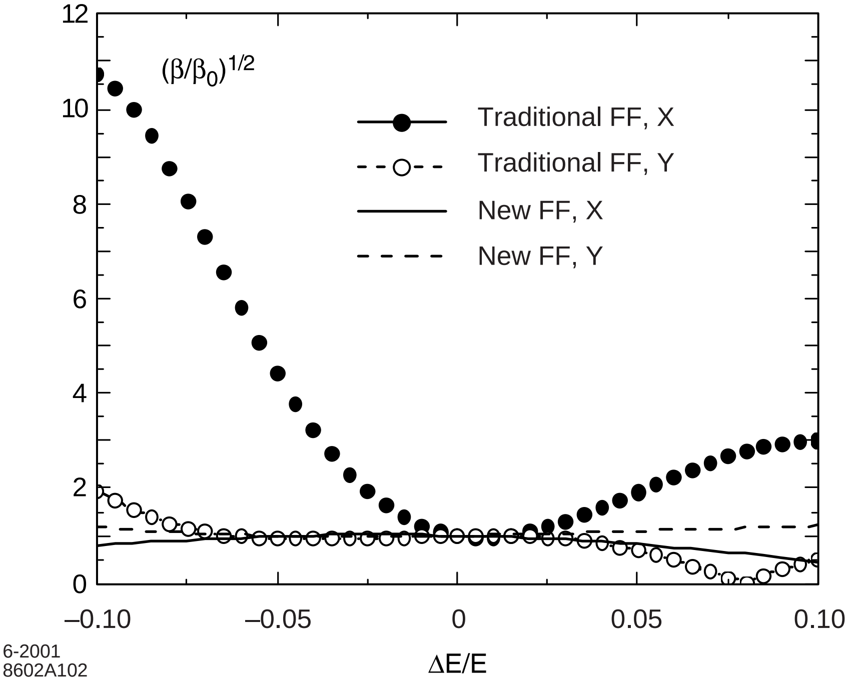

**Figure 6.5:** Energy bandwidth of the FF at the final doublet.

**Drift Tolerance and Performance:** One of the most serious potential sources of emittance dilution is beam line magnet misalignments driven by diffusive ground motion. Figure 6.7 is the result of a simulation that misaligns the elements of the 1-TeV cms NLC BDS configuration according to the 'ATL law,' which describes the effect of this ground motion. Here the mean-squared relative motion of two elements is proportional to the product of the distance between the points (L) and the time that has ensued (T). The constant A varies with the local geology and for this simulation is assumed to be 5x10$^{-7}$ µm$^2$/m/s, which is the ATL coefficient derived from recent ground-motion measurements at SLAC. The curves show that luminosity would degrade under ATL motion in approximately 2 minutes if only the beam-beam deflection collision stabilization feedback was present. If in addition orbit control feedback is allowed to steer the beam through the centers of critical quadrupole and sextupole magnets, the time for luminosity degradation increases to approximately 1 day. Finally, if direct optimization of the main aberrations via global knobs is added to the system, the luminosity lifetime increases to several months, after which a disruptive realignment procedure would be required.

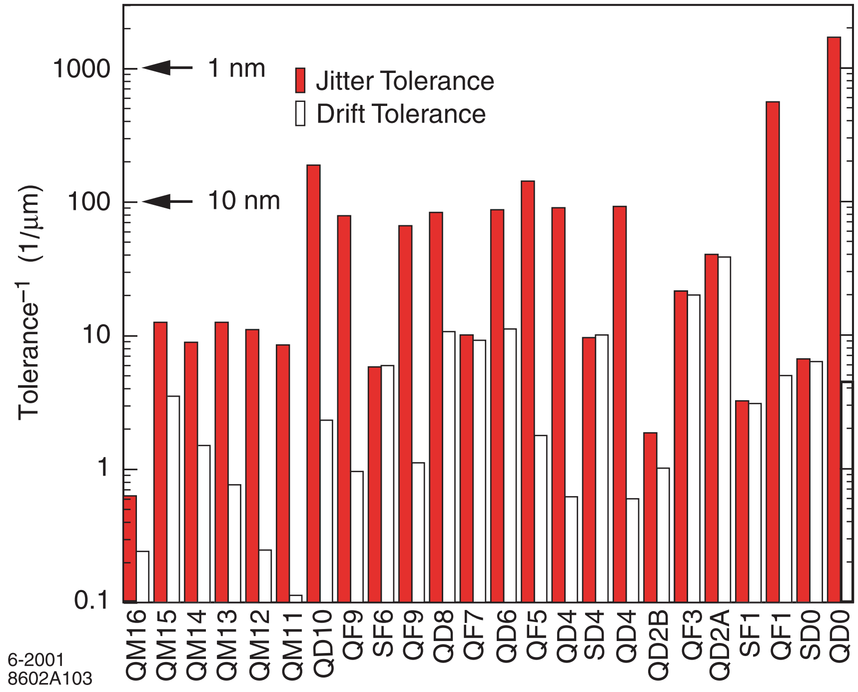

**Figure 6.6:** Magnet position jitter and drift tolerance of the NLC FF. 'Jitter' tolerance relates to the magnet's capacity to steer beams out of collision at the IP, while 'drift' refers to the magnet's capacity to cause the beams at the IP to be too large. Reciprocal tolerances are shown, so in this case bigger is worse. Note the large jitter sensitivity of the final doublet magnets QF1 and QD0.

**Jitter Tolerance and Performance.** Figure 6.6 shows that typical jitter tolerances in the final focus are on the order of 10 nm. Although such tolerances are tight, the situation is not as grave as might naively be expected. In particular, the tolerances in Fig. 6.6 are for incoherent motion of the magnets. The sensitivity of the luminosity to correlated motion is much smaller. As discussed in Chapter 7, the natural characteristics of ground motion are that low-frequency motion, which typically accounts for hundreds of nanometers of rms motion, is highly coherent, while high-frequency motion, which is nearly incoherent, accounts for only a few nanometers of motion. This means that if the magnets are supported in such a way that their motion is identical to the motion of the underlying ground, the luminosity loss from jitter of the quads upstream of the final doublet will be only a few percent. In section 6.2.4, a proof-of-principle magnet support which achieves this goal is discussed. Thus, the tight jitter tolerances of the magnets upstream of the final doublet are not considered a serious limitation on the performance of the final focus.

As Fig. 6.6 shows, the jitter tolerances of the final doublet quadrupoles, QD0 and QF1, are roughly an order of magnitude tighter than those in the rest of the final focus. The final doublet quads are the only ones in the NLC that cannot meet their tolerances through passive stabilization. An additional constraint on the doublet magnets is that they must be mounted within the detector, as shown in Fig. 6.8. Jitter suppression for these magnets must include a combination of passive and active methods. Passive methods include locating the IR hall sufficiently far from cultural sources of vibration, minimizing potential vibration sources under NLC control through proper engineering, and engineering to ensure the detector, magnet technology, and doublet support girders are stable and do not amplify motion. There are R&D programs in active vibration suppression technologies in three different areas: measurement of motion through optical interferometers or accelerometers; active motion control at the nanometer level using piezoelectric or electrostatic movers; and a high-bandwidth beam-based feedback that can correct beam-beam offsets within a single bunch train. It is expected that a combination of passive and active magnet stabilization technologies will provide the jitter control required in the final doublet, and that the high-bandwidth feedback can provide an additional margin of safety and protection against small step-function changes in the accelerator.

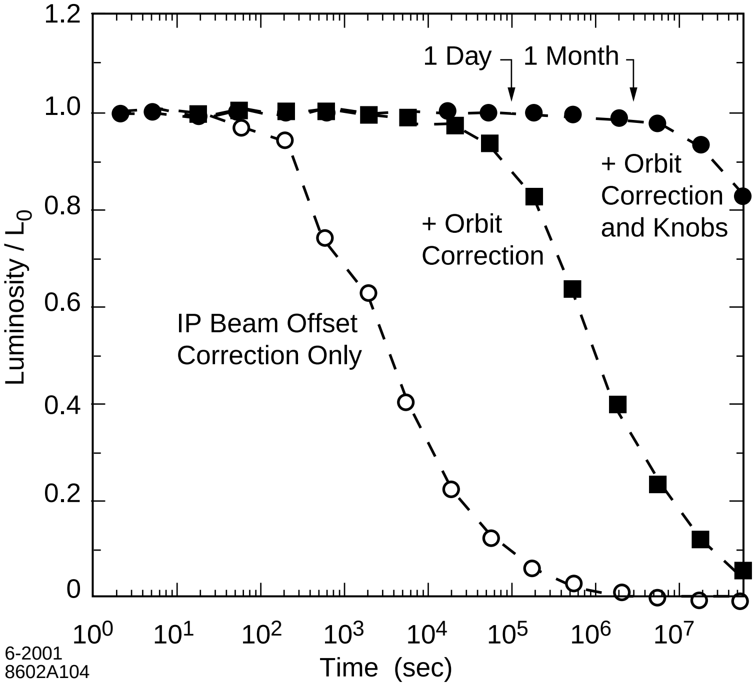

**Figure 6.7:** Degradation of alignment under ATL ground motion with IP beam-beam deflection based feedback only, with orbit feedback added, and with direct luminosity optimization added.

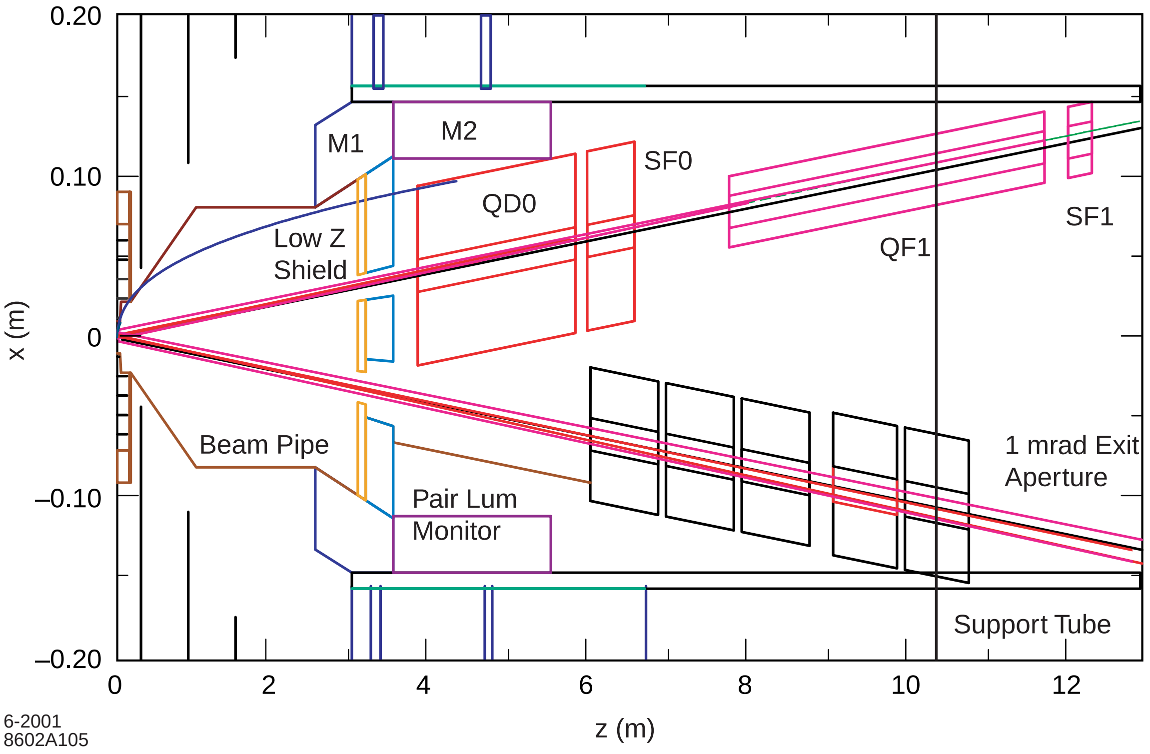

**Figure 6.8:** The IR layout for the NLC Large Detector.

### 6.2.4 FFTB and SLC Experience

The Final Focus Test Beam (FFTB) was a linear collider final focus scaled to the SLAC 47-GeV beams. The FFTB was designed to generate $\beta^*$ values of 10 x 0.1 mm, almost identical to the design values of the NLC. Given the normalized emittances available from the SLAC linac, this would result in rms beam sizes of 1.7 μm by approximately 45 nm at the IP. This would provide a test of the optics designs, tuning techniques, and diagnostic and correction hardware required for the NLC final focus. The actual measurement of a 40-50 nm rms vertical spot size in the FFTB was complicated by both linac-induced incoming beam jitter and the experimental limitations of the laser-interferometer beam size monitor. Figure 6.9 shows the rms vertical beam spot size as measured, with a mean value of 70 ± 1.5 nm. When the beam emittance, betatron functions, jitter between beam and laser interferometer, and the estimated effects of limited tuning precision are folded in, the expected beam size was 58 ± 8 nm, 1.5 σ from that observed.

Each quadrupole and sextupole in the FFTB was mounted on a magnet mover system based on rotating eccentric cams capable of adjusting its position in 300-nm step sizes. Each quadrupole also incorporated a BPM with 1 μm resolution. These sat upon Anocast magnet supports grouted solidly to the sandstone underlying the FFTB tunnel floor. The magnet alignment procedure relied upon beam measurements to achieve a precision beyond the capabilities of conventional surveying and mechanical alignment techniques. Figure 6.10 shows that the alignment resolution achieved was 1-10 μm with the decrease in precision at the end of the beam line due to the lack of BPMs further downstream. Chapter 7 will discuss how this procedure, using movers with a smaller step size of 50 nm and BPMs with 300 nm resolution, will be used to align the NLC linac quadrupoles to a tolerance of 2.5 μm.

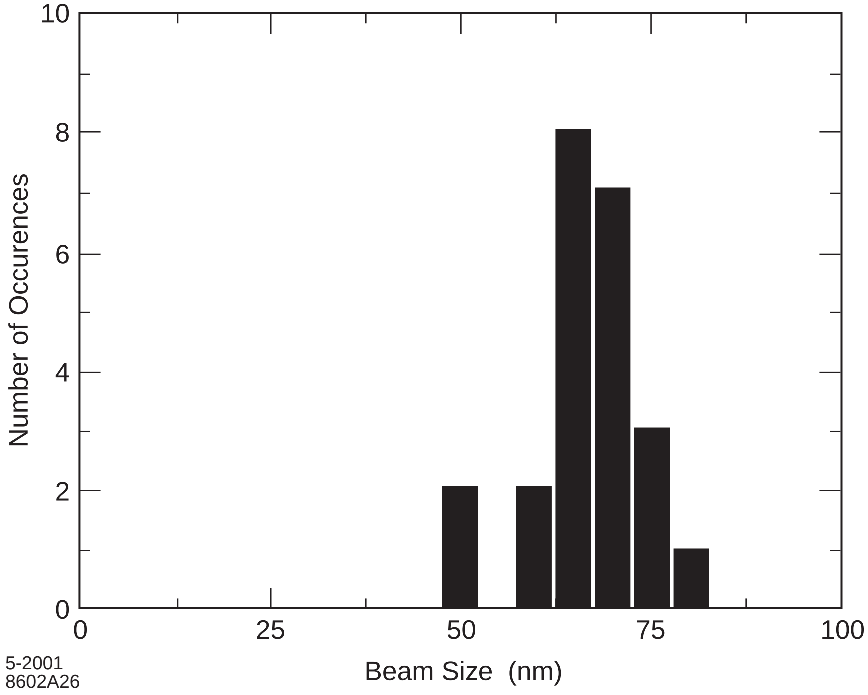

**Figure 6.9:** Spot size measurements at the FFTB.

Many of the engineering issues relevant to stable operation of the FF were investigated at FFTB. Tunnel temperature variation, airflow, and the impact of vibrations caused by flowing magnet-cooling water are examples. Figure 6.11 shows the integrated power spectra of geophones, one of which was mounted on the tunnel floor, and one atop a typical fully powered FFTB quadrupole with cooling water flowing, along with the difference between the magnet motion and the motion of the nearby ground. Above the 3 Hz signal-to-noise cutoff of the geophones used in this measurement there are only 2 nm of relative motion. The performance of the FFTB magnet supports is quite close to that required for NLC quadrupoles.

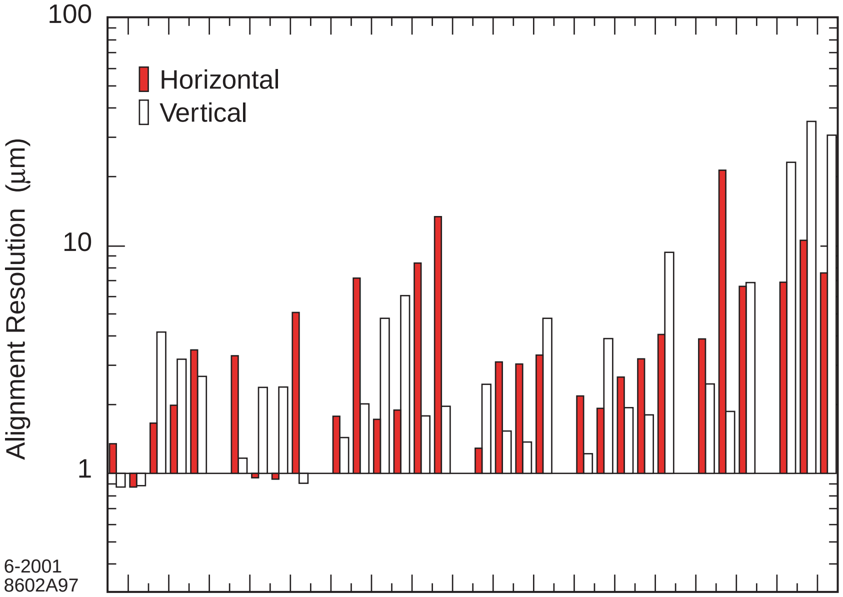

**Figure 6.10:** The horizontal and vertical alignment precision of quadrupoles in the FFTB after beam-based alignment.

The Stanford Linear Collider (SLC) was the first linear collider, and it operated at the energy of the $Z^0$ boson from 1989 through 1998. The SLC is to date the only facility that routinely collided submicron beams and demonstrated the integrated operation of all the components of a linear collider. Figure 6.12 shows the reconstructed vertical position of $Z^0 \rightarrow$ hadron events recorded by the SLD vertex detector over a period of approximately 10 days in 1997. The $Z^0$ events are binned in groups of 30 and the mean $y$ for the group plotted versus time of day. The luminous region for the SLC is approximately 0.5 μm in vertical extent, and Fig. 6.12 shows that over the course of 1 day its vertical position varies by 40 times this distance. Nonetheless, the collision steering feedback keeps the beams centered on each other, and other feedback systems to control the trajectory and optimize the luminosity maintain a steady Z production rate over the entire period.

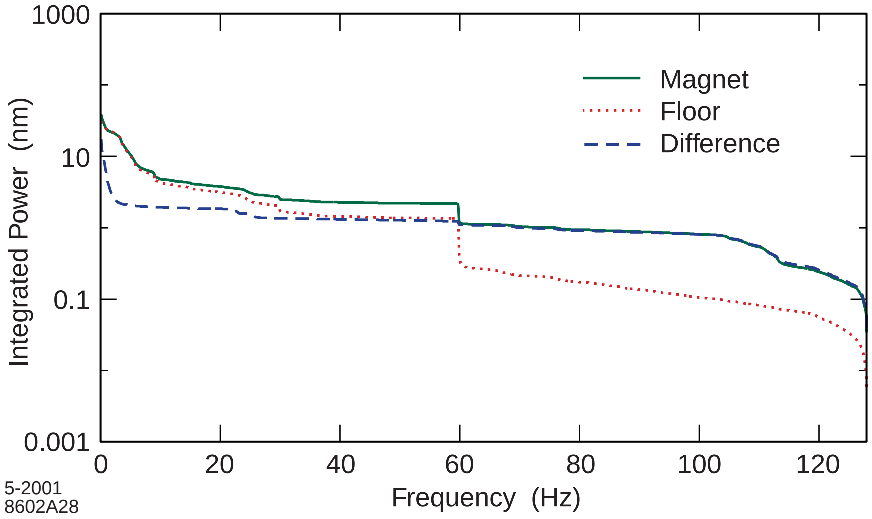

**Figure 6.11:** Integrated power spectrum from the vibration of a fully powered FFTB quadrupole with cooling water running. The additional rms motion of the magnet with respect to the tunnel floor is 2 nm.

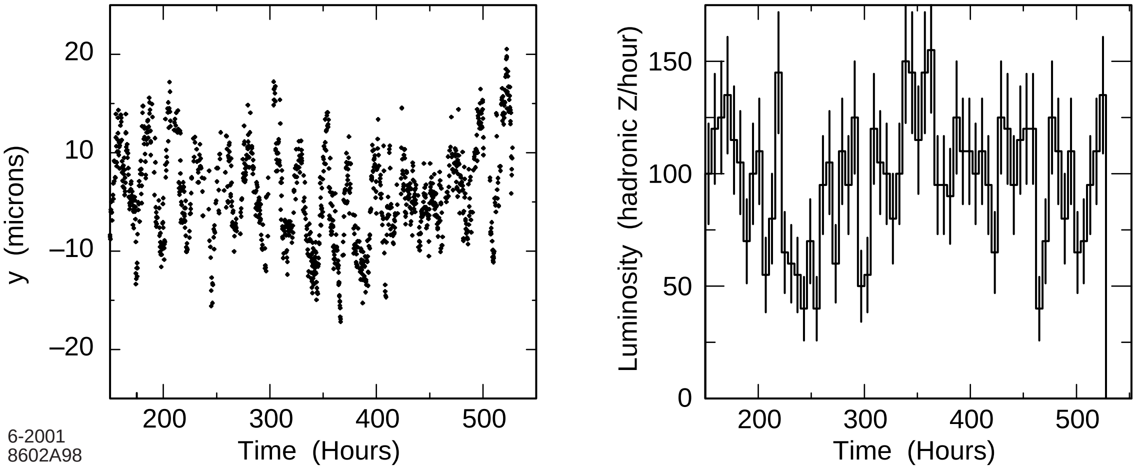

**Figure 6.12:** Average reconstructed vertical position of $Z^0 \rightarrow$ hadron events in the SLD and the measured SLC luminosity over a 10-day period.

## 6.3 Collimation System

The level of backgrounds the SLD detector could tolerate often limited luminosity at the SLC. It is well understood that the backgrounds were due to synchrotron radiation (SR) photons, produced by the beam halo in the final lens system, hitting masks near the IP. Ray tracing studies of the NLC final focus have shown that this is a potentially serious source of backgrounds for the Linear Collider Detector (LCD) as well. Because of the very high beam energy at NLC, the SR photons generated in the final doublet tend to have high energies as well, which makes it untenable to use masking in the IR to shield the detector from these SR photons. Consequently, the NLC collimation aperture is determined by the maximum amplitude with which a particle can pass through the final doublet without emitting SR photons that hit the detector. According to tracking studies, particles which pass through the IP with horizontal angles under 240 microradians, and vertical angles under 1000 microradians, will not produce SR backgrounds in the final doublet. Note that these limits are significantly tighter than would be required to protect the final doublet vacuum chamber from direct impact of primary particles; the SR envelope sets the collimation aperture, not the beam-pipe radius.

Collimation of the NLC beam requires putting material very close to beams with high energy density, which in turn creates a risk that a missteered beam might destroy the collimator. Indeed, protection of the detector from such a beam is a secondary function of the BDS collimation system. In principle, the collimators can be protected from damage by enlarging the beam's transverse dimensions at the collimator locations, but this requires an optics which is itself chromatic and can generate more halo particles. In practice, in order to limit the betatron functions in the collimation region, the design relies on thin (0.25-0.5 radiation length) devices called spoilers which scrape the halo and which, if accidentally struck by the full power beam, will enlarge the spot size via multiple coulomb scattering. The scattered halo and enlarged beam are then stopped on thick (20 radiation length) absorbers. Although the damage threshold of the spoilers is considerably higher than that of the absorbers, the design outlined above still requires an enlarged beam size at the spoiler location if the spoiler itself is to survive damage from an errant bunch train. An additional concern is that spoilers close to the beam may introduce transverse wakefield deflections which would unacceptably degrade the beam quality at the IP.

The number of particles that may be absorbed by the collimation system, and the efficiency with which they are stopped, are both determined by the production and transport of muon secondaries from the collimation process. Simulation studies have shown that as many as $10^9$ primary electrons or positrons per train can be removed by the collimation system without producing an unacceptable muon flux in the detector, although this number depends somewhat upon the exact configuration of the beam line. The number of primary particles that can be stopped close to the detector without unacceptable muon production is only $10^4$.

Based on the considerations above, the requirements of the collimation system can be elucidated. The collimation system optical design must enlarge the beam sufficiently to allow the placement of enough survivable collimation devices to reduce the halo by 5 orders of magnitude. It should allow for potentially frequent off-energy beam trains and occasional orbit variations from equipment failure or operator error. The design must not require tolerances that might lead to emittance growth or collimation apertures so small that their wakefields induce unacceptable beam jitter. The collimators themselves must be made of materials thin enough or robust enough to withstand both the constant beam halo and the occasionally errant beam pulse. Their surfaces must have sufficient smoothness, low enough resistivity, and be shaped so as to produce minimal wakefields. The mechanism that controls the collimator jaw placement must provide adequate control of the gap and its alignment.

### 6.3.1 Collimation System Design

The design of the NLC collimation system has evolved significantly since the 1996 ZDR. At that time the system required a 2.5-km-long beamline to enlarge the beam envelope to such large values that the spoiler systems that removed the beam halo could be guaranteed to survive the occasional errant beam pulse. This requirement put very challenging tolerances on both jitter and the betatron phase matching of certain magnets.

The collimator system currently in the baseline design consists of an upstream energy collimation, based on a dogleg bend and accommodating the linac tune-up beam dump, followed by a betatron collimation system. Because klystron trips causing off-energy beams may be relatively frequent events, and can occur with only microseconds of warning, the energy collimators are designed to be capable of surviving contact with a bunch train. The system combines a large horizontal dispersion and a large vertical betatron function to ensure that the transverse size of beam pulses at the 0.5 radiation length spoilers is large enough that the charge density is below the damage threshold. Multiple coulomb scattering in the spoiler further increases the beam size before the pulse is stopped in an absorber downstream. The betatron collimation system downstream scrapes the beam halo and provides machine protection against infrequent orbit disruption of on-energy beams. Based on the SLC experience, very few of these events are expected to occur in each run. A lattice with more relaxed tolerances has been designed that uses as its basis the concept of 'consumable spoilers.' These are cylindrical spoilers or scrapers that can be rotated to present a clean surface to the beam if damaged by an errant pulse. Their circumference is such that approximately 1000 damaging pulses can be permitted before replacement is necessary. Tracking studies indicate that this system gives the 5 orders of magnitude of halo reduction required.

A recent development in the collimation system is the use of octupole doublets which permit the beam halo in one betatron phase to be reduced in amplitude, while leaving the beam core nearly unaffected. A pair of these doublets has been shown to reduce the halo in the critical final doublet betatron phase by a factor of 4, which in turn would permit equivalently larger collimator apertures in that phase, as shown in Fig. 6.13. This would also dramatically decrease the impact of collimator wakefields, as the wakefields are believed to scale with the inverse square of the gap size. Future modifications to the lattice are under study which integrate the collimation into the final focus, exploiting the increased energy bandwidth and dynamic aperture of the current final focus and also permitting straightforward chromatic correction of the collimation system. These developments suggest that the collimation system will ultimately no longer be a concern, from the point of view of BDS performance.

### 6.3.2 Spoiler Design

The concept of consumable spoilers was introduced in the previous section. Although the use of thin spoilers to enhance protection of downstream components has been used in some limited applications in existing accelerators, the NLC collimation application is unique in many aspects. The NLC spoilers have tight positioning accuracy tolerances, the gap size and gap-center position must be maintained when the spoiler surface is advanced after damage has occurred, and the transverse wakefields from the spoilers must be acceptably small. A further complication is that the NLC spoiler must operate reliably under high vacuum and in a high-radiation environment. Because of these issues, the collimation system spoiler has been the subject of a substantial research program [5].

There are four elements in the baseline design R&D program. The first is the fabrication of a prototype consumable spoiler to investigate the engineering challenge of providing accurately aligned surfaces in a piece of moving machinery that must operate under vacuum. A configuration in which each collimator jaw is a rotating wheel has been selected due to its overall compactness. Figure 6.14 shows a photograph of the prototype device, a drawing to schematically indicate how it operates, and a plot showing, as an example, its ±15 μm gap width stability under rotation. This prototype has pointed the way to minor design modifications and demonstrated that collimation devices of this type can be incorporated reliably into any final system design.

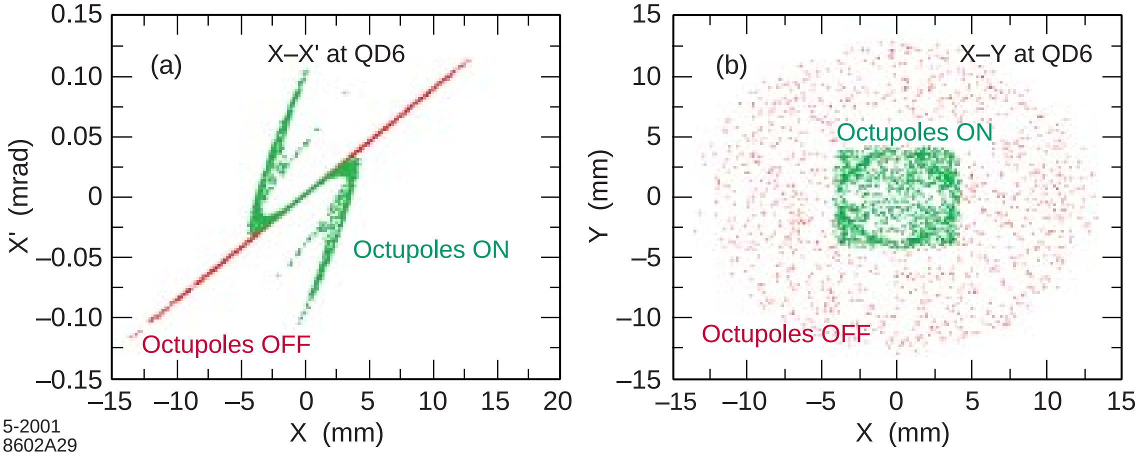

(a) (b)

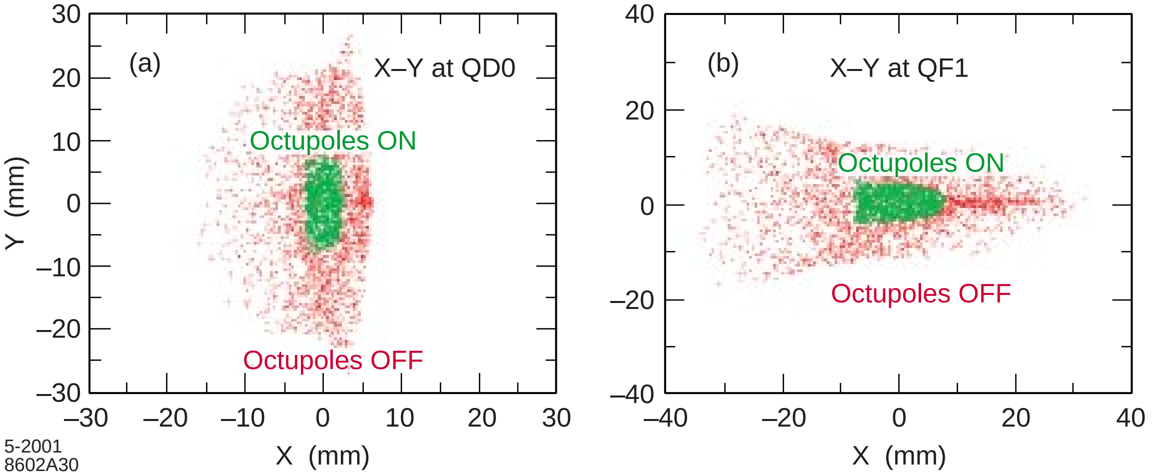

(c) (d)

**Figure 6.13:** Simulation of tail folding by means of two octupole doublets in the new NLC final focus. The top figures show the phase space after a drift following the octupole doublets. The bottom figures show the beam distribution in the final doublet. The input beam has a flat distribution with half width (X, X', Y, Y') = (14mm, 1.2mrad, 0.63mm, 5.2 mrad) in IP units and ±2% energy spread. This corresponds to approximately (65, 65, 230, 230) sigma with respect to the nominal NLC beam.

The second R&D effort is an attempt to use solidifying liquid metal as the basis of a collimator design. In this scheme, the collimator wheel would pass through a bath of liquid metal where it is coated by a thin layer that is pressed onto it by a second roller. The material studies phase of this project is finished and a proof-of-principle prototype has been built based on niobium and molybdenum wheels with tin as the liquid metal. The prototype has yielded very smooth surfaces and pointed out a number of design challenges. If successful, such a collimator could be put so close to the beam that it is damaged by beam image current heating at every pulse and yet be constantly rotated and repaired. Such a collimator would technically be ‘renewable’ rather than ‘consumable,’ and would provide more options for lattice design that could potentially further reduce the required tolerances.

The third element of the collimator R&D effort is a series of beam damage experiments [6]. Samples of various materials have been exposed to single shots of 30-GeV beam of 3-20 x $10^9$ electrons with rms transverse areas of 50-200 $\mu m^2$ at FFTB. The samples were then inspected to understand the resulting damage. To date, thin samples of copper, nickel, titanium, and tungsten-rhenium alloy have been tested. The tests have indicated that, for targets which are less than 1 radiation length in thickness, the damage threshold which is calculated by naively equating the thermal expansion stress of the material to its yield stress is a considerable underestimate of the instantaneous heating which the materials can tolerate. This is believed to be due to the fact that in thin targets the heated material is not fully constrained, and so the thermal expansion stress can be relieved by the heated material ‘bulging’ from the front and back surface of the target. Further tests of samples that more completely approximate an NLC spoiler are planned.

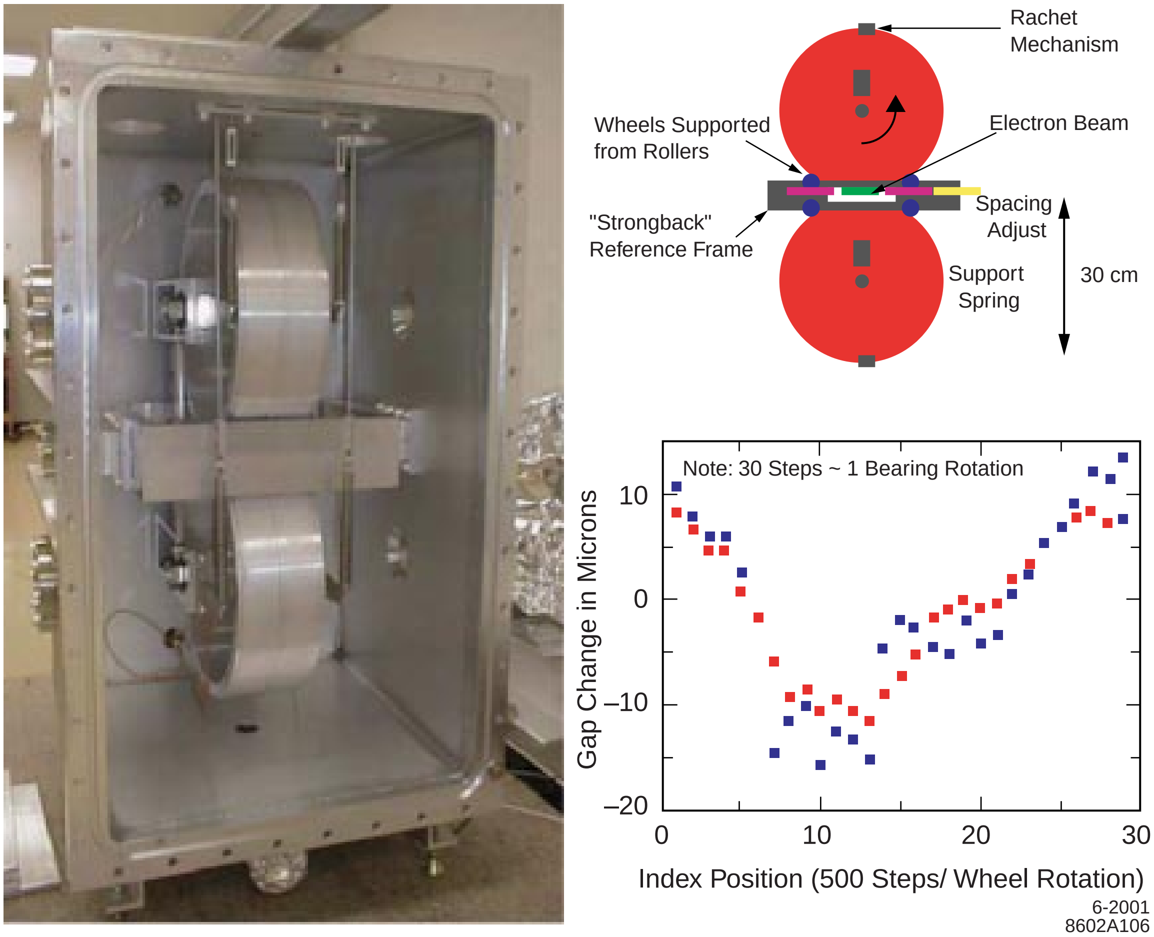

**Figure 6.14:** Rotating consumable collimator prototype.

The fourth element of the collimation system R & D effort is a series of experiments [7] meant to fully explore the impact of collimator wakefields. In the baseline collimation lattice the collimator gaps are on the order of 200 µm x 200 µm. Wakefield effects due to collimator shape, resistivity or smoothness may produce enough jitter amplification to adversely impact luminosity. A first set of measurements has been performed on a set of tapered copper collimator jaws to study the geometric wakefield of such objects. A moveable vacuum enclosure holding four collimator samples plus a standard large-diameter round beam pipe has been installed at the SLAC linac near the ASSET test area. The wakefield kick applied to the beam is measured by BPM arrays as a function of beam location for each collimator and the results compared to analytic and numerical estimates. Figure 6.15 shows the elevation and beam's eye view of the first set of four samples tested along with an example of data taken.

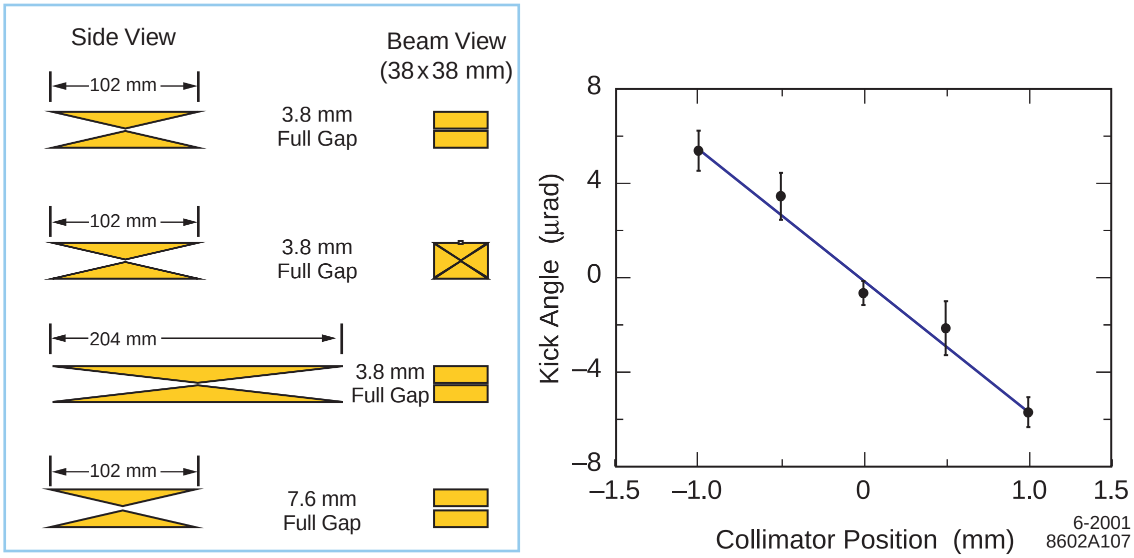

**Figure 6.15:** Collimator Wakefield Experiment results.

Table 6.1 compares the measurement results with analytic theory and simulations. When this series of experiments was originally planned, the only analytic theory available was that labeled 'long taper' in Table 6.1. The results are all much smaller than these predictions and the discrepancy has led to the development of an additional theoretical model applicable in the short taper regime. Both the collimators used in the tests and the eventual NLC collimators will probably fall in between the regions of applicability of the two models and theoretical work to bridge the gap is ongoing. Future tests will focus on the resistivity of the collimator material, where graphite and titanium samples will be compared against copper, and on surface roughness.

**Table 6.1:** Comparison of Collimator Wakefield Experiments with Theory and Simulation.

| SHAPE | ANGLE rad | GAP mm | THEORY SHORT TAPER | THEORY LONG TAPER | MAFIA SIM | ABCI SIM | EXPERIMENT |
|---|---|---|---|---|---|---|---|
| Flat | 0.168 | 3.8 | 6.7 | 30 | 2.3 | - | 3.34 ± 0.31 |
| Square | 0.335 | 3.8 | 13.4 | 3.7 | - | 5.6 | 3.72 ± 0.29 |
| Flat | 0.335 | 3.8 | 6.7 | 58 | 3.1-3.8 | - | 3.72 ± 0.29 |
| Flat | 0.298 | 7.6 | 1.7 | 13 | 1.0 | - | 1.44 ± 0.14 |

## 6.4 Layout

As described in Chapter 2, a final-focus system operates effectively without modification over roughly a factor of four in beam energy. Its length is determined by the highest anticipated operating energy, since the bend magnets in the lattice must be sufficiently weak to limit SR luminosity loss to a few percent. Above the maximum design energy, the emittance growth is proportional to $E^4$ and the luminosity falls accordingly. At lower energies the geometric emittance increases, and this causes the beam size in the magnet apertures to increase. Below some minimum energy, the IP beta function must be increased to limit the beam size in the magnet apertures, and the luminosity falls as $E^2$. Because of the new approach to chromaticity correction described in section 6.2, the final focus is very compact relative to previous designs and scales gracefully to much higher energies. By leaving approximately 800 m of tunnel for the FF, the design can handle center-of-mass energies of up to 5 TeV. Such high energies can only be accommodated in the NLC if other sources of SR luminosity degradation are minimized. Conversely, a final focus which is designed for 500 GeV cms can be as little as 350 meters long and can tolerate substantially more bending over all than a final focus which is designed to accommodate 5 TeV.

The present configuration takes all of the requirements described above into consideration. Two interaction regions are proposed. One interaction region, the HEIR, is free of net bending angles upstream of the final focus. This permits the HEIR to reach extremely high energies. Any bend magnets upstream of the final focus can be reduced in angle while still fitting into the original tunnel. To allow for the 20 mrad crossing angle that prevents parasitic collisions, the linacs are each angled by 10 mrad and are collinear with the beam delivery system tunnels. This is the simplest, least expensive design that can, without additional civil engineering, be used to deliver cms energies up to 5 TeV if required.

The second interaction region, the LEIR, is for use in $\gamma\gamma$ collisions or in $e^+e^-$ collisions up to approximately 1 TeV. The LEIR and HEIR use the same collimation system. Downstream of the collimation is a 25-mrad arc that brings the LEIR beams into collision with a net 30-mrad crossing angle. The HEIR and LEIR have a transverse separation of about 20 m and a longitudinal separation of 440 m, which is achieved by making the beam delivery systems asymmetric in length. This layout allows for seismic isolation of the two IR halls and eliminates the requirement for separate collimation beamlines for each final focus. Tunnel length and installed hardware are minimized in this configuration, as shown in Fig. 6.16. The larger crossing angle of the LEIR is required for the $\gamma\gamma$ option, but 25-mrad bend required to achieve this crossing angle also fundamentally limits the energy reach of the LEIR. There are many other options for the exact configuration of the two IR halls and their supporting beamlines. The selection of a specific design is a balance between the IR hall separation desired, operational issues, and the relative expense of the tunnel lengths and supporting beamlines.

## 6.5 LINX

The R&D effort discussed above has been fairly modest in scope, involving prototype hardware and limited beam tests meant to answer fairly straightforward questions. Ultimately, the individual components that emerge from the R&D program must be integrated into a beamline and must function properly in that environment. Given the importance of the beam delivery system in the production of useful luminosity, an engineering test facility is planned to validate critical aspects of the design. The final focus of the SLC can, with minor modifications, be run in a mode that serves as just such an interaction region engineering test bed. A Letter of Intent to build and operate this facility, named LINX for LINear Collider X-ing, has been presented to SLAC management and to the NLC Machine Advisory Committee.

Table 6.2 shows the basic parameters of LINX. The three goals of LINX are to test stabilization techniques proposed for future linear colliders and demonstrate nanometer stability of colliding beams, to investigate proposed optical techniques for control of beam backgrounds, and to provide a facility where ultra-small and ultra-short beams can be used for a variety of other experiments. The IP beta functions, bunch charge, and bunch length are identical to those in the NLC 500-GeV cms parameters.

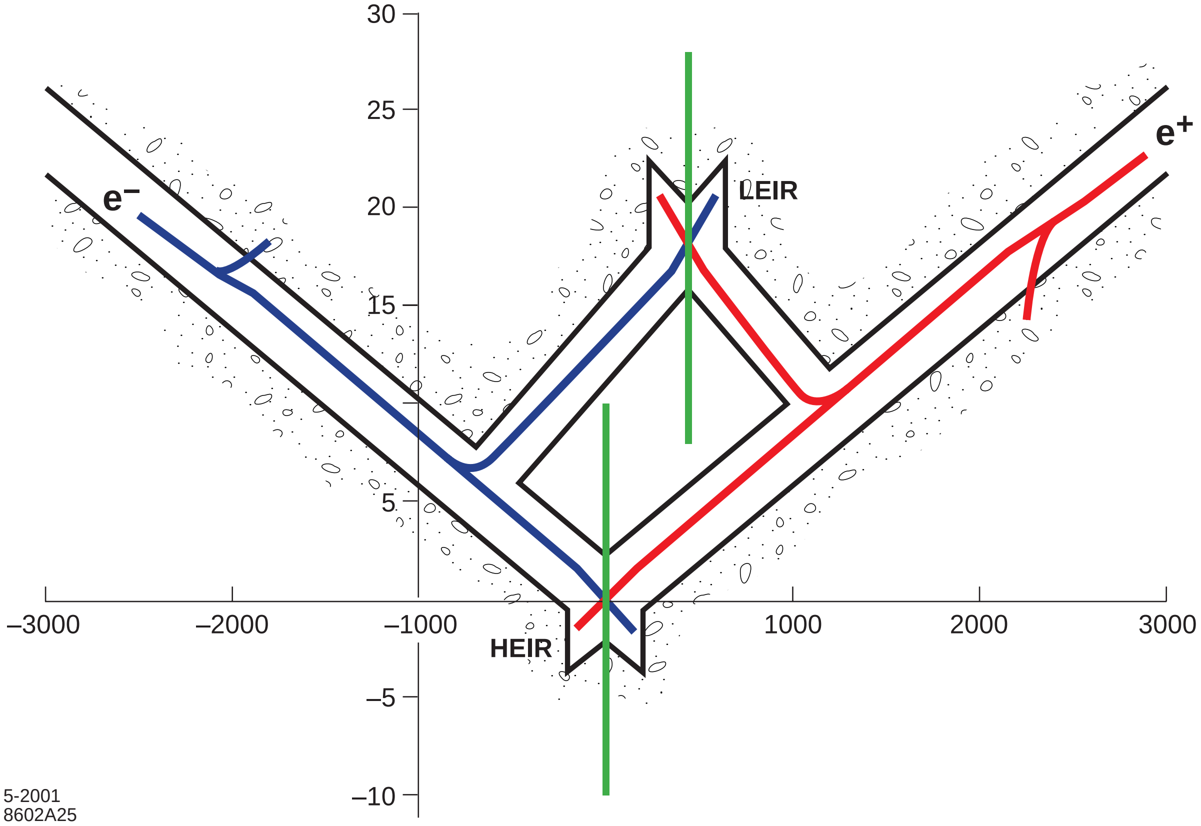

**Figure 6.16:** Anamorphic layout of the beam delivery system in the NLC 2001 configuration.

The discussion of the FFTB spot size measurement above shows that while the FFTB did achieve the desired betatron functions, 40 nm of beam jitter from various sources must be added in quadrature with the ideal result to explain the observations. A key feature of LINX is that it can achieve 1-nm resolution on the pulse-to-pulse beam-beam jitter by using the beam-beam deflection with beams of from 55 nm to 400 nm in height and 1 μm resolution BPMs. Thus, LINX affords an opportunity to demonstrate the required suppression of beam-beam jitter in an accelerator environment.

**Table 6.2:** LINX Parameters

| | |
|---|---|
| Beam energy | 30 GeV |
| IP emittances ($\gamma\epsilon_x/\gamma\epsilon_y$) | 16/1.6 mm-mrad |
| IP betas ($\beta_x/\beta_y$) | 8/0.1 mm |
| Bunch length ($\sigma_z$) | 0.1-1.0 mm |
| IP spot sizes ($\sigma_x/\sigma_y$) | 1500/55 nm |
| Bunch population (N) | N = $6x10^9$ |

The proposed lattice is displayed in Fig. 6.17. Its similarity to that of the NLC FF in Fig. 6.2 is evident. By including an octupole pair in the lattice the concept of using nonlinear optical elements for halo-folding can be experimentally verified. While there is great confidence in the accuracy of the third-order optics programs used to design the FF lattice, detailed experimental conditions, not included in the simulations, sometimes cause less than ideal performance. LINX will provide a basis for confidence in the total integrated beam-delivery system.

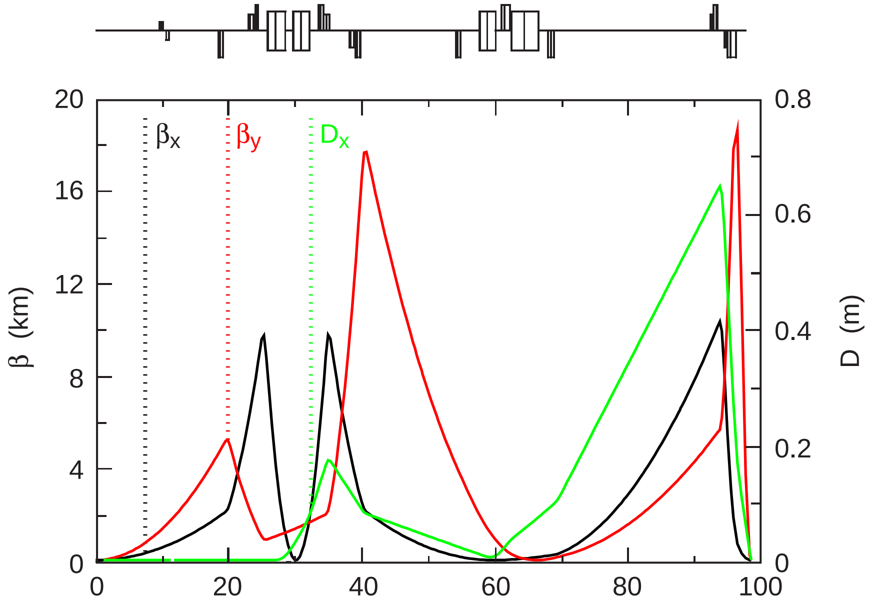

6-2001
8602A58

**Figure 6.17:** Optics of the SLC FF modified according to the new NLC FF design. The final triplets will be replaced by doublets with additional sextupoles interleaved. All the other elements of the SLC FF are left unchanged. One octupole doublet is added for active background control.

## References

[1] Brown, K., “Basic Optics of the SLC Final Focus System,” *Proc. of the Workshop on Physics of Linear Colliders*, Capri, Italy, 1988, SLAC-PUB-4811, December 1988.

[2] Balakin, V., et al., *Phys. Rev. Lett.*, **74**:2479,1995.

[3] Raimondi, P. and Seryi, A., “A Novel Final Focus Design for Future Linear Colliders,” *Phys. Rev. Lett:* **86:**3889, 2001.

[4] Oide, K., “Final Focus System with Odd Dispersion Scheme,” *Proc. 15th International Conference on High Energy Accelerators*, Hamburg, Germany, KEK-PREPR-92.058, 1993.

[5] Frisch, J., et al., “Advanced Collimation Prototype Results for the NLC,” *Proc. 9th Instrumentation Workshop*, Cambridge, Massachusetts, 2000, SLAC-PUB-8463, June 2000.

[6] Ross, M., et al., “Single Pulse Damage on Copper,” *Proc. 20th International Linac Conference*, Monterey, California, 2000, SLAC-PUB-8605, September 2000.

[7] Tenenbaum, P., et al., “Direct Measurement of Geometric Wakefields from Tapered Rectangular Collimators,” *Proc. 20th International Linac Conference*, Monterey, California, 2000, SLAC-PUB-8563, August 2000.

# Chapter 7

## Beam Dynamics and Performance Studies

## 7.1 Introduction

The NLC injectors produce trains of bunches with normalized emittances of 3 mm-mrad in the horizontal and 0.02 mm-mrad in the vertical. Each bunch contains $0.75 \times 10^{10}$ particles and has an rms length of 110 μm. The main linac and beam delivery regions must preserve these small emittances, and must collide beams with transverse sizes of 245 nm by 2.7 nm, in order to achieve the NLC luminosity goals. The main-linac and beam-delivery system designs must ensure that the dual goals of emittance preservation and collision of ultra-small bunches are achievable.

While the horizontal and vertical beam sizes at the NLC IP are both quite small, the large aspect ratio in both spot size and emittance (approximately 100:1) imply that the challenges in the vertical plane will be 1 to 2 orders of magnitude more difficult than those in the horizontal. In almost all regions of the accelerator, the principal performance limitation is alignment. The typical beam-to-quad alignment tolerance throughout the NLC is between 2 μm and 10 μm, and the typical quad jitter tolerance is from 1 nm to 10 nm. All of these tolerances are tight by the standards of today's accelerators. By contrast, the tolerance on absolute quadrupole strength accuracy in the main linac is approximately 0.1%, which does not particularly stress the state of the art. The NLC alignment tolerances can be achieved through the use of beam-based diagnostics and corrections. The NLC design includes diagnostic and correction devices to meet these tolerances with capabilities that are at most an incremental improvement upon existing hardware, as shown in Table 7.1.

In addition to the devices listed in Table 7.1, the NLC will require a set of tuning algorithms that will convert the measurements of the diagnostics into new settings of the correction elements. Here again, the NLC will rely upon widely used and well-understood techniques in accelerator physics: quadrupole shunting, which has achieved beam-to-quad resolutions as small as 1 μm in the FFTB [8]; dispersion-free steering (DFS), which enabled both SLC and LEP to achieve record luminosities [9,10]; and closed orbit bumps for global emittance tuning, which have been used routinely in the SLAC linac for many years [11]. Because the NLC builds on the demonstrated success of existing colliders and test facilities, it is expected that modest advances in a few areas of the technology are all that will be required to achieve the performance goals.

In the remainder of this Introduction the issues of beam emittance, jitter, and accelerator alignment are developed more fully, and the emittance preservation and beam-beam jitter problems are compared and contrasted with one another. This is followed by a discussion of measurements of ground motion, which is considered a principal driver of accelerator misalignments; a description of the techniques which will be used to address the beam-beam jitter issue; and a detailed discussion of emittance preservation in the main linac and the beam-delivery areas of the NLC.

### 7.1.1 Emittance, Jitter, and the Connection to Accelerator Alignment

Although both the beam-beam jitter and the single-beam emittance are related to alignment of the accelerator, the two problems are in practice quite different:

- The amount of transverse beam-beam jitter that can be tolerated before unacceptable luminosity degradation occurs is on the order of the IP beam size, which in turn implies rms vertical motion tolerances on the order of nanometers. The misalignment amplitude that generates luminosity reduction through emittance dilution is larger than this by a factor of $1/\sigma_{\Delta E/E}$, typically a factor of 300. Thus, a level of motion that is detrimental to luminosity because the beams miss each other is negligible for emittance dilution.

- Because the beams are only required to collide at a single point, in principle all sources of transverse beam-beam jitter can be corrected by a single set of dipoles that steer the beams at the IP. Emittance dilutions, on the other hand, need to be corrected close to their sources, which means that a larger number of elements are involved in emittance correction. Ideally, every element in the accelerator will be aligned with sufficient accuracy to eliminate emittance dilution completely. In this limit, “emittance correction” is completely local, and essentially every element is involved.
- Collision jitter is fundamentally a dynamic process. If beam-line elements did not move in time, the beams could be steered into collision once and would continue to collide forever. The emittance dilution problem, by comparison, is almost static in nature. Once a trajectory that preserves the emittance has been determined, it is only necessary to recover this trajectory on timescales of minutes or even hours.

**Table 7.1:** Requirements for NLC diagnostic and correction devices, compared with achieved capabilities of existing equipment.

| ITEM | SPECIFICATION | ACHIEVED | IMPROVEMENT NEEDED |
|---|---|---|---|
| Quadrupole BPMs | 0.3 μm resolution | 1 μm resolution (FFTB striplines) [1] | Factor of 3 |
| | | 0.025 μm resolution (FFTB cavities) [2] | None |
| Rf structure BPMs | 5.0 μm resolution | 2 μm resolution (NLC structure prototypes DDS3 and RDDS1) [3] | None |
| Magnet Movers | 0.05 μm step size | 0.3 μm step size (FFTB magnet movers) [4] | Factor of 6 |
| Rf Girder Movers | 1 μm step size | 0.3 μm step size (FFTB magnet movers) [4] | None |
| Laser Profile Monitor | Measure 1 μm rms beam size | Measure 1 μm rms beam size (SLC laser wire) [5] | None |
| | | Measure 0.06 μm rms beam size (FFTB laser interferometer profile monitor) [6] | None |
| Magnet/Girder Supports | Add < ~3 nm vibration wrt tunnel floor | Add ~2 nm vibration wrt tunnel floor (FFTB quadrupole supports) [7] | None |

The principal similarity between the beam-beam jitter and the single-beam emittance problem is that both problems appear, at first glance, to be intimidating. Both achieving a static alignment tolerance that is measured in microns, and holding beam-line elements still at the level of nanometers, intuitively appear to be daunting tasks. Neither of these jobs is as arduous as it at first appears.

- The amount of natural ground motion at high frequencies ($f \geq 1$ Hz, where $f$ is frequency) is quite small, leading to rms motions of approximately 2 nm. A measurement of the vibration of quadrupoles in the Final Focus Test Beam (FFTB) showed that it is possible to construct magnets in such a way that all additional sources of motion – flowing water, amplification of motion by the support, etc. – can be reduced to 2 nm rms in this frequency range [7].
- Although the amount of natural motion at low frequencies (0.02 Hz $\leq f \leq$ 1 Hz) can be 100 nm rms or even larger, such motions tend to be highly correlated over long distances, and thus result in the entire accelerator moving as a unit. This correlation reduces the impact of the ground motion at the IP. Furthermore, motion in these frequencies is highly amenable to correction by beam-based steering feedback, which is effective at frequencies that are low compared to the beam repetition rate of 120 Hz.
- The amount of ground motion at low frequencies is insufficient to cause emittance dilution. Diffusive motion, which operates at even longer timescales, can eventually cause emittance dilution but it is sufficiently slow that correction is straightforward.
- While the DC alignment tolerances of the NLC would be extremely challenging for conventional survey methods, all subsystems in the accelerator have been designed to permit the use of beam-based techniques to measure misalignments, and precision remotely controlled translation stages to reposition misaligned magnets. Use of beam-based techniques allows a tremendous improvement in the alignment precision over conventional survey methods. In the FFTB, for example, *ab initio* alignment tolerances of 50 μm were achieved by mechanical survey, but beam-based alignment achieved resolutions as small as 1 μm [1,8].

### 7.1.2 Sensitivity, Tolerance and Emittance Budgets

The effect of various accelerator imperfections on performance is often quoted as a sensitivity, which indicates how severe an imperfection is required to generate a fixed degradation of the beam conditions. For example, sensitivities for 2% luminosity loss or for 10% emittance dilution are commonly given. Since the sensitivities are simply comparative, they do not, in and of themselves, tell the engineers what tolerances they must achieve on various parameters. The computation of tolerances from sensitivities requires three additional pieces of information: a performance budget (permitted emittance dilution, permitted rms jitter, etc.) for the accelerator, based on the desired end-to-end performance and a technical judgment of which regions of the machine will tend to experience greater degradation; allocation of the regional budget among the various effects that cause performance degradation; and an understanding of the arithmetic for combining and scaling the degradations.

The emittance and jitter budgets for the 500-GeV cms NLC are given in Tables 7.2 and 7.3 below. The technical considerations for allocating the emittance-dilution budget among components in each region will be discussed later in this chapter. Beam-beam jitter budgets are dominated by quadrupole vibrations. This is because all other potential sources are negligible – for example, the amount of rf girder vibration required to contribute to the beam-beam jitter at the IP is tens of microns.

The arithmetic rules for combining sources of beam-beam jitter and emittance dilution are as follows:

- Beam-beam jitter sources add in quadrature, and scale linearly with amplitude (i.e., a doubling of the quad jitter amplitudes in the main linac will double the beam-beam jitter contribution from this region).
- Emittance dilution sources add linearly, and scale quadratically with amplitude (i.e., a doubling of the rms quad misalignment in the main linac will quadruple the emittance dilution from this source).

Throughout the remainder of this chapter, emittance dilution sensitivities will be quoted for 40% vertical emittance dilution in the main linac or 25% vertical emittance dilution in the beam delivery system (i.e., the sensitivities are such that the given aberration uses up all of the dilution budget for the region of interest). In the rare cases where a main linac tolerance is set by horizontal emittance dilution, 3% dilution will be used to set the sensitivity.

**Table 7.2:** NLC Design Emittance budget for 500 GeV cms parameters.

| REGION | $\gamma\varepsilon_X$, mm-mrad | $\gamma\varepsilon_Y$, mm-mrad |
|---|---|---|
| From Damping Ring | 3.0 | 0.02 |
| From Injector | 0.2 | 0.002 |
| From Main Linac | 0.1 | 0.008 |
| From Beam Delivery | 0.3 | 0.005 |
| Total at IP | 3.6 | 0.035 |

**Table 7.3:** NLC Jitter Budget for 500 GeV cms parameters. Total at IP is sum in quadrature of all preceding rows and luminosity loss is included in luminosity budgets.

| REGION | X JITTER, SIGMAS | Y JITTER, SIGMAS | ENERGY JITTER |
|---|---|---|---|
| From Damping Ring | 0.1 | 0.1 | 0.1% |
| From Injector | 0.1 | 0.1 | 0.1% |
| From Main Linac | 0.1 | 0.3 | 0.2% |
| From Beam Delivery | 0.1 | 0.3 | — |
| From Final Doublet | 0.1 | 0.25 | — |
| Total at IP | 0.22 | 0.51 | 0.25% |
| Luminosity Loss | 1% | 3% | 2% |

## 7.2 Ground Motion

While many sources of accelerator component misalignment can be minimized or eliminated through engineering, the natural ground motion of the NLC site is a potential source of misalignments that is not itself amenable to direct engineering. Given the NLC beam-beam jitter tolerances, a thorough understanding of the impacts of ground motion is essential to evaluating the feasibility of the collider as a whole, and considerable effort has been invested in studies of this phenomenon. The *NLC Zeroth Order Design Report* (ZDR) devoted an entire chapter to the subject. In this section, the most important characteristics of this problem are summarized.

### 7.2.1 Power Spectrum of Ground Motion

Figure 7.1 shows a series of measurements of the power spectrum of ground motion, which have been taken at various sites around the world [12,13]. Included in Figure 7.1 are measurements taken in the SLAC tunnel at 2 AM during a period when the beam and rf structures were off but cooling water was flowing normally, data taken in the LEP, HERA and UHK tunnels, and data taken in the Hiidenvesi cave in Finland. All of the measurements indicate that the power density of natural ground motion is a strong function of frequency, with a characteristic $1/f^4$ dependence. Although high frequencies are potentially the most deleterious from the point of view of beam-beam jitter, Fig. 7.1 shows that natural ground motion contains very little power in frequencies above 1 Hz. Another common feature of all the spectra is a peak at approximately 0.15 Hz. This is the motion of the continents under the influence of ocean waves.

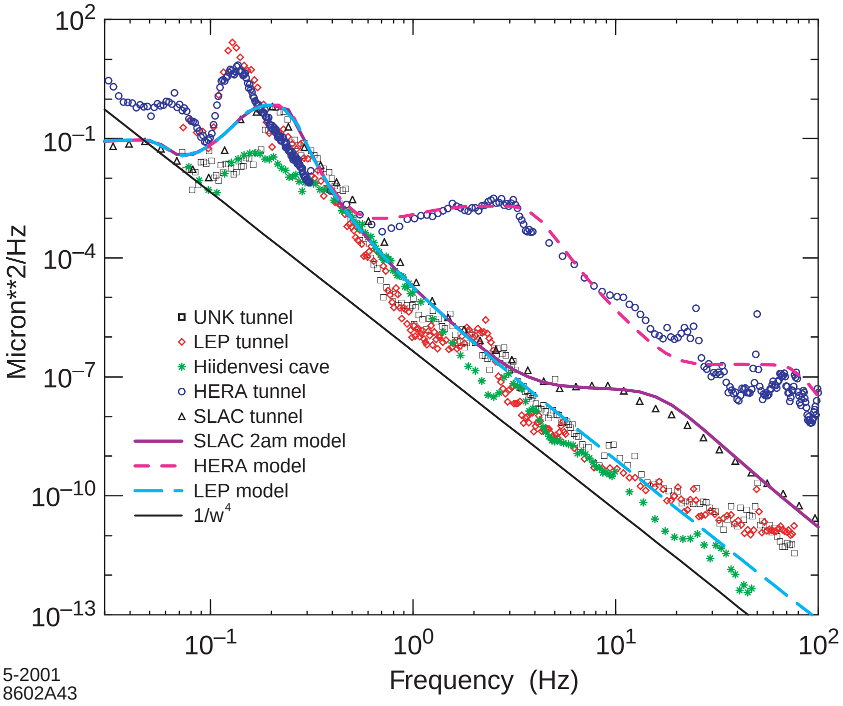

**Figure 7.1:** Power spectrum of ground motion, in units of $\mu m^2/Hz$, from several accelerator tunnels and a cave. The strong peak at 0.15 Hz in all spectra is from ocean waves. The shoulder at 4 Hz in the HERA data is due to cultural noise, vibration sources within the accelerator complex and from the surrounding urban area. The general trend of ground motion power spectra is to follow a $1/f^{4}$ power law.

The measurements also reveal certain site-specific characteristics. For example, the HERA tunnel measurements show a unique 'bump' in the region of 4 Hz and both the SLAC and the HERA measurements contain 'shoulders' between 10 and 100 Hz which are not present in the other measurements. These features are due to a combination of several phenomena: greater 'cultural noise' (noise from automobiles, equipment, or other human activities) at the SLAC and HERA sites; relatively shallow tunnels at these sites; and relatively poor geological conditions in the case of the HERA tunnel. The power spectral density (PSD) at 10 Hz at HERA is 2 orders of magnitude greater than the equivalent PSD at SLAC, which is itself about 2 orders of magnitude higher than the same PSD at LEP. The most important lesson to be learned from the power spectral density measurements is that not all sites are equally viable for the NLC. The NLC beam-beam jitter sensitivity favors a deep tunnel in relatively strong material at a location with minimal cultural noise. Of course, these characteristics can be traded off against each other. A shallow tunnel site at a relatively deserted location can have net noise characteristics comparable to a deep tunnel in a populated area.

### 7.2.2 Integrated Motion of the Ground

The raw PSD of the ground motion at a proposed linear collider site is not an appropriate tool for fully evaluating the site's suitability, because it does not directly indicate how much elements move. A more useful tool is the integrated motion, $\sigma(f)$, which is related to the power spectral density $P(f)$ as follows:

$$\sigma(f) = \sqrt{\int_{f}^{\infty} P(f')\,df'} \tag{7.1}$$

As Equation (7.1) shows, σ(*f*) gives the rms motion of the ground caused by all frequencies above a given 'cutoff,' and thus this is the quantity to consider to estimate motion due to frequencies above 1 Hz.

Figure 7.2 shows the integrated motion of the SLAC site, based on the measurements in Figure 7.1. The abrupt cutoff at the high-frequency end is an artifact of the measurement technique (samples were taken at 128 Hz), and the slow rise at the low-frequency end is due to instrument noise. The measurement included two sensors separated by 100 meters, and both the absolute motion and the relative motion of one sensor with respect to the other are shown. Figure 7.2 shows that while the integrated motion over the full range of the measurement is close to 100 nm, this motion is dominated by low-frequency noise sources and the total motion above 1 Hz is only 2 nm. Furthermore, for frequencies below 1 Hz the relative motion of the two sensors is much smaller than the total motion, while above 1 Hz the relative motion is slightly larger than the absolute motion of either sensor by itself. This indicates that low-frequency ground motion tends to be highly correlated over long distances, while high-frequency motion tends to be uncorrelated. Figure 7.2 shows that 1 Hz is a natural boundary between highly correlated 'low-frequency' and uncorrelated 'high-frequency' motion.

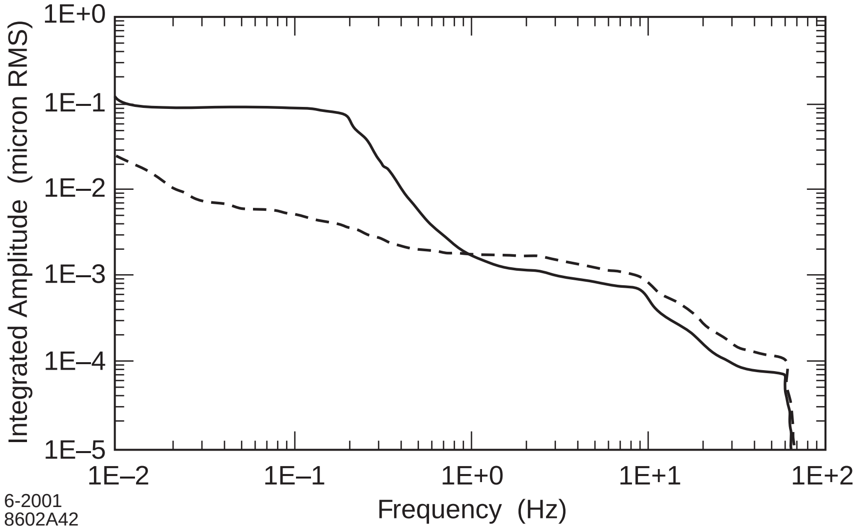

**Figure 7.2:** Integrated motion of the SLAC site, based on power spectral density measurement in Figure 7.1. Both the absolute motion at a single sensor (solid) and the difference in motions between two sensors separated by 100 m (dashed) are shown.

### 7.2.3 Diffusive Ground Motion

Ground motion at frequencies below 0.01 Hz is quite difficult to measure with conventional geophones and seismometers. An assortment of measurements with long time bases, including several accelerator-based measurements, have suggested that ground motion over time scales from hours to months can be modeled by 'space-time ground diffusion.' As accelerator components undergo uncorrelated random walks about their initial positions, the rms transverse misalignment of two accelerator components separated by a longitudinal distance *L* after a time *T* can be modeled as:

$$\sigma_y^2 = A \cdot T \cdot L, \qquad (7.2)$$

where $A$ is a coefficient with units of $\mu m^2$/m/second [14]. Equation (7.2) is often referred to as the 'ATL Law.' ATL motion can be represented in the frequency domain by a power spectral density which is proportional to $1/f^2$, as opposed to the ground motion spectra in Fig. 7.1 which follow an approximate $1/f^4$ law. This implies a limit to the validity of this model at high frequencies, since at some frequency the ATL law would require relative motion of two objects that is greater than their absolute motion.

The magnitude of the coefficient $A$ is crucial in evaluating the impact of ATL motion on any collider. This magnitude appears to be highly variable, with values as large as $2 \times 10^{-4}$ and as small as $10^{-8}$ recorded in different locations around the world. In general, the conditions which are favorable from the point of view of wavelike ground motion – underground siting, quiet surface conditions, strong rock – also appear to have a favorable impact on the magnitude of $A$. Recent measurements of the coefficient $A$ at the SLAC site have indicated a mean value of approximately $5 \times 10^{-7}$ $\mu m^2$/m/s [15]. This level is acceptable for the NLC.

### 7.2.4 Systematic Ground Motion

In addition to the diffusive ground motion described above, large-scale structures such as houses or accelerator tunnels also undergo a form of systematic ground motion. This is due to the uneven distribution of weight in the structures or to variation in the strength of the substrate material over the area of the structure. Qualitatively, systematic ground motion tends to have a similar spatial frequency distribution to diffusive ground motion. In simple terms, this means that a plot of accelerator misalignments from tunnel settling looks a lot like misalignments from diffusive motion. The temporal behavior of systematic motion is completely different, however. Points which begin to move down with respect to the average will continue to move down in systematic motion, while in a diffusive regime points are as likely to change direction as to continue in their original direction. Consequently, several measurements over a period of time are needed to distinguish systematic and diffusive motion. It now appears that many measurements of large $A$ coefficients in ATL motion are due to the misinterpretation of systematic motion as diffusive. In particular, early calculations using measurements of the SLAC linac tunnel overestimated $A$ for this reason.

## 7.3 Maintaining Collisions at the Nanometer Level

The principal obstacle to maintaining collisions of the NLC beams in the vertical plane will be the motion of the many quadrupoles in the beam line. This motion will be driven by natural ground motion, vibrations caused by accelerator equipment such as pumps and cooling water, and other human-generated cultural noise. Other phenomena, such as the tendency of mechanical supports to amplify vibrations in some frequency band, can also make the problem significantly more difficult.

In order to minimize the impact of magnet supports and accelerator equipment vibrations, it will be necessary to subject every piece of hardware in the NLC complex to carefully developed engineering criteria, in essence to establish a 'vibration budget' for the equipment similar to the 'impedance budget' of modern-day storage rings. While achieving the NLC vibration goals will require appropriate planning and design, the excellent performance of the quadrupoles described in [7] demonstrates that these goals are feasible. In addition, the NLC will make extensive use of quadrupoles that use permanent magnet material rather than electric windings to drive their fields. This will eliminate the need for cooling water in all such magnets, and eliminate a potential source of magnet motion. Other sources of cultural noise, for example the use of motor vehicles on site, will be addressed through appropriate selection of a site and a tunnel depth. The LEP tunnel measurements in Fig. 7.1 show that even a tunnel in a suburban area can be made relatively free of cultural noise sources.

Once the sources of motion amenable to engineering have been addressed, there remains an irreducible background due to the natural ground vibration described in the previous section. While the total power in this motion is considerable – up to 100 nm when frequencies from 0.01 Hz to 64 Hz are considered – there are several factors that mitigate the severity of the effect. These are beam-based steering feedback, the highly correlated nature of the low-frequency motion, and the lattice response to long-wavelength correlated motions.

### 7.3.1 Beam-Based Steering Feedback

Beam-based steering feedback – which uses dipole correctors to maintain a desired orbit through a set of beam-position monitors (BPM) automatically – has become commonplace in modern accelerators. The SLC made intensive use of steering feedback throughout the injector, linac, collider arcs, and final-focus regions. These feedback systems were indispensable in preserving luminosity performance in the face of a wide variety of slow changes in the accelerator complex [16].

In a linear collider environment, the beam can only sample the accelerator condition at the beam repetition rate, which is 120 Hz for the NLC. This implies that the Nyquist frequency for beam-based feedback will be 60 Hz, and that no correction of accelerator distortions will be possible for frequencies above this. More generally, the ability of the feedback to suppress slow drifts in the accelerator depends to some extent on the design of the feedback algorithm and is always a strong function of the frequency spectrum of the distortions. Figure 7.3 shows the suppression of steering effects achievable in an ideal feedback with a 120 Hz sample rate under two different algorithm designs: an algorithm which exponentially weights past samples, similar to the SLC design, and an algorithm which uses only the last two pulses to anticipate the position of the next pulse, ignoring any previous pulses (technically known as a 'second-order deadbeat' feedback). The latter algorithm achieves a stronger suppression of low-frequency noise but produces more amplification at high frequency than the SLC-style design. The exact algorithm to be used in the NLC will depend upon the noise characteristics of the site.

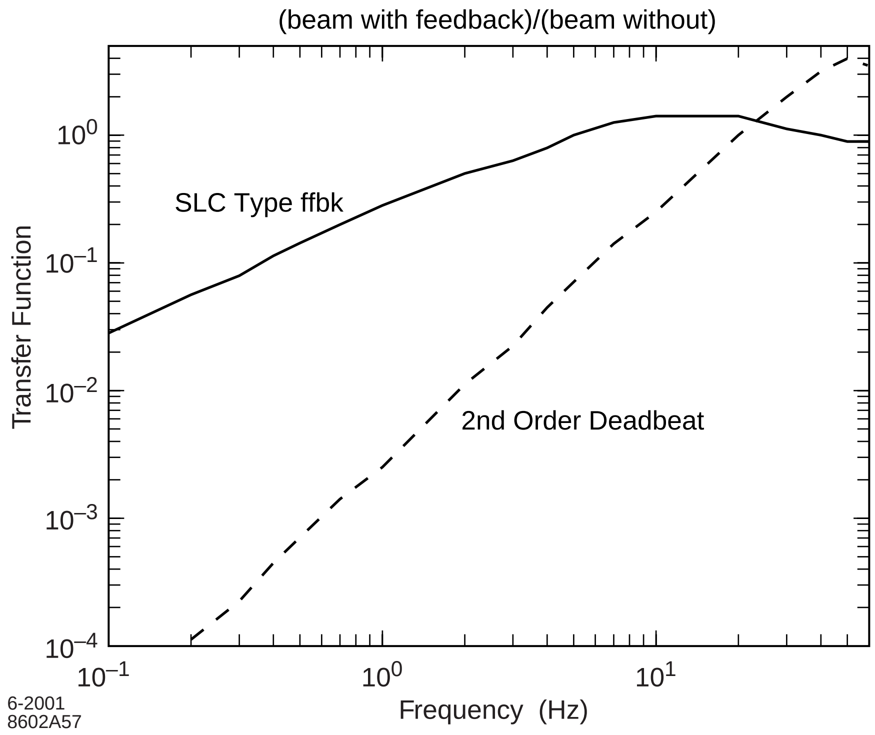

**Figure 7.3:** Feedback response functions for 2 different algorithms, both assuming a 120-Hz sample rate.

In addition to standard steering feedback throughout the NLC, there will be feedback at the IP that uses the beam-beam deflection signal to determine the relative offset of the two beams. This feedback will allow correction of the relative motion of the colliding beams at the nanometer level.

### 7.3.2 Lattice Response and Correlated Motion

The NLC can tolerate extremely large motions of the accelerator as long as those motions are highly correlated over its length. An obvious example of this is that the NLC is nearly impervious to tidal motion, even though the tides cause the accelerator to move a foot or more with respect to the center of the earth, because the entire collider moves as a unit. The relative motion of components in the complex due to the tidal stretching of the earth's surface is quite small although the absolute motion is large.

The tolerance of colliding-beam facilities to long-wavelength motion is quantified in the lattice response function, $G(k)$, where $k$ is the wave number of the motion. Given a spectrum of ground motion characterized by wave number, $P(k)$, the mean-squared motion of the beam at the IP is given by:

$$\sigma_y^2 = \int_0^\infty P(k)G(k)\frac{dk}{2\pi}. \tag{7.3}$$

In the long-wavelength limit, it can be shown that $G(k)$ falls extremely rapidly. Depending upon the optics and layout of the accelerator, $G$ will fall as $1/\lambda^2$ to $1/\lambda^6$ [17] where $\lambda$ is the wavelength. At low frequencies, the motion of the ground is highly wavelike and is characterized by long wavelengths and strong correlations in the motions of distant points. Therefore, the low-frequency motion of the ground will contribute little to the relative motion of the beams at the IP, even if the beam line is such that $G$ obeys the less favorable $1/\lambda^2$ scaling law.

### 7.3.3 Motion of the NLC Quadrupoles

When the influence of beam-based steering feedback, lattice response, and correlated motion are considered, it can be shown that quadrupole motion at frequencies below approximately 1 Hz will generally not contribute significantly to beam-beam jitter at the IP. For most of the quadrupoles in the NLC, considered as an ensemble, rms motion of 10 nm in the frequency range above 1 Hz will be acceptable. If the SLAC integrated ground motion in Fig. 7.2 and the FFTB quadrupole supports described in [7] are used as a basis, the NLC will have rms quadrupole motion of less than 4 nm in this frequency range. This indicates that, for a reasonable choice of site and magnet support technology, it will be possible to provide stability for most of the NLC quads in an entirely passive manner (i.e., *without* geophones and piezoelectric movers on each quad). Note that, while the FFTB support is acceptable for almost all magnets in the NLC, it does not represent a lower limit for support stability, and with a number of minor alterations, even better performance can be achieved.

### 7.3.4 Motion of the NLC Final Doublet

The main exception to the conclusion of the previous section is the final focusing quadrupole doublet in the NLC interaction region. The final doublet magnets are so strong that a 1-nm motion of one doublet with respect to the other will result in approximately a 1-nm offset between the beams at the IP. This implies that even the low level of natural ground motion measured at the SLAC site is too large for the final doublet magnets. A further reduction of ground motion above 1 Hz, on the order of a factor of 2, is required. In addition, the final doublet magnets are supported at least partially by the detector, since they must be as close to the IP as possible. This implies that the doublets cannot be put on supports that are strongly coupled to the ground, and the magnets may experience vibration from sources on the detector itself. Measurements of the vibration spectrum on the SLD detector have shown a level of motion much larger than that of the supporting ground in all frequencies.

Because the final doublets contain a small number of elements in a reasonably compact space, it is possible to contemplate solutions to the doublet motion problem that are too complex to be applied to a larger number of elements. Several options for reducing the motion of the final doublet to an acceptable level are presently being explored. Construction of the final doublet as a set of permanent magnets in a Halbach configuration [18] would minimize the size and weight of the magnets, permit them to be made extremely rigid, and would eliminate the need for power or cooling, both of which are problematic for a vibration-sensitive magnet. Reducing the weight of the magnet will also increase its natural resonant frequency, which is desirable because the power spectrum of natural ground motion falls so quickly at high frequencies.

A lightweight and rigid set of magnets can be mounted on piezoelectric movers or other fast translation-stage technology which would allow constant position adjustment of the magnets at frequencies far above the beam repetition rate. A number of other approaches to supporting the final doublet – most notably soft springs, which attenuate high-frequency motion – are also under consideration. Two different technologies for measuring the motion of the magnets with high resolution over a wide frequency band are under consideration: an optical anchor, which uses laser interferometry to measure the positions of the final doublet magnets with respect to a fixed point on the detector floor; and inertial sensors which can measure the accelerations of the magnets directly. Both technologies would allow the additional vibrations of the detector to be suppressed, and would allow one doublet to be held fixed in position with respect to the other.

A steering feed forward loop, which measures the positions of all the doublet magnets and uses a set of steering coils to steer the beams into collision, is also under consideration. This solution would permit corrections at high frequency by measuring the magnets instead of the beams, and would permit a correction in the case of final doublets that are too heavy or too soft to be moved by piezoelectric stages (for example, if superconducting doublet magnets are used).

### 7.3.5 IP Collision Feedback Within One Bunch Train

The measures described above are expected to limit luminosity loss from beam-beam jitter to a few percent, which is acceptable. An additional measure, which can potentially provide further reduction, is a feedback at the interaction point that operates within a single bunch train. An intratrain collision feedback would use the beam-beam deflection to estimate the relative offset of the two bunch trains from the measured deflections of the first few bunches. This information would then be used to program a high-bandwidth kicker to steer subsequent bunches back into collision. Such a feedback has been studied for the TESLA bunch train [19]. The NLC implementation for such a feedback is made more complicated by the fact that both the bunch train and the intrabunch spacing are much shorter than in TESLA. As a result, ‘next-bunch’ correction based on the first bunch collision offset is not possible. By the time the deflection of bunch 1 has been detected, bunch 10 is almost at the IP, and the correction can only be applied to bunch 19. Nonetheless, a schematic design of the system using available components has been developed, and the resulting feedback could potentially eliminate half the luminosity loss from beam-beam jitter [20].

## 7.4 Emittance Dilution in the Main Linac

As shown in Table 7.2, the normalized emittance dilution budget for the NLC main linac is 0.1 mm-mrad in the horizontal and 0.008 mm-mrad in the vertical, corresponding to 3.3% of the horizontal emittance from the damping ring and 40% of the vertical emittance from the damping ring. In this section the sources of emittance dilution in the main linac, and their cures, will be discussed. In all cases the full 500 GeV per beam NLC main linac is considered, although the tolerance numbers above are for 250 GeV per beam. Consequently this section will somewhat overestimate the difficulty of constructing the Phase I facility (or else build confidence in the feasibility of Phase II).

### 7.4.1 Beam Breakup Instability (BBU)

The single most severe source of emittance dilution in a linear accelerator is the beam breakup instability (BBU). BBU occurs when the beam undergoes a betatron oscillation through the linac. The dipole modes of the rf structures cause the beam tail to receive transverse deflections that are in phase with the betatron oscillation, and thus the amplitude of the tail oscillation grows exponentially down the linac. The BBU instability can occur in a single bunch (as was observed in the SLC), or it can occur in a bunch train, in which case the leading bunches drive strong transverse wakefields that deflect trailing bunch centroids (as was observed in the early history of the SLAC linac). If not addressed, the wakefields in the NLC linac are so strong that a betatron oscillation of a fraction of a sigma would cause enough single-bunch BBU to eliminate all luminosity. The multibunch BBU would be even stronger, since each bunch experiences the wake from all preceding bunches. Fortunately, BBU is quite amenable to well-understood correction mechanisms.

The short-range BBU is corrected by introducing an energy spread between the head and the tail of a single bunch, with the tail being lower in energy than the head. This causes the tail of the beam to experience stronger focusing as it passes through the quads in the linac, which cancels the wakefield deflection acting on the tail. This mechanism is known as BNS damping, after V. Balakin, A. Novokhatsky, and V. Smirnov, who first proposed the solution [21]. The energy spread required is introduced by accelerating the bunch behind the crest of the rf. Since the bandwidth of the final focus is usually smaller than that of the linac, it is then necessary to remove the BNS damping energy spread by accelerating the bunch in front of the rf crest for some distance at the end of the linac. The NLC linac is designed to require a relatively low energy spread to achieve BNS damping. In the present optics, a maximum correlated energy spread of 0.6% to 0.8% is sufficient to eliminate single-bunch emittance growth from a betatron oscillation with an amplitude greater than the beam size.

One solution to the problem of long-range BBU is to reduce directly the amplitude of the long-range wakefield through damping or detuning of the higher-order modes. ‘Detuning’ requires that each cell of the rf structure have a slightly different dipole frequency, such that by the time the second bunch arrives in the structure the wakefields from the different cells have decohered. Detuning permits a very rapid fall-off in the strength of the long-range wakefield, but at some later time the wakefields will recohere and the strength will rise once again. ‘Damping’ requires that the cells be engineered such that the exponential fall-off time for the wakefields is reduced, effectively causing the dipole wakefield power to be dissipated more rapidly in the structure. While damping permanently reduces the strength of the wakefields, it is very difficult to achieve a structure design with sufficient damping to protect a given bunch in the NLC bunch train from the wake of the previous bunch.

The presently accepted NLC design philosophy is to use both damping and detuning to eliminate the long-range BBU instability. The detuning leads to a fast reduction in the wakefield, while moderate damping of the dipole modes prevents recoherence. The principal drawbacks of combining damping and detuning in a structure are that the structure is difficult to design due to its complexity, and difficult to build because the detuning requires extremely precise control over the dipole frequency of each cell and also the structure straightness. Nonetheless, several different variations on the ‘Damped Detuned Structure’ (DDS) have been designed and built successfully, and their wakefields have been measured with beam in the ASSET facility at SLAC. The agreement between predicted and measured wakefields, as shown in Fig. 7.4, is excellent, leading to confidence that the design methodology is correct. In addition, the last structure tested in this manner, RDDS1, achieved construction tolerances almost an order of magnitude better than those required for NLC.

While the combination of damping and detuning is expected to eliminate long-range BBU in the NLC main linacs, an additional reduction can be obtained by extending the BNS damping concept to multibunches. This would require introducing a bunch-to-bunch energy spread within a bunch train, and removing the energy spread at the end of the linac, which can easily be done by under- and overcompensating the long-range beam loading in the structures.

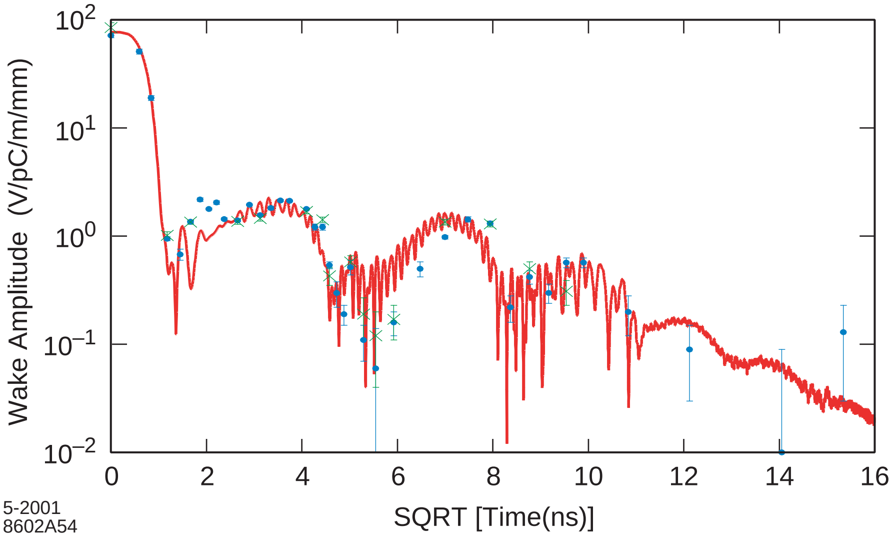

**Figure 7.4:** Predicted dipole wakefield (solid) and measured (points) for RDDS1, a prototype damped and detuned rf structure tested in the ASSET facility at SLAC. In a few nanoseconds the wakefield is reduced by almost 2 orders of magnitude due to the detuning, while light damping prevents recoherence at a later time.

### 7.4.2 Other Sources of Emittance Dilution

While the BNS damping mechanism eliminates emittance dilution from coherent (betatron) oscillations of the beam, the large energy spread will make the beam more sensitive to incoherent misalignments of the quadrupole magnets. Similarly, incoherent rf-structure misalignments will lead to emittance dilution from short-range dipole wakefields, and construction errors in the structures can introduce substantial multibunch emittance dilution. Table 7.4 shows the sensitivity of the NLC linac to various errors. As discussed above, the errors in Table 7.4 are the levels needed to consume the full main-linac emittance budget with each error (i.e., an otherwise perfect linac with 2.5 μm rms beam-to-quad offsets would have 40% vertical emittance growth; an otherwise perfect linac with 30 μm rms beam-to-structure offsets would have 40% emittance growth, etc.). Table 7.4 shows that the most serious sources of emittance dilution are single-bunch effects due to misaligned magnets and rf structures.

The alignment sensitivities in Table 7.4 are beyond what can be achieved by conventional survey techniques. Fortunately, it is possible to use beam-based alignment algorithms to achieve the most challenging tolerances in the NLC main linac. Figure 7.5 shows the beam-line hardware associated with beam-based alignment: remotely controlled translation stages for quadrupoles and rf girders, and high resolution BPMs in the quads and the rf structures. The equipment and instrumentation builds on the successful prototypes demonstrated at the FFTB [1,2,4] and in ASSET [3].

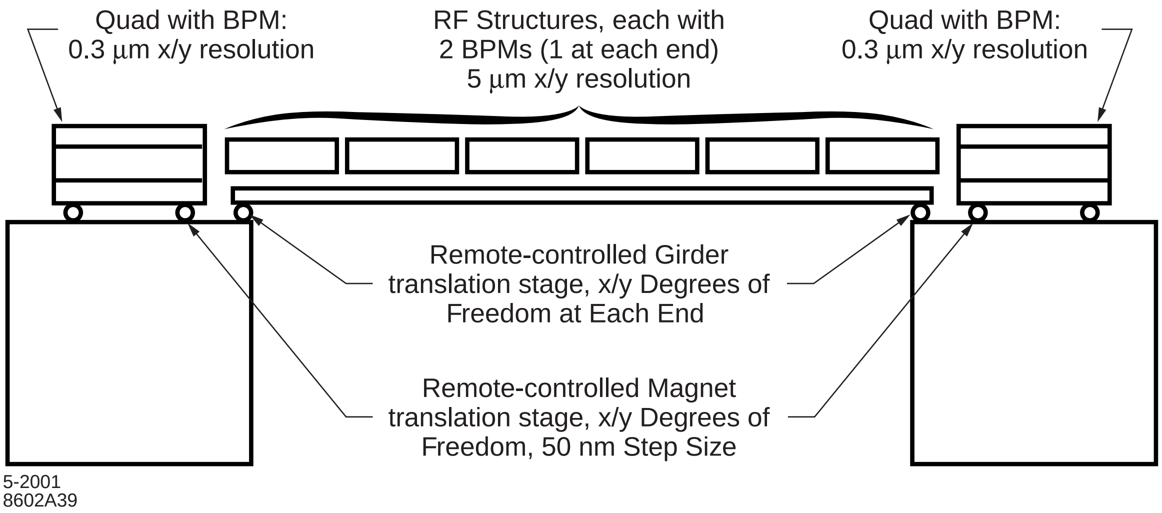

**Figure 7.5:** Beam-based alignment hardware in the NLC main linac.

**Table 7.4:** Single aberration sensitivities given the emittance dilution tolerances for the NLC main linac. Tolerances labeled as approximate ('~') have not been recently revisited. Note that SR horizontal emittance dilution is not a sensitivity but an unavoidable dilution due to bending magnets in main linac diagnostic regions. All misalignments are with respect to the beam, not the survey line.

| DILUTION | SINGLE/ MULTIBUNCH | X/Y LIMITING | SENSITIVITY (RMS) |
|---|---|---|---|
| Quadrupole misalignment | Single | Y | 2.5 µm |
| Rf Structure misalignment | Single | Y | 70 µm |
| Rf Structure pitch angle | Single | Y | 90 µrad |
| Quadrupole Rotation | Single | Y | 650 µrad |
| Quadrupole Strength | Single | X | 0.22% |
| Structure Straightness (bow) | Multi | Y | ~100 µm |
| Structure Straightness (random walk) | Multi | Y | ~7 µm |
| Structure Dipole Frequencies | Multi | Y | ~ 6 MHz (0.04%) |
| Synchrotron Radiation | Single | X | 0.09 mm-mrad, uncorrectable |

**Quadrupole Beam Position Monitors (Q-BPMs):** The BPMs in the Final Focus Test Beam were striplines, with a specification of 1 µm single-pulse resolution at a bunch charge of $10^{10}$. Figure 7.6 shows the readout of a pair of BPMs separated by a few meters in the FFTB. The rms deviation from a straight line indicates that the resolution specification was met. A high-resolution single-cell cavity BPM operating at C-Band (5.712 GHz) was also tested in the FFTB. Figure 7.7 shows the fit residual when a pair of BPMs was used to predict the reading on a third BPM immediately adjacent. The width of the Gaussian indicates that a resolution of 25 nm was achieved at a bunch charge of $6 \times 10^9$. The resolution needed for the NLC quadrupole BPMs is 0.3 µm, which is a factor of 3 better than achieved in the FFTB striplines and a factor of 10 looser than achieved in the single-cavity BPMs.

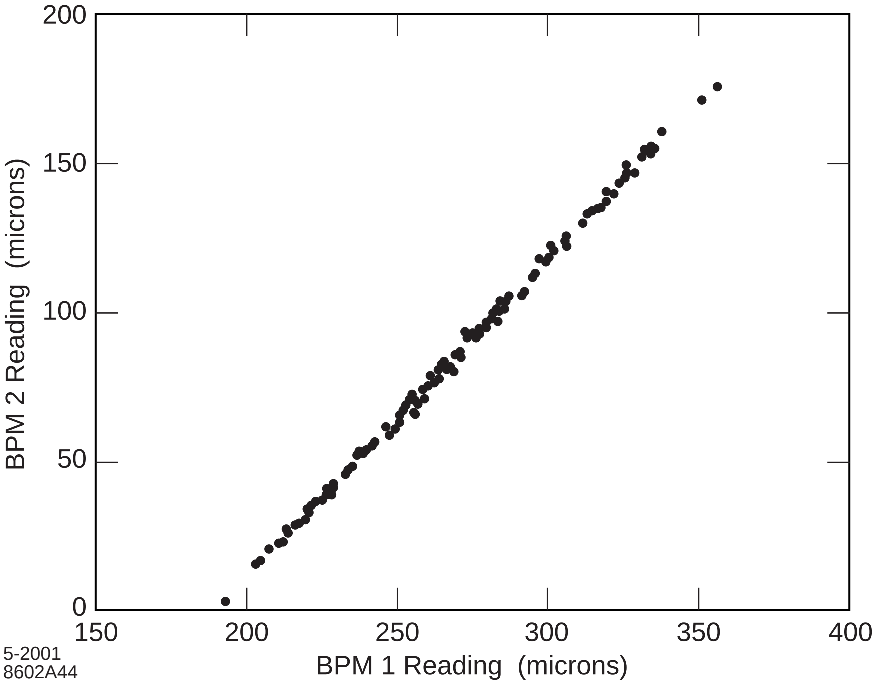

**Figure 7.6:** Correlation of BPM readings in the FFTB. Two BPMs set close to one another were read out on 100 consecutive pulses. The deviation from a straight line indicates a pulse-to-pulse resolution of 1 μm.

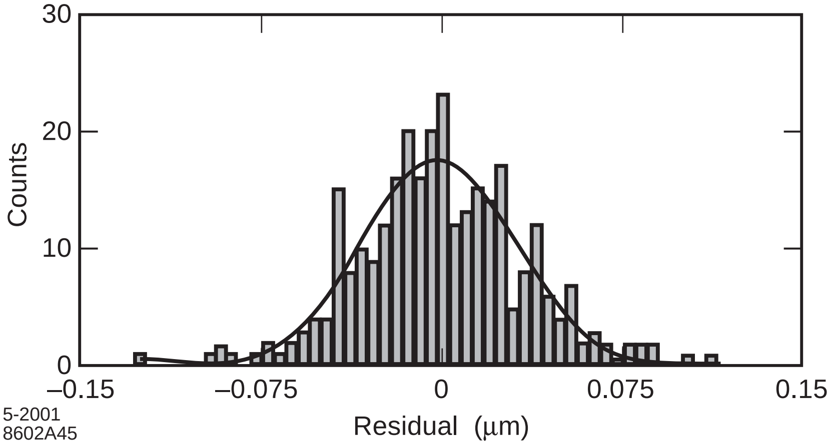

**Figure 7.7:** Resolution of a single-cavity rf BPM. Three BPMs were installed in close proximity, and the readings of the upstream and downstream BPMs were used to predict the reading of the center BPM. The histogram above is the residual of that fit, which indicates a single-pulse resolution of the BPMs of 25 nm.

**Rf-Structure Beam Position Monitors (S-BPMs):** The position of the beam in the rf structure is measured by detecting the amplitude and phase of the dipole wakefield signal (see Chapter 4 for a detailed description of the rf structure design). Each cell in the structure has a unique dipole mode frequency; by selecting the frequency that is measured, the beam position in a given cell can be determined. Figure 7.8 shows a comparison of the beam-to-structure offset measured in this manner (points) and the structure deviation from straightness measured with a Coordinate Measuring Machine (line). The pulse-to-pulse resolution of the structure BPM is 1-2 μm. When potential bowing or other deviations from straightness are included, the BPM has an "effective" resolution of approximately 5 μm (i.e., when the upstream and downstream S-BPMs read zero, the rms beam-to-structure offset is 5 μm).

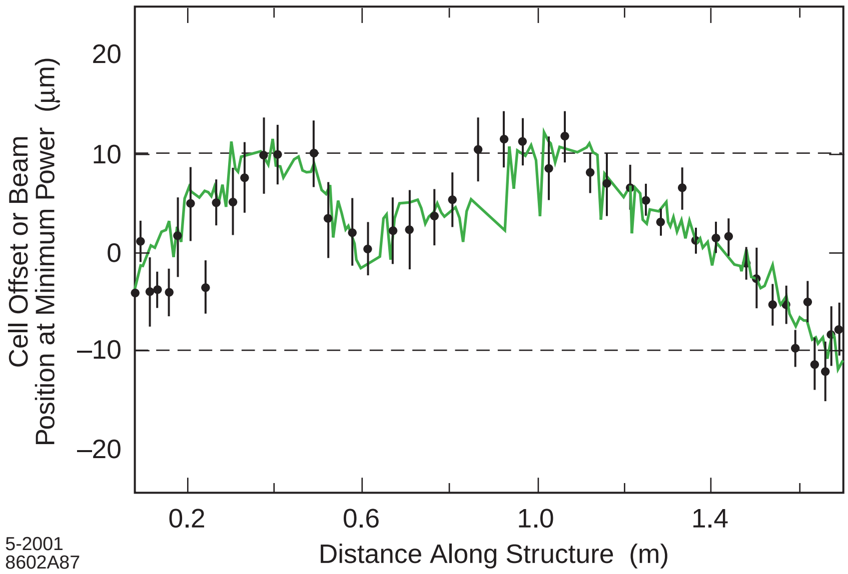

**Figure 7.8:** Comparison of rf structure relative cell positions measured by dipole-mode BPM (points) and Coordinate Measuring Machine (line). Dashed lines show NLC rms structure alignment tolerance.

**Quadrupole and Rf Girder Translation Stages:** Figure 7.9 shows a schematic of the FFTB magnet mover, which permitted the FFTB quads to be moved horizontally or vertically during beam operations. The FFTB mover's single step was 0.3 μm. For the NLC, the extremely small vertical beam sizes imply that the single step must be reduced to about 50 nm, a factor of six smaller than the FFTB mover. This can be achieved by utilizing microstep control over the stepper motors. The step size of the girder mover is not critical and can even be larger than 0.3 μm without deleterious effects.

### 7.4.3 Rf Girder Alignment

The rf structure BPM directly measures the dipole wakefield, which is the quantity which must be minimized to preserve the emittance. Thus, when the S-BPM reads zero, the dipole wakefield is actually close to zero – there is no DC offset in the S-BPM. Consequently, an adequate strategy for rf girder alignment is to read out all of the BPMs on the girder (12 in all) and move the girder to zero the average BPM reading and also the girder slope. With an effective resolution of 5 μm, the resulting emittance dilution from girder alignment is approximately 3%.

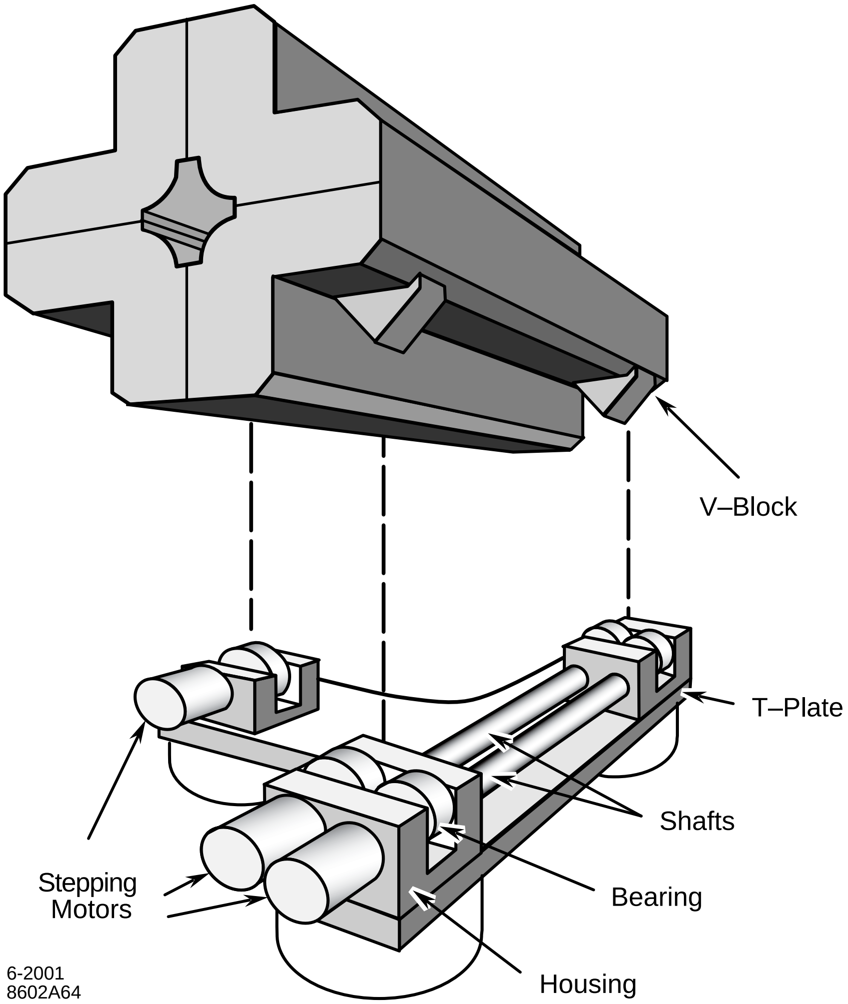

**Figure 7.9:** Schematic of the Final Focus Test Beam magnet mover. The mover had horizontal, vertical, and roll degrees of freedom, and could move magnets by 0.3 µm steps over a range of 3 mm in each degree of freedom.

### 7.4.4 Quadrupole Alignment

Given the sensitivities shown in Table 7.4, it is clear that alignment of quadrupoles to the beam will consume most of the main linac emittance budget. Quadrupole alignment is made more complicated in general by the fact that the electrical center of the Q-BPMs cannot be fiducialized to the magnetic center of the quadrupoles at the micron level. The mechanical alignment and fiducialization procedure probably cannot achieve better accuracy than 100 µm rms, and cabling and electronics calibration can add additional errors. Furthermore, the offset between the Q-BPM electrical center and the quadrupole magnetic center cannot be assumed to be stable over time. Finally, any beam-based quadrupole alignment procedure must take into account the fact that diffusive ground motion (ATL motion, see section 7.2.3) will cause the quadrupoles to slowly change their positions.

Given these issues, the procedure to be used to achieve and maintain adequate alignment of the beam to the quadrupoles is summarized below and then each step is described in more detail. Note that it is assumed that the rf girders can be moved into an aligned position during this procedure at any time required.

- Determine the ‘Gold Orbit’ of the linac. This is the set of Q-BPM readings that corresponds to high luminosity. In the absence of BPM-to-quad offsets, the gold orbit would simply be zero on all BPMs. The procedure for determining the gold orbit can be invasive and incompatible with colliding for luminosity.
- Move the quadrupole magnets until the gold orbit is achieved.
- Use a set of discrete steering feedback systems in the main linac to minimize the orbit drift as a function of time. The steering feedback can operate quickly (at the level of 1 Hz or faster), and is entirely compatible with colliding for luminosity.
- As diffusive ground motion moves the accelerator components, the luminosity will gradually decline. This is because the misalignments between the feedback correctors will become sufficiently large that the feedback can no longer maintain a reasonable approximation of the gold orbit. At this time, recover the gold orbit by moving all of the magnets via their movers. It is assumed that this procedure is compatible with colliding for luminosity, which implies that the magnet mover step sizes are small and that no more than 1 step per linac pulse (at 120 Hz) is taken.
- Over even longer time scales, the gold orbit will gradually cease to provide good luminosity. This is because the electrical centers of the Q-BPMs, the magnetic centers of the quadrupoles, and other parameters are subject to change over time. Once this has happened, return to step 1 and determine a new gold orbit using invasive procedures.

**Determine the Gold Orbit:** This is the most crucial step in the algorithm as the quality of the gold orbit will always determine the maximum luminosity performance of the collider. The best situation imaginable is one in which all of the Q-BPMs are perfectly fiducialized *ab initio* to the centers of their quadrupoles, and the fiducialization is perfectly stable with time. In this case, ‘gold’ is when all of the Q-BPMs read zero.

Since this situation is not achievable in practice, the next best situation is one in which the BPM-to-quad offsets can be measured by the beam. This is a measurement that is routinely performed at accelerators all over the world. The focusing strength of each quadrupole is varied, and the resulting deflection of the beam is measured on downstream BPMs. This allows determination of the beam-to-quad offset, and the quad-to-BPM offset of the nearest BPM can then be deduced by subtraction. This technique is so commonly applied under so many circumstances that when accelerator physicists discuss ‘beam-based alignment,’ they almost invariably refer to the quad-varying technique. This procedure was performed in the FFTB, and statistics-limited resolutions of 1 to 30 μm were repeatedly achieved. For the NLC main linac, a resolution of 1 μm would be straightforward to achieve for each quad, if the technique were not limited by systematic errors. If the quadrupole center position moves as the quad strength is varied, the fitted beam-to-quad offset will not be accurate. The size of the resulting error is inversely proportional to the fractional strength variation of the magnet [22].

Because the accurate determination of the BPM offsets will still provide the most local (hence most stable) correction of the emittance, the quad-varying technique remains the method of choice for determining the gold orbit. However, the sensitivity to quad-center variation suggests that this technique may not be adequate. This is especially true for adjustable quadrupoles energized by permanent magnets, where certain defects in the magnet construction can cause an offset of the magnetic center that cannot be detected by changing the quad strength. An alternative technique for generating a gold orbit, which has been used successfully at a wide variety of laboratories, is Dispersion Free Steering (DFS), in which the dispersion is measured by varying the energy of the beam and measuring the change in the trajectory [23]. This technique is less local than varying a single quad at a time and measuring the resulting deflection, but it directly measures the dispersion (which is the source of emittance dilution from misaligned quadrupoles) and permits a direct correction of it. Furthermore, DFS relies only upon the BPM resolution to achieve an acceptable trajectory, and the NLC BPMs will have a resolution that is much better than the knowledge of the BPM-to-quad offset under almost any imaginable circumstances.

In linear accelerators, a potential source of systematic errors when varying the energy gain is that any deflections due to rf structures (from structure tilts, unbalanced input couplers, etc.) will also vary and affect the accuracy of the measurement. To avoid this, it is possible to change the energy of the beam upstream of the first quad to be aligned while maintaining the energy gain in the region to be aligned. In this way, any rf steering becomes a change in the incoming beam trajectory which can be either corrected or fitted out. This technique has been studied in simulation for the 500 GeV per beam NLC main linac. The emittance dilution after convergence is 20% for 0.3 μm BPM resolution, and 80% for 1.0 μm resolution. The latter simulation assumes a poorer resolution than the BPM specification because experience with model-dependent tuning algorithms indicates that small errors in the knowledge of the beam-line optics typically cause the effective BPM resolution to be somewhat worse than the actual, signal-to-noise resolution figure would indicate.

Additional improvement to the emittance can be achieved by applying closed-orbit bumps over a small region of the linac. These bumps generate dispersion at a particular phase and in a particular location, which can cancel any existing dispersion at that phase and location. The SLC made excellent use of such ‘emittance bumps,’ which were tuned by minimizing the beam size measured on a diagnostic device (typically a wire scanner) while varying the bump amplitude. A simulation has been performed in which a set of dispersion bumps was applied to the main linac after DFS convergence. The number of bumps required is a function of the beam-line chromaticity and the energy spread. The combination of these parameters determines how many lattice periods are required before irreversible phase mixing (‘filamentation’) has occurred. Given the NLC parameters, the appropriate distance scale is approximately 100 quadrupoles, so a total of 14 bumps (2 phases/region and 7 regions) was used. In the case where 0.3-mm BPM resolution was assumed for DFS, the final DFS + bumps emittance dilution is 5%, while in the 1.0-μm resolution case the final DFS + bumps emittance dilution is 25%. Note that the emittance bumps can be applied to the main linac even in the case where quad shunting has been used to determine the gold orbit, and thus the final emittance dilution can in principle be very small. The solution which uses DFS and bumps depends primarily on the BPM resolution, and therefore constitutes the worst case for gold orbit performance.

**Main Linac Steering Feedback:** Section 7.3 indicated that steering feedback which stabilizes the NLC beam trajectory at frequencies up to ~1 Hz is essential to maintain luminosity. Since all of the quadrupoles in the NLC main linac are mounted on translation stages, one can conceptually imagine that every quad is available to participate in ‘steering feedback.’ It is not practical from either a mechanical engineering or a machine protection standpoint to have heavy quadrupole magnets moving around at a few hertz. Therefore the NLC main linac will use several discrete sets of fast, weak dipole correctors to provide steering feedback at 5 to 10 locations within the beam line. Steering feedback played a crucial role in the performance of the SLC over its lifetime, but in the last few years, several limitations to the feedback operation were observed. Considerable beam time and simulation efforts have been invested in understanding those limitations and in finding appropriate remedies. The most significant discoveries were [16,24]:

- The response speed of the steering magnets in the SLC is typically slower than was originally assumed in the design of the feedback, and additional difficulties arose in systems where the correctors had differing response speeds.
- Because a disturbance at the beginning of the linac will change the orbit in all of the feedback regions, the SLC feedback systems communicated with one another to prevent multiple loops from simultaneously trying to correct the same oscillation. In the presence of wakefields, the simple 1-to-1 connectivity of the SLC feedback was not adequate. Therefore as the SLC bunch charge was increased (and wakefields became more intense) the limitations in the system became more significant. Subsequent tests with an improved communication between systems gave better performance.
- The SLC linac had a suboptimal configuration of feedback loops, in terms of the relative spacing and placement of BPMs and corrector magnets. A configuration in which a single feedback loop has several sets of correctors and BPMs that occupy a more extended length of the linac has shown much-improved performance.

The lessons above have been applied to the design of an NLC main linac feedback configuration [16].

The main linac feedback provides partial reduction of the emittance dilution arising from diffusive ground motion. Figure 7.10 shows the emittance as a function of time at the end of the NLC main linac

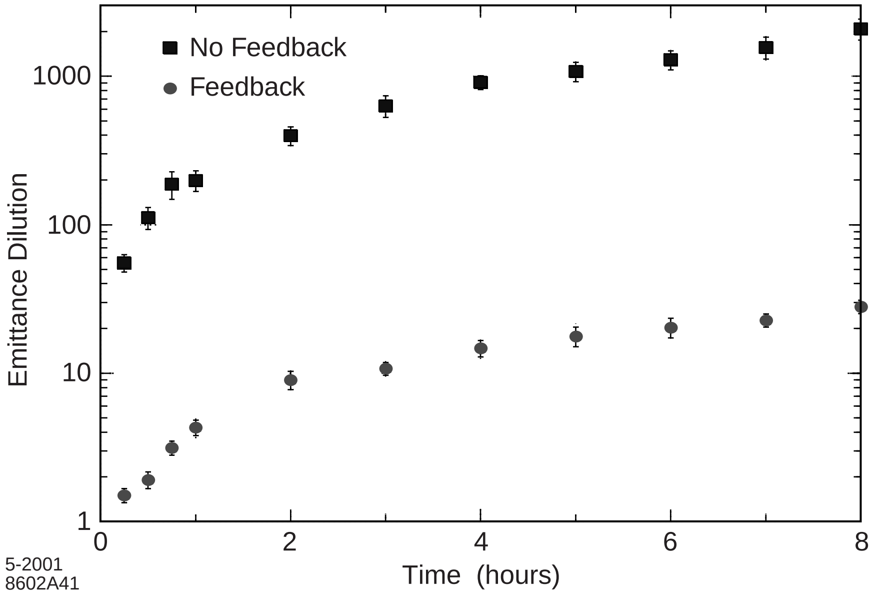

**Figure 7.10:** Emittance dilution (%) in the NLC main linacs due to diffusive ground motion, assuming an ATL coefficient comparable to that measured at SLAC. A case with no linac feedbacks (squares) and a case with the proposed NLC steering feedback architecture (circles) are both considered.

due to ATL motion, assuming a coefficient $A$ of 5 x $10^{-7}$ $\mu m^2/m/s$, both with and without steering feedback in the main linac. Without feedback, the emittance dilution in the main linac would become unacceptable within minutes, while the addition of steering feedback preserves the emittance for hours.

**Steering the Main Linac with Quadrupole Movers:** As Fig. 7.10 shows, the use of steering feedback only delays the time at which the emittance dilution in the main linac reaches unacceptable levels. This is because, while the steering feedback can maintain the gold orbit at discrete locations, the orbit between these locations drifts away and gradually dispersion and wakefields increase in these areas. It is necessary to recover the gold orbit throughout the linac by periodically moving all of the quadrupoles on their magnet movers. This is usually referred to as 'mover steering.'

In theory, mover steering can be seen as a simple inversion of the matrix that relates quadrupole positions to BPM readings. In practice there are other constraints which require additional refinements to the algorithm. A mover steering algorithm that recovers a desired orbit, constrains the rms motion of the quadrupoles in order to prevent their movers from running out of range, and does not introduce other sources of emittance dilution has been designed for the NLC main linac [25]. This algorithm divides the linac into shorter regions that are steered sequentially. Conservative estimates indicate that the algorithm could steer every such region, from the injection end of the main linac to the extraction end, in about 30 minutes. In order to minimize emittance dilution, it is assumed that this algorithm will operate continuously in the NLC linacs. After the last region at the end of the linac is steered to the gold orbit, the algorithm will once again steer the first region at the start of the linac. The time-averaged emittance of the main linac will be increased because the steering algorithm requires a finite time to execute, during which the feedback is solely responsible for minimizing dilution from diffusive ground motion. There will also be some additional dilution because the beam-to-quad offsets will be different by an amount determined by the resolution of the Q-BPMs. Figure 7.10 suggests that the time-averaged luminosity loss from the slow completion of mover steering will be on the order of 2%, while the Q-BPM resolution will introduce perhaps another 0.5% loss.

**Determining a new Gold Orbit:** With the passage of time, the emittance obtained by repeatedly steering to the gold orbit will increase, as the BPM-to-quad offsets change. Once this has happened, it is necessary to repeat the procedure that was used to determine the gold orbit in the first place. The length of time between determinations of the gold orbit is difficult to estimate. Measurements of the BPM centers in the FFTB stripline BPMs suggest that once a month will be adequate, and aggressive use of emittance bumps can further extend the life of a gold orbit. It is unclear how frequently the gold orbit should be reestablished for the NLC, but it will certainly depend on how long the procedure takes and how much integrated luminosity is therefore lost. One of the benefits of the DFS technique is that it is extremely fast, since the energy gain of the linac can be varied on a pulse-by-pulse basis. Assuming that the gold orbit does not change dramatically from measurement to measurement, it is conceivable that use of DFS could take less than one 8-hour shift for the entire linac.

### 7.4.5 Sources of Multibunch Emittance Dilution

Table 7.4 lists several sources of multibunch emittance dilution. These are effects in the main linac which cause the various bunches in a given bunch train to follow different trajectories down the beam line. Assuming that the damping and detuning are sufficiently robust to eliminate long-range BBU instabilities, the rf structure defects which cause multibunch emittance will generate a set of bunch-by-bunch deflections which are nearly constant in time. As a result, the multibunch emittance dilution will be amenable to a feedback that corrects bunch positions within a train. Such a feedback is simultaneously fast (i.e., its BPMs and correctors have a bandwidth of several-hundred MHz) and slow (i.e., the system applies nearly the same set of corrections to each train). The NLC linac design includes several subtrain feedback systems that utilize high-bandwidth BPMs and stripline kickers similar in many ways to the high-bandwidth transverse feedback of modern storage rings. Analytic estimates indicate that such a system can reduce the emittance dilution from multibunch sources by roughly a factor of 10, limited by the system bandwidth and the signal-to-noise performance of the BPMs [26].

### 7.4.6 Summary and Proposed Main Linac Tolerances

The most serious sources of emittance dilution in the NLC main linac are short- and long-range beam-breakup instabilities, which must be cured through a combination of rf structure design, quadrupole lattice design, and introduction of a correlated energy spread to permit damping of the short-range instability. Once this is accomplished, other sources of emittance dilution can be addressed through a combination of tuning, diagnostics, beam-based feedback, and good engineering practices. Table 7.5 shows a tentative distribution of the main linac emittance budget amongst the various sources of dilution. Since the studies in this section were performed with the 1 TeV cms configuration of the NLC, the lower-energy configurations, which have fewer rf structures and thus less challenging beam dynamics, should be substantially better. In addition, Table 7.5 assumes that DFS + bumps must be used for generation of a gold orbit, and that the 1.0 μm effective BPM resolution is achieved.

**Table 7.5:** Tentative distribution of the NLC Main Linac emittance budget and resulting engineering tolerances. Dilutions are applied to the vertical plane except where indicated. Gold Orbit assumes DFS + bumps with 1.0-μm effective BPM resolution, and is converted to an ‘effective quad misalignment’ by use of Table 7.4. Multibunch sources assume factor of 10 suppression via subtrain feedback. Note that the tolerance on structure dipole frequencies is for the worst-case error mode (random cell-by-cell frequency errors which are reproduced in every structure), and all other distributions of frequency errors have considerably looser tolerances.

| EFFECT | TOLERANCE | RESULTING EMITTANCE DILUTION |
|---|---|---|
| Gold Orbit (quad misalignments) | 2.0 μm (effective) | 25% |
| Quad Strength Errors | 0.1% | 0.7% (x)<br>0.5% (y) |
| Structure Misalignments | 30 μm | 7% |
| Structure Tilts | 30 μrad | 4% |
| Quadrupole Rotations | 200 μrad | 4% |
| S-BPM Resolution | 5 μm | 3% |
| Mover Steering Interval | 30 minutes | 2% |
| Structure Straightness (bow) | 50 μm | 1% (inc. feedback) |
| Structure Straightness (random walk) | 3.5 μm | 1% (inc. feedback) |
| Structure Dipole Frequencies | 1 MHz | 1% |
| Synchrotron Radiation | | 3% (x) |
| Total | | 3.7% (x)<br>49% (y) |

## 7.5 Emittance Dilution in the Final Focus

The beam dynamics in the final focus are extremely different from the beam dynamics in the main linac. The number of quadrupoles and the rms beam energy spread are both quite small, so phase mixing in the final focus is not a serious problem. This in turn implies that global correction knobs of various kinds will be more effective than in the linac. The final focus also contains horizontal bend magnets, so it is possible to adjust the dispersion with normal or skew quads at high-dispersion points rather than by varying the beam trajectory, as is done in the linac. On the other hand, the final focus contains many strong aberrations, such as chromaticity, sextupoles, and skew quadrupole effects, which typically are delicately balanced against one another. A related issue is that $\beta^*_y$ is so small compared to $L^*$ that small changes in the strength of the normal quads can reduce the luminosity. The final focus, therefore, has looser tolerances on the conditions that must be met before global corrections are applied than the main linac has, but the tolerances on stability over time are much tighter than in the main linac.

The final focus of the NLC, like the main linac, is designed with powerful diagnostic capabilities and robust correction devices. Every quad and sextupole is on a remotely controlled magnet mover, similar to those in the main linac. Each quad is paired with a BPM with submicron resolution, and in some crucial locations ultra-high resolution cavity BPMs with resolutions better than 100 nm are also used. Laser-based beam-size monitors are installed at critical locations. All sextupoles, bends, and quads except for the final doublet are iron-dominated electromagnets, with high-precision power supplies. In addition, the final focus has two powerful diagnostics not available at other locations, the luminosity and the beam-beam deflection, each of which will be measured on every pulse in order to provide signals for feedback systems.

### 7.5.1 Principal Sources of Emittance Dilution

Several different types of emittance dilution are important in the final focus. Waist shifts arise from strength errors in normal quadrupoles or horizontal misalignments of sextupoles. Dispersion is caused by quadrupole misalignments, errors in quad strength within the dispersive regions, and misalignments of sextupoles. *x-y* coupling can be due to rotated quads, the detector solenoid, or vertical misalignments of sextupoles. Chromaticity is introduced by an imbalance between the final doublet strength and the chromatic correction sextupole strength. Geometric sextupole aberrations come from an imbalance between the matched pairs of sextupoles or construction errors in the quads. Horizontal beam-beam missteering can be caused by a relative phase error in the two crab cavities and vertical beam-beam missteering from relative motion of the quadrupoles. There are also various forms of relative timing errors between the two beamlines and synchrotron radiation from bends and quads.

### 7.5.2 Correction of Static Errors

It is expected that static sources of emittance dilution will be addressed by a procedure similar to that used to tune the FFTB [27,28]. First, the BPM-to-quad offsets will be measured by shunting the quadrupoles, and this information will be used to mover-steer the final focus. Including systematic errors from the shunting technique, a residual rms beam-to-quad misalignment of approximately 10 μm is expected. Next, the sextupoles will be aligned by scanning the horizontal and vertical positions of each magnet and measuring the resulting horizontal deflection. The deflection will be parabolic, with a minimum amplitude at the aligned position. This technique is expected to have similar precision and accuracy to the quad alignment achieved by shunting. Finally, the beams will be steered into collision and the remaining aberrations will be corrected by maximizing the luminosity with a set of orthogonal tuning knobs. These knobs will be a combination of conventional electromagnet strength knobs and sextupole mover knobs (in which the sextupoles are moved horizontally or vertically to generate pure variations in waist, dispersion, or coupling at the IP). It will also be necessary to iteratively tune the luminosity on both the absolute and relative phases of the crab cavities.

### 7.5.3 Correction of Dynamic Errors

Most of the errors listed in section 7.5.1 are either static or have a sufficiently slow time constant as to be effectively static. The errors that are likely to change on a time scale of seconds to minutes are the relative positions of the beams at the IP and the linear optics aberrations (waists, dispersions, coupling). These aberrations are driven by misalignments of the quads, misalignments of the sextupoles, and strength variations in the quads at the level of $10^{-5}$.

The stabilization of the relative positions of the beams at the IP was discussed in section 7.3. In brief, the NLC will use beam-based feedback and active stabilization of the final doublets to achieve the desired performance. In order for these to be effective, it is necessary to select a site with adequate geological and vibration conditions, and to make a diligent effort to preserve these good conditions during operations. The orbit through the sextupoles will be maintained by another beam-based feedback, in order to minimize the linear aberrations which arise from misaligned sextupoles. In order to function properly, this probably will require a BPM of some form to be mated to each sextupole, but the number of sextupoles is so small that this should be straightforward.

The traditional method of correcting slow drifts in linear optics that are not amenable to a standard feedback is to measure periodically the beam size as a function of the global correction knobs for waist position, dispersion, and coupling. This was used at the FFTB, where a laser-interferometer beam size monitor was installed at the IP [6], and at the SLC, where the slope of the beam-beam deflection (deflection versus beam-beam offset) was used [29]. More recently, the SLC developed a technique called 'dither feedback.' Rather than occasionally scanning the global knobs against the beam size, the global knobs are constantly varied through a small range and set to optimize the luminosity [30]. Although the SLC luminosity monitor signal-to-noise performance was poor, the signal was available at the full 120-Hz machine rate, which permitted extensive averaging. It was found that the dither feedback was far better at preserving luminosity than the periodic scanning technique. Consequently, such a system is planned for NLC. It is expected that the dither feedback will probably reduce the luminosity by roughly 2% due to the dithering process, but that this loss will be compensated by the stability it will provide.

The tuning and stabilization of the final-focus optics has not been simulated as extensively as the main linac. In one simulation, the performance of the final-focus system under the influence of diffusive ground motion was studied. If the only correction system present is a beam-beam deflection feedback, diffusive ground motion causes a 10% luminosity reduction in under 10 minutes. This time can be increased to more than one month if, in addition, the orbit through the sextupoles and final doublet is maintained by a feedback, and the standard global correction knobs of waist, coupling, and dispersion are periodically retuned. This simulation indicates that mover-steering the final-focus quads and sextupoles need only be performed once per month or less.

## 7.6 Conclusions

The tolerances which the NLC must achieve are well beyond those required by present accelerators. The most severe challenges are in the form of misalignments, from the nanometer-level disturbances of high-frequency ground motion to the emittance dilutions arising from diffusive ground motion. The NLC must also achieve acceptable performance starting from the *ab initio* condition of the beam lines, but static or dynamic misalignments are by far the most serious performance issues.

The tight tolerances are being addressed through a wide variety of means. High-performance BPMs and magnet movers are included throughout the NLC beam lines. High-bandwidth feedback techniques from contemporary storage rings and active stabilization for a small number of magnets will be used. A thorough understanding of the properties of ground motion is essential. In the NLC main linac, which has been the subject of the greatest scrutiny, simulation studies and performance of prototypes indicate that the emittance dilution budget will be achievable. The final-focus performance requirements are comparable to those of the FFTB and the SLC final focus, which demonstrated most of the key techniques and technologies required. The beam dynamics performance desired in the NLC main linac and final focus can be attained with the diagnostics and tuning techniques described.

# References

[1] Smith, S., Tenenbaum, P., Williams, S.H., "Performance of the Beam Position Monitor System of the Final Focus Test Beam," *Nuclear Instruments and Methods,* **A431**:9, 1999.

[2] Slaton, T. , Mazaheri, G., Shintake, T., "Development of Nanometer Resolution C Band Radio Frequency Beam Position Monitor," *Proceedings of the 1998 Linac Conference,* 1998.

[3] Adolphsen, C., et al., "Wakefield and Beam Centering Measurements of a Damped and Detuned X-Band Accelerator Structure," *Proceedings of the 1999 Particle Accelerator Conference,* 3477 1999.

[4] Bowden, G., et al., "Precision Magnet Movers for the Final Focus Test Beam," *Nuclear Instruments and Methods,* **A368**:579, 1996.

[5] Alley, R., et al., "A Laser-Based Beam Profile Monitor for the SLC/SLD Interaction Region," *Nuclear Instruments and Methods* **A379**:363, 1996.

[6] Tenenbaum, P., and Shintake, T., "Measurement of Small Electron Beam Spots," *Annual Review of Nuclear and Particle Science,* **49**:125, 1999.

[7] Fenn, R.J., Slaton, T., Woods, M. "Quadrupole Vibration Measurements for QM1B and QC3 in the Final Focus Test Beam at SLAC," LCC-0036, a SLAC/NLC Linear Collider Note, 2000.

[8] Tenenbaum, P., "Expanded Studies of Linear Collider Final Focus Systems at the Final Focus Test Beam," SLAC-Report-475, 1995.

[9] Raimondi, P., et al., "Recent Luminosity Improvements at the SLC," *Proceedings of the 1998 Conference on High Energy Accelerators,* 1998.

[10] Assmann, R., Raimondi, P., Roy, G., Wenninger, J., "Emittance Optimization with Dispersion Free Steering at LEP," *Physics Review:* Special Topics – Accelerators and Beams **3**:121001, 2000.

[11] Seeman, J.T., Decker, F.-J., Hsu, I., "The Introduction of Trajectory Oscillations to Reduce Emittance Growth in the SLC Linac," *Proceedings of the 1992 Conference on High Energy Accelerators*, 879, 1992.

[12] Seryi, A., Napoly, O. "Influence of Ground Motion on the Time Evolution of Beams in Linear Colliders," *Physical Review* **E53**:5323, 1996.

[13] Baklakov, B., et al., "Ground Vibration Measurements for Fermilab Future Collider Projects," *Physical Review:* Special Topics – Accelerators and Beams **1**:031001, 1999.

[14] Shiltsev, V., "Space-Time Ground Diffusion: the ATL Law for Accelerators," in *Proceedings of the 1995 International Workshop on Accelerator Alignment*, 352, 1995.

[15] Seryi, A., "Investigations of Slow Motions of the SLAC Linac Tunnel," in *Proceedings of the 2000 Linac Conference,* 62, 2000.

[16] Hendrickson, L., et al., "Feedback Systems for Linear Colliders," in *Proceedings of the 1999 Particle Accelerator Conference,* 338, 1999.

[17] Adolphsen, C., et al., *A Zeroth-Order Design Report for the Next Linear Collider,* 1054, 1996.

[18] Halbach, K., "Design of Permanent Multipole Magnets with Oriented Rare Earth Cobalt Material," *Nuclear Instruments and Methods,* **169**:1, 1980.

[19] Napoly, O., Reyzl, I., Tesch, N., "Interaction Region Layout, Feedback, and Background Issues for TESLA," presented at the *4th International Workshop on Linear Colliders,* 1999.

[20] Smith, S.R., "Design of an NLC Intra-Pulse Feedback System," LCC-0056, a SLAC/NLC Linear Collider Note, 2001.

[21] Balakin, V.E., Novokhatsky, A.V., Smirnov, V.P., "VLEPP: Transverse Beam Dynamics," in *Proceedings of the 12th Conference on High Energy Accelerators*, 119, 1983.

[22] Tenenbaum, P. and Raubenheimer, T.O., "Resolution and Systematic Limitations in Beam Based Alignment," *Physics Review:* Special Topics – Accelerators and Beams **3**:052801, 2000.

[23] Raubenheimer, T.O., Ruth, R.D., "A Dispersion Free Correction Technique for Linear Colliders," *Nuclear Instruments and Methods,* **A302**:191, 1991.

[24] Hendrickson, L., Phinney, N., Raimondi, P., "Beam-Based Feedback Testing and Simulations for the SLC Linac," *Proceedings of the 2000 Linac Conference,* 515, 2000.

[25] Tenenbaum, P., "Simulation Studies of Main Linac Steering in the Next Linear Collider," *Proceedings of the 1999 Particle Accelerator Conference,* 3459, 1999.

[26] Tenenbaum, P., "Spectral Content of the NLC Bunch Train Due to Long-Range Wakefields," LCC-0015, 1999.

[27] Oide, K., "Design of Optics for the Final Focus Test Beam at SLAC," *Proceedings of the 1989 Particle Accelerator Conference,* 1319, 1989.

[28] Tenenbaum, P., et al., "Beam-Based Optical Tuning of the Final Focus Test Beam," *Proceedings of the 1995 Particle Accelerator Conference,* 749, 1995.

[29] Bambade, P., Erickson, R., "Beam-Beam Deflections as an Interaction Point Diagnostic for the SLC," *Proceedings of the 1986 Linac Conference,* 475, 1986.

[30] Hendrickson, L. et al., "Luminosity Optimization Feedback in the SLC," *Proceedings of the 1997 International Conference on Accelerator and Large Experimental Physics Control Systems (ICALEPCS)*, 450, 1997.

# Chapter 8

## Gamma-Gamma Interaction

### 8.1 Gamma-Gamma Interaction Region

The scientific advantages of incorporating high-energy $\gamma\gamma$ collisions into an $e^+e^-$ collider design have been discussed from the earliest collider physics meeting in Saariselka, Finland in 1989. $\gamma\gamma \rightarrow$Higgs is a fundamental process that opens a window on new physics beyond the standard model. In the past, the technical challenges posed by the laser system and the interaction region seemed to be overwhelming and kept the option of a $\gamma\gamma$ collider out of the mainstream program. Recently, there has been sufficient progress on both these fronts to change that view and to allow the $\gamma\gamma$ collider to be considered a feasible addition to the LC project [1].

The required laser power is now available from the Mercury laser developed at LLNL for fusion applications. It is a relatively straightforward R&D effort to take the 100-joule, 10-Hz output of a Mercury laser and to shape its time structure to match that of the NLC running in $\gamma\gamma$ mode with 95 bunches separated by 2.8 ns. Only twelve such lasers would be required for both the electron and positron beams. Schemes being discussed as recently as 1995 called for hundreds of lasers costing billions of dollars; the current picture is technically and fiscally more viable.

The breakthrough in IR design has been the development of large annular optics which permit the laser beams to be focused to the required 10 micron spots without putting any material in the path of the residual electrons, noninteracting photons or charged particle debris arising from the beam-beam collision. These unwanted particles now can pass unimpeded down the extraction line. The performance of a fully engineered IR design based on such optics was simulated, and found to be adequate. While much work needs to be done in detailing the measures required to control the laser-beam quality in the IR environment, the fundamental problem has been resolved.

### 8.2 Laser Architecture

For maximum luminosity, every electron bunch should collide with a laser pulse of sufficient intensity that 63% of the electrons undergo a primary Compton backscatter. The laser pulse energy required to achieve this is minimized when the Raleigh range of the laser focus and the laser pulse width is matched to the 100-micron length of the electron bunch. However, to avoid nonlinear QED effects the maximum intensity must also be limited. A pulse of 1 joule in 1.8 ps FWHM optimizes the conversion. This corresponds to a peak power in the terawatt range. Such high peak power was made possible by the invention in 1985, of chirped pulse amplification [2,3].

For $\gamma\gamma$ operation, The NLC bunch structure consists of trains of 95 bunches separated by 2.8 ns, with 120 trains per second. This means that 11,400 laser pulses per second must be produced, requiring an average laser power of 10 kilowatts. Additionally, these pulses have to be produced with the correct temporal spacing to match the electron-bunch structure. No current laser architecture can achieve all of these requirements at once. However, the Mercury laser, developed for a laser-fusion application, can be modified to deliver the required pulse format. The Mercury laser, as shown in Fig. 8.1, has two amplifier heads, allowing four amplification passes. Running at 10 Hz it can produce pulses of 100 joules with a pulse width of a couple of nanoseconds. The single pulse of 100 joules can be subdivided into 100 1-joule pulses separated by 2.8 ns either through modification of the front end or through a combination beam splitter and optical delay line. A set of twelve of these lasers, each running at 10 Hz, could then be combined to provide the 120 Hz required for the NLC.

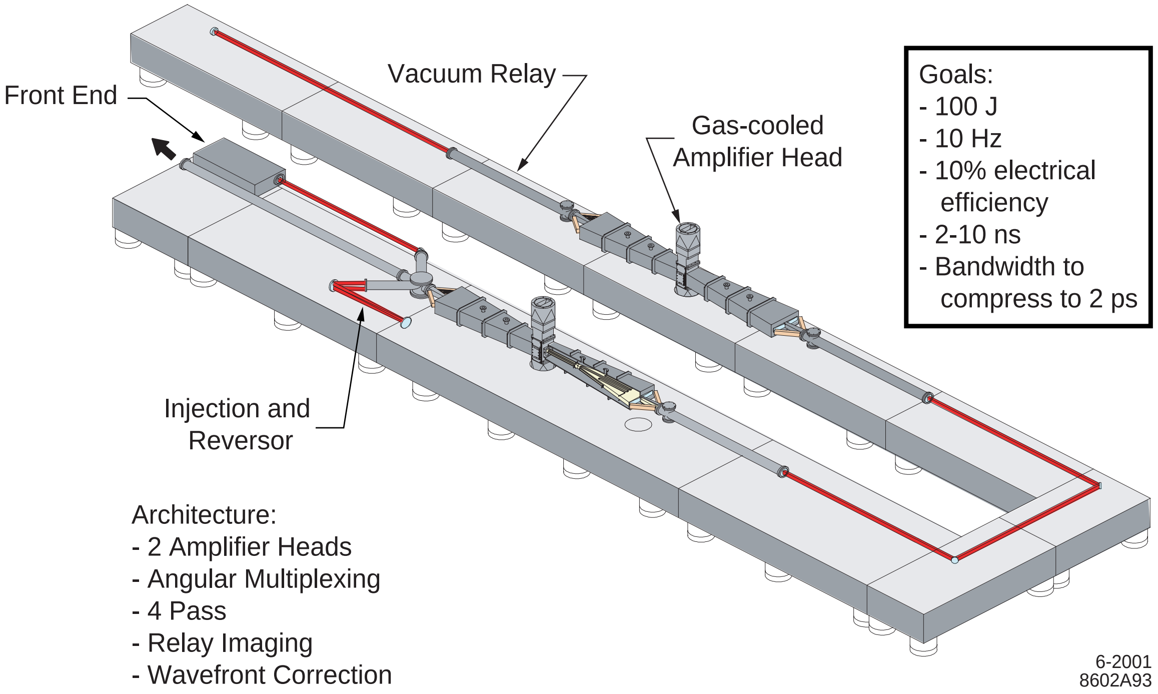

**Figure 8.1**: The diode-pumped solid state Mercury laser is a high pulse rate, next-generation laser fusion driver.

The Mercury laser combines several key technologies (see Fig. 8.2) to achieve the required performance. The Ytterbium-Strontium-Fluorappetite Yb:S-FAP crystals are pumped by diode arrays. Since the diode output can be tuned to the pump band of the crystals, they can achieve an efficiency of 10% for converting wall plug power to laser light. The long upper-state lifetime of the crystals allows the laser to be pumped more slowly, reducing the required peak diode power. This is a great advantage since the diode arrays are the cost driver for the system. The waste heat deposited in the crystal is removed by helium gas flowing perpendicular to the crystal plates. This minimizes thermal distortion and allows the laser to produce high average power while retaining good beam quality.

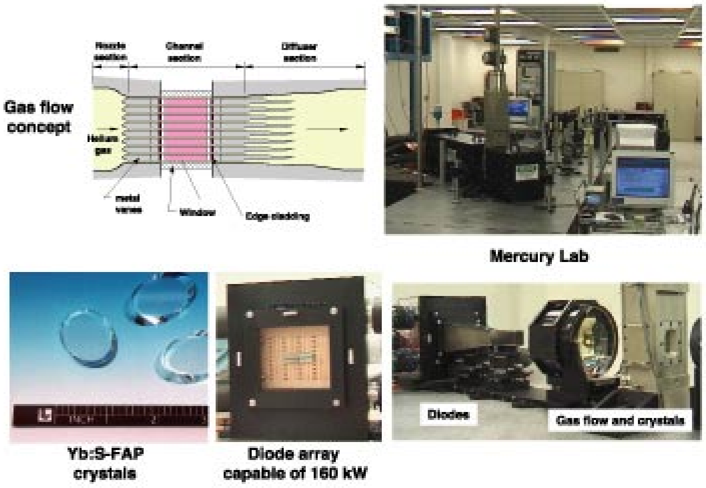

**Figure 8.2:** The Mercury laser will utilize three key technologies: gas cooling; diodes; and Yb:S-FAP crystals to deliver 100 J at 10 Hz with 10% efficiency.

## 8.3 Optics and Interaction Region

The laser pulse and the electron bunch intersect 5-mm away from the interaction point. The optics required to focus the laser must be located in the confined space of the interaction point (IP). They must be situated such that they do not interfere with the accelerator or degrade the performance of the detector. Figure 8.3 shows a schematic of the interaction region with the beam pipe, masks, detector components and optics, starting from the standard design of the $e^+e^-$ interaction region. The intensity of the laser beams requires that they be propagated in vacuum and that transmissive optics be kept to a minimum. Therefore, the optics are located in the beam pipe which is enlarged to accommodate them. The three small mirrors provide the ability to adjust the focus while the large final optic allows the beam to be focused to a 10-micron diameter spot. Not shown in Fig. 8.3 is a complementary set of mirrors on the other side of the IP. They catch the laser pulse, reflect it and refocus it onto the opposite electron beam. Thus each laser pulse does double duty and reduces the total required laser power.

To prevent the material of the mirrors from contributing to detector backgrounds they have been placed such that they avoid the incoming and outgoing beams and the pair background. The smaller mirrors pose no problem but the large mirror requires a large hole in the center to prevent the pair background from showering in it. This requires the laser pulse to be preshaped to be cylindrical.

One other modification to the interaction region is required. The extraction-line aperture must be increased to +/– 10 milliradians to accommodate the increased outgoing beam divergence in $\gamma\gamma$ collisions. To prevent interference between the extraction line and the final- focus quadropole, the crossing angle is increased from 20 to 30 milliradians. Once a detailed design of the final-focus quadrupole is available this angle should be made as small as possible. The increased extraction-line aperture has an effect on the detector. The first two layers of the SVX now have a direct line of sight back to the beam dump and will

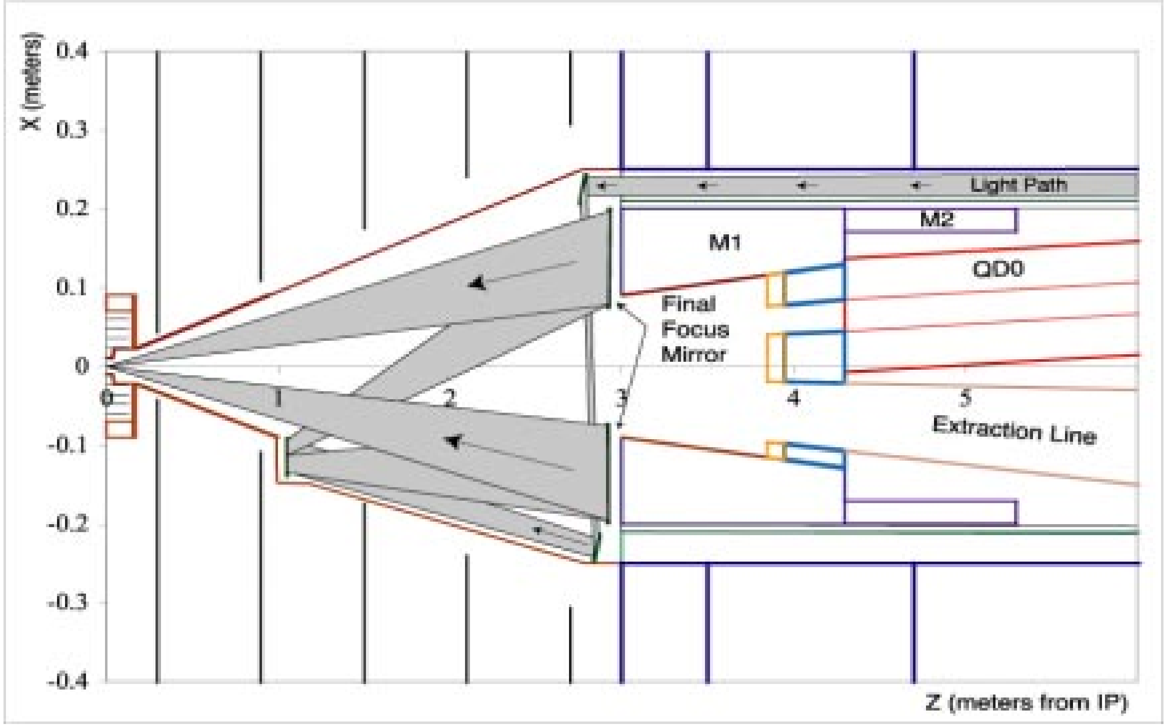

**Figure 8.3**: Optical configuration to inject the laser light into the Interaction Region. The high subpulse intensity requires all these optics to be reflective and mounted inside the vacuum enclosure.

see a flux of $10^{11}$ neutrons/cm$^2$/year. The standard CCDs will need to be replaced with a more radiation-hard technology.

## 8.4 The Benchmark $\gamma\gamma \rightarrow H \rightarrow b\bar{b}$ mode

The measurement of the two-photon width of the Higgs is one of the main physics analyses for a photon collider. Since $\gamma\gamma \rightarrow H$ proceeds through a loop diagram and all particles with mass and charge can contribute to it, this mode is an excellent probe of new physics beyond the standard model. For this design of the laser and optics, the CAIN [4] program has been used to simulate the $\gamma\gamma$ luminosity spectrum. Figure 8.4 shows the calculated luminosity for running conditions optimized for a 120-GeV Higgs. The high-energy peak is dominated by photons from primary Compton backscatters. The low-energy tail comes from photons produced when spent electrons multiply interact with the laser and from beamstrahlung photons. Using 80% electron polarization and 100% circular polarization of the laser enhances the peak luminosity and allows control of the spin state. This allows an enhancement of the spin 0 $\gamma\gamma \rightarrow H$ mode and suppression of the standard model background $\gamma\gamma \rightarrow b\bar{b}$ which proceeds through spin 2 [5].

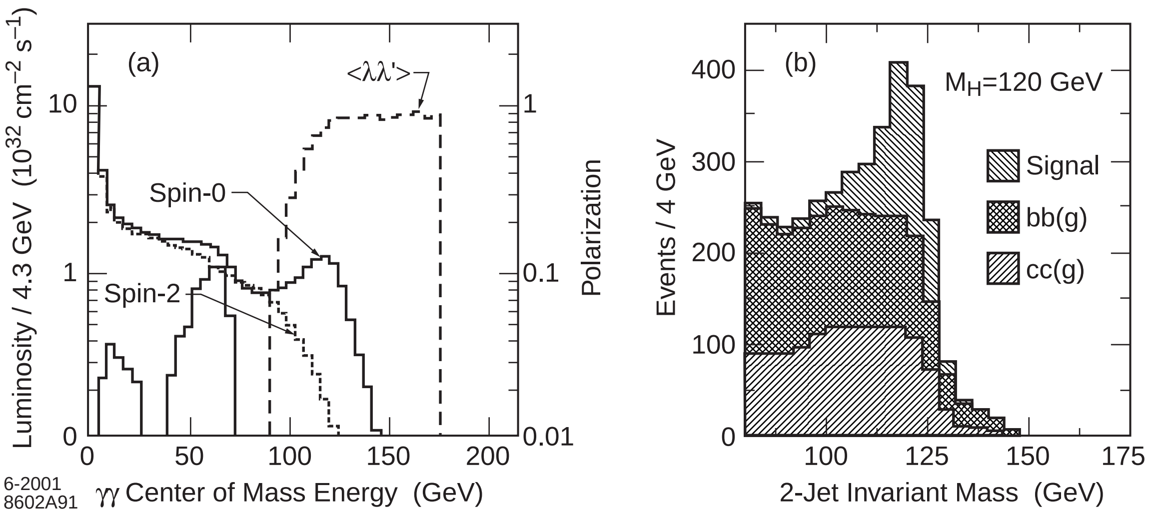

**Figure 8.4:** $\gamma\gamma$ luminosity distribution for Higgs factory running is shown in plot (a) as luminosity per 4.3-GeV bin and the Higgs to $b\bar{b}$ signal and backgrounds are shown in (b) as events per 4 GeV bin after integrating $10^7$ s.

## References

[1] American Linear Collider Working Group, *Linear Collider Physics Resource Book for Snowmass 2001*, BNL-52627, CLNS 01/1729, Fermilab-Pub-01/058-E, LBNL-47813, SLAC-R-570, UCRL-ID-143810-DR, LC-REV-2001-074-US.

[2] Strickland, D. and Mourou G., "Compression of amplified chirped optical pulses," *Opt. Commun.* **56**:219-221, 1985.

[3] Perry, M.D. and Mourou G., "Terawatt to petawatt sub-picosecond lasers," *Science*, **264**:917-924, 1994.

[4] Yokoya, K., "A Computer Simulation Code for the Beam-Beam Interaction in Linear Colliders", KEK Report 85-9, October 1985.

[5] Asner, D., Gronberg, J., Gunion, J. and Hill T., UCRL-ID-143967.